

Rare-earth aluminosilicate ($\text{RE}_2\text{O}_3\text{-Al}_2\text{O}_3\text{-SiO}_2$) glasses and their application as solders for joining of silicon carbide components

Zur Erlangung des akademischen Grades

Doktor der Ingenieurwissenschaften

Der Fakultät für Maschinenbau

Karlsruher Institut für Technologie (KIT)

genehmigte

Dissertation

von

M.Sc. Sarfraz Ahmad

Tag der mündlichen Prüfung: December 20, 2017

Hauptreferent: Prof. Dr. Hans Jürgen Seifert

Korreferent: PD. Dr.-Ing. Wolfgang Lippmann

Table of Contents

THESIS SUMMARY	1
ZUSAMMENFASSUNG	5
1 INTRODUCTION.....	10
1.1 MOTIVATION	10
1.2 OBJECTIVES	12
1.3 WORK PACKAGES.....	12
1.4 THESIS ORGANISATION.....	13
2 RARE-EARTH ALUMINOSILICATE GLASSES	14
2.1 GLASS	14
2.1.1 <i>Introduction</i>	14
2.1.2 <i>Glass transformation</i>	15
2.2 GLASS FORMATION THEORIES.....	16
2.2.1 <i>Structural theories of glass formation</i>	16
2.2.2 <i>Kinetic theories of glass formation</i>	18
2.3 RARE-EARTH ALUMINOSILICATE GLASSES	25
2.3.1 <i>Introduction</i>	25
2.3.2 <i>Structure</i>	28
2.3.3 <i>Properties</i>	28
2.3.4 <i>Applications</i>	29
2.4 MICROWAVE HEATING.....	30
2.5 RARE-EARTH ALUMINOSILICATE GLASSES CONTAINING NUCLEATING AGENTS	31
2.6 RARE-EARTH ALUMINOSILICATE GLASSES CONTAINING NITROGEN	31
2.7 CHARACTERIZATIONS OF GLASSES.....	34
2.7.1 <i>Infrared spectroscopy of glasses</i>	34
2.7.2 <i>Raman spectroscopy of glasses</i>	35
2.7.3 <i>Nuclear magnetic resonance spectroscopy of glasses</i>	36
2.7.4 <i>Thermal analyses of glasses</i>	36
3 JOINING OF SILICON CARBIDE COMPONENTS	39
3.1 SILICON CARBIDE	39
3.1.1 <i>Fabrication of silicon carbide</i>	39
3.1.2 <i>Structure</i>	39
3.1.3 <i>Properties</i>	39
3.1.4 <i>Application</i>	40
3.2 JOINING TECHNOLOGIES.....	40
3.2.1 <i>Introduction</i>	40
3.2.2 <i>Different joining techniques</i>	40
3.2.3 <i>Spark plasma sintering joining</i>	43
3.2.4 <i>Laser joining</i>	43
4 MATERIALS AND EXPERIMENTAL METHODS	45
4.1 PREPARATION OF GLASSES	45
4.1.1 <i>Preparation of rare-earth aluminosilicate glasses</i>	45
4.1.2 <i>Preparation of TiO₂ and ZrO₂ containing yttria and neodymia aluminosilicate glasses</i>	47
4.1.3 <i>Preparation of nitrogen-containing yttria and neodymia aluminosilicate glasses</i>	48
4.2 CHARACTERIZATION INSTRUMENTS/TECHNIQUES	49
4.2.1 <i>X-ray powder diffraction</i>	49

4.2.2	<i>X-ray fluorescence</i>	50
4.2.3	<i>Spectroscopy</i>	50
4.2.4	<i>In-situ XRD</i>	51
4.2.5	<i>Scanning electron microscopy and electron microprobe analysis</i>	51
4.2.6	<i>Differential scanning calorimetry</i>	51
4.2.7	<i>Differential thermal analysis</i>	51
4.2.8	<i>Dilatometry</i>	52
4.2.9	<i>Thermal diffusivity</i>	52
4.2.10	<i>Density measurement</i>	52
4.2.11	<i>Thermal conductivity</i>	52
4.2.12	<i>Refractive indices measurement</i>	52
4.2.13	<i>Micro-hardness measurement</i>	52
4.2.14	<i>Leakage test</i>	52
4.2.15	<i>4-point bending test</i>	52
4.2.16	<i>Joint preparation of SiC components</i>	53
4.2.17	<i>Laser joining of SiC components</i>	53
4.2.18	<i>Joining of SiC components using spark plasma sintering process</i>	53
5	RESULTS	54
5.1	STRUCTURAL ANALYSES OF RARE-EARTH ALUMINOSILICATE GLASSES	54
5.1.1	<i>Chemical analyses of rare-earth aluminosilicate glasses</i>	55
5.1.2	<i>XRD analyses of rare-earth aluminosilicate glasses</i>	55
5.1.3	<i>Infrared analyses of rare-earth aluminosilicate glasses</i>	55
5.1.4	<i>Raman analyses of rare-earth aluminosilicate glasses</i>	57
5.1.5	<i>Solid NMR analyses of rare-earth aluminosilicate glasses</i>	59
5.2	THERMAL ANALYSES OF RARE-EARTH ALUMINOSILICATE GLASSES	61
5.2.1	<i>Differential thermal analyses of glasses</i>	61
5.2.2	<i>Softening analysis of glass</i>	62
5.2.3	<i>Differential scanning calorimetry of glasses</i>	63
5.2.4	<i>Specific heat capacities of glasses</i>	64
5.2.5	<i>Dilatometer analyses of glasses</i>	64
5.2.6	<i>Thermal diffusivity of glasses</i>	65
5.2.7	<i>Thermal conductivity of glasses</i>	65
5.3	PHYSICAL PROPERTIES OF GLASSES	66
5.3.1	<i>Densities measurement of glasses</i>	66
5.3.2	<i>Hardness measurement of glasses</i>	66
5.3.3	<i>Refractive indices measurement of glasses</i>	66
5.4	CRYSTALLIZATION STUDIES OF RARE-EARTH-ALUMINOSILICATE GLASSES	67
5.4.1	<i>Hot-stage XRD of Yttrium-aluminosilicate glasses</i>	67
5.4.1	<i>Heat-treatment of Yttrium-aluminosilicate glasses</i>	69
5.4.2	<i>Raman analyses of heat-treated samples</i>	73
5.4.3	<i>IR analyses of heat-treated samples</i>	73
5.4.4	<i>Crystallization of Ytterbium-aluminosilicate glasses</i>	74
5.4.5	<i>Crystallization of Holmium-aluminosilicate glasses</i>	77
5.4.6	<i>Crystallization of Dysprosium-aluminosilicate glasses</i>	81
5.4.7	<i>Crystallization of Neodymium-aluminosilicate glasses</i>	84
5.4.8	<i>Crystallization of Scandium-aluminosilicate glasses</i>	89
5.5	JOINING OF SiC COMPONENTS USING RARE-EARTH ALUMINOSILICATE GLASS SOLDERS	92
5.5.1	<i>Joining of SiC parts via laser process</i>	92
5.5.2	<i>Characteristics of the joining process</i>	92

5.5.3	<i>Characterizations of the joints</i>	93
5.6	MICROWAVE HEAT-TREATMENT OF RARE-EARTH ALUMINOSILICATE GLASSES	96
5.6.1	<i>Structural analyses of microwave heat-treated samples</i>	97
5.7	YTTRIA AND NEODYMIA ALUMINOSILICATE GLASSES CONTAINING NUCLEATING AGENTS	102
5.7.1	<i>Structural analyses of glasses containing nucleating agents</i>	102
5.7.2	<i>Thermal analyses of glasses containing nucleating agents</i>	105
5.7.3	<i>Crystallization of nucleating agents containing Yttrium- aluminosilicate glasses</i>	110
5.7.4	<i>Crystallization of nucleating agents containing Neodymium-aluminosilicate glasses</i>	116
5.8	NITROGEN-CONTAINING YTTRIA AND NEODYMIA ALUMINOSILICATE GLASSES.....	122
5.8.1	<i>Structural analyses of nitrogen-containing glasses</i>	123
5.8.2	<i>Thermal analyses of nitrogen-containing glasses</i>	125
5.8.3	<i>Crystallization of nitrogen-containing rare-earth aluminosilicate glasses</i>	126
5.8.1	<i>Thermal treatment of samples under nitrogen</i>	127
5.8.2	<i>Thermal treatment of samples under argon</i>	129
5.8.3	<i>Thermal treatment of samples under vacuum</i>	130
5.8.1	<i>Thermal treatment of samples under air</i>	130
5.9	JOINING OF SiC WITH NITROGEN-CONTAINING YTTRIA AND NEODYMIA GLASSES	132
5.10	SPARK PLASMA SINTERING JOINING OF SiC COMPONENTS	133
5.10.1	<i>Joining of SiC components using Yttrium-aluminosilicate glass solders</i>	133
5.10.2	<i>Characterizations of the joined samples</i>	134
6	DISCUSSION	136
6.1	RARE-EARTH ALUMINOSILICATE GLASSES	136
6.1.1	<i>Structural characterization of rare-earth aluminosilicate glasses</i>	136
6.1.2	<i>Thermal characterization of rare-earth aluminosilicate glasses</i>	137
6.1.3	<i>Physical properties of rare-earth aluminosilicate glasses</i>	138
6.1.4	<i>Crystallization studies of rare-earth-aluminosilicate glasses</i>	138
6.1.5	<i>Laser-joining of SiC components using rare-earth aluminosilicate glasses</i>	139
6.2	CRYSTALLIZATION OF GLASSES USING MICROWAVE PROCESSING	141
6.3	YTTRIA AND NEODYMIA GLASSES CONTAINING NUCLEATING AGENTS	142
6.4	NITROGEN-CONTAINING YTTRIA AND NEODYMIA ALUMINOSILICATE GLASSES.....	144
6.5	SPARK PARK PLASMA SINTERING JOINING OF SiC COMPONENTS.....	147
7	CONCLUSION AND RECOMMENDATIONS	148
	ACKNOWLEDGEMENTS	151
8	REFERENCES	152

Thesis Summary

Rare-earth aluminosilicate glasses ($\text{RE}_2\text{O}_3\text{-Al}_2\text{O}_3\text{-SiO}_2$, RE: rare-earth elements) have shown great potential for many technical applications due to their high value of hardness, good resistance to oxidation and corrosive environment, high glass transition temperatures, and low coefficients of thermal expansion. These properties make rare-earth aluminosilicate glasses possible candidates to be used to produce refractory glass-to-ceramic seals. This potential application makes it essential to investigate and understand their glass structures, properties and crystallization behaviour under long heat-treatment conditions. The joining of ceramic components, especially SiC materials, for assembling complex structures is a scientific and engineering challenge. SiC materials cannot be joined using conventional welding processes due to their non-melting nature. Therefore, soldering materials and joining processes are needed which can join SiC components in short period of time and maintaining superior properties of the produced joints at higher temperatures for longer duration.

In the present study, $\text{RE}_2\text{O}_3\text{-Al}_2\text{O}_3\text{-SiO}_2$ (RE = Y, Yb, Ho, Dy, Nd and Sc) glasses were prepared using the melt-quench route. Pure oxide powders of Y_2O_3 , Yb_2O_3 , Ho_2O_3 , Dy_2O_3 , Nd_2O_3 , Sc_2O_3 , SiO_2 and Al_2O_3 , respectively were used for the preparation. The well-known SiO_2 -rich eutectic composition 12.18% Y_2O_3 -22% Al_2O_3 -65.82% SiO_2 (mole %) was used as main composition and Y_2O_3 was replaced by the same amount of Yb_2O_3 , Ho_2O_3 , Dy_2O_3 , Nd_2O_3 and Sc_2O_3 , respectively. The chemical compositions of produced glasses were determined using X-ray fluorescence technique (XRF) and found closely matching with the initial compositions of oxide mixtures. X-ray diffraction (XRD) revealed typical amorphous structures. Infrared (IR) spectra of glasses indicated symmetric and asymmetric stretching of Si-O-Si bands. Raman spectra revealed high amount of Q^3 and Q^4 structural units in these glasses. It was found that high contents of Q^3 structural units were due to the uniform distribution of the rare-earth ions and the non-bridging oxygen (NBO). The magnetic susceptibility analyses showed that glasses with Y- and Sc-cations, respectively, have diamagnetic nature, glasses containing Yb-, and Nd-cations, respectively, showed intermediate character in the range of diamagnetic and paramagnetic and glasses consisting of Ho-, and Dy-cations, respectively, have paramagnetic nature. ^{27}Al spectra of glasses containing Y-, Yb-, and Nd-cations, respectively showed high fractions of AlO_5^-7 and AlO_6^-9 groups and the glass containing Sc-cation have 4-, 5-, and 6-fold-coordinated aluminum. This high Al-coordination is due to higher field strength of rare-earth cations.

Prepared glasses were thermally analyzed to determine their glass transition temperatures, crystallization temperatures, specific heats, thermal diffusivities, thermal conductivities and coefficients of thermal expansion. It was found that glasses containing Yb-cations show the highest value of glass transition temperature which could be attributed to the smaller ionic radius of Yb^{+3} as compared to Y^{+3} , Ho^{+3} , Dy^{+3} and Nd^{+3} . Smaller ionic radii increase cationic field strength and tighten the structures as compared to ions with larger radii, which results in higher glass transition

temperatures. Crystallization temperatures of glasses containing Y-, Yb-, Ho- and Dy-cations were found in the range of 1175–1210 °C. Glasses with Sc-cation showed lowest crystallization temperature (~ 1065 °C), while glasses with Nd-cations started to flow after glass transformation temperature and did not show any pronounced crystallization peak. Specific heat values of glasses were measured up to 800 °C using the 3-step method in DSC. Thermal diffusivities values of the produced glasses were determined up to 700 °C with laser flash method. Thermal conductivities of glasses at room temperature were calculated by multiplying their specific heat values with thermal diffusivities and densities. The coefficients of thermal expansion of prepared glasses were determined up to 700 °C with dilatometer and the measured values were found closely matching with SiC.

Physical properties such as densities, hardness and refractive indices of glasses were determined to establish a structure-property relationship. It was found that densities of these glasses are depending on the atomic mass and on the radius of the rare-earth ion. Glasses containing Nd-cations show the highest density while glasses with Sc-cations have the lowest. The measured hardness values of the produced glasses increase with decreasing radii of the rare-earth ions. Glasses with Sc-cations reveal the highest hardness and glasses containing Nd-cations have the lowest. The refractive indices of glasses were found in the range of 1.68 – 1.74. One can summarize that rare-earth ion type had minor effect on the refractive indices of these glasses.

Powder samples of glasses were heated at 10 K/min from room temperature up to 1200 °C during hot-stage XRD analyses at interval of 50 °C with holding time of 30 minutes during each span to evaluate crystallization behaviour and related phase formations. The diffraction patterns showed complete amorphous structures up to 900 °C without any reflections. The maximum crystallization in Y-, Yb-, Ho-, and Dy-containing glasses took place between 1100–1200 °C and for Sc-containing glasses in the range of 1050–1100 °C. Then glasses were heat-treated at higher temperature (1200 °C) for different periods of time (1h and 50h) to characterize the formed crystalline phases. The main phases observed were silicates of rare-earth elements and mullite. Feathers-like crystals of yttrium-disilicate were in large excess in the yttrium-aluminosilicate partially crystallized sample surrounded by mullite. Needles-like crystals of neodymium-disilicate were observed in neodymium-aluminosilicate samples embedded in the remaining glassy matrix with small amount of mullite phase. These Nd-disilicate crystals were extended from the surface towards the centre of the samples which shows that surface crystallization process occurs in this glass system. Raman spectra of heat-treated samples revealed high contents of Q^3 structural units due to uniform distribution of RE^{+3} ions and NBO. IR-spectra indicated strong asymmetric and symmetric stretching of Si-O-Si modes with slightly different wave numbers.

Prepared glasses were used as soldering materials for joining of SiC components via a laser-based process at TU Dresden. The joints were investigated using scanning electron microscopy (SEM), electron probe microanalyses (EPMA), helium leakage tests and 4-point bending experiments.

All glasses showed good wettability with SiC surfaces and produced glassy interlayer between SiC components except scandium-aluminosilicate glasses which crystallized into crystals of scandium-disilicate and mullite. Joints produced with yttrium-aluminosilicate and neodymium-aluminosilicate glasses showed the highest bending strength (~135 MPa and ~150 MPa respectively).

Microwave heating has shown a great potential to process materials, control their structures and properties. It provides many advantages as compared to conventional heating processes due to its rapid and selective heating, less processing time and improved quality of products. The effects of microwave heating on the crystallization of $\text{RE}_2\text{O}_3\text{-Al}_2\text{O}_3\text{-SiO}_2$ (RE stands for Nd, Y) glasses were established. These glasses were heat-treated for different periods of time (no holding time, 15 min and 30 min) at high temperatures (1200 °C) using microwave-heating as power source. Microwave-processed samples were structurally analysed using XRD, SEM, IR- and Raman spectroscopy and compared with crystallized samples annealed at 1200 °C for 50h in a conventional furnace. The crystal nucleation and growth mechanisms were more homogenous in microwave annealed samples. It was found that microwave heating enhanced crystallization kinetics in $\text{Y}_2\text{O}_3\text{-Al}_2\text{O}_3\text{-SiO}_2$ glass samples. However, its effects on $\text{Nd}_2\text{O}_3\text{-Al}_2\text{O}_3\text{-SiO}_2$ samples were not so pronounced.

Properties of glasses can be controlled by changing their compositions, with controlled heat-treatment and by addition of nucleating agents. Proper amount of nucleating agents affect microstructures and properties significantly. The effects of different nucleating agents (TiO_2 , ZrO_2) and their amounts (4–8 mass %) on the properties and the structures of $\text{RE}_2\text{O}_3\text{-Al}_2\text{O}_3\text{-SiO}_2$ (RE stands for Nd, Y) glasses were explored. Structures of these nucleating agents containing glasses were investigated using ex/in-situ XRD and different spectroscopic techniques. It was observed that the addition of TiO_2 has significant influence on the structural units and transition temperatures as compared to ZrO_2 . Thermal analyses showed that additions of TiO_2 results in decreased glass transition and crystallization temperatures. A decrease by around 50 °C in glass transition temperature and nearly 100 °C in crystallization temperature was noticed for $\text{Y}_2\text{O}_3\text{-Al}_2\text{O}_3\text{-SiO}_2$ glasses containing 8 % TiO_2 . However, the effects of ZrO_2 addition on transition temperatures were minor as compared to TiO_2 . Moreover, nucleating agents containing glasses were annealed at 1200 °C for 50h to evaluate the effects of long heat-treatment on their structures. XRD of TiO_2 containing yttrium-aluminosilicate samples showed reflections of mullite, Y-disilicate, cristobalite, and yttrium-titanium oxide. Yttrium showed the tendency to react with TiO_2 to form yttrium-titanium oxide and the amount of this ternary oxide increased with increasing TiO_2 contents in the sample. XRD of yttrium-aluminosilicate samples with ZrO_2 showed reflections of mullite, Y-disilicate, cristobalite, and yttrium-zirconium oxide. It was found that the addition of nucleating agents strongly enhanced the crystallization process in these glasses.

Glasses ($\text{RE}_2\text{O}_3\text{-Al}_2\text{O}_3\text{-SiO}_2\text{-Si}_3\text{N}_4$, RE stands for Nd, Y) containing different amount of nitrogen contents (4 and 8.33 mole %) were prepared to determine the effects of anions on the structures and the properties of rare-earth aluminosilicate glasses. The nitrogen-containing glasses were structurally investigated to find out the effects of nitrogen additions on the structural units and stretching modes. Thermal analyses showed that addition of nitrogen significantly increases glass transition temperatures, an increase of 40 °C and 60 °C for glass transition temperature of yttrium glasses were found by increasing nitrogen contents from 4 to 8.33 mole %, respectively. These glasses were heat-treated for different periods of time at 1200 °C under atmospheres of nitrogen, argon, vacuum and air, respectively. This work was done to find the effects of various atmospheres on crystallization process and oxidation resistance in these glasses. It was found that the addition of nitrogen has strong influence on the crystallization process and different modifications of Y-disilicate were observed at the sample edges and at the centre. The D-phase ($\text{YSi}_2\text{AlO}_4\text{N}_2$) was observed only in glasses containing 8.33 mole % nitrogen contents. The nitrogen-containing glasses show low oxidation resistance, and have porous structures due to escaping of nitrogen from glass structures after aging in air. Neodymium-aluminosilicate glasses containing nitrogen contents have the lowest oxidation resistance and experienced viscous flow at 1200 °C, which is almost 200 °C lower temperature as compared to findings from DSC.

The nitrogen-glasses were used as solders for joining SiC structural components via a laser-assisted process. The qualitative and quantitative phase analyses of the produced joints showed a sound joint between SiC surfaces and the glassy interlayer. It was found that nitrogen-containing glasses can be used as soldering materials for joining SiC parts. However, it is important that the joining process should be performed under inert atmospheres (argon, nitrogen) to avoid oxidation of glasses.

Spark plasma sintering (SPS) is a localized heating process and provides a number of advantages due to rapid heating and short process time. $\text{Y}_2\text{O}_3\text{-Al}_2\text{O}_3\text{-SiO}_2$ glasses were used as solders for joining SiC components using SPS process. The process parameters for SPS joining were optimized to obtain a sound joint between SiC parts. The characterization of the interface layer between SiC matrix and glassy solder showed crystals of Y-disilicate and mullite.

This work showed that rare-earth aluminosilicate glasses have great potential to be used as solders for joining structural ceramics components using laser-based joining process. These glasses showed good wettability with SiC surfaces and produced tight joints with high mechanical strength. However, joint properties varied and depending upon solder compositions.

Zusammenfassung

Seltenerd-Aluminosilikat-Gläser ($\text{RE}_2\text{O}_3\text{-Al}_2\text{O}_3\text{-SiO}_2$, RE: Seltenerdelemente) haben aufgrund der hohen Härte, der guten Oxidations- und Korrosionsbeständigkeit, der hohen Glasübergangstemperaturen und der geringen Wärmeausdehnungskoeffizienten für viele technische Anwendungen ein großes Anwendungspotenzial. Diese Eigenschaften machen Seltenerd-Aluminosilikat-Gläser zu möglichen Kandidaten für die Herstellung von hochschmelzenden/hochtemperatur-stabilen Glas-zu-Keramik-Dichtungen. Angesichts dieser Anwendungsmöglichkeit ist es zwingend notwendig die Glasstrukturen, Eigenschaften und das Kristallisationsverhalten der Seltenerd-Aluminosilikat-Gläser während langen Wärmebehandlungen zu untersuchen und zu verstehen. Das Zusammenfügen von keramischen Bauteilen, insbesondere von SiC-Werkstoffen, zum Aufbau komplexer Strukturen ist eine wissenschaftliche und technische Herausforderung. Da sich SiC-Materialien nicht aufschmelzen lassen, können sie nicht mittels konventioneller Schweißprozesse verbunden werden. Daher sind Lötmaterialien und Fügeprozesse erforderlich, die in kurzer Zeit SiC-Komponenten verbinden und die überlegenen Eigenschaften der erzeugten Fügebindungen bei hohen Temperaturen für längere Dauer aufrechterhalten.

In der vorliegenden Arbeit wurden $\text{RE}_2\text{O}_3\text{-Al}_2\text{O}_3\text{-SiO}_2$ (RE = Y, Yb, Ho, Dy, Nd und Sc) Gläser unter Verwendung der "Melt-quench route" hergestellt/synthetisiert. Für die Herstellung wurden reine Pulver der Oxide Y_2O_3 , Yb_2O_3 , Ho_2O_3 , Dy_2O_3 , Nd_2O_3 , Sc_2O_3 , SiO_2 und Al_2O_3 verwendet. Die bekannte SiO_2 -reiche eutektische Zusammensetzung 12.18% Y_2O_3 -22% Al_2O_3 -65.82% SiO_2 (Mol-%) wurde als Hauptzusammensetzung verwendet und Y_2O_3 wurde durch die gleiche Menge an Yb_2O_3 , Ho_2O_3 , Dy_2O_3 , Nd_2O_3 bzw. Sc_2O_3 ersetzt. Die chemischen Zusammensetzungen der hergestellten Gläser wurden unter Verwendung der Röntgenfluoreszenztechnik (XRF) überprüft, wobei die Ergebnisse gut mit den Anfangszusammensetzungen der Oxidgemische übereinstimmten. Röntgenbeugung (XRD) zeigte typische amorphe Strukturen mit inhärent ungeordneter Struktur auf den Zwischen- und größerin-Längenskalen. Infrarot Spektren (IR) der Gläser zeigten symmetrische und asymmetrische Streckungen der Si-O-Si-Bänder. Raman-Spektren zeigten eine hohe Menge an Q^3 - und Q^4 -Struktureinheiten in diesen Gläsern. Es wurde festgestellt, dass hohe Gehalte an Q^3 -Struktureinheiten auf die gleichmäßige Verteilung der Seltenerd-Ionen und von Nicht-Brücken Sauerstoff (NBO) zurückzuführen waren. Die magnetischen Suszeptibilitätsanalysen zeigten, dass Gläser mit Y- und Sc-Kationen diamagnetischer Natur sind; Gläser, die Yb- und Nd-Kationen enthalten, zeigten einen intermediären Charakter zwischen diamagnetischem und paramagnetischem Bereich und Gläser, bestehend aus Ho- und Dy-Kationen verfügten über eine paramagnetische Natur. ^{27}Al -Spektren der Gläser, die Y-, Yb- und Nd-Kationen enthielten, zeigten jeweils hohe Anteile an AlO_5^{-7} und AlO_6^{-9} -Gruppen. Das Sc-Kationen enthaltende Glas wies 4-, 5- und 6-fach-koordiniertes Aluminium auf. Diese hohe Al-Koordination ist auf eine höhere Feldstärke der Seltenerd-Kationen zurückzuführen.

Die hergestellten Gläser wurden thermisch analysiert, um die jeweiligen Glasübergangstemperaturen, Kristallisationstemperaturen, spezifischen Wärmen, thermische Diffusivitäten, Wärmeleitfähigkeiten und Wärmeausdehnungskoeffizienten zu bestimmen. Es wurde festgestellt, dass Gläser mit Yb-Kationen weisen die höchste Glasübergangstemperatur auf, die auf den kleineren Ionenradius von Yb^{+3} im Vergleich zu Y^{+3} , Ho^{+3} , Dy^{+3} und Nd^{+3} zurückzuführen war. Kleinere Ionenradien erhöhen die kationische Feldstärke und straffen die Strukturen im Vergleich zu Ionen mit größeren Radien, was wiederum zu höheren Glasübergangstemperaturen führt. Kristallisationstemperaturen der Gläser, die Y-, Yb-, Ho- und Dy-Kationen enthielten, lagen im Bereich von 1175–1210 °C. Gläser mit Sc-Kation wiesen eine niedrige Kristallisationstemperatur (~ 1065 °C) auf, während Gläser mit Nd-Kationen nach der Glasumwandlungstemperatur flossen und über keine ausgeprägte Kristallisation zeigten. Spezifische Wärmewerte der Gläser wurden bis 800 °C mittels DSC gemessen. Die thermischen Diffusivitätswerte der hergestellten Gläser wurden bis zu 700 °C mit der Laser Flash Methode bestimmt. Die Wärme leitfähigkeiten der Gläser bei Raumtemperatur wurden durch Multiplikation der jeweiligen spezifischen Wärmewerte mit den thermischen Diffusivitäten und Dichten berechnet. Die Wärmeausdehnungskoeffizienten der hergestellten Gläser wurden bis zu 700 °C mit Dilatometrie bestimmt. Diese stimmten eng mit Messwerten für SiC überein.

Physikalische Eigenschaften wie Dichte, Härte und Brechungsindizes der Gläser wurden bestimmt, um Struktur-Eigenschafts-Beziehungen herzustellen. Es wurde festgestellt, dass die Dichten dieser Gläser von der Atommasse und vom Radius des Seltenerd-Ions abhängen. Gläser, die Nd-Kationen enthalten, zeigen die höchsten Dichtewerte, während die Dichte bei Gläsern mit Sc-Kationen den niedrigsten Wert aufweist. Die gemessenen Härtewerte der hergestellten Gläser nehmen mit abnehmenden Radien der Seltenerd-Ionen zu. Gläser mit Sc-Kationen besitzen die höchste Härte und Gläser mit Nd-Kationen hingegen die niedrigsten Härtewerte. Die Brechungsindizes der Gläser wurden im Bereich von 1,68–1,74 ermittelt. Zusammenfassend kann gesagt werden, dass der Seltenerd-Ionen-Typ eine geringe Auswirkung auf die Brechungsindizes der untersuchten Gläser hatte.

Um das Kristallisationsverhalten und die damit verbundenen Phasenbildungen zu untersuchen, wurden Pulverproben der Gläser von Raumtemperatur bis 1200 °C mit Hochtemperatur-XRD untersucht. Es wurden Temperaturintervalle von 50 °C, Haltezeiten von 30 Minuten und Heizraten von 10 K/min verwendet. Die Beugungsmuster zeigten vollständig amorphe Strukturen bis zu 900 °C ohne Reflexe. Die maximale Kristallisation erfolgte bei Y-, Yb-, Ho-, Dy- und Nd-haltigen Gläsern zwischen 1100-1200 °C und für Sc-haltige Gläser im Bereich von 1050-1100 °C. Anschließend wurden die Gläser bei höheren Temperaturen (1200 °C) für verschiedene Zeiten (1 Std. und 50 Std.) wärmebehandelt, um die gebildeten kristallinen Phasen zu charakterisieren. Die beobachteten Hauptphasen waren Seltenerd- und Mullitsilikate. Die federartigen Kristalle des Yttrium-Disilikats waren im großen Mengen in der partiell kristallisierten Probe des Yttrium-Aluminosilikats vorhanden, umgeben von Mullit. In Neodym-Aluminosilikat-Proben wurden nadelförmige Kristalle von Neodym-

Disilikat beobachtet, die in die verbleibende glasartige Matrix mit einem geringen Anteil an Mullit eingebettet waren. Diese Nd-Disilikat-Kristalle wuchsen von der Oberfläche zur Mitte der Proben, was veranschaulicht, dass der Oberflächenkristallisationsvorgang in diesem Glassystem auftritt. Raman-Spektren von wärmebehandelten Proben zeigten einen hohen Gehalt an Q^3 -Struktureinheiten aufgrund einer gleichmäßigen Verteilung von RE^{+3} -Ionen und NBO. IR-Spektren zeigten eine starke asymmetrische und symmetrische Streckung der Si-O-Si mit leicht unterschiedlichen Wellenzahlen.

Die hergestellten Gläser wurden als Lötmaterial zum Verbinden von SiC-Komponenten mit einem laserbasierten Verfahren verwendet. Die Verbindungen wurden unter Verwendung von Rasterelektronenmikroskopie (SEM), Elektronensonden-Mikroanalysen (EPMA), Helium-Leckage-Tests und 4-Punkt-Biegeversuchen charakterisiert. Außer den Scandium-Aluminosilikat-Gläser, welche zu Scandium-Disilikat- und Mullitkristallen kristallisierten, zeigten alle anderen Gläser eine gute Benetzbarkeit der SiC-Oberflächen und erzeugten eine glasartige Zwischenschicht zwischen den SiC-Komponenten. Verbindungen, die mit Yttriumaluminosilikat- und Neodymaluminosilikat-gläsern hergestellt wurden, zeigten die höchsten Biegefestigkeiten (~ 135 MPa bzw. ~ 150 MPa).

Mikrowellenheizen hat sich als eine hervorragende Möglichkeit erwiesen, Materialien zu verarbeiten und deren Strukturen und Eigenschaften zu kontrollieren. Es bietet viele Vorteile gegenüber herkömmlichen Heizprozessen aufgrund der schnellen und selektiven Heizung, der geringeren Bearbeitungszeit und der verbesserten Produktqualitäten. Die Effekte des Mikrowellenheizens auf die Kristallisation von $RE_2O_3-Al_2O_3-SiO_2$ (RE steht für Nd, Y) Gläser wurden festgestellt. Diese Gläser wurden für verschiedene Zeiträume (keine, 15 min und 30 min Haltezeit) bei hohen Temperaturen ($1200\text{ }^\circ\text{C}$) unter Verwendung von Mikrowellenerwärmung als Wärmequelle wärmebehandelt. Mittels Mikrowellen verarbeitete Proben wurden unter Verwendung von XRD-, SEM-, IR- und Raman-Spektroskopie strukturell analysiert und mit kristallisierten Proben, die bei 1200°C für 50 Stunden in einem herkömmlichen Ofen getempert wurden, verglichen. Die Kristallkeimbildungs- und Wachstumsmechanismen waren in mikrowellengeglühten Proben homogener. Es wurde festgestellt, dass die Mikrowellenerwärmung die Kristallisationskinetik in $Y_2O_3-Al_2O_3-SiO_2$ -Glasproben verstärkte. Allerdings waren die Auswirkungen auf $Nd_2O_3-Al_2O_3-SiO_2$ -Proben wenig ausgeprägt.

Die Eigenschaften der Gläser können durch Veränderung ihrer Zusammensetzungen mit kontrollierter Wärmebehandlung und durch Zugabe von Keimbildnern gesteuert werden. Die richtige Menge an Keimbildnern beeinflusst die Mikrostrukturen und Eigenschaften erheblich. Die Wirkungen verschiedener Keimbildner (TiO_2 , ZrO_2) und deren Mengen (4 und 8 Masse %) auf die Eigenschaften und Strukturen von $RE_2O_3-Al_2O_3-SiO_2$ (RE steht für Nd, Y) Gläser wurden untersucht. Die Strukturen dieser Keimbildner enthaltenden Gläser, wurden unter Verwendung von ex/in-situ XRD und verschiedenen spektroskopischen Techniken untersucht. Es wurde beobachtet, dass die Zugabe von TiO_2 im Vergleich zu ZrO_2 einen signifikant höheren Einfluss auf die Struktureinheiten und

Übergangstemperaturen hat. Thermische Analysen zeigten, dass die Zugabe von TiO_2 zu verringerten Glasübergangs- und Kristallisationstemperaturen führt. Für $\text{Y}_2\text{O}_3\text{-Al}_2\text{O}_3\text{-SiO}_2$ -Gläser mit 8% TiO_2 wurde eine Abnahme der Glasübergangstemperatur um etwa 50°C und der Kristallisationstemperatur um nahezu 100°C festgestellt. Allerdings waren die Auswirkungen der ZrO_2 -Beigaben auf die Übergangstemperaturen im Vergleich zu TiO_2 gering. Darüber hinaus wurden Gläser, die Keimbildner enthielten, bei 1200°C für 50 Stunden getempert, um die Effekte einer langen Wärmebehandlung auf ihre Strukturen zu bewerten. Röntgen-Analysen von TiO_2 -haltigen Yttriumaluminosilicat-Proben zeigten Reflexe von Mullit, Y-Disilikat, Cristobalit und Yttrium-Titanoxid. Yttrium zeigte die Tendenz, mit TiO_2 zu reagieren und Yttrium-Titanoxid zu bilden. Die Menge dieses ternären Oxids nahm mit zunehmenden TiO_2 -Gehalt in der Probe zu. Yttriumaluminosilicatproben mit ZrO_2 -Keimbildnern zeigten die Bildung von Mullit, Y-Disilikat, Cristobalit und Yttriumzirkonoxid. Es wurde festgestellt, dass die Zugabe von Keimbildnern den Kristallisationsvorgang in diesen Gläsern stark verstärkte.

Gläser ($\text{RE}_2\text{O}_3\text{-Al}_2\text{O}_3\text{-SiO}_2\text{-Si}_3\text{N}_4$, RE steht für Nd, Y) mit unterschiedlichen Stickstoffgehalten (4 und 8,33 Mol-%), wurden hergestellt, um die Effekte von Anionen auf die Strukturen und die Eigenschaften von Seltenerd-Aluminosilicat-Gläser zu untersuchen. Die stickstoffhaltigen Gläser wurden strukturell untersucht, um die Auswirkungen von Stickstoffzugaben auf die Struktureinheiten und Streckmodi zu untersuchen. Thermische Analysen zeigten, dass durch einen höheren Stickstoffgehalt die Glasübergangstemperaturen signifikant anstiegen. Bei einer Erhöhung des Stickstoffgehalts von 4 auf 8,33 Mol-% wurde eine Zunahme der Glasübergangstemperatur von 40°C und 60°C für Yttrium-Aluminosilicat-gläser ermittelt. Diese Gläser wurden für verschiedene Zeiträume bei 1200°C unter Atmosphären aus Stickstoff, Argon, Vakuum und Luft wärmebehandelt. Diese Arbeit wurde durchgeführt, um die Auswirkungen von unterschiedlichen atmosphärischen Bedingungen auf die Kristallisation und Oxidationsbeständigkeit der untersuchten Gläser zu erfassen. Es wurde festgestellt, dass die Zugabe von Stickstoff einen starken Einfluss auf den Kristallisationsvorgang hat. Weiterhin wurden verschiedene Modifikationen des Y-Disilikats an den Probenkanten und in der Mitte beobachtet. Die D-Phase ($\text{YSi}_2\text{AlO}_4\text{N}_2$) wurde nur in Gläsern beobachtet, die einen Stickstoffgehalt von 8,33 Mol-% enthielten. Die stickstoffhaltigen Gläser zeigen eine geringe Oxidationsbeständigkeit und haben aufgrund des Austritts von Stickstoff während der Alterung an Luft eine poröse Struktur. Stickstoffhaltige Neodym-Alumosilikate haben die niedrigste Oxidationsbeständigkeit und bei einer Temperatur von 1200°C findet bei den verwendeten Silikaten ein viskoses Fließen statt. Dieser Temperaturwert ist verglichen mit den mittels DSC erzielten Resultaten um nahezu 200°C niedriger.

Die stickstoffhaltigen Gläser wurden als Lötmaterial zum Fügen von SiC-Strukturkomponenten bei einem laserunterstützten Verfahren verwendet. Die qualitativen und quantitativen Phasenanalysen der erzeugten Fügenähte zeigten eine starke Verbindung zwischen den SiC-Oberflächen und der glasartigen Zwischenschicht. Es wurde festgestellt, dass als Lötmaterial zum Verbinden von SiC-

Teilen stickstoffhaltige Gläser verwendet werden können. Es ist jedoch wichtig, dass der Fügeprozess in inerter Atmosphäre (Argon, Stickstoff) durchgeführt wird, um eine Oxidation der verwendeten Gläser zu vermeiden.

Spark Plasma Sintering (SPS) ist ein lokaler Heizprozess und bietet aufgrund der schnellen Erwärmung und kurzen Prozesszeiten eine Reihe von Vorteilen. $Y_2O_3-Al_2O_3-SiO_2$ -Gläser wurden als Lötmedium zum Verbinden von SiC-Komponenten unter Verwendung des SPS-Verfahrens verwendet. Die Prozessparameter für die SPS-Verbindung wurden optimiert, um eine feste Verbindung zwischen SiC-Teilen zu erhalten. Die Charakterisierung der Grenzschicht zwischen SiC-Matrix und glasartigem Lot zeigte Y-Disilikat- und Mullitkristalle.

Diese Arbeit zeigt, dass Seltenerd-Aluminosilikat-Gläser ein großes Verwendungspotenzial haben, als Lötmedium zum Verbinden von Strukturkeramik-Komponenten, unter Verwendung eines laserbasierten Fügeprozesses, genutzt zu werden. Diese Gläser zeigten eine gute Benetzbarkeit mit SiC-Oberflächen und erzeugten starke Verbindungen mit hohen mechanischen Festigkeiten. Die Verbindungseigenschaften variierten jedoch und hingen von den Zusammensetzungen der Lote ab.

1 Introduction

This work was started from the objectives to investigate the rare-earth glasses and their potential application as solders for joining ceramic parts. Rare-earth glasses were chosen as soldering material due their high temperature stability and low coefficient of thermal expansion. Six elements (Y, Yb, Ho, Dy, Nd and Sc) were chosen for preparation of rare-earth aluminosilicate glasses using the melt-quench technique. These elements were selected due to their high transition temperatures, low thermal expansion and good wetting characteristics. An emphasis was given to explore structures of these glasses and their crystallization behavior under different heat-treatment conditions. These in-house produced glasses were used as glassy slurry for joining SiC components via an optimized laser processing technique. SiC is an important structural ceramic material that finds application in different fields of science and technology.

In this chapter details of the motivation to start this project and objectives of the present work are presented. Moreover, information regarding work packages and thesis organization is also included.

1.1 Motivation

Applications of glasses have been increased tremendously during last few decades. Glasses are used in home appliances, electronics devices, medical science, energy industry, optical industry, automotive industry, nuclear industry and many other fields [1-3]. These wide spread applications of glasses are due to their tunable properties that can be varied over broad range depending upon the glass components, their concentration and heating/cooling histories. Therefore, glasses provide a great potential to optimize their properties depending upon the user applications and requirements. The possible compositions of glasses are in billions because more than seventy percent of natural elements show potential to some extent to react with each other in different amounts to form glasses [2]. Therefore, a lot of research work is still needed to unfold the structures, properties and applications in the glass world.

Rare-earth aluminosilicate ($\text{RE}_2\text{O}_3\text{-Al}_2\text{O}_3\text{-SiO}_2$) glasses are of great importance because of their potential applications in different fields of science and technologies. Their developments provide high temperature stability of non-oxide ceramic materials such as liquid phase sintered SiC-, Si_3N_4 - and SiAlON-materials [4-7]. These glasses are used as drug delivery vehicle in medical science and for the radioactive waste immobilization [8, 9]. Moreover, they find applications in optical industry as fibers, optical amplifiers and solid state lasers [10]. They can be used to produce sealing between glass and ceramic/metals components due to their high glass transition temperatures and low thermal expansion coefficients [11, 12]. These extensive applications of rare-earth aluminosilicate glasses are due to their higher glass transition temperatures, good resistance to oxidation and corrosive

environment as compared to alkali/alkaline aluminosilicate glass systems [13-16]. These superior properties make these glasses a good choice to be used in high temperature technical applications.

Joining of ceramic parts especially for silicon carbide (SiC) components is a scientific and engineering challenge. SiC is an important structural ceramic material that finds applications in many industries including nuclear industry, aerospace industry, automotive industry, heat exchangers, ball valves, etc. [17, 18]. Such widespread applications of SiC are due to its superior properties in corrosive atmosphere and in severe conditions at elevated temperatures [17]. To design large scale components the joining of SiC parts may be required. In industry diffusion bonding and reaction bonding are mainly used for joining SiC components. However, these methods require high temperatures and pressures for longer period of time that makes joining expensive and complicated. Furthermore, it is not feasible in most cases to heat up the whole components at higher temperatures for longer duration [19]. The applications of metallic solders for joining of SiC components provide alternative options. The metallic brazing can enhance ductility in the joints but metallic materials normally show relatively higher coefficients of thermal expansion as compared to SiC and the risk of high residual stresses in the joints cannot be excluded [20]. Therefore, such soldering materials are essential for joining SiC components that show lower coefficients of thermal expansion and maintain superior joint properties at higher temperatures for longer period of times. Rare-earth aluminosilicate glasses could be a good choice for joining of SiC components due to their low coefficient of thermal expansions and high temperature stability. This potential application makes it essential to investigate structures, properties and crystallization behaviour of these glasses under long heat-treatment conditions.

In this work, $RE_2O_3-Al_2O_3-SiO_2$ (RE = Y, Yb, Ho, Dy, Nd and Sc) glasses should be prepared and investigated extensively using different structural and thermal analyses tools/techniques. They will be used as solders for joining of SiC components via optimized laser process. The prepared joints will be investigated to check the potential of these glasses as soldering materials for hermetic sealing.

Microwave heating provides several advantages over conventional furnace heating due to its selective heating. This technique will be used for crystallization of glasses at high temperature for different periods of time. Microwave-crystallized samples will be characterized using structural analyses techniques and compared with conventional furnace annealed samples.

Properties of glasses can be varied by changing their constituents, controlled heat-treatment processes and addition of nucleating agents. The effect of different nucleating agents (TiO_2 and ZrO_2) and their amounts on the structures and the properties of glasses will be determined.

The effect of different amounts of nitrogen contents on rare-earth aluminosilicate glasses will be explored. The addition of nitrogen replaces non-bridging oxygen which makes the network tighter affecting significantly the structures and the properties of glasses. Lastly, the potential of rare-earth aluminosilicate glasses to join SiC components via SPS joining process will be evaluated.

1.2 Objectives

The objectives of this work include preparation of $\text{RE}_2\text{O}_3\text{-Al}_2\text{O}_3\text{-SiO}_2$ (RE = Y, Yb, Ho, Dy, Nd and Sc) glasses using melt-quench method as well as their structural investigations using XRF, in-situ/ex-situ XRD, IR-, Raman and NMR spectroscopy, respectively. This work will be carried out to reveal the short range bonding and vibrational spectra for the interpretation of molecular structures in these glasses. Thermal analyses of glasses will be performed to find out glass transition temperatures (T_g), crystallization temperatures (T_c), specific heat capacities, thermal diffusivities, thermal conductivities and coefficients of thermal expansion. Physical properties of glasses such as refractive indices, hardness and densities will be determined to develop a structure-property relationship. The crystallization studies of glasses will be carried out at 1200 °C for different period of time (1h, 50h) to analyze the crystalline structures. The potential of produced glasses as solders will be explored for the joining of SiC components using laser-assisted process. Characterizations of the prepared joints will be performed to evaluate their tightness and strength.

The effects of microwave heating on the crystallizations of $\text{RE}_2\text{O}_3\text{-Al}_2\text{O}_3\text{-SiO}_2$ (RE stands for Nd, Y) glasses will be determined for different period of times at high temperatures. Microwave-processed samples would be structurally analysed and compared with conventional furnace heat-treated samples.

$\text{RE}_2\text{O}_3\text{-Al}_2\text{O}_3\text{-SiO}_2$ (RE stands for Nd, Y) glasses containing different amounts of nucleating agents (TiO_2 , ZrO_2) will be prepared to explore the effects of nucleating agents and their amounts on the structures and the properties of glasses.

$\text{RE}_2\text{O}_3\text{-Al}_2\text{O}_3\text{-SiO}_2$ (RE stands for Nd, Y) glasses containing different amounts of nitrogen contents (4 and 8.33 mole %, respectively) will be prepared to determine the effects of nitrogen contents on the structures and the properties of these glasses. The annealing of glasses at 1200 °C for 50 hours will be carried out under atmospheres of nitrogen, argon, vacuum, and air, respectively to analyze crystalline structures and oxidation resistance. The application of nitrogen-containing glasses as solders for joining SiC components via laser assisted process will be determined.

Last but not least spark plasma sintering joining process will be performed to establish the possibility of joining SiC-components using the prepared glasses as solders.

1.3 Work packages

This work consists of five work packages.

1. Preparation of $\text{RE}_2\text{O}_3\text{-Al}_2\text{O}_3\text{-SiO}_2$ (RE = Y, Yb, Ho, Dy, Nd and Sc) glasses, structural and thermal investigation of the prepared glasses, their crystallization studies at higher temperature (1200 °C) for longer period of time (50 hours), selection of promising glasses for joining SiC components via laser-supported process and characterizations of the resultant joints.

2. Determination of the effects of microwave heating on the crystallization of $\text{RE}_2\text{O}_3\text{-Al}_2\text{O}_3\text{-SiO}_2$ (RE stands for Nd, Y) glasses for different period of times at 1200 °C. Structural analyses of these microwave-processed samples and their comparison with conventional furnace heat-treated samples.
3. Study the effects of nucleate agents (TiO_2 , ZrO_2) on the structure and the properties of $\text{RE}_2\text{O}_3\text{-Al}_2\text{O}_3\text{-SiO}_2$ (RE stands for Nd, Y) glasses.
4. Preparation and structural investigations of nitrogen containing rare-earth glasses, their crystallization evaluation at 1200 °C for different time periods under atmospheres of nitrogen, argon, vacuum, and air, respectively, application of these glasses for joining SiC components.
5. Spark plasma sintering joining of SiC components using the prepared glasses as solders.

1.4 Thesis organisation

This thesis is divided into seven chapters and each chapter is further subdivided as discussed below:

The first chapter contains introduction, objectives and motivation of this work. The fundamental literature review of glasses and their formation theories, rare-earth aluminosilicate glasses, microwave technology, effects of nucleate agents on the structure of glasses, effects of nitrogen addition on the structure and the properties of glasses are discussed in chapter two. Moreover, details of different characterization techniques are also presented in this chapter.

A description of SiC, its structures, properties, applications and different joining techniques are discussed in chapter three. The glass preparation procedures, details of substances, methods and techniques for the characterization of glasses are presented in chapter four.

The results of this study are presented in chapter five. This chapter is subdivided into five parts. Each part consists of a separate work package. Structural and thermal investigations of $\text{RE}_2\text{O}_3\text{-Al}_2\text{O}_3\text{-SiO}_2$ (RE = Y, Yb, Ho, Dy, Nd and Sc) glasses, their crystallization studies, selection criteria as solders for joining of SiC components using laser-assisted process and properties of the joints are discussed in details in first part of this chapter. The effects of microwave heating on the crystallization of $\text{RE}_2\text{O}_3\text{-Al}_2\text{O}_3\text{-SiO}_2$ (RE stands for Nd, Y) glasses are presented in second part of this chapter. The effects of different nucleating agents on the crystallization behaviour and properties of $\text{RE}_2\text{O}_3\text{-Al}_2\text{O}_3\text{-SiO}_2$ (RE stands for Nd, Y) glasses are discussed in third part. The fourth section contains details of nitrogen-containing rare-earth glasses, their crystallization studies under atmospheres of nitrogen, argon, vacuum, and air, respectively, and their application as solders for joining of SiC components. The joining of SiC components using spark plasma sintering process is presented in fifth part.

Chapter six consists explanations and discussions of results mentioned in chapter five. The conclusion of all work discussed in last chapters, findings and recommendations for the future work on this topic is presented in chapter seven.

2 Rare-earth aluminosilicate glasses

This chapter contains review of fundamental literature of glasses and their formation theories, rare-earth aluminosilicate glasses, microwave technology, effects of nucleate agents and addition of nitrogen on the structures of glasses. Moreover, details of different characterization techniques are also presented in this chapter.

2.1 Glass

Glasses are important amorphous materials that find broad applications in optical industry, home appliances, medical science and technology. This section contains an introduction of glass science and their formation theories.

2.1.1 Introduction

The story of glass started around 4000 years ago when men produced glasses for the ancient art of pottery. The attractive properties of glasses has kept human busy to investigate them throughout mankind history. Glasses were used for jewellery, glass containers, windows, mirrors and finally, with revolution of science, man learnt to make lenses to explore the hidden treasures of nature. These extended applications of glasses were due to their favourable shaping properties. The scientific studies of glasses started from famous Joseph von Fraunhofer (1787-1826) who determined that glass properties of interest can be obtained by altering its compositions. Later, George Stokes (1819-1903) worked on “chemistry of glass”, while Ernst Abbe (1840-1905) and Otto Schott (1851-1935) studied the optical properties of glasses extensively in mid nineteenth century at Jena University, Germany. Their work brought a new era not only in optical technology but also in glass technology [21].

During last century, thousands of peoples worked to understand and explore the world of glass. These researchers not only explored the science of glass but also find its potential applications in the fields of chemistry, physics, optical technology, medical science, communication, energy and many other fields of science and technology [2]. Glasses provide great opportunities to develop engineering materials of their choice for new applications by changing glass compositions, their properties and structures.

There are many definitions and explanations to describe the term “glass”, but most commonly it can be described as “Glass is an amorphous solid that is totally missing long range periodic atomic arrangement and shows a region of glass transformation behavior” [22].

The world of glass is so wide that people are unable to estimate the possible compositions of glass systems. One can roughly estimate it in billions, since more than seventy percent of natural elements show tendency towards each other to some extent to form glasses. Glasses are divided into large numbers of subgroups such as silicate glasses, oxide glasses, boride glasses, nitride glasses,

alkali glasses, rare-earth glasses etc. Each subgroup is further categorized depending upon compositions, structures, properties and applications.

2.1.2 Glass transformation

The glass transformation behavior is an important characteristic for glassy materials. It can be explained by volume versus temperature profile or enthalpy versus temperature diagram as shown in Fig. 2.1. For explanation of this figure, one can assume a liquid substance at temperature above its melting temperature. The atomic structure of the substance (melt) depends upon temperature, changes during cooling process and strongly depends on cooling rate. The material converts into crystalline state at slow cooling rate below melting temperature. The enthalpy of the system decreases abruptly, as melt converts into crystalline state. This decrease in enthalpy continues because of the heat capacity of formed crystals [22].

A supercooled liquid can be obtained with fast cooling rate that avoids crystallization process during cooling of molten liquid. The enthalpy of the system changes with decreasing temperature without any abrupt change during this fast cooling process. The structure of liquid also changes with decreasing temperature and forms discontinuous structural rearrangement due to fast cooling. The viscosity of the supercooled liquid is increasing with lowering temperature and eventually atoms cannot completely rearrange as in the equilibrium liquid structure. Consequently, the viscosity of the system increases so much that structure of the liquid not dependent anymore on temperature. The temperature section between the boundaries of the enthalpy of the equilibrium liquid and the frozen solid is known as the glass transformation region or glass transformation temperature (T_g) as shown in Fig. 2.1. Therefore, one can summarize T_g as the approximate temperature where a supercooled liquid converts into solid on cooling [21, 22]. The glass transformation happens over a temperature range therefore it is appropriate to consider different thermal history of glasses. If one can extrapolate the glass and supercooled liquid lines in Fig. 2.1, they cross at a temperature known as the fictive temperature (T_f). This fictive temperature provides useful information regarding effects of cooling rates on glass structures and properties. In Fig. 2.1, $T_{f_{\text{Slow}}}$ stands for fictive temperature of a glass with relative slow cooling rate whereas $T_{f_{\text{Fast}}}$ represents fast cooling rate [22]. Fictive temperature reflects the current structural state of the glass to be characterized.

However, in the present study glass transition temperatures of prepared rare-earth aluminosilicate glasses were find out using differential thermal analyses techniques (DTA/DSC). During thermal analyses a glass change to rubber/liquid state on heating. Rare-earth aluminosilicate glasses show high glass transition temperatures (~ 900 °C). Moreover, glass transition temperatures are affected by thermal history of glasses and heating rates.

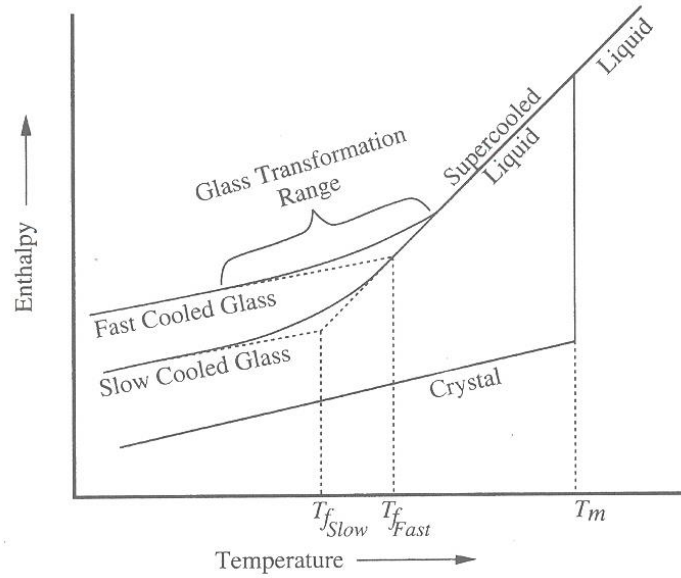


Figure 2.1: Temperature effect on the enthalpy of a glass forming melt [22].

2.2 Glass formation theories

Glasses found in nature are formed due to very fast cooling of molten rocks or lava. Silica is a major constituent of these naturally found glasses together with a wide variety of other components such as alkali, alkaline earths and transition metal oxides. Moreover, glasses developed before 1900 were mainly silicate glasses with few exceptions of non-silicate glasses. Therefore, first theories presented to explain glass formation from selective materials were based heavily on the existing knowledge of silicate melts and the structure of silicate crystals. These theories are often called as *Structural Theories of Glass Formation* [21, 22].

The development of large number of non-silicate glasses, non-oxide glasses, inorganic glasses, polymeric glasses and metallic glasses in recent past raises questions regarding essential conditions to form a glass from any material. The kinetics of glass formation from melt address these essential conditions required to produce glasses. Furthermore, due to the development in the glass processing technology the emphasis shifted from control of glass formation by selection of materials to the control of glass processing. These developments in the field of glass science bring a new approach to explain the glass formation known as *Kinetic Theory of Glass Formation*. This new theory has largely replaced the earlier structural theories [21, 22].

2.2.1 Structural theories of glass formation

Goldschmidt in 1926 presented his theory regarding formation of glasses based on general formula R_nO_m . He suggested that such compounds having cation to anion (oxygen) ionic radius ratio in the range 0.2–0.4 can form glasses. It produced cations surrounded tetrahedrally by four oxygen ions. Goldschmidt supposed that merely such melts can produce glasses during melt which have

tetrahedrally-coordinated cations. This contention was purely empirical without any logical or scientific explanation why tetrahedral coordination is so favourable to glass formation [22].

Zachariasen [23] published a paper in 1932 which extended the ideas of Goldschmidt and tried to explain why certain coordination numbers might favour glass formation. He noticed that such silicate crystals formed glasses which have opposed to close-packed structures network. These networks consist of tetrahedrons linked at all four corners similarly as in crystals. However these networks are not periodic and symmetrical as compared to crystals. Moreover, they are extended in all three dimensions that give isotropic properties to glasses. He suggested that formation of such networks provide necessary conditions for glass formation and proposed following conditions to form glasses from melt [21-23].

- The material should contain a high amount of such cations which are fenced by either oxygen triangles or oxygen tetrahedrons to produce a continuous structure.
- These polyhedra should be connected only by their corners to form an open network structure.
- There must be some atoms of oxygen connected to only two such cations. These connected oxygens should not make additional bonds with other cations.

He also recommended that melt must be cooled under proper conditions for glass formation, which anticipate the kinetics of the glass formation process. He classified the glass cations into three categories [23];

- I. Network-formers: These cations have a coordination number of generally 3-4 such as Si^{+4} , B^{+4} , P^{+5} , Ge^{+3} , As^{+2} , Be^{+2} etc.
- II. Network-modifiers: These cations have coordination number 6 or more than this. Examples of network modifiers include Na^{+1} , K^{+1} , Ca^{+2} , Ba , Y^{+3} , Nd^{+3} , Ho^{+3} .
- III. Intermediates: They have coordination numbers 6-8 and reinforce the network but cannot form glass alone.

Warren *et al.* [24, 25] in 1936 and 1941 reinforced Zachariasen` network hypothesis proposed. This network theory provided a further leap step to know the structure of glasses. In 1942, Dietzel [26] studied the solidification of a melt to explore the effect of interaction forces between cations and anions. He introduced the term field strength (F);

$$F = \frac{Z_c}{a^2} \quad (1)$$

Here Z_c refers for ionic loading (valence charge) and a stands to radius of ions.

The classification of cations made by Zachariasen can be correlated with their field strength: for network-modifier F varies from 0.1 to 0.4; while for network-former this value is large ($F = 1.4-2$) and for intermediate F varies between 0.5 and 1.

There are some other theories of glass formation which are based on the nature of the bonds in the material. Smekal [27] suggested that such melts having intermediate bonding character (between purely covalent and purely ionic) can produce glasses. Stanworth [28] attempted to quantify the mixed bond concept by using the partial ionic character model of Pauling. He classified oxides into three groups depending upon the electronegativity of the cations.

- *Network formers*: Such cations act as *network formers* which form bonds with oxygen having near 50% ionic character.
- *Intermediates*: Those cations which have ability to form slightly more ionic bonds with oxygen and contain slightly lower electronegativity cannot form glasses themselves. They can partially replace cations from the network formers and known as *intermediates*.
- *Modifiers*: Those cations with very low electronegativity and form highly ionic bonds with oxygen are known as *modifiers*. These cations never act as network formers and serve only as modifier.

The glass formation abilities were also explained depending upon bond strength. Sun [29] suggested in 1947 that strong bonds endorse glass formation and avoid crystalline structure during cooling. Rawson [30] proposed in 1967 that Sun ignored the importance of temperature in his model. He suggested that a material with large single bond strength and low melting temperature will be a much better glass former as compared to materials with higher melting temperature and same bond strength [22]. Glasses can have same structural units as found in crystalline materials, however glassy materials lack in long range and periodic arrangements of atomic structures as shown in Fig. 2.2.

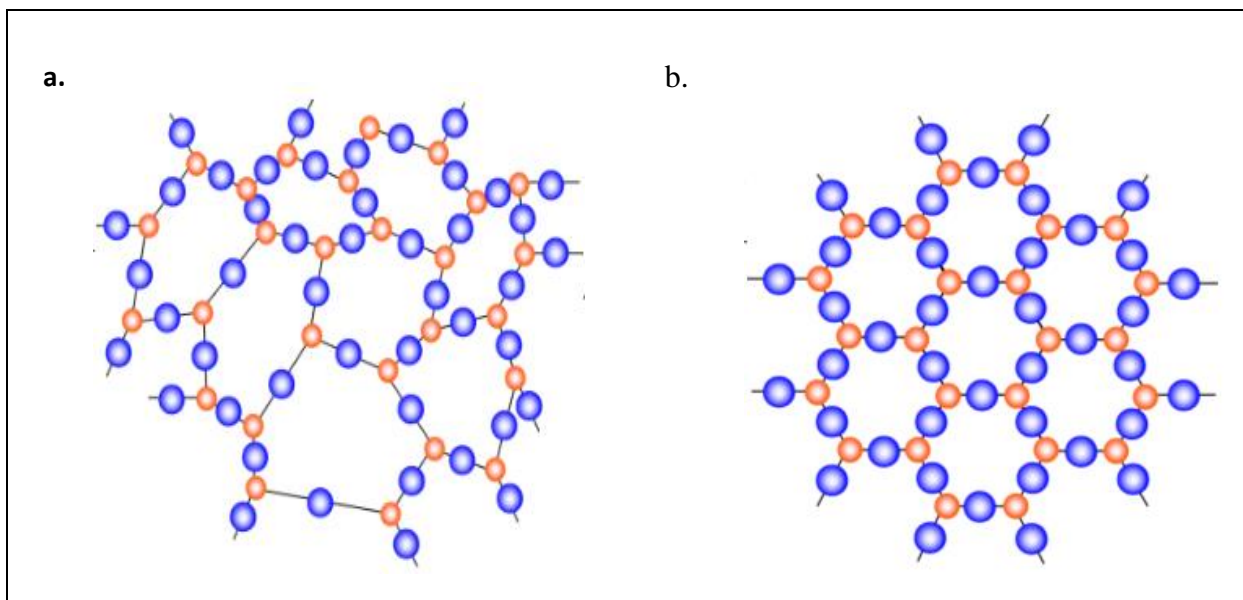


Figure 2.2: Structures of materials; (a) glass, (b) crystalline material [22].

2.2.2 Kinetic theories of glass formation

The developments of fast cooling processes make it possible formation of glasses from any material with rapidly cooling so that long range periodic arrangement of atoms is avoided. The

important factor is how fast a liquid material must be cooled to avoid detectable crystallization. Therefore, recent theories of glass formation reconsidered the criteria for defining a substance as a glass-former [22].

The crystallization phenomenon consists of two processes named as (1) *nucleation* and (2) *crystal growth*. There are two conditions necessary for a melt to form a glass during cooling. Firstly, it does not contain any nuclei as crystal growth could not take place without nucleus. Secondly, it may have low volume fraction of extreme small size nuclei but their growth has been suppressed by fast cooling. The nucleation process is divided into two types called as (1) *homogeneous nucleation* (2) *heterogeneous nucleation*. The homogenous nucleation takes place spontaneously within the melt while heterogeneous nucleation proceeds at pre-existing surfaces such as due to an impurity, crucible wall, etc. [21, 31].

2.2.2.1 Nucleation

The classical nucleation theory addressed homogeneous nucleation processes [32]. The nuclei are formed with equal probability throughout the bulk of the melt during homogenous nucleation process. These formed nuclei are extremely small in size and not easily detectable. The concentration of the formed nuclei is usually determined with an experiment that involves firstly an isothermal heat treatment at the nucleation temperature and then quenching the sample to freeze nuclei. That sample is again reheated to required temperature essential for nuclei growth to a detectable size for analysis. There are different processes mentioned in literature for calculating nucleation rate “I” [22, 31]. There are two factors which control the formation of a nucleus named as (1) *thermodynamic barrier*, and (2) *kinetic barrier*.

Thermodynamic barrier considers change in free energy of the system as a nucleus is formed. Kinetic barriers take into account the essential factors required for the growth of a crystal from a disordered liquid. The overall process for the formation of nucleus is described by the expression (2):

$$I = A \exp \left[- \frac{(W^* + \Delta G_D)}{kT} \right] \quad (2)$$

A is a constant, W^* is kinetic free energy barrier to nucleation, ΔG_D is thermodynamic barrier, k is the Boltzmann constant and T represents temperature (K).

The pre-exponential constant A can be described by equation (3):

$$A = 2 n_v V^{\frac{1}{3}} \left(\frac{kT}{h} \right) \left(\frac{\gamma}{kT} \right)^{\frac{1}{2}} \quad (3)$$

n_v represents the number of formula units, V is the volume, γ represents the crystal-melt interfacial free energy and h is Planck's constant. James *et al.* [33] found that for a good approximation A can be expressed as follows:

$$A = n_v \left(\frac{kT}{h} \right) \quad (4)$$

The crystalline state has a lower free energy as compared to the melt. Therefore, free energy of a crystalline material is lower as compared to glass made by same composition of melt. The volume free energy of the system decreases as a result of nucleus formation. This decrease in free energy is countered by an increase in surface energy because creation of a new interface between regions of different structures. The net change in energy W of the system for a spherical nucleus with radius r can be calculated as follows:

$$W = -\frac{4}{3} \pi r^3 \Delta G_v + 4\pi r^2 \gamma \quad (5)$$

The surface energy term dominates for very low values of r and the form nucleus is unstable. The net change in energy W increases with increasing r . When nucleus grow to a relatively large size, the volume free energy term becomes greater than the surface energy change. The nucleus becomes stable and W begin to decrease with increasing nucleus size [22]. The value for r where the nucleus just becomes stable can be derived by taking the derivative of equation (5) with respect to r and set it equal to zero as described in equation (6):

$$\frac{dW}{dr} = 4\pi r^2 \Delta G_v + 8\pi r \gamma = 0 \quad (6)$$

This value of the critical radius r^* can be calculated using the following equation:

$$r^* = -\frac{2\gamma}{\Delta G_v} \quad (7)$$

The net change in the energy of the system W^* for nucleus with critical value r^* can be derived by putting the value of r^* from equation (7) into equation (5) as below:

$$W^* = \frac{16\pi\gamma^3}{3 \Delta G_v^2} \quad (8)$$

The free energy change per mole of the system can be described by equation (9).

$$\Delta G = V_m \Delta G_v \quad (9)$$

Here V_m represents the molar volume of the crystal phase and ΔG is the bulk free energy change per mole. By putting the value of ΔG_v in equation (8) W^* can be written as:

$$W^* = \frac{16\pi\gamma^3 V_m^2}{3\Delta G_v^2} \quad (10)$$

The kinetic barrier for nucleation ΔG_D can be described in terms diffusion coefficient “D” as follows:

$$D = \left(\frac{kT\lambda^2}{h} \right) \exp \left(- \frac{\Delta G_D}{kT} \right) \quad (11)$$

Here “ λ ” is the atomic jump distance. In some cases D can be correlated with the viscosity η of the melt by using Stokes-Einstein relation:

$$D = \frac{kT}{3\pi\lambda\eta} \quad (12)$$

By using equations (11, 12) for the relation of ΔG_D equation (2) can be rewritten as follow:

$$I = \left(\frac{Ah}{3\pi\lambda^3\eta} \right) \exp \left(- \frac{W^*}{KT} \right) \quad (13)$$

Putting the value of A from Eq. (4) in above equation:

$$I = \left(\frac{n_v KT}{3\pi\lambda^3\eta} \right) \exp \left(- \frac{W^*}{KT} \right) \quad (14)$$

The above expressions are derived for the case of homogeneous nucleation.

James *et al.* [33] expressed that an equation similar to Eq. 2 can be used for heterogeneous nucleation. In this case:

$$I_{het} = A_{het} \exp \left[- \frac{(W^* + \Delta G_D)}{KT} \right] \quad (15)$$

Here subscript “het” represents heterogeneous nucleation. A_{het} can be described by expression similar to Eq. (4):

$$A_{het} = n_s \left(\frac{KT}{h} \right) \quad (16)$$

Here n_s represent the number of formula units of the melt in contact with the substrate per unit area.

$$I_{het} = n_s \left(\frac{KT}{h} \right) \exp \left[- \frac{(W^* + \Delta G_D)}{KT} \right] \quad (17)$$

The expressions (11) and (17) can be used to predict the shape of the curve for the nucleation rate (I) versus temperature (T).

Nucleation in glasses is an important process to control and predict devitrification in glasses. The devitrification of glasses can be carried out by following thermal treatment above glass transition temperatures. In glass-forming systems nucleation takes place either in volume or the surface of the sample. Surface nucleation process is more common in glasses as compared to volume nucleation and sensitive to the condition of the glass surface. Whereas volume nucleation took place during heat-treatment of glasses or/and addition of nucleating agents. Volume nucleation took place homogeneously in glass systems that undergo liquid phase separation having temperature and compositions between the spinodal and binodal boundaries. Glasses are non-homogeneous materials and phase separation has been suggested as an initial step for driving nucleation. At/near glass transformation range diffusion rates reduce and transient nucleation effects become important [21, 22].

2.2.2.2 Temperature-dependence of the nucleation rate

Glasses are produced typically by cooling a melt that is initially held at a temperature above its melting temperature (T_m). The effect of temperature on the nucleation rate is shown in Fig. 2.3, which follows from higher toward lower temperature. There will be no nucleation till melt is kept at a temperature above T_m . The value of ΔG_v will be very small at temperature near to T_m and the critical radius required for a stable nucleus will be very large. The chance for such a large size nucleus is very little therefore the melt remains effectively free of nuclei even though the temperature is slightly below than T_m [22, 32, 34]. The value of ΔG_v increases with decreasing temperature and the required critical radius for nucleus decreases. Further decrease in temperature reduces the critical radius size so small that the probability of formation of a nucleus with radius larger than the critical radius increases and nuclei form in detectable quantities. A significant degree of undercooling is essential to decrease critical radius of nuclei. This effect leads to a metastable zone of undercooling that must exist before radius of formed nuclei increase to a size above of critical nucleus radius. The thermodynamic barriers decrease with decreasing temperature and nuclei formation rate increases. The nucleation rate increases speedily with decreasing temperature as ΔG_v increases. However, kinetic barriers to nucleation increase rapidly with decreasing temperature as viscosity of melt decrease. The increasing kinetic barriers eventually force the nucleation rate to decrease [22, 34]. These changes in the thermodynamic and kinetic barriers affect nucleation rate [21, 22].

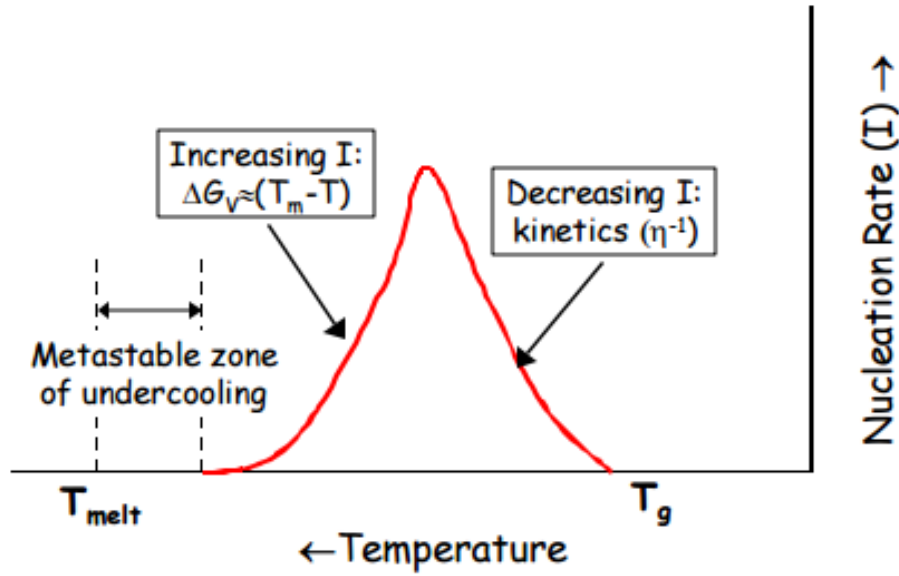


Figure 2.3: Effect of temperature on nucleation rates for a glass forming melt [22].

2.2.2.3 Crystal Growth

There are many expressions available in literatures that describe crystal growth [22, 32, 34-36]. These equations deal with specific models for different crystal growth mechanisms. A general equation for the crystal growth rate (U) is given below:

$$U = a_0 v \exp\left(-\frac{\Delta E}{KT}\right) \left[1 - \exp\left(\frac{\Delta G}{KT}\right)\right] \quad (18)$$

Here a_0 is the interatomic separation distance, v is the vibrational frequency, ΔE is kinetic barrier and ΔG is thermodynamic barriers to crystal growth. The above crystal growth expression can be modified using same arguments as for nucleation rate as follow:

$$U = \left(\frac{KT}{3a_0^2 \pi \eta}\right) \left[1 - \exp\left(\frac{\Delta G}{KT}\right)\right] \quad (19)$$

Temperature-dependence of the crystal growth rate is expressed in equation (19), which is similar to the nucleation rate. The principal difference is that there is no metastable zone for crystal growth. The growth of crystals can occur at any temperature below T_m as long as a nucleus is available. The growth rate will be high at lower viscosity of the melt but viscosity will increase rapidly with decreasing temperature that will slow the crystal growth and eventually stop it [22]. The resulting curve of U versus temperature will exhibit a maximum and eventually decrease to zero at lower temperatures.

A melt which is free of potential heterogeneous nuclei can be cooled more easily to form a glass as compared to a melt with large concentration of heterogeneous nuclei. Therefore glass

formation can also be influenced by external factors such as impurities in the melt, crucible material and size etc. [22, 32].

2.2.2.4 General kinetic treatment of glass formation

The models for nucleation and crystal growth rates described in above sections consider nucleation and crystal growth as independent phenomena. However, in real practice nucleation and crystal growth take place side by side and rates of nucleation and crystal growth change continuously during cooling. A practical approach is needed to deal the interaction between these processes during glass formation from melt [22, 32]. The volume fraction of crystals in a sample can be described as V_x/V where V_x is the volume of crystals and V is the sample volume:

$$\frac{V_x}{V} = 1 - \exp \left[\int_0^t I_v \left(\int_{t'}^t U dt \right)^3 dt' \right] \quad (20)$$

Here I_v is the nucleation rate per unit volume and U is the linear crystal growth rate. Since I_v and U are time dependent processes due to their temperature-dependence. For isothermal conditions eq. (20) can be simplified as follow:

$$\frac{V_x}{V} = 1 - \exp \left(-\frac{\pi}{3} I_v U^3 t^4 \right) \quad (21)$$

Here t represents the duration the sample was held at the experimental temperature. The time required to form a specific volume fraction of crystals at a given temperature can be determined by using information of I_v and U .

2.2.2.5 Glass-ceramic

Glass-ceramics are produced from amorphous glasses by controlled heat-treatment process. They have substantial level of crystallinity (~70-99 %) and combine the nature of crystalline ceramics and glass [37]. Glass-ceramics were discovered in 1950's by Don Stookey [38] and shown superior properties as compared to conventional glass or traditional ceramics materials. They provide opportunities to prepare crystalline materials of choice by changing initial chemical composition of the glass and controlled heat-treating process. The potential applications of glass-ceramics have increased tremendously in technical and domestic appliances. They showed good combination of mechanical, thermal, chemical, electrical, and physical properties [22, 37].

For preparation a glass-ceramic, it is important that crystallization could not start during cooling of molten liquid. Figure 2.4a shows an isothermal cooling transformation diagram (TTT) for a glass, here one observe that a transformation line crossed during slow cooling of glass start uncontrolled nucleation and growth process. Nucleation of the crystalline phase is controlled with a heat treatment process for specific number of nuclei. At slightly lower nucleation temperature the rate

of nucleation would be maximum as shown in Fig. 2.4b. Once nucleation started, crystallization process is controlled by the growth rate of the crystals. The growth rate will be maximize at elevated temperature. For a favoured glass-ceramic system, temperature difference between nucleation rate maxima and growth rate maxima should be large so that two peaks are separated and could not overlap. For preparing glass-ceramic from a pure glass two stage heat-treatment process is needed, which include firstly nucleation step at relatively lower temperature followed by the crystallization (crystal growth) step [37, 38].

However in the present work glasses are partially crystallized. Since nucleation and growth temperatures of rare-earth aluminosilicate glasses are not well defined. Therefore crystallization of glasses in the present study was carried at crystallization temperature determined by thermal analyses.

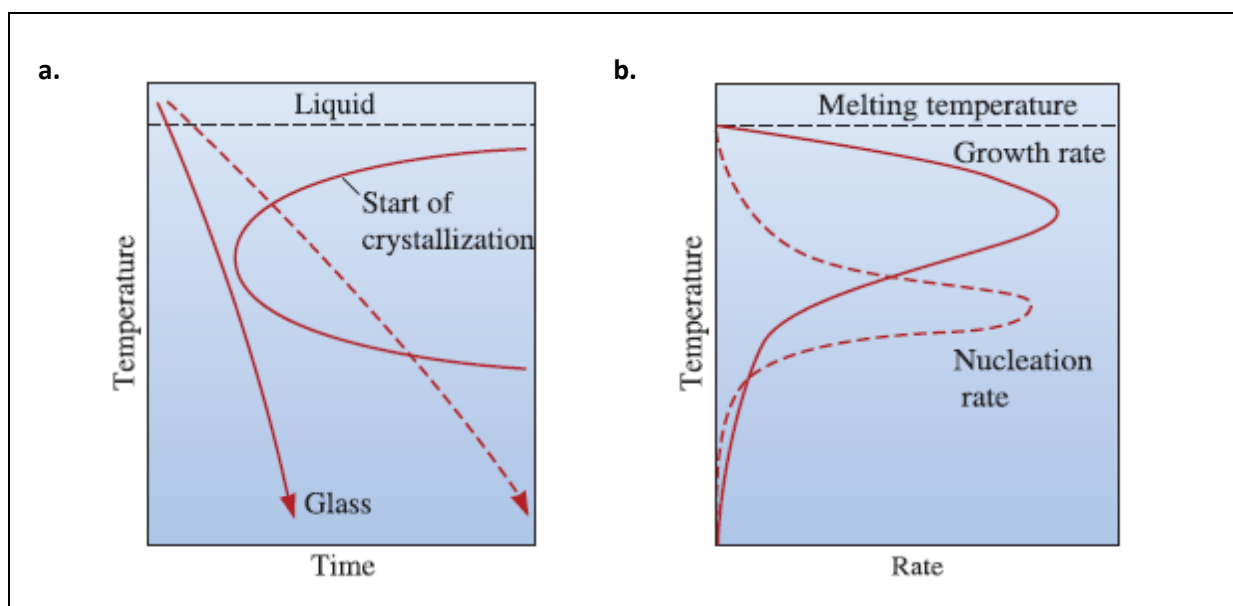


Figure 2.4: Producing a glass-ceramic, (a) Time-Temperature-Transformation curve for a glass forming melt (b) Rate of nucleation and crystal growth [37].

2.3 Rare-earth aluminosilicate glasses

This section contains details of structural characteristics of rare-earth aluminosilicate glasses and their applications in different field of science and technology.

2.3.1 Introduction

The term rare-earth elements refers to the group of lanthanides, additionally yttrium and scandium is also included in this group due to their similarities in properties with rare-earth elements. The radii of these rare-earth elements determined by Shannon [39] for six fold coordination and 3+ valence are given in Table 2.1. The amounts of rare-earths in different glasses describe their role as dopants, modifiers or primary components of the glass composition. The applications of rare-earths in different glass compositions have been increased tremendously in recent past. These oxides are used for the production of optical glasses having high refractive index and low dispersion. They have been

used as minor components in various glass compositions for favored glass colorants. Silicate glasses containing rare-earths as primary components were developed in the late 20th century. The formation of rare-earth aluminosilicate glasses depends upon several factors such as availability of furnaces that can reach the required melting temperatures (1500–1700 °C) and of crucible materials which can withstand at such a high temperature without making interaction with glass melt [40].

Glass forming regions for rare-earth aluminosilicate glasses are reported in literature [13, 40-45]. Glass-forming regions in RE₂O₃–Al₂O₃–SiO₂ systems are typically situated in the SiO₂ rich section of the phase diagram as shown in Fig. 2.3. The extension of the glass-forming region is not a fixed property and depends on the quenching conditions and compositions. The range of possible compositions that produce homogenous glasses depends upon field strength of RE³⁺ cations and becomes narrow with increasing field strength of RE³⁺ cations. Lu₂O₃–Al₂O₃–SiO₂ glasses involving the smallest lanthanide ion could not be prepared as phase-pure glasses but always contained additional crystalline compounds [44, 45]. Makishima *et al.* [42] were first ones who prepared different rare-earth glasses and determined their properties. Later, Hyatt *et al.* [13] published their extensive report on the formation of yttrium-aluminosilicate glasses and their properties. The effects of rare-earth oxides on the structures and properties of silicates glasses are extremely interesting [13-16, 43-48]. The miscibility gaps in yttria-silica and alumina-silica systems limit the glass formation regions. Shelby *et al.* [40, 49] found that glasses with large amount of silica are phase separated. They observed silica droplets in a matrix rich in yttria and alumina from transmission electron microscopy studies. Kohli *et al.* [45] reported glass formation regions of aluminosilicate ternary systems containing Neodymium, Praseodymium, Terbium, Ytterbium oxides. They found that glass formation regions in these glasses depend upon the ionic radii of rare-earth ion and decrease in size for smaller rare-earth cation. Kolitsch *et al.* [50, 51] published extensive data reports regarding phase relationships in RE₂O₃–Al₂O₃–SiO₂ glasses.

Structures of rare-earth aluminosilicate glasses composed of network forming units of tetrahedrally coordinated Si⁴⁺, Al³⁺ ions and RE³⁺ ions primarily act as modifiers. However cationic field strength of RE³⁺ ions is high, which result significant amounts of higher-coordination of AlO₅⁻⁷ and AlO₆⁻⁹ polyhedra in RE–Al–Si–O glasses [52, 53].

This work focuses on the investigation of rare-earth glasses (RE₂O₃–Al₂O₃–SiO₂), where RE denotes: Yttrium (Y), Ytterbium (Yb), Holmium (Ho), Dysprosium (Dy), Neodymium (Nd) and Scandium (Sc). Each glass composition is composed of three oxides: RE₂O₃, Al₂O₃, SiO₂ and 4 elements: rare-earth metal (RE), Si, Al, O. Rare-earth aluminosilicate glasses studied in this work show high potential to be used as solders for joining of SiC components via laser assisted process.

Table 2.1: Ionic radii and field strength of rare–earth elements having six fold coordination [39].

Element	Ionic radius (10^{-10} m)	Field strength (10^{-10} m)	Element	Ionic radius (10^{-10} m)	Field strength (10^{-10} m)
La ³⁺	1.03	2.817	Dy³⁺	0.91	3.607
Ce ³⁺	1.01	2.941	Ho³⁺	0.90	3.695
Pr ³⁺	0.99	3.061	Er ³⁺	0.89	3.787
Nd³⁺	0.98	3.105	Tm ³⁺	0.88	3.874
Pm ³⁺	0.99	3.188	Yb³⁺	0.87	3.982
Sm ³⁺	0.96	3.269	Lu ³⁺	0.86	4.047
Eu ³⁺	0.95	3.345	Y³⁺	0.90	3.704
Gd ³⁺	0.94	3.409	Sc³⁺	0.75	5.405
Tb ³⁺	0.92	3.521			

Bold are elements used in this thesis.

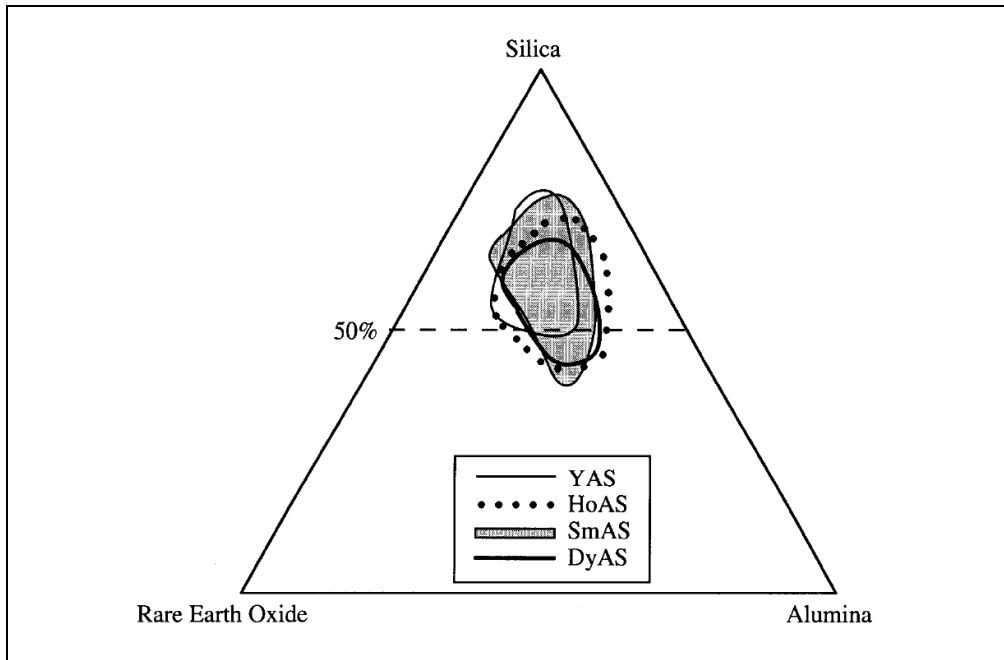


Figure 2.3: Glass forming regions for rare-earth aluminosilicate glasses (mole %) [46].

2.3.2 Structure

Structures of RE-aluminosilicate glasses are not completely well defined as compared monovalent alkali- or divalent alkaline-earth metals. Structural roles of rare-earth cations in glasses are determined by their valence and size. The valence of rare-earth cations is generally 3+ although some of them have two possible charges such as Ce, Pr, Tb (4+ and 3+) and Sm, Eu, Yb (3+ and 2+). The ionic radii of rare-earth elements are quite small (Table 2.1) and decrease in lanthanide series as atomic number of rare-earth increases, called as lanthanide contraction [54]. Pauling's rules can be applied for the calculation of coordination number between rare-earth-oxygen bonds. According to the rare-earth-oxygen radius ratios, the rare-earth cations can have six to nine fold coordination to oxygen [52]. Field strength of rare-earth cations are relatively large (Table 2.1) when compared with alkali/alkaline earth cations but smaller than network former cations like Si^{4+} or Al^{3+} . This higher field strength of rare-earth cations are due to their smaller ionic radius, which has considerable effects on their local structure as well as on the properties of glasses [52, 53].

Structural analyses of rare-earth containing glasses conducted by IR, Raman and electron spin resonance spectroscopy showed that rare-earth cations act as network modifiers in the glass structure [37, 55]. These studies showed rare-earth cations containing glasses had highly disordered structure. MAS-NMR (^{27}Al and ^{29}Si) studies of yttrium aluminosilicate glasses suggested highly disordered structures consisting of simultaneous presence of different structural units [56, 57]. In the present work, $\text{RE}_2\text{O}_3\text{-Al}_2\text{O}_3\text{-SiO}_2$ (RE = Y, Nd, Yb, Dy, Ho and Sc) glasses are prepared using melt-quench route. The eutectic temperatures of these glass systems are given in Table 2.2. Structural analyses of glasses are performed by using different vibrational spectroscopic techniques to investigate the short range bonding and vibrational spectra in them.

Table 2.2: Comparison of eutectic temperatures in the $\text{RE}_2\text{O}_3\text{-Al}_2\text{O}_3\text{-SiO}_2$ systems (mole %).

Glass system	Eutectic temperatures
$\text{Y}_2\text{O}_3\text{-Al}_2\text{O}_3\text{-SiO}_2$	~1375 °C [50]
$\text{Yb}_2\text{O}_3\text{-Al}_2\text{O}_3\text{-SiO}_2$	~1500 °C [58]
$\text{H}_2\text{O}_3\text{-Al}_2\text{O}_3\text{-SiO}_2$	~1375 °C [46]
$\text{Dy}_2\text{O}_3\text{-Al}_2\text{O}_3\text{-SiO}_2$	~1389 °C [58]
$\text{Nd}_2\text{O}_3\text{-Al}_2\text{O}_3\text{-SiO}_2$	~1336 °C [59]
$\text{Sc}_2\text{O}_3\text{-Al}_2\text{O}_3\text{-SiO}_2$	~1390 °C [60]

2.3.3 Properties

Properties of rare-earth glasses depend upon the amount and type of the rare-earth ions present in the glass [40]. They show high glass transition temperatures (T_g) as reported in literature [45, 49].

Tanabe *et al.* [61] found T_g value increases with decreasing ionic radii of the rare-earth ions. Densities of glasses are found a linear function of the amount and identity of rare-earth cations. They had relatively higher densities (2.8–4.5 g/cm³) as compared to alkali/alkaline oxide glasses. These glasses show high values of hardness (6.5–9.3 GPa), elastic modulus (95–135GPa) and good durability under oxidation conditions [41, 44, 61, 62]. A linear increase in Vickers hardness number (VHN) is expected with rare-earth cations having higher atomic number. Makishima *et al.* [41] mentioned in their work that hardness values of yttrium aluminosilicate glasses increases with increasing yttria contents due to high packing density of the atoms in the glass structures. Kohli *et al.* [44] determined coefficients of thermal expansion for different rare-earth glass systems and found them in the range between 4–8 x 10⁻⁶ K⁻¹. Moreover, they show low electrical conductivity, extremely low He permeability, high DC electrical resistivity and high refractive indices [40, 43]. A linear increase in refractive indices was found for a series of yttrium aluminosilicate glasses as the amount of yttria increased from 5–25 mole % [43, 44].

These improved properties of rare-earth containing glasses are due to high field strength and small size of rare-earth cations (Table 2.1), which result in high packing density of atoms. Additionally, they create relatively strong bonds with the surrounding oxygen which provides high temperature stability. These bonds are considerably stronger than bonds created by other alkaline-, or alkaline-earth modifier ions but weaker than silicon-oxygen bonds [52].

2.3.4 Applications

Rare-earth aluminosilicate glasses have broad range of applications such as:

- They increase the high temperature stability of non-oxide ceramic-materials such as liquid phase sintered SiC-, Si₃N₄- and SiAlON-materials [4-7].
- The optical and magnetic properties of these glasses make them suitable to be used in solid state lasers, fibers, sensors and optical amplifiers [10].
- The micro spheres of different rare-aluminosilicate glasses (Y, Dy, Ho) activated by neutron bombardment can be used as radiation delivery vehicles and allowed an in-vivo radiotherapy of cancerous organs. These glass spheres are insoluble in body and delivered large doses of radiations to the diseased organs. Therefore, they provide a targeted radiation treatment for tumors without damaging the surrounding healthy tissue [46, 63].
- They are used as model systems for storage of long-lived actinides [64].
- These glasses can be used to produce tight seals between glass and ceramic/metals. [11, 12].
- Some glasses showed high paramagnetic susceptibility and find applications in various magneto-optical devices such as Faraday rotators, isolators, modulators, and fast optical switches [65].

2.4 Microwave heating

Potential applications of microwave heating have increased tremendously for home appliances, science and different industries [66, 67]. Microwave technology was developed during in 1940s for sintering of ceramic materials [68]. Commercially processing of ceramic materials using microwave energy started much later [69]. It showed many advantages as compared to conventional heating processes such as rapid and selective heating, reduction processing time, saving energy consumption and improved quality of products [66, 67, 70-73]. Microwave heating provides uniform heating in all sections and reduces thermal stresses considerably. It enhances kinetic rates for reactions as compared to conventional heating known as “microwave effect”. Microwave heating techniques are used in ceramics for sintering, joining and melting [66, 74-76]. Different factors which take into account during absorption of microwave energy are microwave frequency, the distribution of the electric field and properties of substance such as dielectric etc. It is important to measure accurate temperature in microwave processing [77].

During conventional heating the surface of the sample experience is heating first and then heat diffuses into the center of sample, whereas in microwave heating, heat is produced in total volume with almost same rate. Therefore, one can observe different rates of heat flow in materials from surface to interior part of sample during conventional heating and microwave processing [66, 67, 70-73]. For applying microwave techniques to material processing, it is needed to understand microwave-material interactions. Important factors required to consider during microwave heating are moisture contents in materials and environment, size and geometry of the sample, changing dielectric properties of the sample, position of the sample according to microwave field [69, 73]. The mechanism of dipolar polarization in glass and ceramics materials consists on molecular dipoles rotation. Structure of glass and binding energy of cations define particular time required for polarization. There are no grain boundaries at room temperature in glasses therefore polarization does not affect them greatly. However at higher temperature due to development of grain boundaries/phases such as during crystallization of glasses the effects of polarization are accountable [67, 73, 74]. Effects of microwave heating are studied extensively on crystallization of Lithium disilicate (LS2) glasses [59].

The primary goal of present study is to investigate the potential for crystallizing $Y_2O_3-Al_2O_3-SiO_2$ and $Nd_2O_3-Al_2O_3-SiO_2$ glasses using microwave processing technique. A second goal was to experimentally investigate the microstructures of these microwave processed samples and make comparison with samples heat-treated using conventional furnace heating.

2.5 Rare-earth aluminosilicate glasses containing nucleating agents

Crystallization of glasses produces high quality crystalline structures depending upon initial glass composition and subsequent controlled heat-treatment. Pure glasses are kinetically unstable whereas crystallization is favored process in terms of kinetic and thermodynamic. If nucleation and crystal growth temperatures of particular glass composition are known, then controlled nucleation and growth mechanisms during crystallization of glasses provide fine grained microstructures e.g. glass-ceramics [78]. Properties of glasses and glass-ceramics can be controlled by chemical compositions, final phase assemblage, with heat treatment and by addition of nucleating agents [67]. However, nucleation and crystal growth temperatures for rare-earth aluminosilicate glasses studied in present work are not well defined. Therefore, during crystallization of glasses structures obtained were partially crystalline.

There is a long list of nucleating agents such as ZnO_2 , TiO_2 , ZrO_2 , Nd_2O_3 that can enhance nucleation and crystal growth phenomena in glasses. These nucleating agents act as centers for initiating crystallization. However, nucleating mechanism initiated by these nucleating agents is a complicated phenomenon. It depends on the type of nucleating agent, its amount, the parent glass composition, thermal history of the parent glass and heat treatment conditions. It is important to consider the maximum solubility of nucleating agents in particular glass systems. Most nucleating agents can produce liquid phase separation prior to the occurrence of crystal nucleation as they form an extensive immiscibility region with silica [78]. Oxide nucleating agents (TiO_2 , ZrO_2) make compounds by mixing with components of the glass and act as preferred location for heterogeneous nucleation and enhance crystallization of glassy matrix. TiO_2 showed pronounced effects on transition temperatures of silicate glasses. Addition of higher amounts of titania (15–18 % mass) in silicate glasses resulted in fine-grained partially crystalline and fully crystalline structures [56,77] which contain phases of anorthite and minor phases of wollastonite. In the present work, different amounts of TiO_2 and ZrO_2 are used as nucleating agents to enhanced crystallization in yttrium-aluminosilicate and neodymium-aluminosilicate glasses. Moreover, effects of these nucleating agents on the structures and transition temperatures are investigated.

2.6 Rare-earth aluminosilicate glasses containing nitrogen

Oxynitride glasses appear as grain boundary phases in silicon nitride ceramics. They appeared at triple point junctions or produced an intergranular film. They are formed in $M-Si-O-N$ and $M-Si-Al-O-N$ systems, where M represents cations of elements such as Ca^{2+} , Mg^{2+} , Y^{3+} , and rare-earth elements. The revolutionary world of ceramic materials provides motivation to investigate properties and structures of such glasses. Numerous investigations on these glasses are carried out to explore their formation, structures and properties [4, 7, 79-84].

These glasses were prepared in the late 60's when it was discovered accidentally that oxygen present in the glass structure could be partially replaced with nitrogen via a reaction between molten glass and NH_3 [85]. Mulfinger [86] was pioneer who proposed that nitrogen may replace oxygen atoms in the tetrahedral of glass network. He incorporates a small amount of nitrogen (< 1 mass %) into silicate glasses by bubbling of NH_3 gas through a sodium silicate system melt. Jack [79] achieved 10 at % nitrogen incorporation in $\text{SiO}_2\text{-Al}_2\text{O}_3\text{-Si}_3\text{N}_4$ and $\text{SiO}_2\text{-Y}_2\text{O}_3\text{-Si}_3\text{N}_4$ systems.

Figure 2.4 shows Jänecke prism of the system $\text{Si}_3\text{N}_4\text{-Y}_2\text{O}_3\text{-Al}_2\text{O}_3\text{-SiO}_2\text{-YN-AlN}$ [97Lid], which represents the most important secondary phases obtained by using the most technically customary additive system of SiO_2 , Y_2O_3 and Al_2O_3 during liquid phase sintering process and subsequent devitrification [75Will, 85Neg]. Main phases contained are Apatite $\text{Y}_{10}(\text{SiO}_4)_6\text{N}_2$, Melilith $\text{Y}_2\text{Si}_3\text{O}_3\text{N}_4$, Woehlerite $\text{Y}_4\text{Si}_2\text{O}_7\text{N}_2$ and Wollastonite YSiON_2 .

It has been mentioned in literature extensively that nitrogen incorporation significantly increase hardness, elastic modulus, refractive indices, glass transition temperature, and softening temperatures of oxynitride glasses, rigidity, fracture toughness, and resistant against water-assisted subcritical crack growth [7, 82, 83, 89-93]. Furthermore, they are less susceptible to chemical attack by acids, bases and water. However, these glasses are more susceptible to oxidation as compared to oxide glasses and origin of this effect can be found in the structure, where nitrogen is incorporated with atmosphere [94-97].

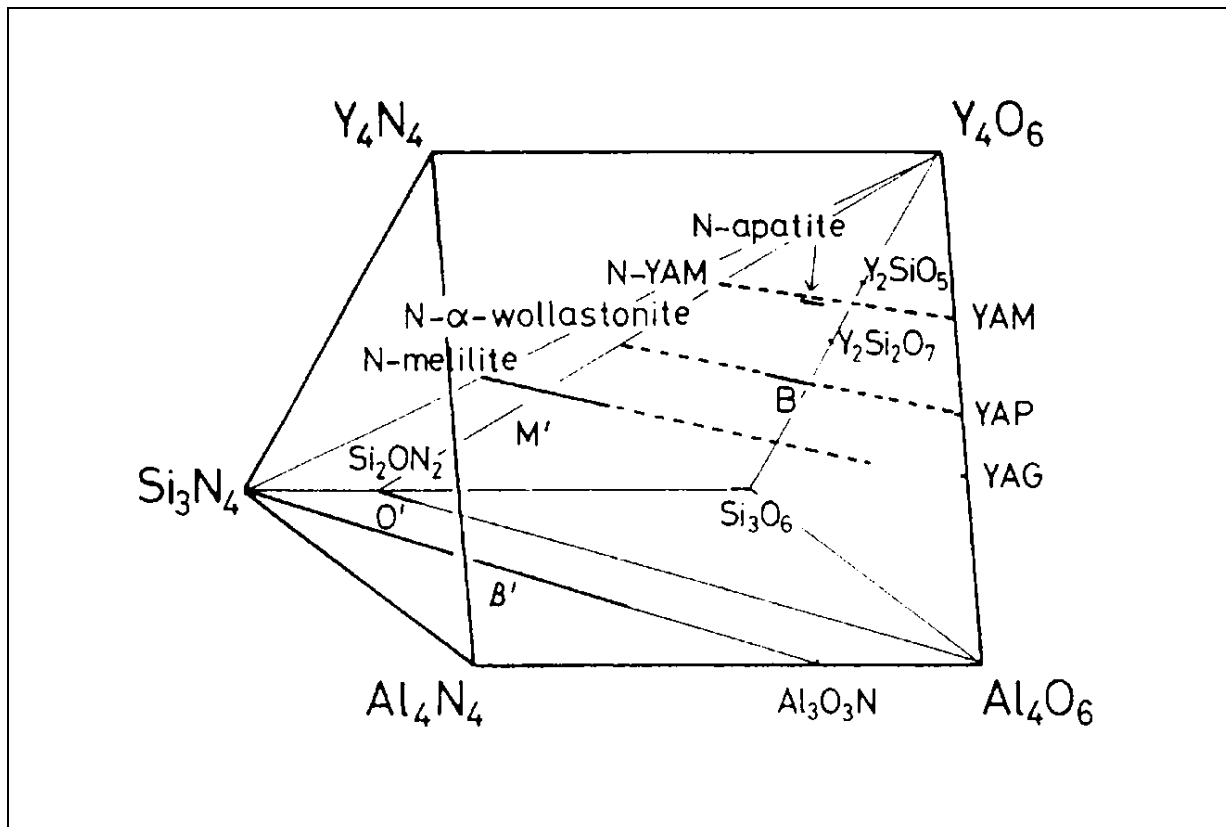


Figure 2.4: Jänecke prism for the system $\text{Si}_3\text{N}_4\text{-Y}_2\text{O}_3\text{-Al}_2\text{O}_3\text{-SiO}_2\text{-YN-AlN}$ [87, 88].

These improved properties are due to partially replacement of oxygen in the SiO_4 tetrahedral by nitrogen atoms which increase the coordination index of the non-metallic atoms. This increase in coordination index make glass network stiffer and compact due to higher bond density [7, 84]. The schematic representation of elements in the oxynitride glass structure is shown in Fig. 2.5. Structure of such glasses consist two types of cations named as network former and network modifier similar to oxide glasses. However, they contain two types of anions, oxygen (O^{2-}) and nitrogen (N^{3-}). Network formers are small cations which form covalent bonds with oxygen and nitrogen. The modifiers possess oxidation state equal or lower than three and coordinate with oxygen to form ionic bonds. The modifier cations locally weaken the largely covalent network by introducing ionic bonds. Oxygen atoms connected with two network formers are known as bridging oxygen, whereas, oxygen atoms connected to the modifier cations are called as non-bridging oxygen. The oxidation state of nitrogen is 3 and binds three network-forming cations as compared to oxygen which can bind two at most. The replacements of some oxygen atoms by nitrogen have a great effects only on the structure but also on properties of glasses [93, 96, 98].

In this study, different rare-earth oxynitride glasses have been prepared by partially replacing the oxygen in the glass structures by nitrogen. Glasses are investigated structurally and thermally to determine the effects of nitrogen on local bonding and transitions temperatures. High-temperature long heat treatments of glasses are conducted under different atmospheric conditions to reveal their crystal structures and oxidation resistance.

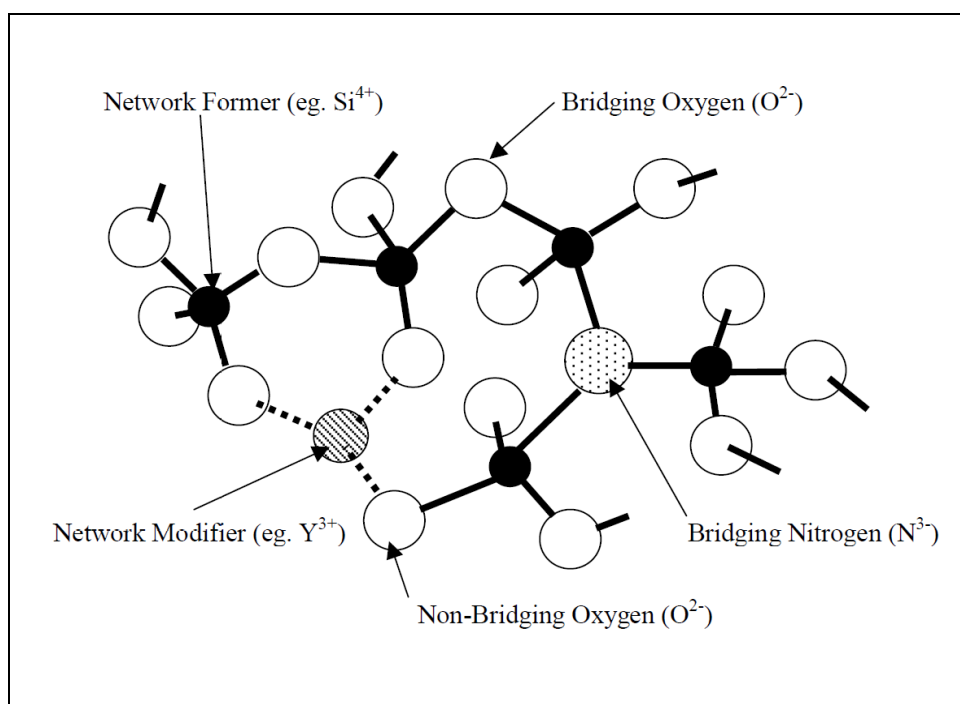


Figure 2.5: Schematic representation of element as cations in the oxynitride glass structure [7].

2.7 Characterizations of glasses

The characterizations of glasses have been done extensively in recent times to explore their structural, thermal, physical and optical properties. In this section a short introduction about different characterization techniques is presented, which are used in this work.

2.7.1 Infrared spectroscopy of glasses

Applications of vibrational spectroscopy have been increased tremendously to explore the structures of materials. Since glasses lack long range ordering therefore impact of vibration spectroscopy to investigate the structural modes in glasses is more pronounced as compared to crystalline materials. Infrared (IR) spectroscopy has been used broadly to study the structures of oxide glasses and silicate glasses. In IR spectroscopy, when sample is exposed to infrared light as a result of material light interactions difference phenomenon such as absorbance, transmittance or reflectance may take place. Vibrations frequencies of bonds in glasses absorb light of specific frequencies which correspond to them [99, 100].

The IR spectrum depends on a change in the dipole moment and provides information on the short range ordering in structures. Therefore, it finds broad range of applications in glasses for the evaluation of structural modifications due to its non-destructive characteristics. The nature and specific type of bonds in glasses are quantified with particular characteristics of the IR-absorption peaks [99, 101, 102]. Since every material consists of specific arrangement of atoms therefore IR spectra of different materials can be distinguished. IR spectroscopy is used extensively for identification of different kinds of material and compounds [99, 101].

The structure of glasses cannot be defined clearly in terms of nearest neighbour co-ordination number, bond lengths and bond angles as compared to crystalline solids. Silicate glasses do not show long-range structural periodicity due to a random distribution of Si-O-Si bond angles. Their IR spectra help to evaluate structural changes and properties in them. The prominent bands envelopes in aluminosilicate glasses for IR spectra consisted in the high frequency (1200-800 cm^{-1}), middle frequency (800-650 cm^{-1}) and low frequency (650-400 cm^{-1}) region. The infrared spectrum in high frequency region includes symmetric Si-O stretching bands together with antisymmetric stretching of non-bridging and bridging Si-O bonds. The middle-range envelope (800-650 cm^{-1}) is composed of minimum two band components with moderate strength [51, 103]. McMillan [38] described band at around 800 cm^{-1} in silica glass is mainly associated with motion of Si atoms against their tetrahedral oxygen cage due to little displacement of associated oxygen. The mid-range band also includes an additional contribution from Si-O-Si bridge bending. The strong IR band near 470 cm^{-1} is normally assigned to bridging oxygen where O vibrates perpendicular to the Si-O-Si plane. A weak shoulder near 550 cm^{-1} present bending character where oxygen motion bisects the Si-O-Si bond angle. One can assume that bands in low frequency region mainly indicate bending modes together with stretching

modes which involve a high degree of oxygen displacement at Si-O-Si bridges. In this work, IR spectra of prepared glasses and partially crystalline glasses are determined and compared with literature.

2.7.2 Raman spectroscopy of glasses

Raman spectroscopy is an important analytical tool used in different fields of science and technology such as in pharmaceuticals, thin films, semiconductors, chemical industry and material science. It depends on a change in polarizability of molecules and measures relative frequencies at which specimen scatters radiation. This technique is being practice excessively for the determination of structure, identification of the structural groups and dynamics of glassy materials [104].

The Linear Raman Effect was experimentally demonstrated by Raman and Kirishnan in 1928 [103], which base on an inelastic light scattering process. In this phenomenon, laser light interact with sample and some of its photons go to a non-stationary state for $\sim 10-15$ s and re-emitted instantaneously. The frequency of the re-emitted photons described as *Raman shift*. Moreover, frequency of re-emitted photons described either it was anti-Stokes Raman Effect or Stokes effect. It describes transitions (vibrational, rotational, etc.) in structural units of the sample being analyzed [100].

Raman spectroscopy is extensively used to determine vibrational and molecular structures of silicate glasses. The term molecular structure describes the average or static geometrical arrangements of bound atoms, or to describe the geometry of a particular unit within the glass structure. The Raman bands at high frequency in silicate glasses reveal symmetric silicate stretching motions involving the non-bridged oxygens. The modes in the $400-700\text{ cm}^{-1}$ region describe vibrations of bridged oxygen and sensitive to the Si-O-Si bond. A detailed information regarding Si-O, Si-O-Al and Si-O-Si vibrations at specific raman bands for aluminosilicate glasses is mentioned in literature [55, 105, 106].

When Raman spectroscopy is compared with IR spectroscopy, IR spectra represent a change in the dipole moment; whereas Raman bands produce from polarizability effects. IR spectroscopy is based on absorption, reflection or transmission interaction of light with material while in Raman spectroscopy scattering phenomena take place. In Raman analyses monochromatic radiation in the visible range (laser) is use for characterization as compare to polychromatic infrared radiation. A Raman spectrum is based on linear intensity process whereas representation of the IR spectrum is established on absorption. IR spectra revealed stretching and bending modes of (-Si-O-Si-) bond in glasses and Raman spectra provide information regarding structural environment around SiO_4 tetrahedral in them [102, 107].

In the present work Raman spectra of the prepared rare-earth aluminosilicate glasses and partially crystalline glasses are determined to reveal structural units in them.

2.7.3 Nuclear magnetic resonance spectroscopy of glasses

Nuclear magnetic resonance (NMR) explores the local environment of a nucleus. It is an element specific technique and has the ability to study particular atoms without any interference of other atoms with same atomic mass. A NMR-active nucleus possesses spin angular momentum and behaves like a small magnet to interact with any surrounding magnetic field. NMR spectra are useful for studying glassy materials due to their short range ordering characteristics and provide valuable information regarding packing arrangements and coordination numbers. Moreover, it also finds out the nature of the bonded atoms and different degree of polyhedral regularity in them. There is a directly proportional relationship between peak intensities of NMR signal and the amount of the specific species. NMR spectroscopy provides quantitative information for short range ordering and spin interactions, which help to understand coordination geometry and connectivity [108, 109].

NMR spectroscopy plays an important role to understand the effects of rare-earth ions in silicate glasses. It provides coordination numbers and constrains of cation grouping. Rare-earth cations show relatively higher field strength as compared to common network modifiers such as Na^+ , Ca^{+2} etc. Rare-earth cations lack 4f electrons, therefore show unpredictable ligand field effects on bonding and coordination. Structural role of rare-earth cations are dependent on their amounts in the glass system and reveals possible R–O–R clusters together with Si–O–Si units [137, 138]. However, it is mentioned in literature that Al can break R–O–R linkages and formed R–O–Al units [138]. The reason for this transformation could be describe in terms of charge balance for the $[\text{AlO}_4]$ unit. The effects of different rare-earth ionic radii make strong effects on their coordination numbers. It was noticed that coordination number change from 7 or 8 to 6 with decreasing ionic radii of rare-earth cations. ^{27}Al NMR spectra of yttrium-aluminosilicate glasses showed higher disorder network as Y^{3+} cations have higher field strength of [110]. In this work, ^{27}Al spectra of different rare-earth aluminosilicate glasses are revealed.

2.7.4 Thermal analyses of glasses

Thermal analysis consists of a group of methods used to measure properties of a material under controlled temperature program as a function of temperature (or time). Two important techniques which are used for determining thermal properties of glasses are differential thermal analysis and differential scanning calorimetry. They are used to find out glass transitions temperatures, nucleation temperatures, crystallization temperatures, softening temperatures etc.

2.7.4.1 Differential thermal analysis

In Differential thermal analysis (DTA) a test sample and an inert reference material is heated and cooled under similar settings/environment, temperature difference is recorded between them and plotted against time or temperature. DTA not only provides information regarding thermal properties rather it can also be used to identify phase changes.

A differential thermal analysis device consists of two containers for sample and reference material, sample holder connecting thermocouples, furnace for heating under controlled temperature (heating/cooling rates) and signal recording system. The recording system must be sufficient sensitive to reproduce variations in the experimental set up. Other important factors to consider are mass of the sample and heating rates which strongly affect the shape of DTA peak. Lower heating rates are recommended as they produce sharper peaks with better resolution. Since test sample and reference specimen have different thermal properties/behavior in terms of heat capacities and conductivities. Therefore, it is highly recommended to calibrate DTA system for every new measurement and heating rate. DTA systems for temperature measurements are calibrated by using pure metals whose melting points are precisely known such as Ag, Au etc. so that temperature lags can be avoided. The onset of a DTA peak represents the starting temperature of physical/chemical change [111].

In this work, DTA is utilized to find out glass transition temperatures and crystallization temperatures of prepared rare-earth aluminosilicate glasses.

2.7.4.2 *Differential scanning calorimetry*

In Differential scanning calorimetry (DSC) the difference of the heat flow rate between sample and reference material is determined under a controlled temperature program. Signals measured in differential calorimeters are proportional to a heat flow rate. Temperature difference in DSC is obtained as electric voltage transferred to units of μW or mW [112]. In this work, heat capacities and transition temperatures of the produced glasses were find out using heat flux DSC.

In heat flux DSC the temperature of the complete sample unit (consisting of sample probe and reference sample) changes within a specified program. It measured difference in temperature between reference and sample probes as a function of temperature. Temperature difference revealed intensity of heat exchange, which is proportional to resultant heat flow rate. Heat flux DSC having disk type measuring system allows medium heating and cooling rates due to small sample volume and limited heat exchange. Other commercial type of heat flux DSC includes a turret type measuring system consisting small hollow cylinders for heat exchange. It allows higher heating and cooling rates and had showed high sensitivity. DSC with cylinder type measuring system is famous due to their sensitivity and relatively large sample sizes. However, heating rates in them are relatively low. Figure 2.6 shows heat flux DSC used in the present work for determination of glass transition temperatures, crystallization temperatures, specific heats etc. The measuring signal is temperature difference and an electric voltage proportional to temperature difference is calculated. A detailed knowledge is required to interpolate DSC curves so that misunderstanding can be avoided. Moreover, it is highly recommended that DSC should be calibrated by using pure metals of known melting point. A detailed literature is available for calibration and interpolation of obtained peaks [111, 112].

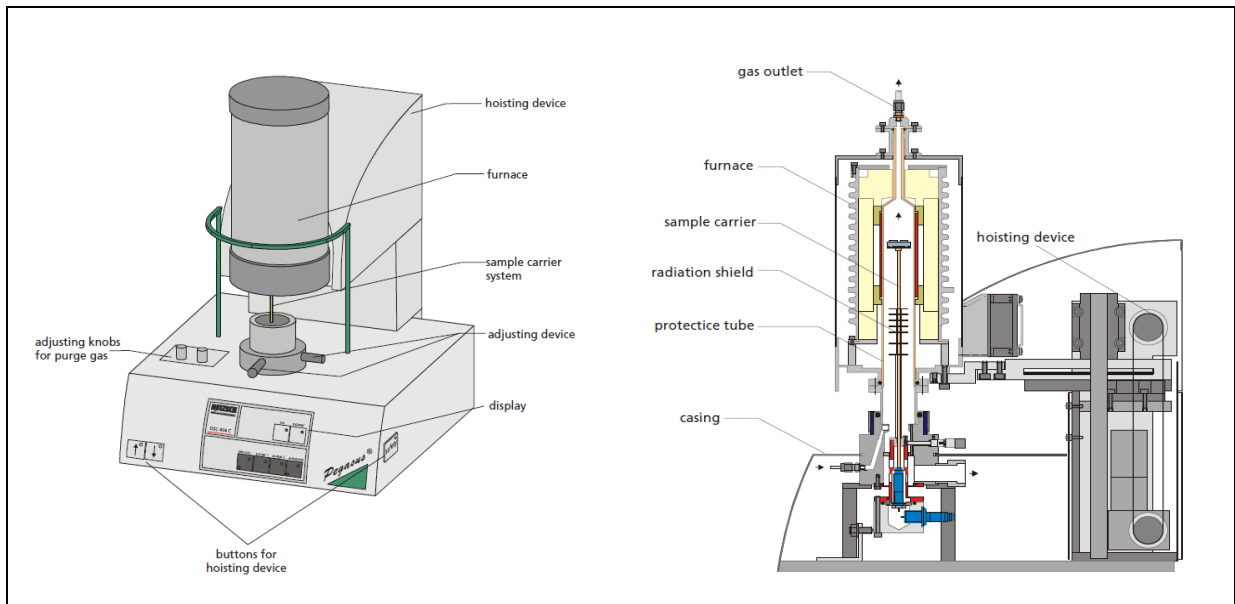


Figure 2.6: Heat flux DSC 404 C from Netzsch used in this work [Netzsch GmbH].

3 JOINING OF SILICON CARBIDE COMPONENTS

This chapter contains description of silicon carbide, its structures, properties, applications and joining techniques.

3.1 Silicon carbide

Silicon carbide (SiC) is an important structural ceramic material that shows good properties in terms of strength, thermal conductivity and oxidation resistance. SiC containing components are used in engine and turbine parts, for construction of reactors, development of microelectronic devices, as cutting tools and for many other high-temperature applications. In the present work, silicon sintered silicon carbide (SSiC) components (capsules and rods) from H.C. Starck GmbH are used for joining.

3.1.1 Fabrication of silicon carbide

SiC is prepared by different processes/routes and its mechanical properties strongly depend on their fabrication route. SiC was first synthesized by Acheson in 1891 during an electrochemical reaction [17]. This reaction was carried out in an electric furnace between high purity silica sand and carbon. SiC prepared by this technique is commercially named as carborundum. Other techniques used for the synthesis of SiC are sintering, direct conversion, gas phase reaction and polymer pyrolysis. The sintering process is dependent on different types of sintering agents, possible techniques of consolidation and procedures of pressurization. The direct conversion technique is based on reaction-bonding mechanism. Pure β -SiC and highly crystalline SiC modifications are most commonly synthesized via chemical vapor deposition (CVD) technique [113, 114]. Polymer pyrolysis was used to produce porous SiC and continuous SiC fibers [115, 116].

3.1.2 Structure

The excellent properties of SiC are due to high percentage (up to 88%) of covalent chemical bonding between atoms of silicon and carbon. It also shows slightly ionic character as a result of the different electronegativity values of silicon and carbon atoms. A stoichiometric composition resulted in stable compound of SiC [17].

α -SiC has many polytypes due to the different stacking of Si-C close-packed atomic planes [117, 118]. A large number of polytypes (> 200) are stated in literature due to different favored stacking sequences [119]. 4H, 6H and 15R are most commonly used/quoted polytypes, here H and R represents hexagonal and rhombohedral symmetry, whereas the leading numbers indicate the replication of the Si-C pair. The stability of SiC polytypes depends upon temperature range. β -SiC (3C-SiC) shows cubic symmetry and stable below 2373 K [120].

3.1.3 Properties

SiC materials show higher values of specific heat (670 J/kg K, at room temperature) as compared to other refractory carbides and nitrides. Specific heat values show temperature dependent

behaviour with linear increase at lower temperature and gradual increase at higher temperatures [121]. SiC materials show high values of thermal conductivity (350 W/m K) which depend upon temperatures, grain size and nature of grain boundaries [122, 123]. Thermal expansion coefficients are relatively low in the range of $4.4 \times 10^{-6} \text{ K}^{-1}$. These materials exhibit high mechanical properties (elastic modulus 460 GPa, shear modulus 195 GPa, Weibull modulus 2–12, fracture toughness 2.6–3.4 MPa $\text{m}^{0.5}$) [17].

3.1.4 Application

SiC materials are used for making turbine components, ball valves, heater elements, bearings, heat exchangers and as cutting tools. Moreover, they find applications in nuclear industry for the construction of reactor vessels and as a potential candidate for nuclear claddings. Furthermore, their excellent thermal stability, high creep resistance coupled with low density and high conductivity make them good choice for ceramic devices operating at high temperature in the fields of aviation, aerospace, automotive and machinery construction [17, 120].

3.2 Joining Technologies

This section contains an overview of different joining techniques which are being utilized in industry and laboratory for joining of SiC assemblies/components.

3.2.1 Introduction

Structural SiC materials show good resistance to corrosion, oxidation and radiological atmospheres. Moreover, they provide good mechanical and higher temperature properties as discussed in above section. These interesting properties make SiC materials valuable candidates to be used in severe condition of temperatures and corrosive atmospheres. However, this great potential of SiC is impaired due to some technological issues with SiC assemblies. One important issue is joining of SiC components; it is not possible to join their components and assemblies using conventional welding processes due to their non-melting behaviour. This makes it difficult to prepare complex SiC geometry structures with thick and thin sections [124].

3.2.2 Different joining techniques

The joining of SiC-based components for assembling complex structures is a scientific and engineering challenge. There are different processes which are being used in industry for joining of SiC components. A short overview of these processes is presented in this section.

3.2.2.1 Diffusion bonding

Diffusion bonding is an important technique for joining SiC and other ceramic components with and without using refractory interlayer. A strong bond is obtained between different parts and assemblies of SiC through solid state diffusion. This joining/bonding method requires higher application temperatures and pressures as compared to other joining techniques. It can be used to join

sections of different thickness. The resultant joints have almost the same composition and strength as base materials. It requires lower temperature gradient as compared to fusion welding and causes less residual stresses. However, it brings some disadvantages when compared with other joining processes. It is carried out in vacuum under application of high temperature and pressure; therefore requires costly equipment and longer joining time. Moreover, whole components experience same temperatures that may affect properties of assemblies. Furthermore, size of kiln limits the size of components/assemblies to be joined [125, 126]. Metal diffusion bonding method is most commonly used to join SiC components. It involves conversion of an inserted metal into compounds with host elements (e.g silicide or carbide with SiC). Metals used for metal-diffusion bonding include titanium, molybdenum, tantalum, niobium, and tungsten [127].

3.2.2.2 *Reaction/Chemical bonding*

Reaction bonding is carried out to join SiC components by direct reaction of silicon and carbon. During this process the pre-mixed joining composition is heated to slightly above the melting point of silicon (1414 °C) and the joint is made with almost the same composition as base SiC. However this joining process contains several drawbacks such as volume expansion upon conversion of carbon into SiC that leads to micro-cracks in the formed structure. Molten silicon flows into un-reacted areas due to capillary force until the carbonaceous precursor is fully consumed. The resultant joint microstructures consist of two phases; one is crystalline phase and second un-reacted metallic silicon. The volume fraction of un-reacted silicon may be reduced to 10% when the process is optimized for reduced silicon content in the final product. This process is not feasible for nuclear applications due to detrimental effect of the SiC–Si dual-phase microstructures on radiation stability [128, 129].

3.2.2.3 *Application of pre-ceramic polymers*

Pre-ceramic polymers (polycarbosilanes, polysiloxanes) are used recently for joining of SiC assemblies. They are mostly used together with inert and/or reactive fillers [130, 131]. The overall process completed at much lower temperatures as compared to diffusion bonding and reactions bonding. The joints produced with this technique are of moderate strength (5–30 MPa). Other difficulty involved in this method is mass loss of pre-ceramic polymers, which can exceed up to 50%. These polymer-derived joints are unstable in a radiation environment. Although, certain polymers combined with crystallization treatment have the potential to produce near-stoichiometric SiC in the joints which showed stability under radiation. However, mechanical properties of these polymers derived SiC after being fully crystallized is expected to be low [132, 133].

3.2.2.4 *Metallic brazing joining*

Metallic brazing joining technique is used extensively in industry for joining of ceramic components. This joining technique was first commercially utilized by Snecma *et al.* [134], they prepared different alloys for joining of SiC assemblies. These alloys are commercially known as

BraSiC™, which are primarily M:Si alloys. These are alloys of Si with metals of Cr, V, Ti, Rh, etc. Joining is achieved using a pressureless process in the temperature range 1200–1800 °C. Joints made with these metallic brazes show good mechanical properties and could provide toughness in the joints as compared to brittle ceramic joints. The important issue with this technique is the mismatch of thermal expansion coefficients between metallic fillers and ceramic matrix. Furthermore, this process requires an inert atmosphere and preparation of SiC surfaces to be joined [129, 135].

3.2.2.5 *Transient eutectic phase joining*

Transient eutectic phase joining (TEP), also known as liquid phase sintering (LPS) process, produces silicide ceramics in monolithic form. TEP techniques use a combination of dissolution and re-precipitation processes. It contains silicide ceramics with eutectic mixture of silica-alumina-rare-earth oxide to produce a dense body. Pressurized sintering is utilized to increase volume fractions of SiC that leads to superior performance. Katoh *et al.* [136] used a special category of pressurized TEP process named nano-infiltration and transient eutectic-phase (NITE) process for manufacture of SiC-matrix materials/composites. NITE SiC-based joining was successfully carried out to produce joints of very high quality. This process can be carried out either by mixing powder in slurry or using a commercial green sheet. For optimized results, the joining process is carried out at pressure of 5– 20 MPa and at high temperature of 1800 °C [124, 137].

3.2.2.6 *MAX-phase joining*

MAX-phase ceramics (e.g. Ti_3SiC_2) show high-temperature strength, pseudo-ductility and good oxidation resistance [138]. There are different routes of joining SiC component using MAX-phase ceramics. Solid state diffusion bonding of SiC with inserted titanium produced Ti_3SiC_2 phase under certain processing conditions [127]. Dong *et al.* [139] reported successful joining of SiC parts via hot pressing using pre-synthesized Ti_3SiC_2 powder as the bonding compound. Moreover, bulk composite material consisting of SiC– Ti_3SiC_2 with small amounts of TiC was prepared with the displacement reaction between Si and TiC. The joint composition can be adjusted by varying the TiC: Si ratio [124].

3.2.2.7 *Joining using glass/glass-ceramic fillers*

Glasses have potential to be used as soldering material to join ceramics and composites. They provide self-healing properties due to presence of residual glassy phase. Certain glasses have shown great potential as filler materials to produce gas-tight joints due to their tuneable properties. Glass properties such as coefficients of thermal expansions and structures can be altered to some extent by changing their compositions, their constituents and heat treatment processes. Joining of ceramic components with glasses/glass-ceramics provides potential advantage to control microstructures in joint layers. These properties help to produce a tight joint by using different glassy/glass-ceramics materials. Ferraris *et al.* [140, 141] used silica–alumina–yttria and calcia–alumina glasses for joining of SiC parts.

Lippmann *et al.* [142] have done an extensive work regarding joining of SiC components by using different compositions of yttrium aluminosilicate glasses. They revealed that joint properties strongly depend on glass compositions. Herrmann *et al.* [11, 143] produced strong and tight joints of SiC capsules and rods by using an optimal composition of 16.55 Y₂O₃–26.05 Al₂O₃–57.40 SiO₂ (mole %). The application of yttrium glasses as soldering materials make it interesting to explore further rare-earth aluminosilicate glasses as choice of material. In the present work different rare-earth aluminosilicate glasses are used as soldering material for joining SiC components.

3.2.3 Spark plasma sintering joining

Spark plasma sintering (SPS) utilizes uniaxial force and a pulse of direct current for consolidation of materials/powders under low atmospheric pressure. It is consisted on the electrical spark discharge phenomenon. Spark plasma is generated due to high energy and low voltage spark pulse current. This spark is generated for a limited period time at elevated temperatures. A SPS system contains of a sintering setup with vertical single-axis, water cooled vacuum chamber, vacuum exhaust unit, direct electrical current pulse generator and SPS controller. Specimens are loaded on the sintering stage in the chamber between the dies and punch. The energized pulse generates temperature quickly up to 1000~2500 °C and high quality sintered compact structure is produced in few minutes. SPS has been employed to achieve high quality joints due to its intrinsic advantages such as localized heating, low energy consumption, rapid processing, less deformation of the joined parts and highly controllable reaction of the interlayer between the joined parts. The electric field promote migration of ions trough the joining interface [79, 144].

In present study, yttrium aluminosilicate glasses are used as soldering material for joining SiC components by utilizing optimized parameters of SPS process.

3.2.4 Laser joining

A high energy laser beam can be used for joining different materials such as metals, ceramics and composites. It is characterized with a focused high density energy laser beam to heat up material rapidly and joining process completed in few minutes. The laser beam is created by photons, so it doesn't require electric continuity, vacuum and not influenced by magnetism. Moreover this joining process is not limited to electrically conductive materials. The manipulative ability of the laser makes it ideal for automation and robotics. Laser welding/joining processes are used in critical high volume applications such as medical device, firearms, aerospace, and automotive production [142, 145, 146]. Important factors which affect laser welding/joining are type of laser, the incident power density, surface conditions of the base metal. Most important parameters to be optimized during laser joining process included laser power, focus position, spot size and beam duration. The successful laser joining also depends on selection of proper soldering materials, their properties and size of the joining layer. The important properties of solders needed to consider during joining are their coefficient of thermal expansion, melting/liquid temperatures, wettability characteristics and laser absorption properties.

There are different types of laser that can be used for joining such as CO₂ lasers, solid state lasers (Nd: YAG) and diode lasers [142, 145]. A radiation pyrometer is used extensively in laser joining processes to detect surface temperature of SiC surfaces and helps to control laser power.

Lippmann *et al.* [142] used an optimized laser process for joining of SiC components. They utilized CO₂ laser and Nd: YAG lasers for joining. Later, Herrmann *et al.* [11, 143] used diode lasers for joining of SiC capsules and rods by using yttrium aluminosilicate glasses as soldering materials. Present work was carried out to extent the choice of soldering materials by considering rare-earth aluminosilicate glasses. For this purpose different rare-earth aluminosilicate glasses have been prepared and structurally investigated with different qualitative and quantities techniques/methods. These prepared glasses are used as soldering materials for joining SiC components using optimized laser joining process. This work has enhanced choice of soldering materials which can produce tight joints of high mechanical strength.

4 MATERIALS AND EXPERIMENTAL METHODS

This chapter contains details of substances, glass preparation procedures, methods and techniques for the characterization of the prepared glasses.

4.1 Preparation of glasses

Pure high quality (99.9%) powders of Y_2O_3 , Yb_2O_3 , Dy_2O_3 , Nd_2O_3 , Ho_2O_3 , Sc_2O_3 , (1-5 micron; 99% pure) alumina, (< 5 micron; 99 % pure) silicon nitride, (1-3 micron; 99 % pure) boron nitride, (99% pure) titania, (99% pure) zirconia from Abcr GmbH and (> 99.8%) amorphous silica from Evonik GmbH were used for the preparation of glasses.

4.1.1 Preparation of rare-earth aluminosilicate glasses

Oxide powders (Y_2O_3 , Yb_2O_3 , Dy_2O_3 , Nd_2O_3 , Ho_2O_3 , Sc_2O_3 , and Al_2O_3) were first dried in a kiln for 12 hours at 1000 °C, while amorphous SiO_2 was annealed at 800 °C. These powders were stored in desiccators. The well-known SiO_2 rich eutectic composition 12.18% Y_2O_3 –22% Al_2O_3 –65.82% SiO_2 (mole %) was used as main composition. The glass forming regions for this composition is already well defined as shown in Fig. 4.1. Y_2O_3 was replaced by the same amount (mole %) of Yb_2O_3 , Ho_2O_3 , Dy_2O_3 , Nd_2O_3 , and Sc_2O_3 for preparation of rare-earth aluminosilicate glasses. This composition falls in eutectic zone of glass-forming regions for respective glass-systems and produce clear glasses without crystalline phases. These oxide powders were weighed and mixed according to the composition given in Table 4.1 (a, b). The oxides mixtures were mixed in isopropanol and homogenized for 30 minutes in an ultrasonic bath. The powder mixtures were then dried in an oven at about 100 °C. Platinum crucible placed in an alumina ceramic boat was used for the melting of these mixtures. Batches of 10 g dry powder mixture were melted at 1550–1650 °C depending upon the mixture composition. A heating rate of 10 K/min was used in a high-temperature chamber furnace with $MoSi_2$ heating elements (Nabertherm GmbH). The melts were held for 1h at the maximum temperature for homogenization and then quenched in water to obtain the glass pieces. These glass pieces were of few millimetres in size and grinded by using a ball mill to get glass powder of less than 5 μm . The ultimate aim of the present work was to use prepared glasses as soldering material for joining of SiC components. For this, optimum amount of fine powders of these in-house produced glasses were used to prepare slurry with ethanol. Therefore, glasses were grinded to produce fine powders.

It is important that mortar of the ball mill should be selected according to size of the sample to be milled. In case of small amount of sample the tearing of balls can alter the stoichiometric ratios of oxides in mixture.

Table 4.1a: Starting composition of the glass mixtures (mole %) and melt process temperatures.

Sample	System	Al ₂ O ₃	SiO ₂	Y ₂ O ₃	Yb ₂ O ₃	Ho ₂ O ₃	Dy ₂ O ₃	Nd ₂ O ₃	Sc ₂ O ₃	T _m (°C)
P1	AlSiY	22	65.82	12.18						1550
P2	AlSiYb	22	65.82		12.18					1550
P3	AlSiHo	22	65.82			12.18				1550
P4	AlSiDy	22	65.82				12.18			1550
P5	AlSiNd	22	65.82					12.18		1550
P6	AlSiSc	22	65.82						12.18	1650

Table 4.1b: Starting composition of the glass mixtures (mass %) and melt process temperatures.

Sample	System	Al ₂ O ₃	SiO ₂	Y ₂ O ₃	Yb ₂ O ₃	Ho ₂ O ₃	Dy ₂ O ₃	Nd ₂ O ₃	Sc ₂ O ₃	T _m (°C)
P1	AlSiY	25.07	30.74	43.19						1550
P2	AlSiYb	20.40	35.96		43.65					1550
P3	AlSiHo	20.77	36.62			42.61				1550
P4	AlSiDy	20.88	36.82				42.30			1550
P5	AlSiNd	21.79	38.41					39.81		1550
P6	AlSiSc	28.48	50.20						21.32	1650

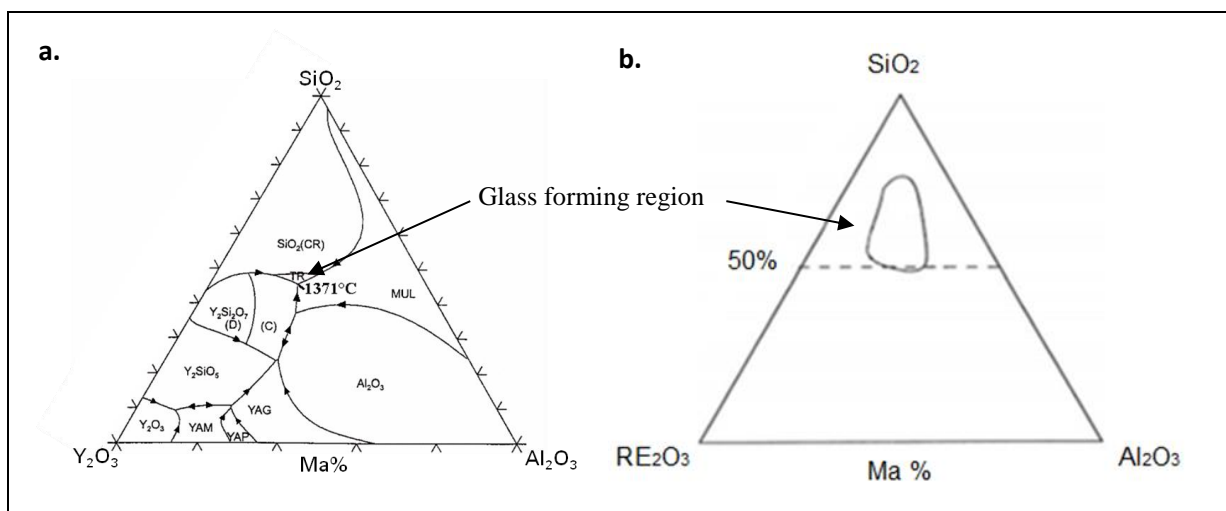


Figure 4.1: Glass forming regions; (a) Y₂O₃-Al₂O₃-SiO₂ system [50], (b) RE₂O₃-Al₂O₃-SiO₂ system whereas RE stand for Y, Yb, Ho, Dy, Nd and Sc.

4.1.2 Preparation of TiO₂ and ZrO₂ containing yttria and neodymia aluminosilicate glasses

Y-aluminosilicate and Nd-aluminosilicate glasses containing TiO₂ and ZrO₂ (4 and 8 mass %, respectively) as nucleating agents were prepared. For this, oxides were mixed according to the compositions given in Table 4.2 (a–d). The powder mixtures were mixed in isopropanol and homogenized in ultrasonic bath for 30 minutes. The powder mixtures were then dried in an oven at about 100 °C. Platinum crucible placed in an alumina ceramic boat was used for the melting of mixture. Batches of 10g dry powder mixture were melted at 1550 °C using a heating rate of 10 K/min in a high temperature chamber furnace with MoSi₂ heating elements (Nabertherm GmbH). The melt was hold for 1h at the maximum temperature for homogenisation and then quenched in water to obtain the glass pieces. The glass pieces were grinded in a ball mill to get glass powders.

Table 4.2a: Starting compositions of the TiO₂ containing Y-aluminosilicate glasses (mass %).

Sample	System	Al ₂ O ₃	SiO ₂	Y ₂ O ₃	TiO ₂
P1-4T	AlSiY4%TiO ₂	24.06	42.43	29.51	4
P1-8T	AlSiY8%TiO ₂	23.06	40.66	28.28	8

Table 4.2b: Starting compositions of the ZrO₂ containing Y-aluminosilicate glasses (mass %).

Sample	System	Al ₂ O ₃	SiO ₂	Y ₂ O ₃	ZrO ₂
P1-4Z	AlSiY4%ZrO ₂	24.06	42.43	29.51	4
P1-8Z	AlSiY8%ZrO ₂	23.06	40.66	28.28	8

Table 4.2c: Starting composition of the TiO₂ containing Nd-aluminosilicate glasses (mass %).

Sample	System	Al ₂ O ₃	SiO ₂	Nd ₂ O ₃	TiO ₂
P5-4T	AlSiNd4%TiO ₂	20.92	36.87	38.21	4
P5-6T	AlSiNd6%TiO ₂	20.48	36.10	37.42	6
P5-8T	AlSiNd8%TiO ₂	20.04	35.34	36.62	8

Table 4.2d: Starting compositions of the ZrO₂ containing Nd-aluminosilicate glasses (mass %).

Sample	System	Al ₂ O ₃	SiO ₂	Nd ₂ O ₃	ZrO ₂
P5-4Z	AlSiNd4%ZrO ₂	20.92	36.87	38.21	4
P5-6Z	AlSiNd6%ZrO ₂	20.48	36.10	37.42	6
P5-8Z	AlSiNd8%ZrO ₂	20.04	35.34	36.62	8

4.1.3 Preparation of nitrogen-containing yttria and neodymia aluminosilicate glasses

Y-aluminosilicate and Nd-aluminosilicate glasses containing different amount of nitrogen (4 and 8.33 mole %, respectively) were prepared. Powder batches of 10g were prepared by weighing proper amounts of oxides and silicon nitride as given in Table 4.3. The chosen compositions fall in the glass formation regions mentioned by Drew *et al.* [147] in Jänecke triangular prism as shown in Fig. 4.2. The powder mixtures were mixed in isopropanol and homogenised in ultrasonic bath for 30 minutes. These mixtures were dried in an oven at about 100 °C for overnight. Then powder mixture was compacted with an uniaxial press up to 50 kN to obtain mixture tablets of 10 mm diameter. The compacted tablet was packed in air-sealed plastic bag and pressed up to 2000 kN in cold isostatic pressing. The maximum pressure (2000 kN) was applied for 1 min. For each composition 5 tablets (2g/each) were prepared. A powder bed was made in BN crucible with an equimolar mixture of the sample powder and BN powder. The compacted tablets were put on this powder bed. BN crucible with lid was then kept in a graphite crucible on a Si₃N₄:SiO₂ (1:1) powder bed. This graphite crucible was closed with lid. This procedure was used previously by Lofaj *et al.* [96] for preparation of nitrogen containing rare-earth aluminosilicate glasses. The samples were melted at 1650 °C with 20 K/min up to 1400 °C and 10 K/min from 1400 °C to 1650 °C. The samples were kept at maximum temperature (1650 °C) for 4 h under nitrogen overpressure of 2.2 MPa. Then samples were cooled to room temperature with sufficiently high cooling rate (100 K/min) using water-cooled furnace shell to get the glass samples. Prepared glasses were in blackish shades as shown in Fig. 4.3. The glass pieces were grinded in a ball mill to get glass powders.

Table 4.3: Starting composition of the nitrogen-containing rare-earth aluminosilicate glasses (mole %).

Sample	System	Al ₂ O ₃	SiO ₂	Si ₃ N ₄	Y ₂ O ₃	Nd ₂ O ₃
P7	AlSiYON	12	60	4	24	---
P8	AlSiYON	12.50	50	8.33	29.16	---
P9	AlSiNdON	12	60	4	---	24

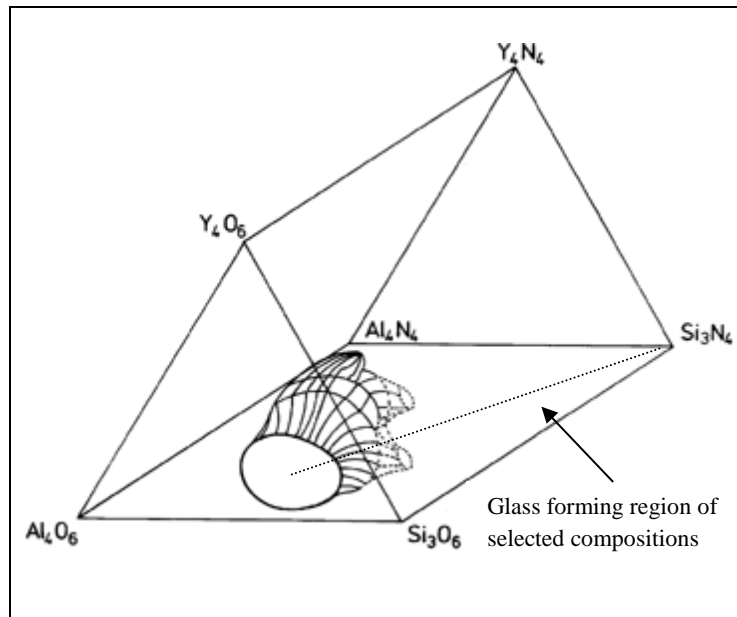


Figure 4.2: Jänecke's triangular prism representation of the Y-Si-Al-O-N system showing the oxynitride glass forming region calculated by Drew *et al* [147].

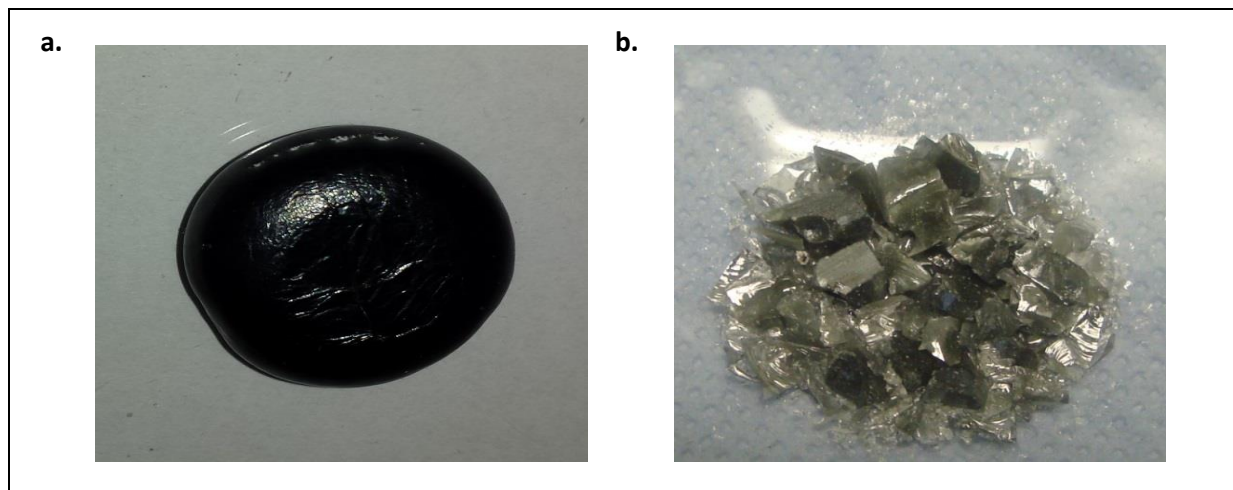


Figure 4.3: Prepared nitrogen-containing rare-earth glass; (a) Glass button, (b) Glass pieces.

4.2 Characterization instruments/techniques

4.2.1 X-ray powder diffraction

In the present study, X-ray investigations of glasses and heat-treated samples were recorded using a Seifert diffractometer (MZ4) with meteor detector, $K\alpha$ radiation of Cu ($\lambda=1.5418 \text{ \AA}$) with a voltage of 40 kV and current of 30 mA on Bragg-Brentano geometry ($\theta/2\theta$). As glasses are amorphous materials which do not possess long periodicity and atoms are randomly distributed in 3D space. Due to amorphous nature the distance between the atoms cannot be defined as in the case of ordered structures, thus eliminating concentration of reflections at defined positions produce typical glassy hub.

4.2.2 X-ray fluorescence

The chemical compositions of glasses in the present work were determined using X-ray fluorescence (XRF) technique with a WDXRF from Bruker AXS (S4 PIONEER).

4.2.3 Spectroscopy

Spectroscopy techniques are extensively utilized in materials science for characterizations. They utilize interaction of different frequency components of the electromagnetic spectrum with sample. There are different processes such as absorption, transmission, reflection, scattering and photoluminescence taking place when an electromagnetic radiation interacts with materials. In the present work, Raman spectroscopy, IR spectroscopy and NMR spectroscopy were utilized for structural investigation of glasses.

4.2.3.1 Raman spectroscopy

Raman spectra of glasses and heat-treated samples in the present study are obtained with a Renishaw 1000 Raman microscope. For Raman spectra of the prepared glasses, bulk glass samples were mounted in epoxy and fine polished by using ceramographical preparation steps. An argon laser with a wavelength of 514.5 nm (Modu-Laser Mod. Aries-163) was used for exciting Raman scattering. A UV-enhanced CCD detector was used which was operated at -70 °C and spectra measured in the range of 400–1400 cm^{-1} with a sampling time of 120 s.

4.2.3.2 Infrared spectroscopy

For infrared (IR) analyses, glass splitters of the prepared glasses were grinded to get fine glass powders. IR spectra of glasses and heat-treated samples in this study were measured using a Bruker Tensor27 spectrometer (Bruker Optics, Ettlingen, GER) equipped with a Bruker Platinum® ATR accessory (diamond crystal, single reflection, 1 mm^2 sampling area) and a deuterated tri-glycine sulfate detector (DTGS) against an air background. For each sample 32 scans were collected with a spectral resolution of four wave numbers and a bandwidth from 370–4000 cm^{-1} .

4.2.3.3 Solid state nuclear magnetic resonance spectroscopy

^{27}Al solid NMR spectra of glasses in this study were analyzed using NMR signal acquisition technique. The glass powders experienced magic angle spinning (MAS), where sample holder subtends the “magic angle” relative to the external magnetic field direction. Bruker Avance-III 500 MHz widebore and Bruker Avance-I 600 MHz widebore spectrometers were used with magic angle spinning at 25 kHz spinning speed for acquired ^{27}Al spectra and Measurements were acquired with a single pulse excitation. Sample was in a 2.5mm outer diameter rotor, which was measured in a two-channel (HX) 2.5 mm MAS probe from Bruker. The recycle delay was 0.5s and pulse length of the central transition was 10 μs (microseconds).

4.2.4 In-situ XRD

In-situ XRD is used to study crystalline phase transformations in samples during heating at higher temperature range. In this work, in-situ XRD measurements of glasses were conducted with a Bruker D8 diffractometer. It was equipped with high-temperature chamber HTK1200N from an Anton Paar and a LynxEye position-sensitive detector. An alumina ceramic sample holder with a diameter of 18 mm was used for powder glass samples. A constant heating rate of 10 K/min was used to collect diffraction patterns at room temperature and in a temperature range of 700–1200 °C at 50 °C steps. $K\alpha$ radiation of Cu with a voltage of 40 kV and 40 mA was utilized and scans were recorded in the range of 15– 60° 2 θ .

4.2.5 Scanning electron microscopy and electron microprobe analysis

Scanning electron microscope (SEM) images of heat-treated samples were taken with a SEM Cambridge Instruments, Stereoscan 200 model that contains back scatter electron (BSE) detector and an Energy-dispersive X-ray spectroscopy (EDS) system. Electron microprobe analyser (EPMA) was used for structural and quantitative phase analyses of the specimens. The samples were embedded in graphite and analyses were carried out by using a JEOL device with wave length dispersive analysis (WDS) system.

4.2.6 Differential scanning calorimetry

In the present work a commercial differential scanning calorimeter (DSC, Netzsch 404C) was used for determining specific heats, glass transition temperatures and crystallization temperatures of glasses. The measurements were performed with 5 mm diameter compacted powder samples in alumina crucibles with a lid at a heating rate of 15 K/min up to 1300 °C under argon. There was no reaction found between alumina crucibles and prepared glasses for defined temperature range. For DSC measurements the calibration was carried out using Ag/Au as temperature standards. Crystallization temperatures of glasses were found by using peak maximum methods whereas glass transition temperatures were obtained by extrapolated onset procedure.

The specific heat capacities of glasses were determined between 50–800 °C. The measurements were carried out under argon in platinum crucible using sapphire as calibration standard. The specific heat values were determined using the 3-step method.

4.2.7 Differential thermal analysis

Differential thermal analyses (DTA) of glasses were performed using SETSYS (SETARAM, Germany) with a heating rate of 5 K/min in the temperature range of 400–1400 °C under argon atmosphere. The measurements were carried out in platinum crucibles.

4.2.8 Dilatometry

In the present work the sintering effects and coefficients of thermal expansion of glasses were determined using a dilatometer (Netzsch- Dil 402C) under argon. Thermal expansion coefficients of glasses were determined with a heating rate of 5 K/min up to temperature of 700 °C.

4.2.9 Thermal diffusivity

Thermal diffusivities of glasses were determined up to 700 °C using a commercial Laser flash apparatus (LFA 427, Netzsch), with a heating rate 5 K/min under helium atmosphere.

4.2.10 Density measurement

Density of a substance is the relationship between the mass of the substance and its volume. Densities of glasses in this work were determined using Accu Pyc II 1340 Pycnometer. For each sample ten measurements were made and their average was used as measured quantity.

4.2.11 Thermal conductivity

Thermal conductivities of glasses in this work were calculated by multiplying the measured values of thermal diffusivity, specific heat and density.

4.2.12 Refractive indices measurement

Refractive indices of materials show their interaction with electromagnetic radiation. It is important to determine the refractive indices of glasses due to their applications in optical industries and structure clarity. There are different techniques/methods to find out the refractive indices of materials such as interferometry, deviation methods, critical angle method, index match method, Brewster angle method, microscopy and scattering methods etc. In the present work the refractive indices of the prepared glasses were found using laser light source operating at $\lambda=580$ nm and Brewster angle (θ_B) method from the equation $n=\tan(\theta_B)$.

4.2.13 Micro-hardness measurement

In this work, hardness of the polished glass surfaces embedded in epoxy was determined using micro-hardness indenters. For each sample five measurements were made using a load of 50g for 10 second and their average was used as measured quantity.

4.2.14 Leakage test

The tightness of the joined capsules was determined by the integral measurement of Helium leak test after the joining process of capsules as mentioned in literature [143]. (This work was performed at TU Dresden by Dr. Marion Herrmann).

4.2.15 4-point bending test

The mechanical strength of the joined rods was measured using 4-point bending strength test and in agreement with DIN EN 843-1 on a test machine type Z010 (Fa. Zwick/Roell). The leading

power amounted 2N with $35 \text{ N}\cdot\text{s}^{-1}$ velocity of the loading pins. Further details of bending test are provided in previous work [12, 143]. (This work was performed at TU Dresden by Dr. Marion Herrmann).

4.2.16 Joint preparation of SiC components

Commercially sintered silicon carbide (SSiC) capsule halves (StarCeram S, H.C. Starck) were used in the joining experiments with diameter of 12.5 mm, length of 16 mm and wall thickness of 2 mm. The geometry of these capsules are discussed in previous work [143]. The pairs of capsule were joined via laser-assisted process. The joint capsules were used for the microstructural analysis and for the joints tightness experiments. Furthermore, SSiC rods (diameter: 6 mm, length: 35 mm) of the same quality were joined and used for the mechanical strength investigation.

4.2.17 Laser joining of SiC components

Laser joining of SSiC components (capsules and rods) by using the prepared glasses as solders were performed at TU Dresden. A diode laser (DL0301Q, ROFIN) of wavelengths 808 nm and 940 nm was utilized for the heating of the samples to be joined. The laser beam was guided via a scanner (power SCAN33, Scan-lab) to allow for damage-free heating of the samples. Two different experimental setups for laser-assisted heating were used to join capsules and rods. In the first setup, the SSiC capsules rotate with a speed of 120 rpm during heating and pressed against each other with an axial force of 10N as described elsewhere [143]. In the other setup for rods joining, the samples were fixed during heating and the laser beam was guided with a high reflecting copper mirror to the areas to be joined. The absolute value of laser power was determined through the softening temperature of the filler. The temperature measurement during the laser processing was performed with an infrared camera (VarioCAM hr head, InfraTec) with integrated software “IRBIS 3 professional” as explained in literature [11, 12, 143].

4.2.18 Joining of SiC components using spark plasma sintering process

Spark plasma sintering process was used for joining rods (diameter: 5 mm, length: 10 mm) and plates (length: 25 mm, width: 25 mm, thickness: 4 mm) of SiC by using in-house prepared glasses as solders. For joining process rods and plates were cleaned by using ultrasound to remove dust particles and greasy substances. The surfaces of these components were fine-polished by following ceramographical specimen preparation steps. SPS system from FCT system GmbH (Type: KCE®-FCT HP D 250) was used to join SiC components. The electrical and thermal conductivity of SiC at room temperature is ($0.5 \times 10^4 \text{ S/m}$ and 135 W/m K) comparable to the constitutive graphite of the SPS mould ($6 \times 10^4 \text{ S/m}$ and 70 W/m K). The lower electrical conductivity of SiC as compared to graphite results in a preferential current across the SPS moulds [137].

5 RESULTS

In this chapter structural and thermal analysis of the prepared glasses, their crystallization studies, application as solders for joining of SiC components using laser assisted process and properties of the joints are presented. The results of microwave heating on the crystallization of $\text{RE}_2\text{O}_3\text{-Al}_2\text{O}_3\text{-SiO}_2$ (RE stands for Nd, Y) glasses for different period of times at high temperatures are also included in this chapter. Moreover, the effects of different nucleating agents on the crystallization behaviour and properties of glasses are discussed. Furthermore, the results of glasses containing nitrogen contents, their crystallization under different atmospheres and application as solders for joining of SiC components also included in this chapter. The joining of SiC components using spark plasma sintering process is presented in the last part of the chapter.

5.1 Structural analyses of rare-earth aluminosilicate glasses

The glass pieces formed as a result of quenching the prepared glass melts in water are shown in Fig. 5.1. These glass splitters were of typically a few mm in size. Colored glasses in P3, P4, P5 glass systems were due to intrinsic color properties of Ho_2O_3 , Dy_2O_3 and Nd_2O_3 , respectively. These glasses were extensively characterized using different structural analyses techniques such as XRD, IR, Raman and solid state NMR spectroscopy. Structural analyses were carried out to determine short range ordering, structural modes and coordination numbers in the glasses.

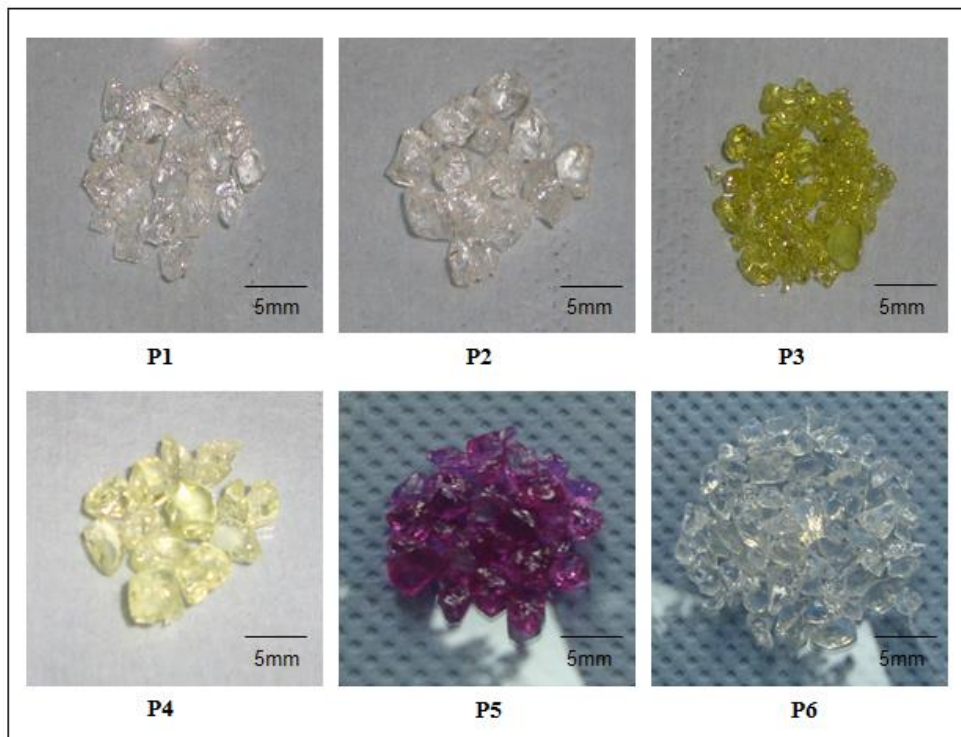


Figure 5.1: Optical images of the prepared glasses; P1 (AlSiY), P2 (AlSiYb), P3 (AlSiHo), P4 (AlSiDy), P5 (AlSiNd) and P6 (AlSiSc).

5.1.1 Chemical analyses of rare-earth aluminosilicate glasses

For chemical analyses, fine powders of the prepared glasses were obtained using ball mill. The chemical compositions of glasses were determined using XRF method and given in Table 5.1. The chemical compositions of glasses were found closely matching with the initial compositions of the oxides mixtures as shown in Table 4.1b. One can notice a small deviation in amounts of rare-earth oxides in initial compositions and their amount determined with XRF in the prepared glasses.

Table 5.1: Chemical composition of prepared rare-earth aluminosilicate glasses (mass %).

Sample	System	Al ₂ O ₃	SiO ₂	Y ₂ O ₃	Yb ₂ O ₃	Ho ₂ O ₃	Dy ₂ O ₃	Nd ₂ O ₃	Sc ₂ O ₃
P1	AlSiY	25.2	30.9	43.9					
P2	AlSiYb	20.6	36.6		43				
P3	AlSiHo	20.8	36.5			42.01			
P4	AlSiDy	21.2	36.4				41.90		
P5	AlSiNd	22.3	38.3					39.3	
P6	AlSiSc	28.7	50.6						21.28

5.1.2 XRD analyses of rare-earth aluminosilicate glasses

X-ray diffractions of these glasses are shown in Fig.5.2, which revealed typical amorphous structure as explained in section 4.2.1. Prepared glasses showed intrinsically random structures.

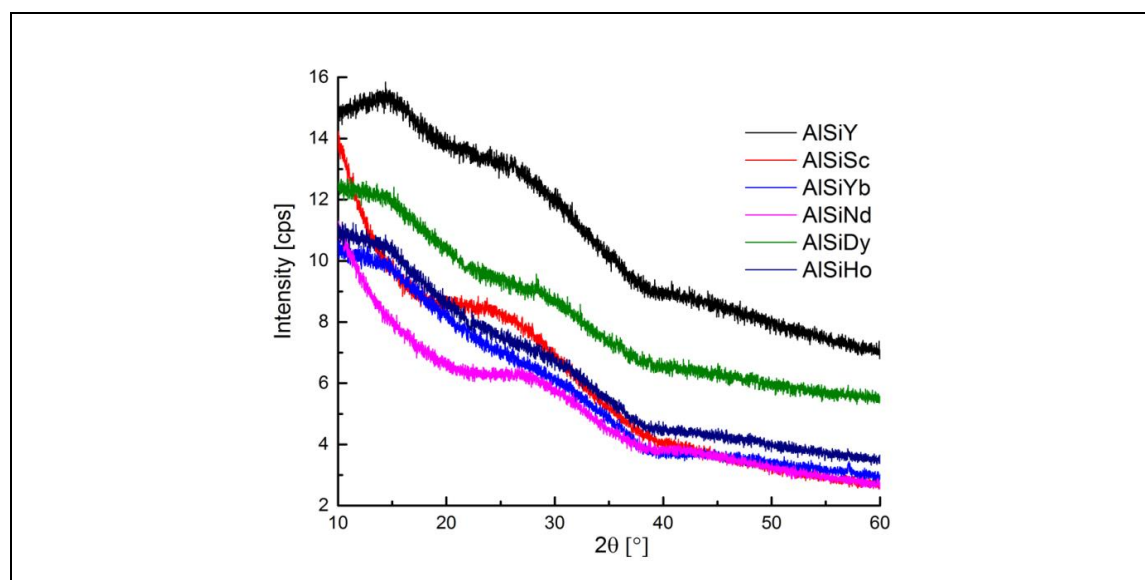


Figure 5.2: XRD of prepared rare-earth aluminosilicate glasses.

5.1.3 Infrared analyses of rare-earth aluminosilicate glasses

IR spectra of glasses in the range 400–1400 cm⁻¹ wave numbers are shown in Fig. 5.3, due to the special interest of vibration modes in this range. Assignments of the IR bands for the prepared glasses are given in Table 5.2. IR analyses revealed symmetrical stretching of Si-O-Si and asymmetric

stretching Si-O-M, where M stands for Al^{3+} and/or respective rare-earth ions. IR spectra of P1–P4 glass systems were almost identical with stretching mode of Si-O band at around 893 cm^{-1} , for the P5 glass system it was near 902 cm^{-1} and for the P6 glass it was found around 885 cm^{-1} wave number. The band at around 890 cm^{-1} wave number is due to the non-bridging oxygen stretching mode of the Si-O⁻ band [37, 148]. Moreover, asymmetric stretching of Si-O-Si bonds was found for glasses around 1055 cm^{-1} wave numbers. The IR spectrum of the P6 glass showed an additional peak for symmetric stretching of Si-O-Si at 787 cm^{-1} wave number.

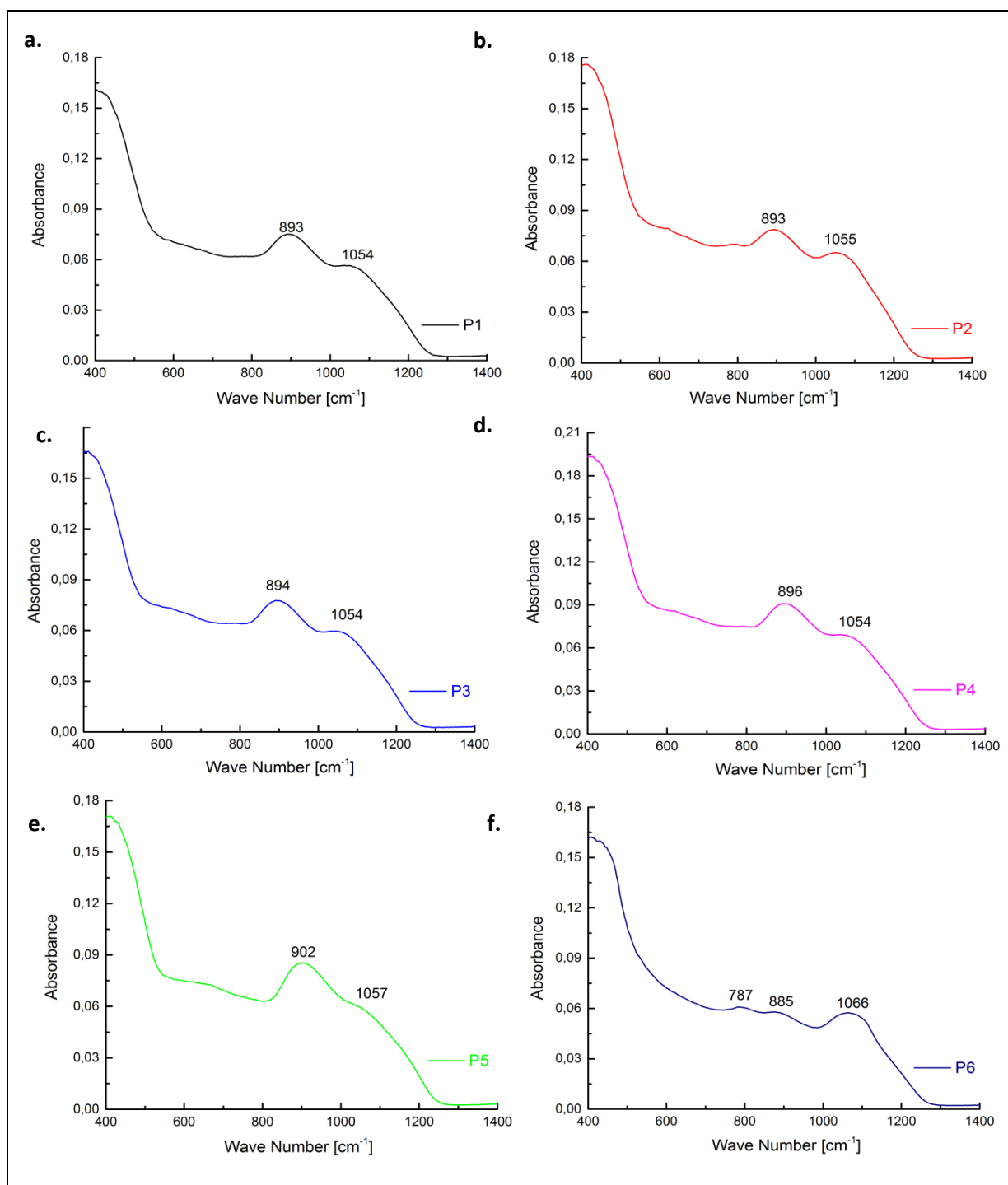


Figure 5.3: IR spectra of glasses; (a) P1 (AlSiY), (b) P2 (AlSiYb), (c) P3 (AlSiHo), (d) P4 (AlSiDy), (e) P5 (AlSiNd) and (f) P6 (AlSiSc).

Table 5.2: IR peak assignments of rare-earth aluminosilicate glasses.

Sample	Peak position (cm ⁻¹)	Peak assignment [100, 102]
P1(AlSiY)	893	(Si-O ⁻) NB stretching
	1054	(Si-O-Si) asymmetric stretching
P2(AlSiYb)	893	(Si-O ⁻) NB stretching
	1055	(Si-O-Si) asymmetric stretching
P3(AlSiHo)	894	(Si-O ⁻) NB stretching
	1054	(Si-O-Si) asymmetric stretching
P4(AlSiDy)	896	(Si-O ⁻) NB stretching
	1054	(Si-O-Si) asymmetric stretching
P5(AlSiNd)	902	(Si-O ⁻) NB stretching
	1057	(Si-O-Si) asymmetric stretching
P6(AlSiSc)	787	(Si-O-Si) symmetric stretching
	885	(Si-O ⁻) NB stretching
	1066	(Si-O-Si) asymmetric stretching

5.1.4 Raman analyses of rare-earth aluminosilicate glasses

Raman spectra of the prepared rare-earth aluminosilicate glasses were determined to reveal the structural bands in them. The number of bonding oxygen (n) per Si tetrahedron is denoted as Q^n and description of the structural units SiO_4 tetrahedra (Q species) is shown in Fig. 5.4 for Q^4 , Q^3 and Q^2 structures, respectively.

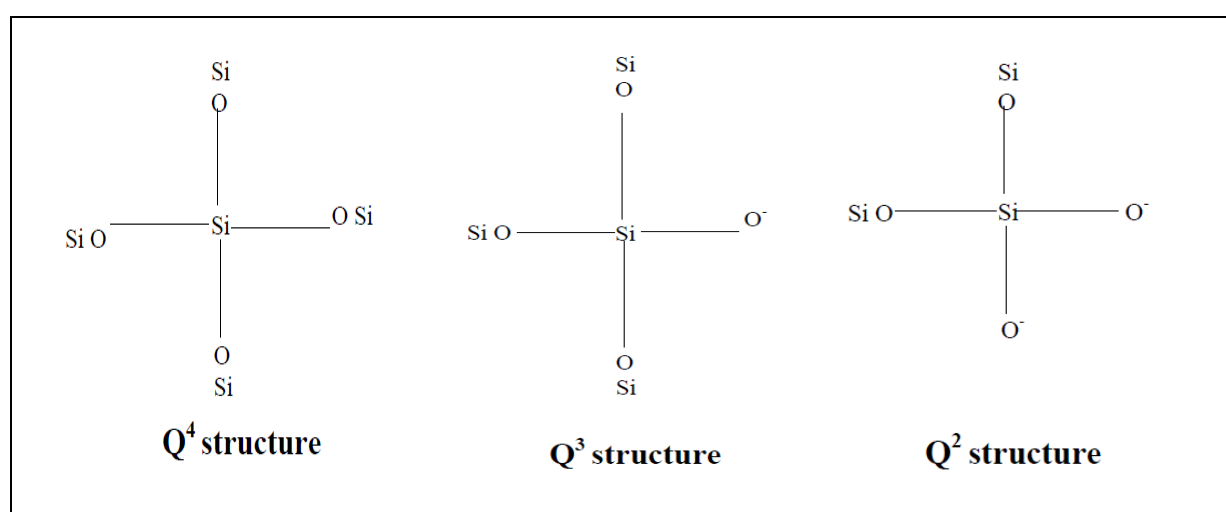


Figure 5.4: Illustration of the Q species in the SiO_4 tetrahedra [103, 149].

Q^4 structure describe SiO_4 tetrahedra that shared four corner oxygen to form a continuous three dimensional network and it consisted of four bridging oxygen per Si with zero non-bridging

oxygen. Structure contains three bridging oxygen and one non-bridging oxygen per Si atom represents as Q^3 . Whereas Q^2 structures consist two bridging and two non-bridging oxygen per Si atom [103].

The measured Raman spectra of rare-earth aluminosilicate glasses are shown in Fig. 5.5. Assignments for Raman bands observed in these glass samples are given in Table 5.3.

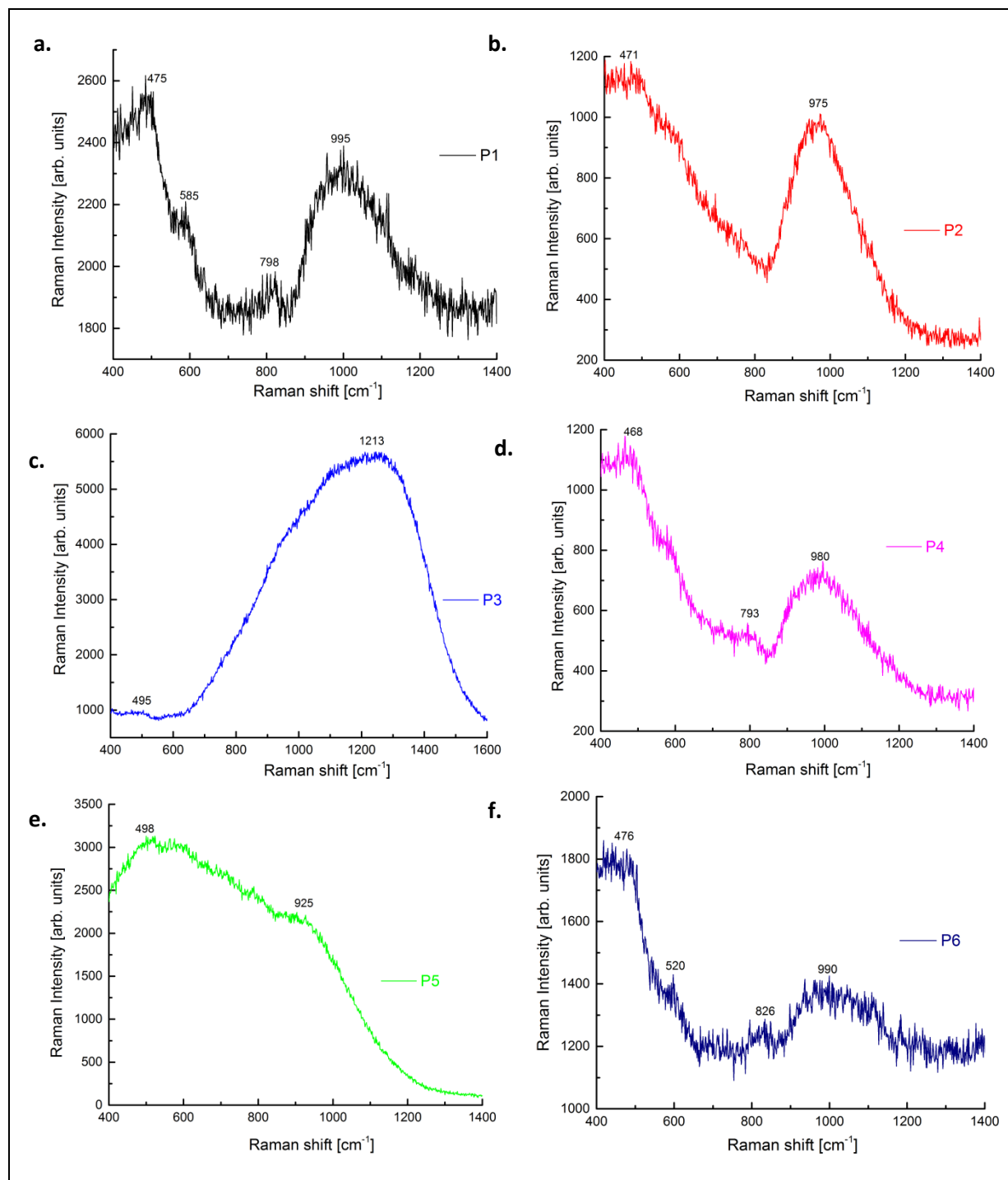


Figure 5.5: Raman spectra of glasses; (a) P1 (AlSiY), (b) P2 (AlSiYb), (c) P3 (AlSiHo), (d) P4 (AlSiDy), (e) P5 (AlSiNd) and (f) P6 (AlSiSc).

It was found that these glasses contained high amount of Q^4 and Q^3 structural units. The high contents of Q^3 structural units showed uniform distribution of the rare-earth ions as well as the non-

bridging oxygen (NBO). Raman spectra of the P1 glass contains of Q^4 structure, bending mode for Si-O-Si (Q^4) at around 585 cm^{-1} , stretching mode for Si-O-Si (Q^4) near 798 cm^{-1} and Si-O-M stretching mode in Q^3 at 995 cm^{-1} , where the associated Si atom is replaced by Y or Al. Raman spectra of the P2 glass system contained typical Q^4 structure and Si-O-M stretching in Q^3 at around 975 cm^{-1} . Raman spectra of the P3 glass showed a very broad peak at around 1213 cm^{-1} , which represents high portion of Q^2 structuring units. Raman spectrum of the P4 glass was almost identical to P1 glass system with peaks at $468, 793$ and 980 cm^{-1} respectively. It consists of Q^4 structure, stretching mode of Si-O-Si and Si-O-M stretching in Q^3 mode. Spectra of the P5 glass system were broader and it was not possible to distinguish between Q^4 and Q^3 . Raman spectra of the P6 glass showed peaks at $476, 520, 826$ and 990 cm^{-1} respectively. It contained Q^4 structure, stretching mode of Si-O-Si in Q^4 structure and Si-O-M stretching in Q^3 mode.

Table 5.3: Assignment of Raman bands for rare-earth aluminosilicate glasses.

Sample	Raman bands (cm^{-1})	Assignment of Raman bands [55, 102]
P1(AlSiY)	475	Q^4
	585	Si-O-Si bending
	798	Si-O stretching in Q^3
	995	Si-O stretching in Q^3
P2(AlSiYb)	471	Q^4
	975	Si-O stretching in Q^3
P3(AlSiHo)	495	Q^4
	1213	Q^3
P4(AlSiDy)	468	Q^4
	793	Si-O stretching in Q^3
	960	Si-O stretching in Q^3
P5(AlSiNd)	498	Q^4
	925	Q^2
P6(AlSiSc)	476	Q^4
	520	Si-O-Si bending
	826	Si-O stretching in Q^3
	990	Si-O stretching in Q^3

5.1.5 Solid NMR analyses of rare-earth aluminosilicate glasses

In this study, the local environments of ^{27}Al structural units (coordination numbers) in the prepared glasses were determined using solid state NMR analyses. Rare-earth cations have major effect on the silicate network to control the solubility and liquid-liquid phase separation. These cations also strongly affect the liquid viscosity-temperature curve. Therefore, it is necessary to explore the structural role of rare-earth cations in silicate glass network. First, magnetic susceptibility of glasses

was found using magnetic probe and are given in Table. 5.4. P1 and P6 glasses have diamagnetic nature, P2 and P5 glasses had intermediate magnetic susceptibility in the range of diamagnetic and paramagnetic. It was not possible to determine coordination numbers for P3 and P4 glasses due their paramagnetic nature. ^{27}Al spectra of these glasses are shown in Fig. 5.6. The spectra showed a central transition region with asymmetric peak shape typically observed in aluminosilicate glasses.

Table 5.4: Relative magnetic susceptibility of glasses.

Glass sample	Magnetic susceptibility
P1	2.0×10^{-6}
P2	5.3×10^{-6}
P3	18.3×10^{-6}
P4	14.0×10^{-6}
P5	2.3×10^{-6}
P6	0.6×10^{-6}

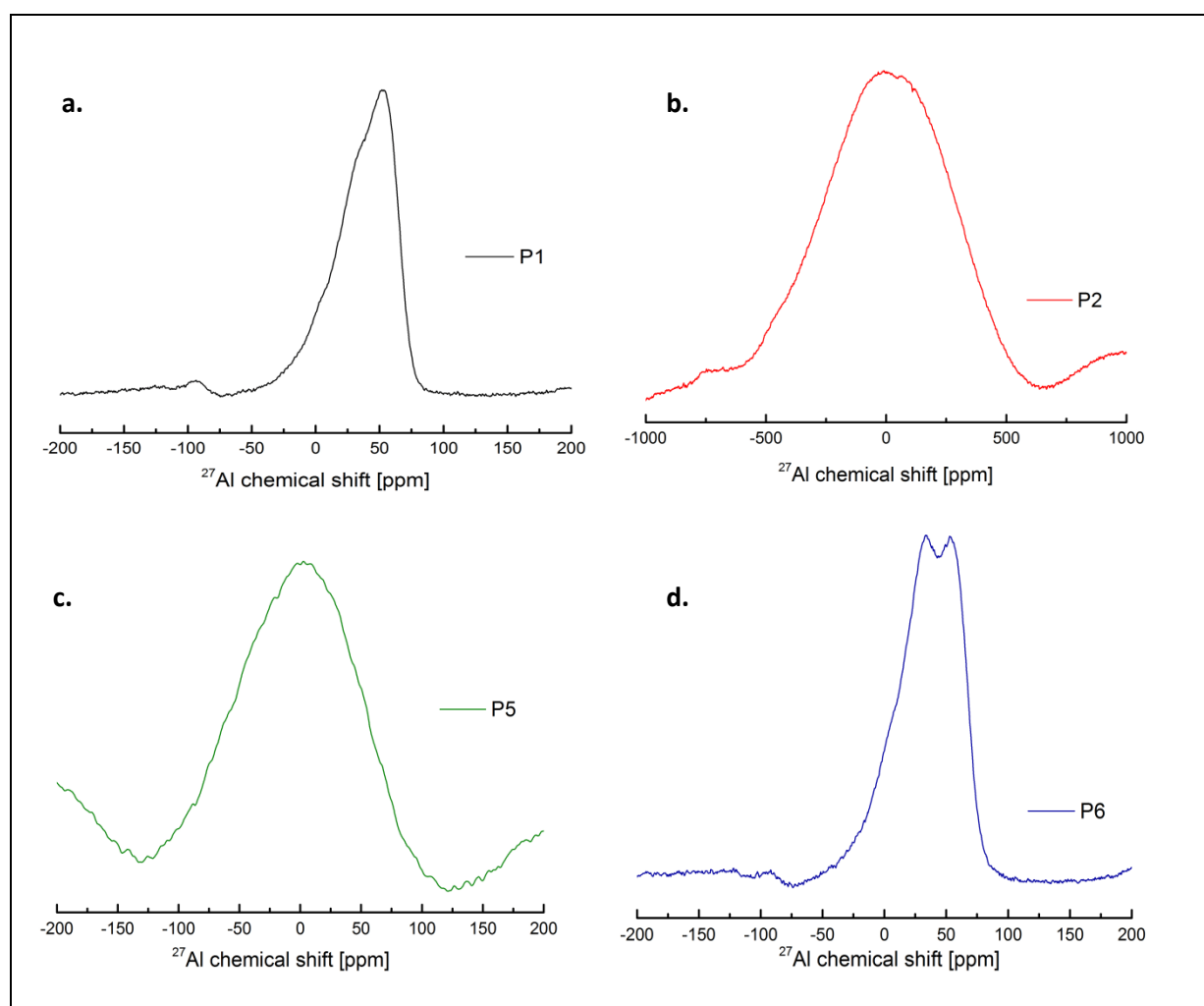


Figure 5.6: ^{27}Al solid NMR spectra of glasses; (a) P1, (b) P2, (c) P5 and (d) P6.

5.2 Thermal analyses of rare-earth aluminosilicate glasses

Thermal analyses of the prepared glasses were conducted to find out glass transition temperatures (T_g), crystallization temperatures (T_c), specific heats (C_p), coefficients of thermal expansion, thermal diffusivity and thermal conductivities.

5.2.1 Differential thermal analyses of glasses

Differential thermal analyses (DTA) of the P1 glass powder is shown in Fig. 5.7. The glass transition temperature (T_g) of P1 glass was found at 914 °C. A strong sintering effect was noticed at temperature around 1000–1100 °C for P1 glass. The first crystallisation temperature peak (T_{c1}) was recorded at 1180 °C, while a second crystallization peak (T_{c2}) was found at around 1345 °C and eutectic temperature was observed at around 1375 °C. These measured transition temperatures for the P1 glass were found matching with values mentioned in literature [44, 150, 151]. Transition temperatures for all glasses determined using DTA are shown in Fig. 5.8. A summary of the observed temperatures for all glasses is listed in Table 5.5.

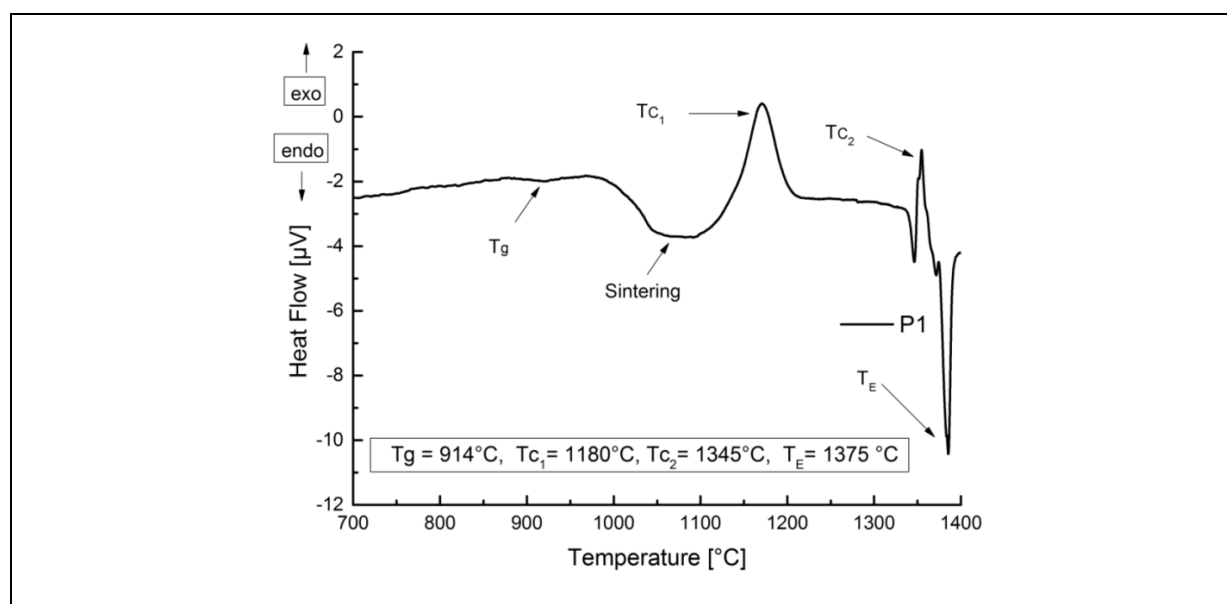


Figure 5.7: Differential thermal analysis of the P1 glass system.

Table 5.5: DTA values of the prepared glasses.

Glass sample	T_g (°C)	T_c (°C)	T_E (°C)
P1	914	1180, 1345	1375
P2	918	1175	1460
P3	912	1217	1370
P4	910	1210	1350
P5	884	---	1285
P6	893	1067	---

The P2 glass showed the highest value of glass transition temperatures which can be due to the smaller ionic radius of Yb^{+3} as compared to other rare-earth elements used in this study. The smaller ionic radius is expected to tighten the structures and results in higher glass transition temperatures.

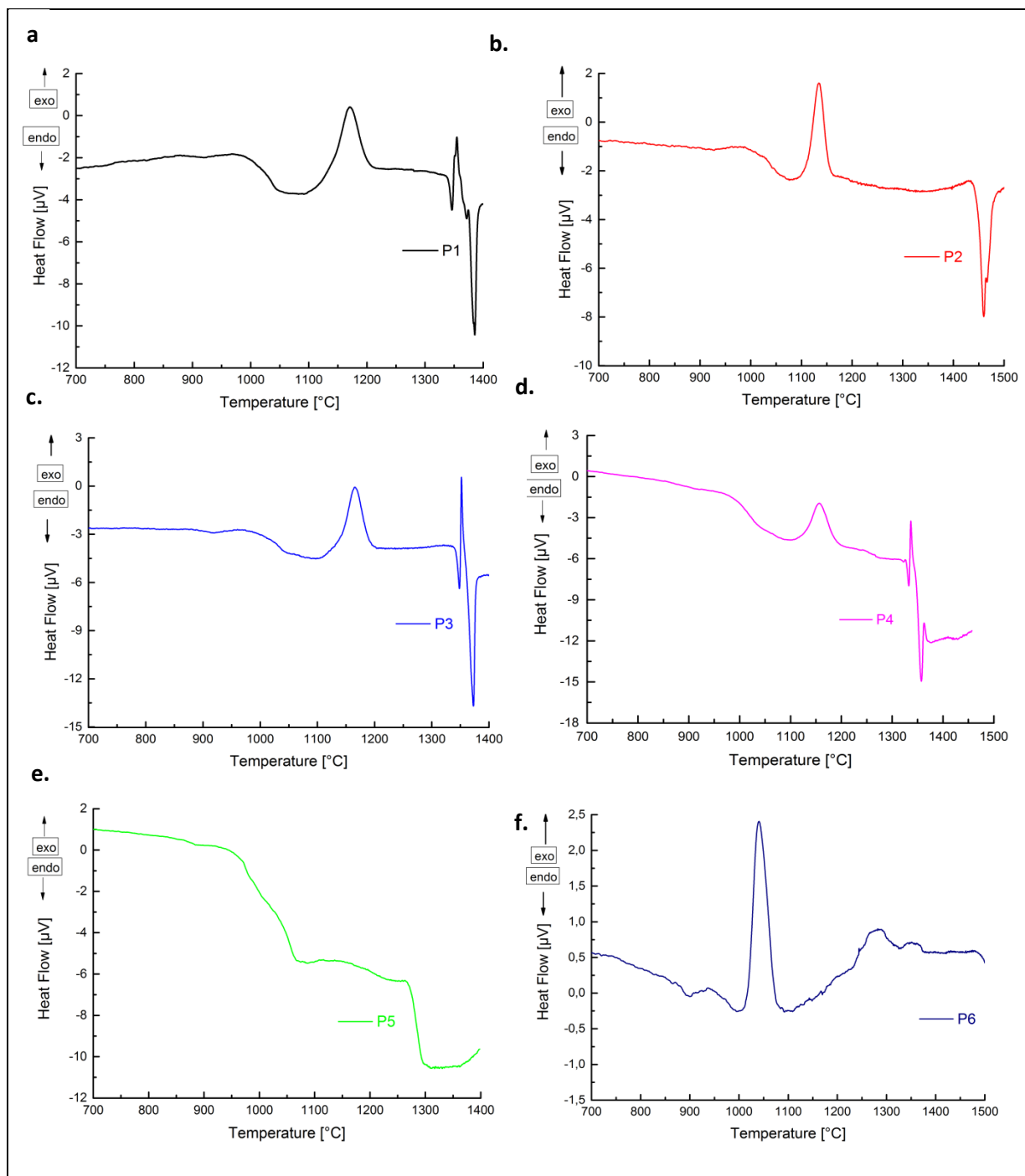


Figure 5.8: Differential thermal analyses of glasses; (a) P1, (b) P2, (c) P3, (d) P4, (e) P5 and (f) P6.

5.2.2 Softening analysis of glass

The softening behavior of the P1 compacted glass powder sample was analyzed during dilatometer experiment and shown in Fig. 5.9. The pressed glass sample did not change its shape up to a temperature of approximately 900 °C and experienced strong sintering effect after it. This sintering

effect was dominating at temperatures between 1000–1100 °C that fits with DTA observations. The starting temperature of glass softening (~900 °C) was also found in agreement with the glass transition temperature measured during DTA for the P1 glass.

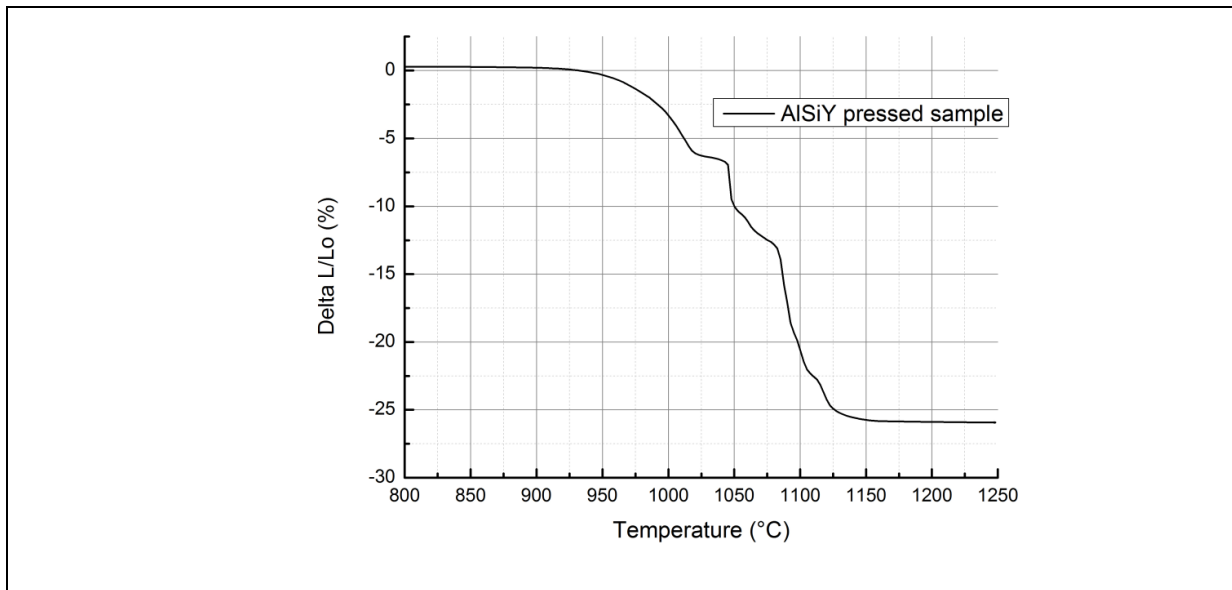


Figure 5.9: Dilatometer analysis of the P1 glass.

5.2.3 Differential scanning calorimetry of glasses

Transition temperatures of glasses were also determined with DSC to compare with transition temperatures obtained with DTA. DSC analyses of the prepared glasses are shown in Fig. 5.10.

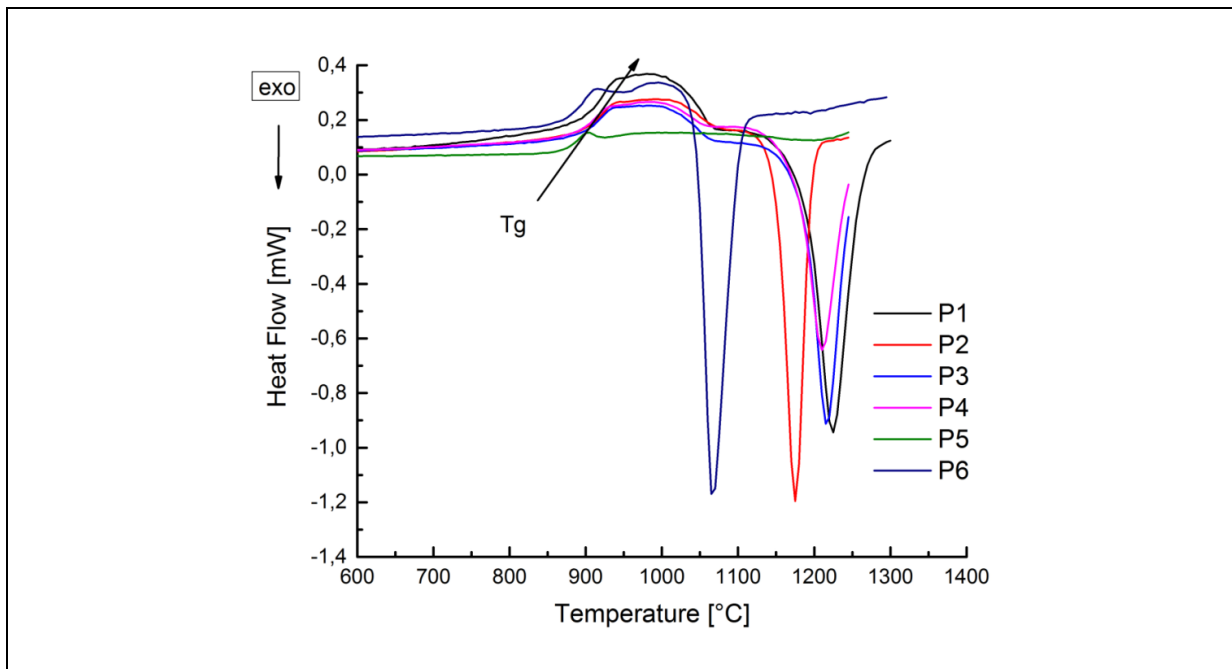


Figure 5.10: DSC of the prepared glasses.

It was observed that the lower the ionic radius of rare-earth ions, the higher the glass transition temperature with the exception of the P6 (AlSiSc) glass. The P5 glass started to flow after the glass

transformation temperature and did not show any crystallization temperature peak till 1250 °C. The measured temperatures values from the DSC experiments are summarized in Table 5.6.

Table 5.6: DSC values of the prepared glasses.

Glass sample	T _g (°C)	T _c (°C)
P1	917	1224
P2	918	1175
P3	912	1217
P4	910	1210
P5	884	----
P6	893	1067

5.2.4 Specific heat capacities of glasses

Specific heat (C_p) values of the prepared glass samples measured up to 800 °C using the 3-step method is summarized in Table 5.7.

Table 5.7: Specific heat capacities value of the prepared glasses.

T (°C)	P1 C _p (J/(g·K))	P2 C _p (J/(g·K))	P3 C _p (J/(g·K))	P4 C _p (J/(g·K))	P5 C _p (J/(g·K))	P6 C _p (J/(g·K))
50	0.644	0.577	0.601	0.568	0.542	0.757
100	0.731	0.626	0.636	0.605	0.554	0.870
200	0.821	0.681	0.680	0.667	0.587	0.938
300	0.874	0.719	0.716	0.714	0.617	0.968
400	0.916	0.761	0.747	0.742	0.628	1.001
500	0.944	0.787	0.766	0.762	0.625	1.033
600	0.964	0.815	0.780	0.778	0.619	1.056
700	0.980	0.838	0.791	0.792	0.603	1.072
800	1.001	0.859	0.798	0.803	0.578	1.094

5.2.5 Dilatometer analyses of glasses

Thermal expansion coefficients of glasses were determined with a heating rate of 5 K/min up to temperature of 700 °C. The measured values of coefficients of thermal expansion for these glasses are provided in Table 5.8. Thermal expansion coefficient values for P1 and P5 glasses were found matching closely with literature data [13, 152].

Table 5.8: Thermal expansion coefficients of glasses.

Glass sample	Coefficient of thermal expansion 100–700 °C (10^{-6} K^{-1})
P1	4.36
P2	3.02
P3	7.52
P4	6.89
P5	6.01
P6	5.25

5.2.6 Thermal diffusivity of glasses

Thermal diffusivity (α) values of glasses were determined up to 700 °C and are summarized in Table 5.9. A decrease in values of thermal diffusivities with increasing temperature was observed for glass systems.

Table 5.9: Thermal diffusivities of the prepared glasses.

T (°C)	P1 α (mm²/s)	P2 α (mm²/s)	P3 α (mm²/s)	P4 α (mm²/s)	P5 α (mm²/s)	P6 α (mm²/s)
25	0.288	0.236	0.199	0.241	0.244	0.718
100	0.256	0.221	0.184	0.225	0.204	0.650
200	0.240	0.214	0.171	0.217	0.198	0.592
300	0.226	0.213	0.158	0.203	0.181	0.583
400	0.210	0.210	0.145	0.199	0.162	0.528
500	0.196	0.208	0.143	0.187	0.160	0.485
600	0.189	0.202	0.137	0.167	0.157	0.441
700	0.181	0.200	0.134	0.137	0.145	0.463

5.2.7 Thermal conductivity of glasses

Thermal conductivities (κ) of glasses at room temperature were calculated by multiplying their specific heat values with thermal diffusivities and densities. Thermal conductivities of glasses at room temperature are given in Table 5.10. If one assumes that the volume of glasses remains constant, thermal conductivities can be calculated over a temperature range up to 700 °C using data given in Tables 5.7 and 5.9.

Table 5.10: Thermal conductivities of the prepared glasses.

Glass sample	T (°C)	α (mm ² /s)	C _p (J/(g·K))	ρ (g/cm ³)	κ (W/mK)
P1	25	0.288	0.644	2.81	0.521
P2	25	0.236	0.577	2.77	0.377
P3	25	0.199	0.601	2.78	0.342
P4	25	0.241	0.568	2.84	0.394
P5	25	0.244	0.630	2.92	0.449
P6	25	0.718	0.757	2.34	0.761

5.3 Physical properties of glasses

Prepared glasses were studied using different quantitative tools to determine their physical properties such as density, hardness and refractive indices.

5.3.1 Densities measurement of glasses

The measured densities values of glasses are presented in Table 5.11. It was found that the densities of these glasses were depending on the atomic masses and on the radii of the rare-earth ions.

5.3.2 Hardness measurement of glasses

The measured hardness values of glasses are summarized in Table 5.11. Increased hardness values were found with decreasing radii of the rare-earth ions.

5.3.3 Refractive indices measurement of glasses

The determined refractive indices of the prepared glasses are shown in Table 5.11. The refractive indices of these glasses were found in the range of 1.68 –1.74. One can summarize that rare-earth ion type had minor effect on the refractive indices of glasses.

Table 5.11: Physical properties of the prepared glasses.

Glass sample	Refractive indices	Density (g/cm ³)	Hardness (HV)
P1	1.68	2.81	852.52
P2	1.71	2.77	857.92
P3	1.73	2.78	888.62
P4	1.74	2.84	847.20
P5	1.71	2.92	745.39
P6	1.70	2.34	955.42

5.4 Crystallization studies of rare-earth-aluminosilicate glasses

Crystallization studies of glasses were carried out to evaluate their crystallization behavior and resulting microstructures under different heat-treatment conditions. For this purpose tablets of glass powders (P1– P6) having 8 mm diameter and 5 mm thickness were prepared using uniaxial pressing with 50 kN force. These compacted samples (P1– P6) were heat-treated at heating rate 15 K/min up to 1200 °C for different periods of time in a chamber furnace. Firstly, samples were heated up to 1200 °C and cooled down to room temperature without providing any holding time. Secondly, compacted glass specimens were hold at 1200 °C for 50h to evaluate the effects of long heat-treatment on their crystallization structures. These heat-treated samples were mounted in epoxy and fine-polished by stepwise ceramographical specimen preparation techniques. Structural examinations of annealed samples were done via XRD, IR and Raman spectroscopy. Moreover, qualitative and quantitative phase analyses of heat-treated samples were conducted using SEM. Furthermore, hot stage XRD studies of the prepared glass powders were performed up to 1200 °C to evaluate crystals growth behaviour and phase formation in these glass systems.

5.4.1 Hot-stage XRD of Yttrium-aluminosilicate glasses

The P1 glass powder sample was heated at 10 K/min up to 1200 °C for hot-stage XRD analyses. It was not possible to go beyond 1200 °C due to instruments limits. The first scan was recorded at 25 °C, the second at 700 °C, the third at 800 °C, the fourth at 850 °C and hold there for 30 minutes then scans were taken after every 50 °C steps up to 1200 °C with holding time of 30 minutes at each scan. The diffraction patterns recorded for the P1 glass powder at different temperatures are shown in Fig. 5.11. A complete amorphous structure was observed till 900 °C without any reflection peaks. At 1050 °C first reflections were noticed but their intensities were very weak except a cristobalite peak that was pronounced. After 1100 °C, the peaks of mullite (JCPDS card # 15-776), cristobalite (JCPDS card # 46-1045), yttrium-disilicate (JCPDS card # 22-1103) and unknown phase (X) were prominent. The intensities of these crystalline phases remained constant beyond 1150 °C. It was observed that the maximum crystallization took place between 1150-1200 °C that fits well with DTA/DSC data.

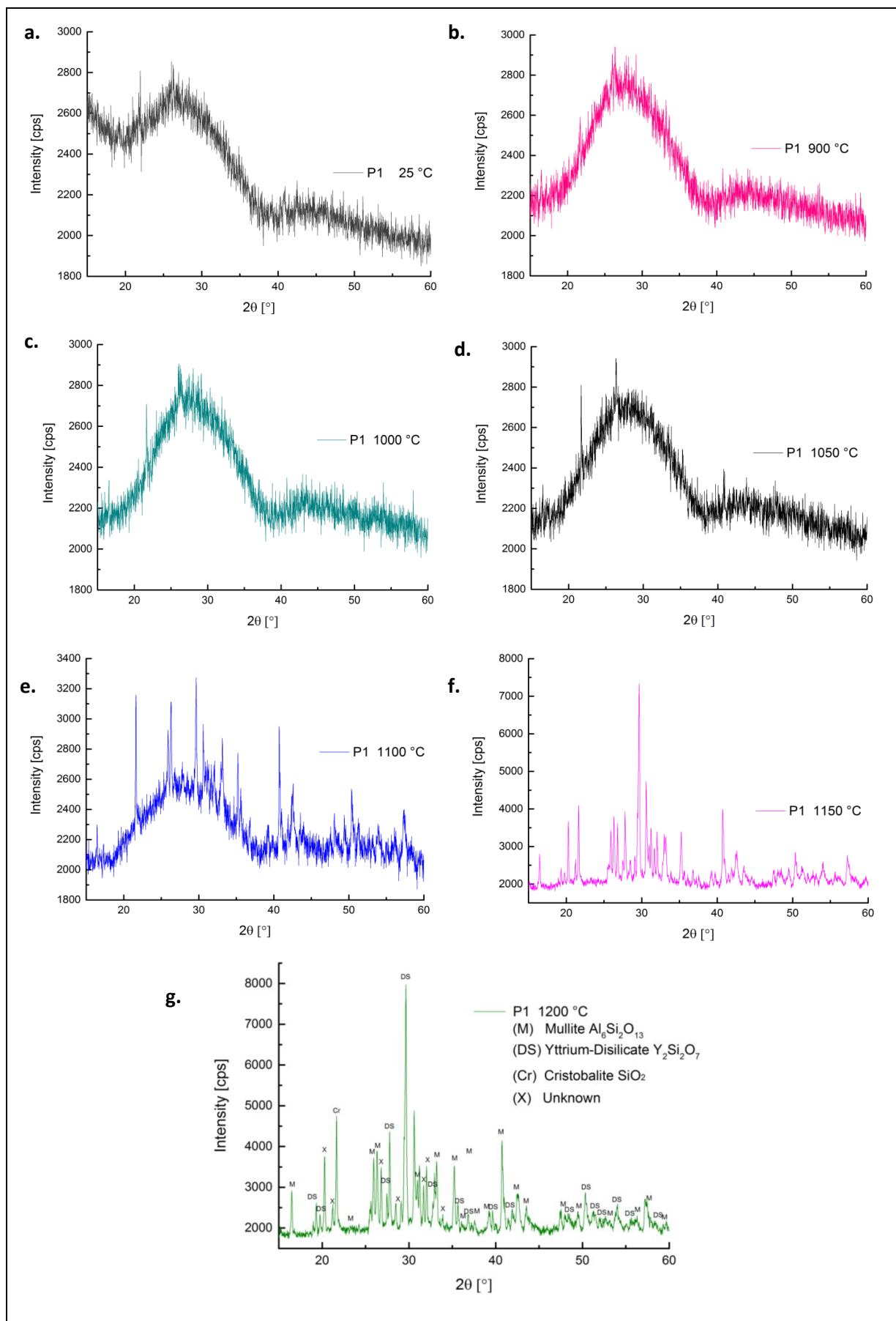


Figure 5.11: In-situ XRD of P1 glasses with 30 min holding at (a) 25 °C, (b) 900 °C, (c) 1000 °C, (d) 1050 °C, (e) 1100 °C, (f) 1150 °C, and (g) 1200 °C.

5.4.1 Heat-treatment of Yttrium-aluminosilicate glasses

Two compacted glass powder samples of P1 were heat-treated in a chamber furnace with a heating rate of 15 K/min up to 1200 °C. The first sample was cooled down without providing any holding time (P1–1200°C), while the second sample was kept for 50 h at 1200 °C (P1–1200°C–50h). The diffraction patterns of these heat-treated samples are shown in Fig. 5.12. XRD patterns contain reflections of mullite (JCPDS card # 15-776), yttrium-disilicate (JCPDS card # 22-1103) and cristobalite (JCPDS card # 46-1045). The intensities of mullite and yttrium-disilicate (Y-disilicate) were more prominent in sample P1–1200°C–50h as compared to P1–1200°C.

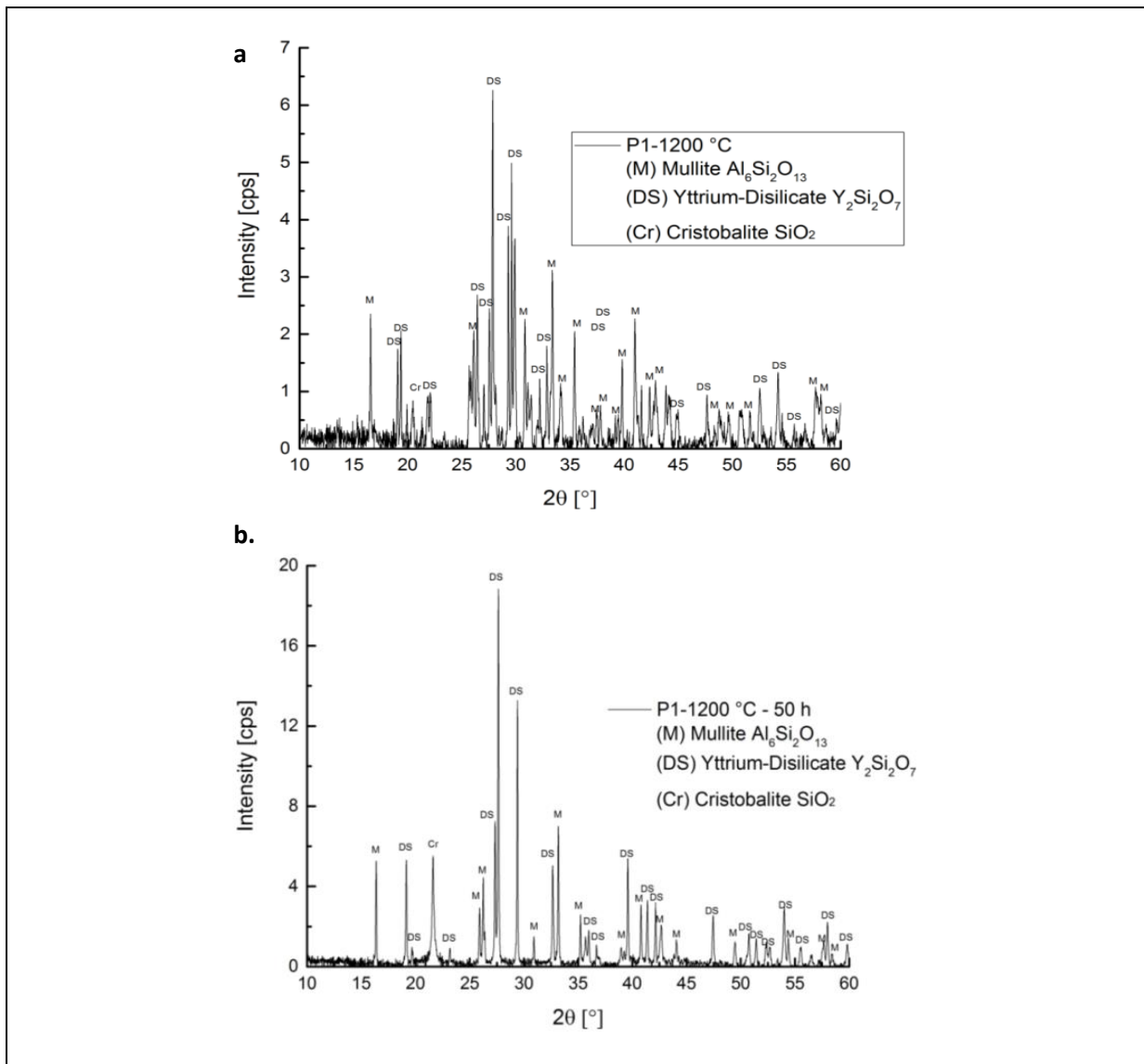


Figure 5.12: XRD analyses of P1 glasses annealed at 1200 °C; (a) without holding, (b) 50 h holding.

SEM analyses of the P1–1200 °C sample is shown in Fig. 5.13, which contain embedded Y-disilicate ($Y_2Si_2O_7$) crystals in remaining glassy matrix and mullite crystals. It was found that specimen edges in the P–1200 °C sample were more extensively crystallized as compared to the centre region.

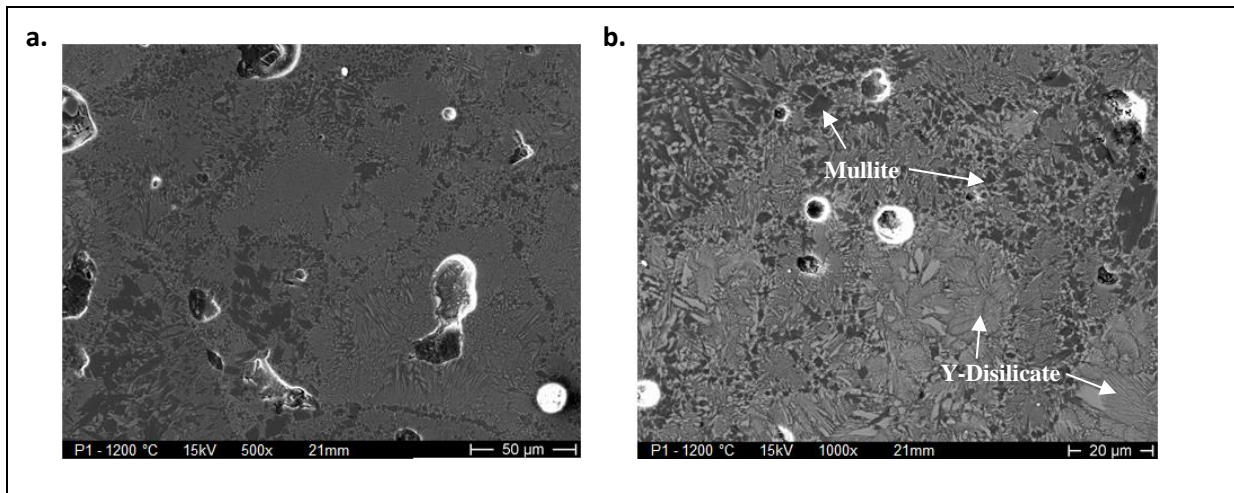


Figure 5.13: SEM images of the P1 glass heat-treated at 1200 °C with no holding time; (a) at magnification 500x, (b) magnification 1000x.

SEM images of sample P1–1200°C–50h sample are shown in Fig. 5.14. They show that feathers-like crystals of Y-disilicate were more abundant at edges as compared to the centre of the sample. EDX analyses of P1–1200°C–50h sample are shown in Fig. 5.15, which confirmed the formation of Y-disilicate and mullite crystals.

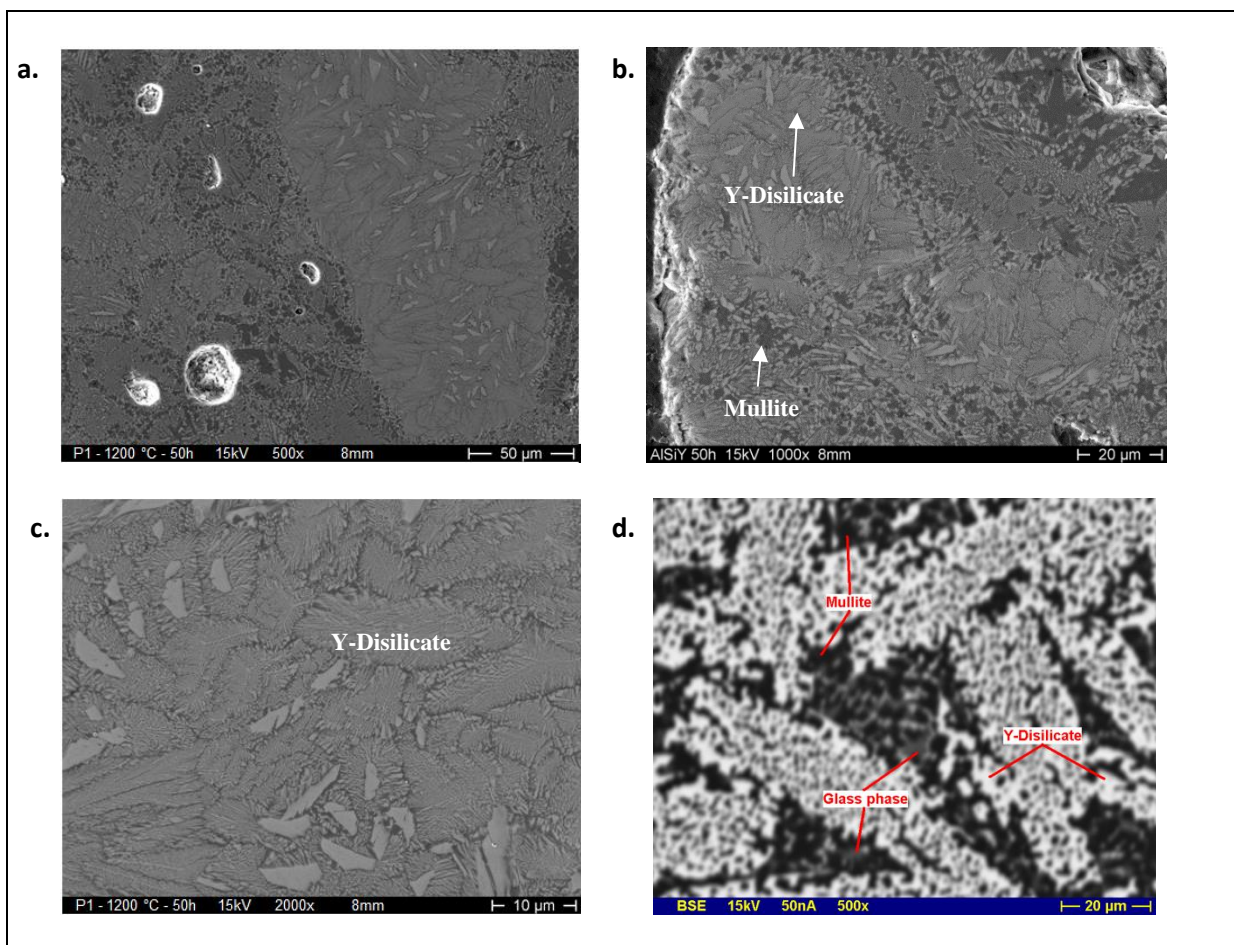


Figure 5.14: SEM images of the P1 glass annealed at 1200 °C for 50h; (a, b) corner of the sample at magnification of 500x and 1000x, respectively, (c) center of the sample at magnification of 2000x (d) BSE image of the sample at magnification of 500x.

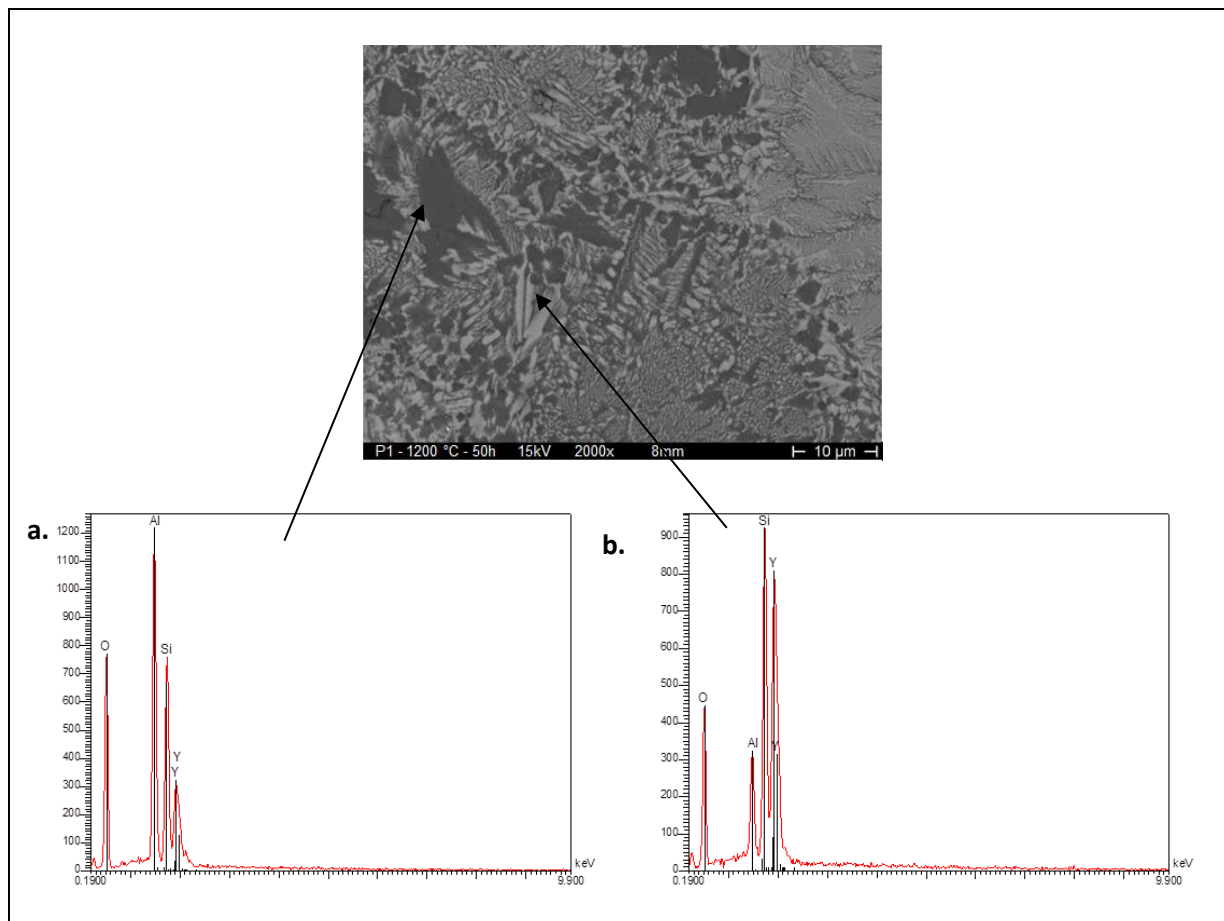


Figure 5.15: EDX analyses of P1 glass annealed at 1200 °C for 50 h; (a) mullite, (b) yttrium-disilicate.

A compacted P1 glass powder sample was annealed with heating rate of 15 K/min at 1250 °C for 100h in a closed chamber furnace. Figure 5.16a shows the diffraction pattern of this aged sample which contains reflections of mullite (JCPDS card # 15-776), Y-disilicate (JCPDS card # 22-1103) few reflections of X phase and strong glassy hub which represent remaining glassy phase in the sample. This X phase was not observed in samples P1–1200°C and P1–1200°C–50h as shown in Fig.5.12. DTA of the P1 glass showed a second crystallization peak at around 1340 °C that represent formation of new phase or different microstructure at this temperature. For characterization of phase assemblages at 1340 °C, a compacted sample of P1 was annealed at 1340 °C for 100h in a chamber furnace. The diffraction pattern of this sample is shown in Figure 5.16b, which contains reflections of mullite (JCPDS card # 15-776), Y-disilicate (JCPDS card # 22-1103), strong reflections of the earlier mentioned X phase and relatively weak glassy hub. A fine grained microstructure with needle shape structure was observed for the sample P1–1340°C–100h, as shown in Fig. 5.17. The formation of needle shape microstructure produced secondary crystallization peak during DTA analyses of P1 glasses. SEM images revealed that the microstructure of this sample consists of mullite, cristobalite, Y-disilicate, X-phase and residual glass. This X phase has an average composition of Y = 8.42, Si = 16.43, Al = 12.85 and O = 62.28 (at. %) according to the electron microprobe analyses and matching with phase mentioned by Ludwig in his work [151].

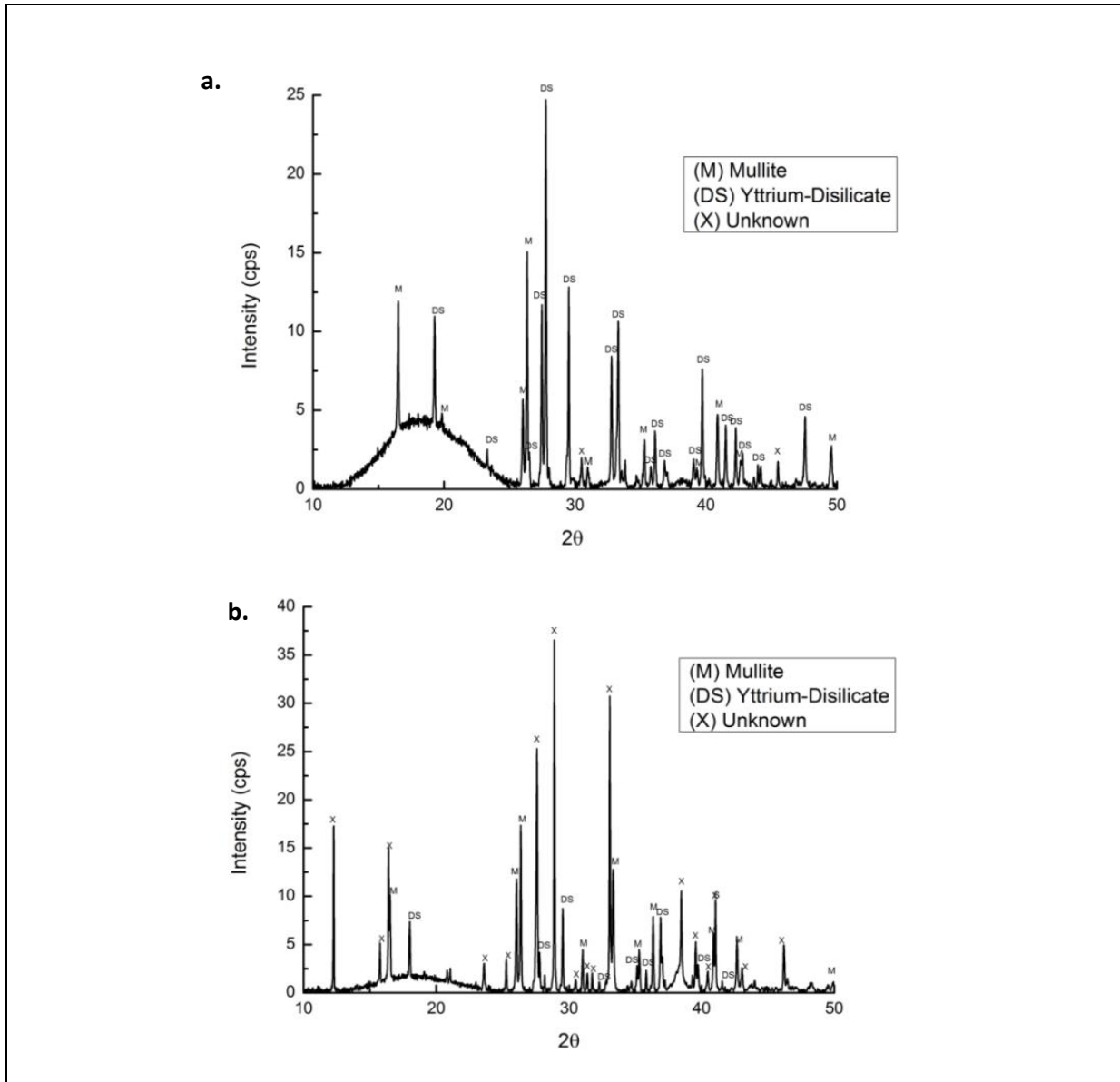


Figure 5.16: XRD analyses of P1 glasses; (a) annealed at 1250 °C for 100 h, (b) annealed at 1340 °C for 100 h.

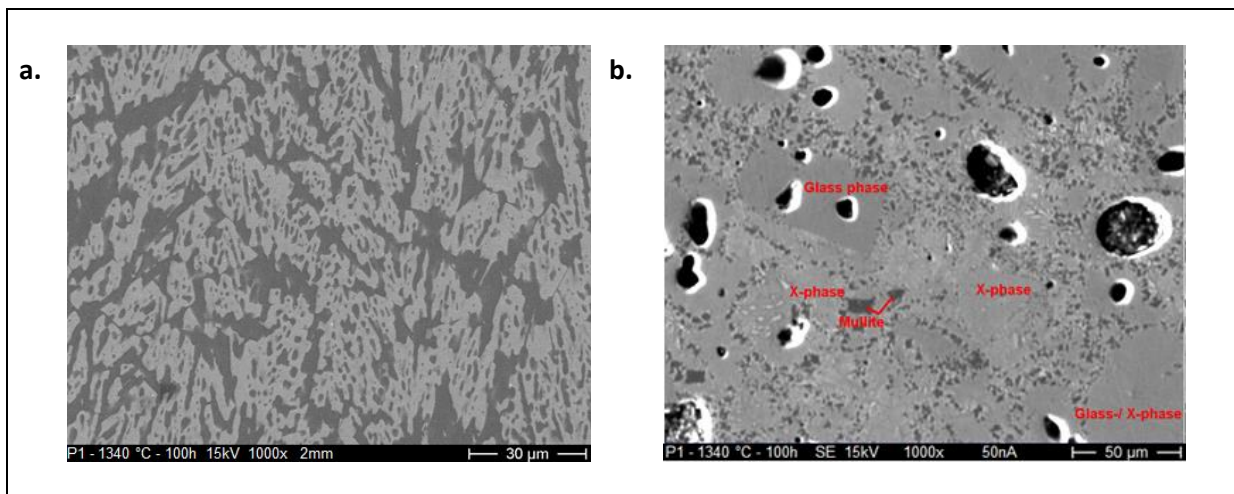


Figure 5.17: SEM images at mag. 1000x of P1 glasses annealed at 1340 °C for 100 h; (a) edge of the sample, (b) center of the sample.

5.4.2 Raman analyses of heat-treated samples

Raman spectra of P1–1200°C and P1–1200°C–50h samples are shown in Fig. 5.18. Spectra of both samples were similar in shape, however a pronounced peak at $\sim 952 \text{ cm}^{-1}$ wave number was observed in P1–1200°C–50h sample as compared to P1–1200°C. Spectra of these annealed samples showed that Q^3 are major structural units in them. The assignment of Raman bands for P1–1200°C–50h sample is given in Table 5.12.

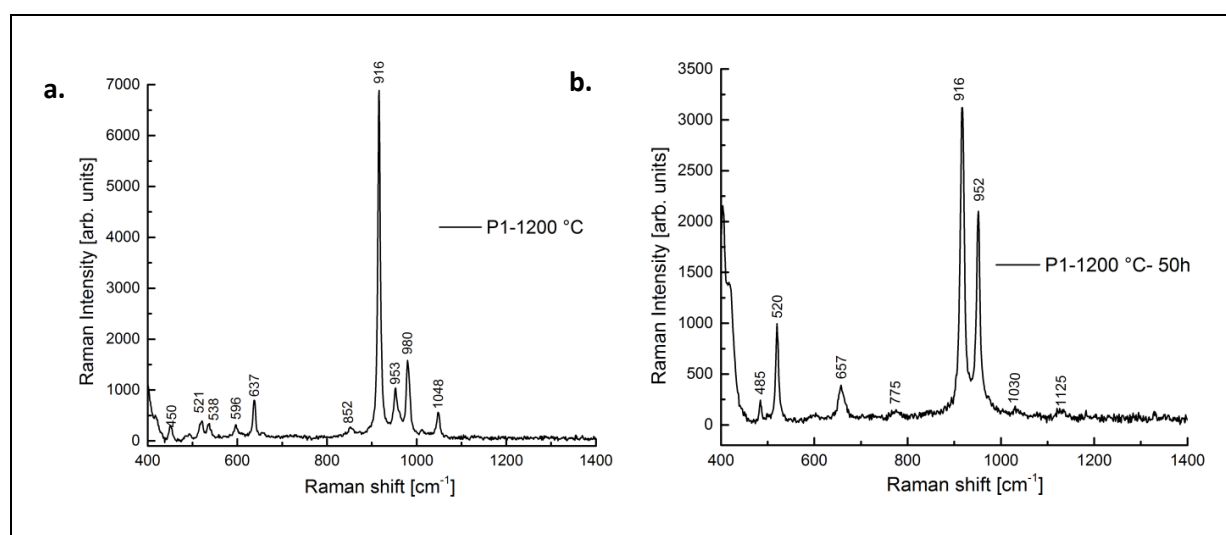


Figure 5.18: Raman spectra of P1 glasses annealed at 1200 °C; (a) no holding time, (b) 50h holding.

Table 5.12: Raman bands for P1 glasses annealed at 1200 °C for 50 h.

Raman band	Assignment of bands
485	Q^4
520, 657	Si-O-Si bending
916	Si-O stretching in Q^3
952	Si-O stretching in Q^3

5.4.3 IR analyses of heat-treated samples

IR spectra of P1–1200°C and P1–1200°C–50h samples are shown in Fig. 5.19. IR spectra of both samples were almost identical with exception of a higher peak in P1–1200°C–50h at $\sim 1071 \text{ cm}^{-1}$, which were not so pronounced in P1–1200°C. This peak corresponds to Si-O-Si asymmetric stretching. However, both samples showed strong symmetric stretching of Si-O-Si at wave numbers ~ 723 , ~ 786 , ~ 835 and $\sim 885 \text{ cm}^{-1}$, respectively. Peak assignment of IR spectrum of P1–1200°C–50h sample is given in Table 5.13.

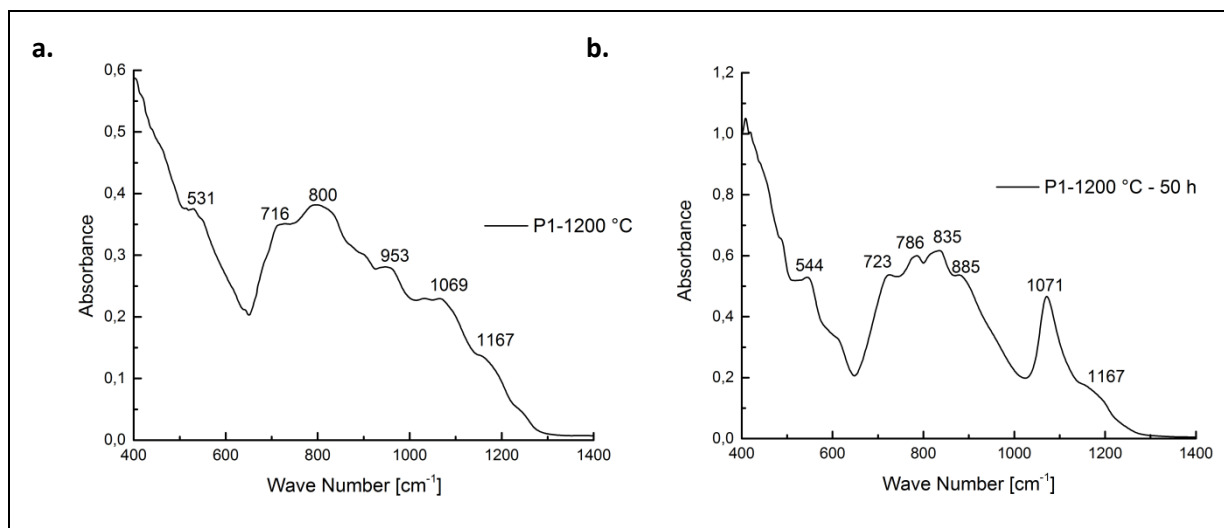


Figure 5.19: IR spectra of P1 glasses annealed at 1200 °C; (a) no holding time, (b) 50h holding time.

Table 5.13: IR peak assignment for P1 glass annealed at 1200 °C for 50h.

Peak position	Peak assignment
544	(O-Si-O) bending mode
723, 786, 835, 885	(Si-O-Si) symmetric stretching
1071	(Si-O-Si) asymmetric stretching

5.4.4 Crystallization of Ytterbium-aluminosilicate glasses

This section includes results of hot-stage XRD, diffractions and SEM images of samples heat-treated at 1200 °C. Moreover, results of Raman and IR analyses of these heat-treated samples are mentioned.

5.4.4.1 Hot-stage XRD of Ytterbium-aluminosilicate glasses

Hot-stage XRD analyses of the P2 glass powder was conducted by using the same scheme for heating rate, holding temperature and time as discussed above in section 5.4.1. The diffraction patterns of the P2 glass powder recorded for 1000–1200 °C are shown in Fig. 5.20. It was found that the bulk crystallization process in the P2 glass started after 1050 °C and completed at 1100 °C. Peaks of mullite (JCPDS card # 15-776) and Yb-disilicate (JCPDS card # 27-966) were found at 1100 °C. There was no change in peak intensities after 1150 °C and was found almost same from 1150–1200 °C. This observation of the bulk crystallization temperature range fits well with DTA/DSC data.

5.4.4.2 Thermal treatment of Ytterbium-aluminosilicate glasses

The diffraction patterns of P2–1200°C and P2–1200°C–50h samples are shown in Fig. 5.21. They consist of reflections of mullite (JCPDS card # 15-776), Yb-disilicate (JCPDS card # 27-966). The intensities of reflections in both samples were identical, which showed that bulk crystallization process completed in P2 glasses, once crystallization temperature reached.

SEM images of P2-1200°C-50h are shown in Fig. 5.22, which contain crystals of mullite and Yb-disilicate ($\text{Yb}_2\text{Si}_2\text{O}_7$). Yb-disilicate crystals are embedded in the remaining glassy matrix. It was noticed that under the same heat-treatment conditions, the formed crystals in P2-1200°C-50h samples were smaller in size as compared to P1-1200°C-50h sample.

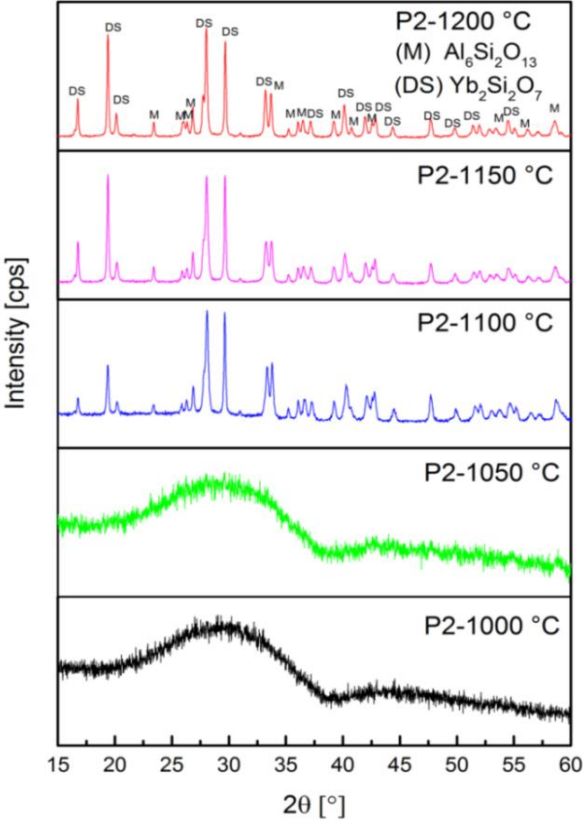


Figure 5.20: In-situ XRD of the P2 glass system.

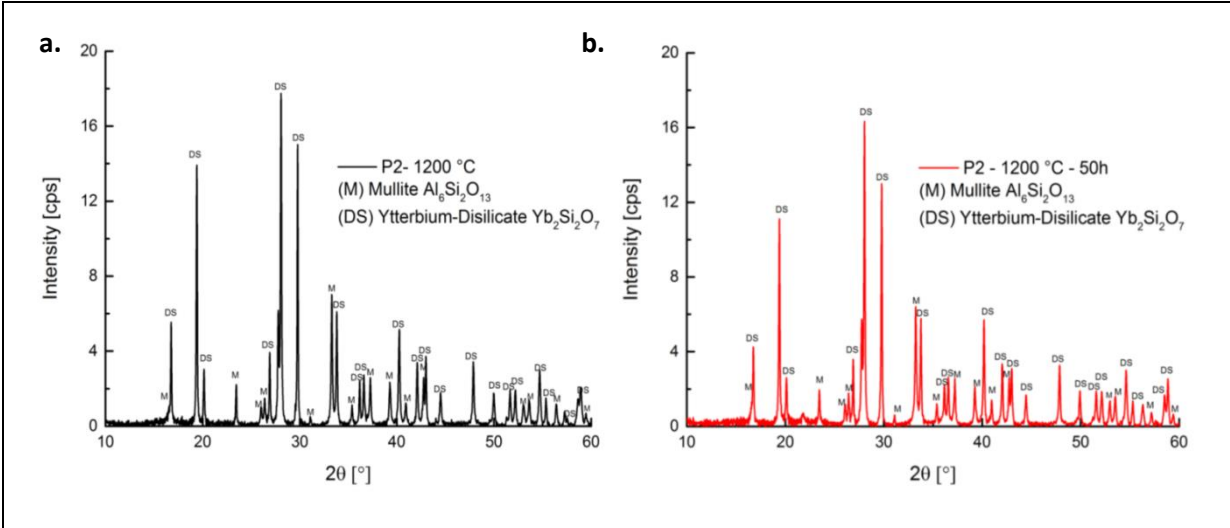


Figure 5.21: XRD analyses of P2 glasses aged at 1200 °C; (a) no holding time, (b) 50 h holding.

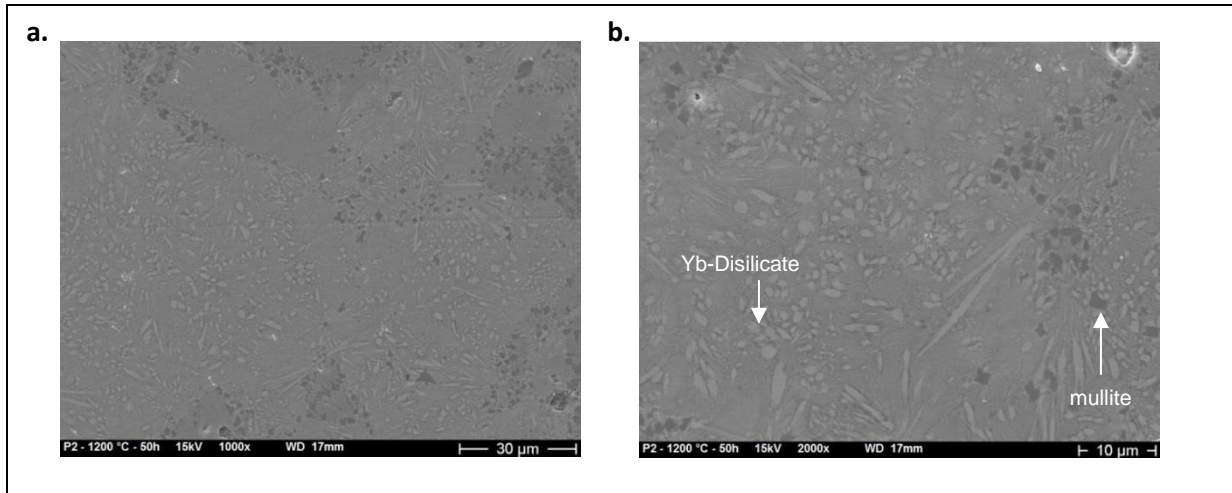


Figure 5.22: SEM images of P2 glasses annealed at 1200 °C for 50h; (a) at mag.1000x, (b) at mag. 2000x.

5.4.4.3 Raman analysis of the heat-treated samples

The recorded Raman spectra of P2–1200°C and P2–1200°C–50h samples are shown in Fig. 5.23. Raman spectra of both samples were similar in shape with high content of Q³ units. The assignment of Raman bands for P2–1200°C–50h sample is given in Table 5.14.

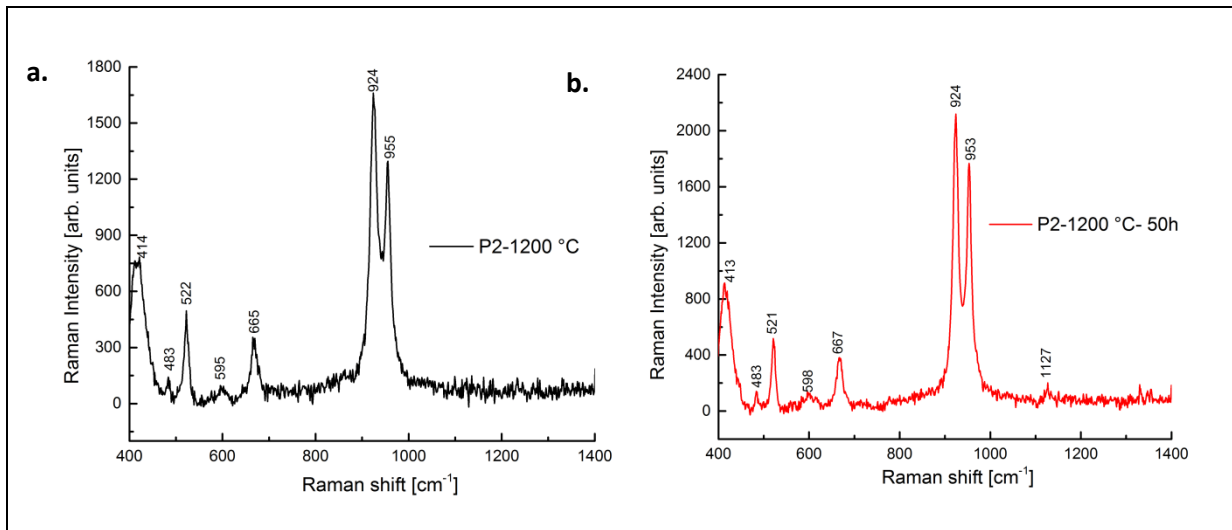


Figure 5.23: Raman spectra of P2 glasses annealed at 1200 °C; (a) no holding time, (b) 50h holding.

Table 5.14: Raman bands for P2 glasses annealed at 1200 °C for 50h.

Raman band	Assignment of bands
413	Q ⁴
521, 667	Si-O-Si bending
924	Si-O stretching in Q ³
953	Si-O stretching in Q ³

5.4.4.4 IR analysis of the heat-treated samples

IR spectra of P2–1200°C and P2–1200°C–50h samples are shown in Fig. 5.24. The recorded spectra of both samples were almost identical with exception of higher peak in P2–1200°C–50h at ~1081 cm⁻¹, which were not so pronounced in P2–1200°C. This peak corresponds to Si-O-Si (Q⁴) asymmetric stretching. Both samples showed strong symmetric stretching of Si-O-Si at wave numbers ~724, ~801 and ~953 cm⁻¹, respectively. Peak assignment of IR spectra for P2–1200°C-50h sample is given in Table 5.15.

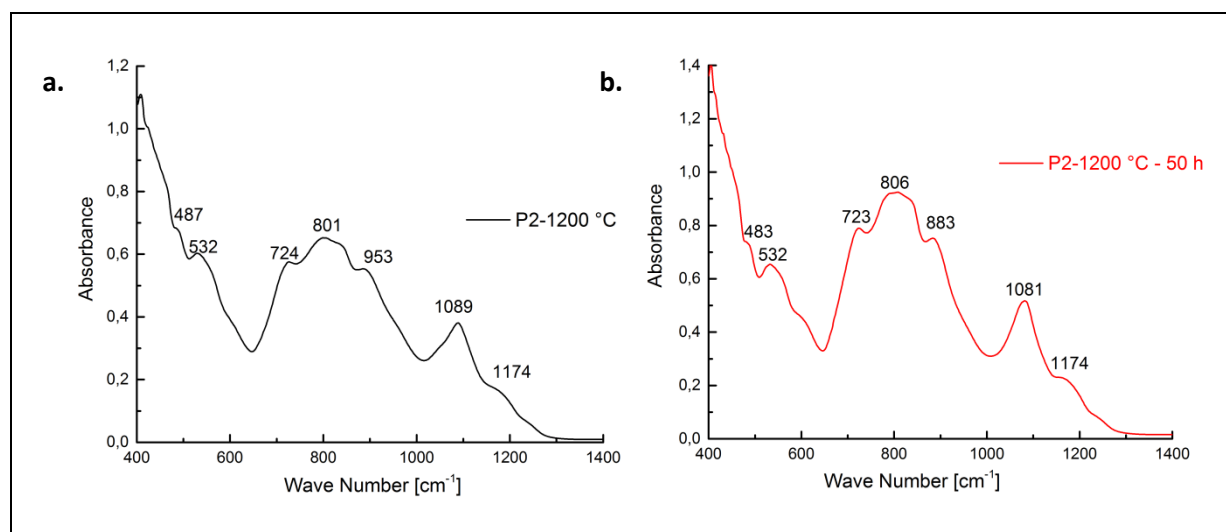


Figure 5.24: IR spectra of P2 glasses annealed at 1200 °C; (a) no holding time, (b) 50h holding.

Table 5.15: Peak assignment for P2 glasses annealed at 1200 °C for 50h.

Peak position	Peak assignment
532	(O-Si-O) bending mode
723, 806, 883	(Si-O-Si) symmetric stretching
1081	(Si-O-Si) asymmetric stretching

5.4.5 Crystallization of Holmium-aluminosilicate glasses

This section includes results of hot-stage XRD, diffractions and SEM images of samples heat-treated at 1200 °C. Moreover, results of Raman and IR analyses of these heat-treated samples are mentioned.

5.4.5.1 Hot-stage XRD of Holmium-aluminosilicate glasses

Figure 5.25 shows hot-stage XRD reflections of the P3 glass powder from 1000–1200 °C. These reflections were recorded by following the same scheme of heating rate, holding time and temperature as described in section 5.4.1. At 1050 °C, the crystal growth process started, but intensities of the reflections were relatively small. The diffraction pattern at 1100 °C showed partly crystalline structure, and maximum crystal growth took place between 1100–1150 °C. The observed phases were crystals of holmium-silicate (JCPDS card # 36-147) and mullite (JCPDS card # 15-776)

with a small reflection of cristobalite. There was almost no change in peak reflection and their intensities between 1150–1200 °C. This observation matched closely with DTA/DSC results.

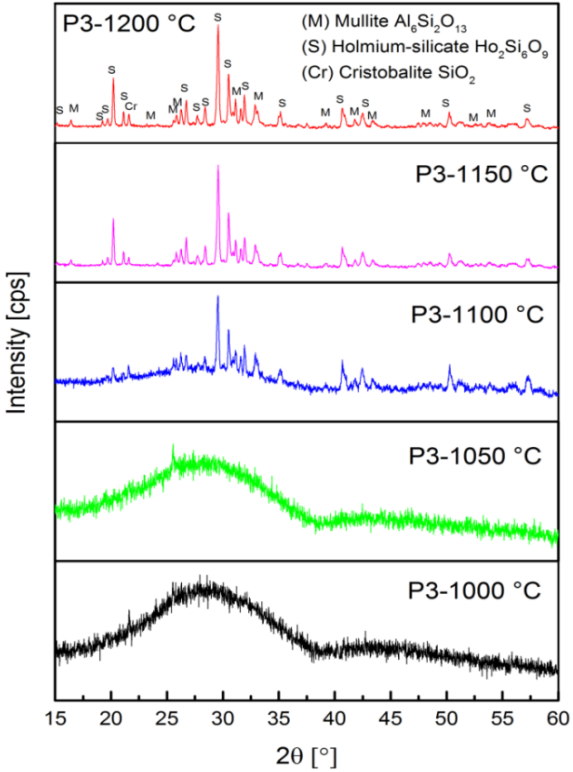


Figure 5.25: In-situ XRD of the P3 glass system.

5.4.5.1 Thermal treatment of Holmium-aluminosilicate glasses

Compacted powder sample of P3 glass was heat-treated at 1200 °C for 50h to evaluate the effects of heat-treatment on their crystallized structures. The recorded diffraction pattern of this annealed (P3–1200°C–50h) sample is shown in Fig. 5.26. It consists of reflections of mullite (JCPDS card # 15-776) and holmium-silicate (JCPDS card # 36-147).

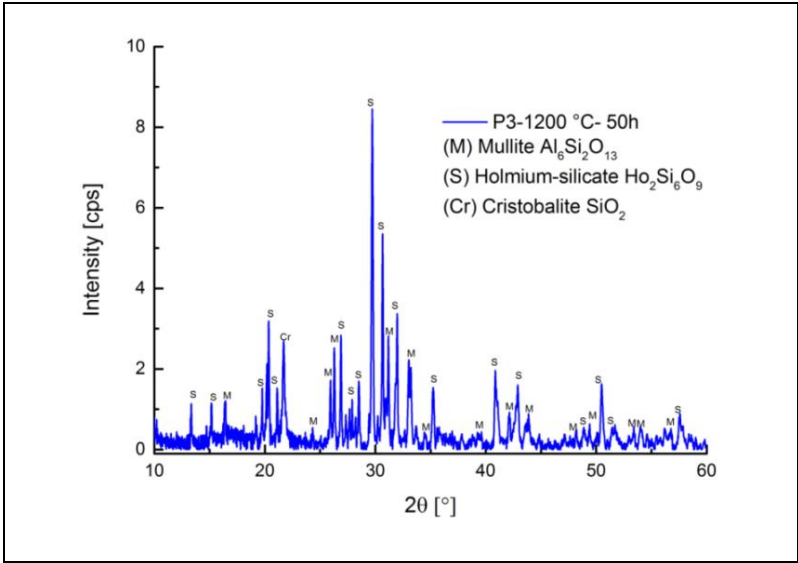


Figure 5.26: XRD analysis of the P3 glass heat-treated at 1200 °C for 50 h.

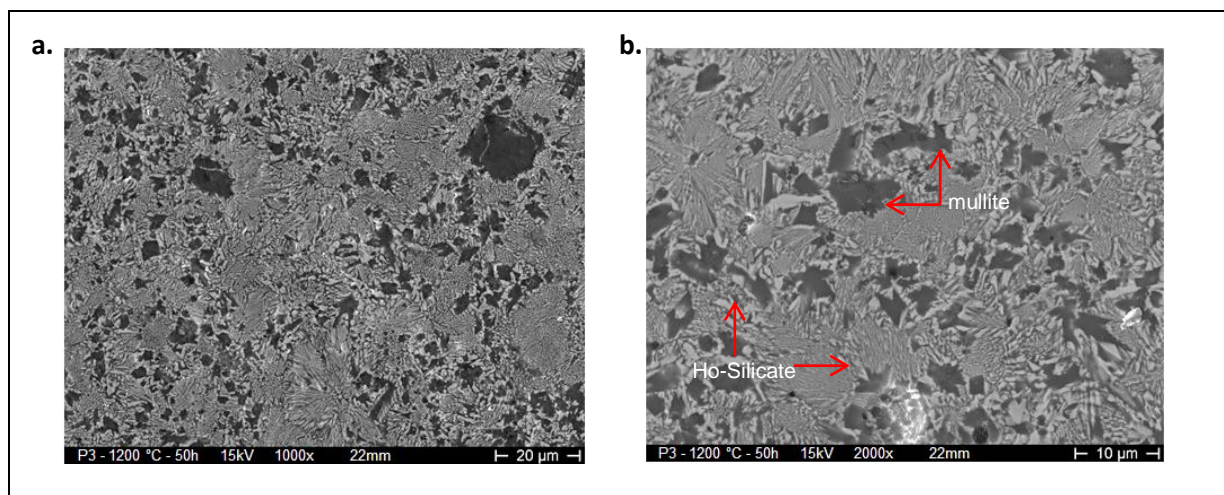


Figure 5.27: SEM images of P3 glass annealed at 1200 °C for 50h; (a) at mag.1000x, (b) 2000x.

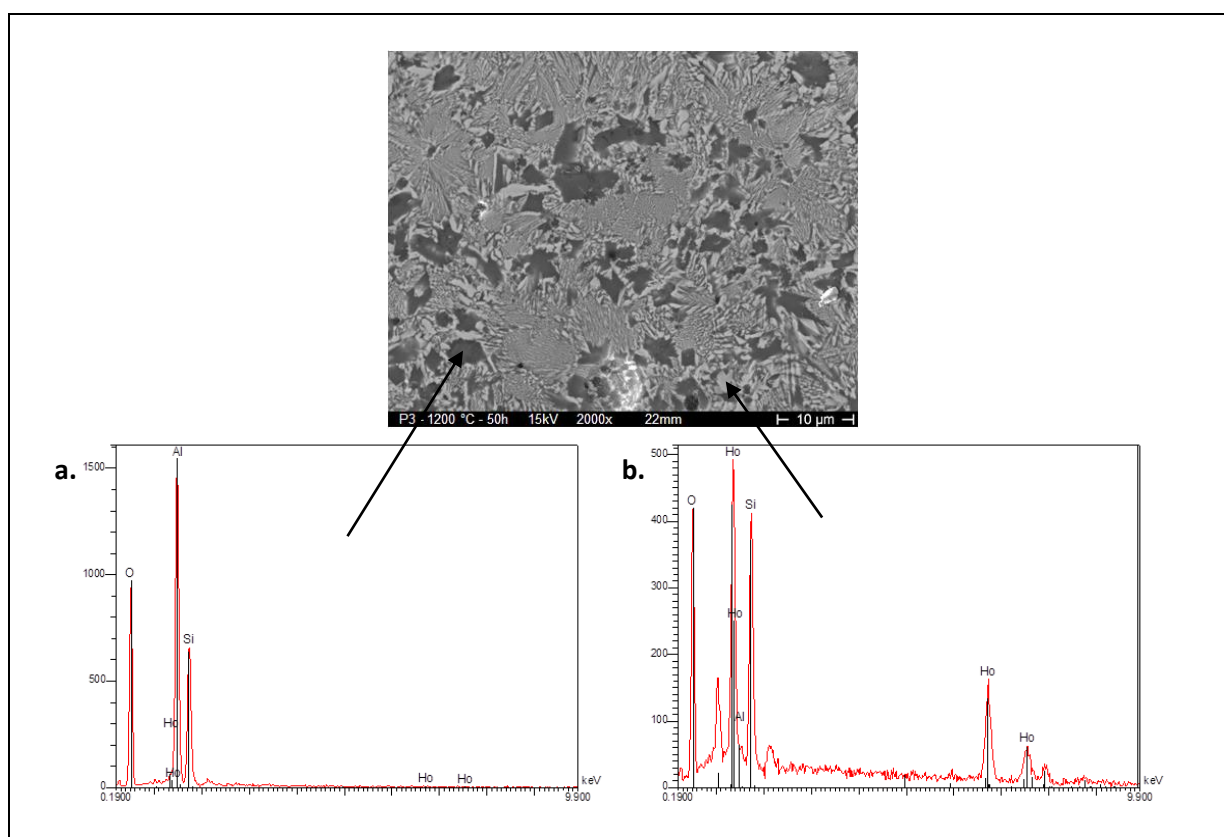


Figure 5.28: EDX analyses of P3 glass sample annealed at 1200 °C for 50h (a) mullite, (b) Ho-silicate.

5.4.5.2 Raman analysis of the heat-treated samples

Raman spectra of P3–1200°C and P3–1200°C–50h samples are shown in Fig. 5.29. The spectrum of the P3–1200°C sample was scattered with pronounced peaks at ~ 721 and ~ 902 cm^{-1} , respectively. These peaks correspond to Si-O-Si bending and Si-O⁻ stretching in Q³ structural unit. The Raman spectrum of the P3–1200°C–50h sample show high contents of Q³ structural units due to the uniform distribution of the Ho⁺³ ions. The assignment of Raman bands for the P3–1200°C–50h sample is given in Table 5.16.

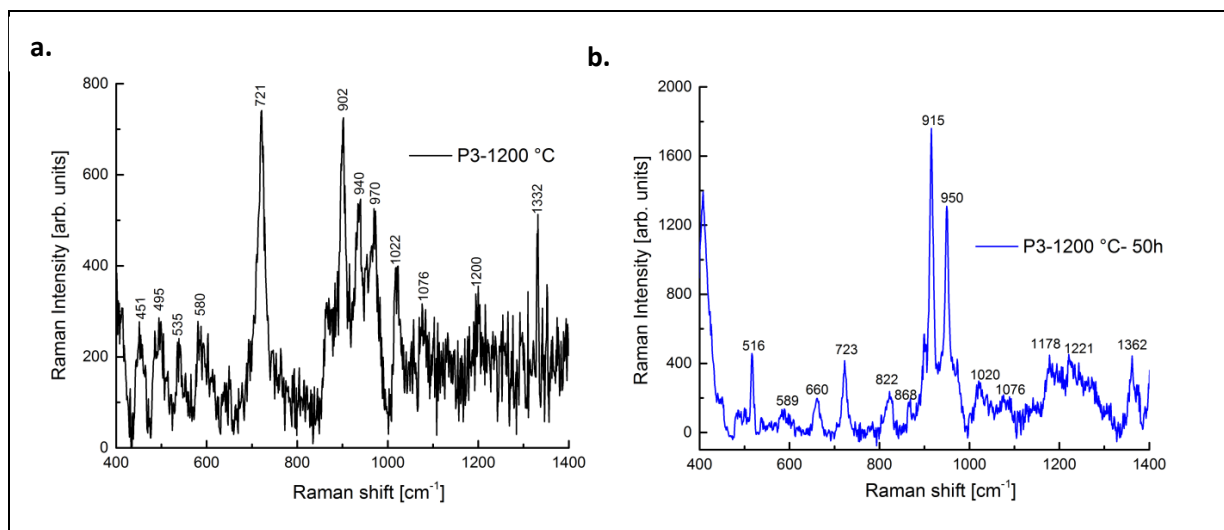


Figure 5.29: Raman spectra of P3 samples annealed at 1200 °C; (a) no holding time, (b) 50h holding.

Table 5.16: Raman bands for P3 sample aged at 1200 °C for 50h.

Raman band	Assignment of bands
516, 660, 723	Si-O-Si bending
915	Si-O stretching in Q ³
952	Si-O stretching in Q ³

5.4.5.3 IR analysis of the heat-treated samples

IR spectra of P3–1200°C and P3–1200°C–50h samples are shown in Fig. 5.30. The spectrum of P2–1200°C–50h sample showed a higher peak at ~1075 cm⁻¹ wave number, which were not so pronounced in P2–1200°C. This peak corresponds to Si-O-Si asymmetric stretching. Peak assignment of IR spectra for the P3–1200°C–50h sample is given in Table 5.17.

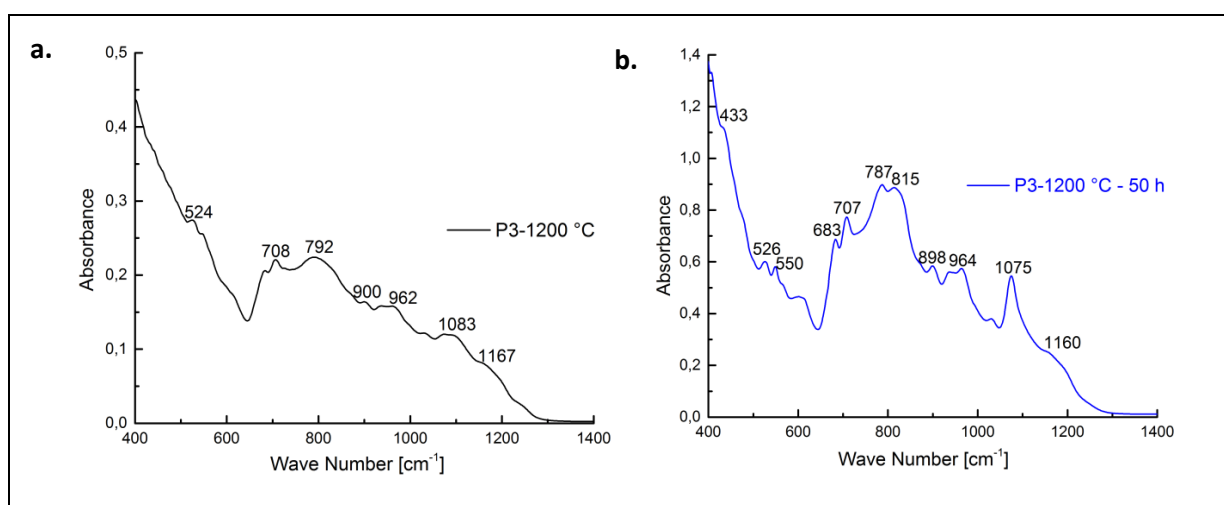


Figure 5.30: IR spectra of P3 samples annealed at 1200 °C; (a) no holding time (b) 50h holding time.

Table 5.17: Peak assignment for P3 sample annealed at 1200 °C for 50h.

Peak position	Peak assignment
526, 550	(O-Si-O) bending mode
683, 707, 787, 815,	(Si-O-Si) symmetric stretching
1075	(Si-O-Si) asymmetric stretching

5.4.6 Crystallization of Dysprosium-aluminosilicate glasses

This section includes results of hot-stage XRD, diffractions and SEM images of samples heat-treated at 1200 °C, Raman and IR analyses of these heat-treated samples.

5.4.6.1 Hot-stage XRD of Dysprosium-aluminosilicate glasses

Hot-stage XRD of the P4 glass powder was conducted by following the same scheme of heating rate, temperatures, holding time and scan schedules as discussed earlier in section 5.4.1. The diffraction patterns of the P4 glass powders from 1000–1200 °C are shown in Fig. 5.31. It was noticed that crystal nucleation process started at temperature around 1000 °C in this glass system and crystal growth was observed above 1050°C. The maximum crystal growth completed around 1100 °C and intensities of the developed phases were almost same from 1150–1200 °C.

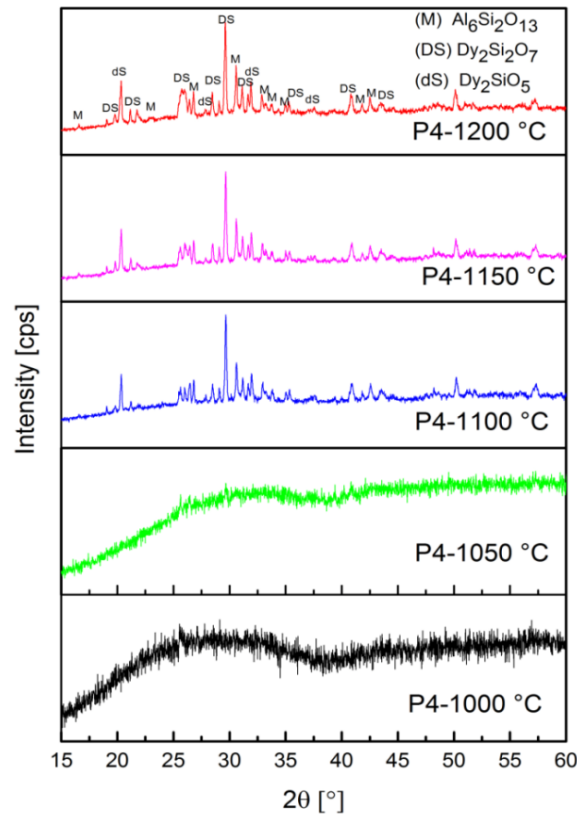


Figure 5.31: In-situ XRD of the P4 glass system.

5.4.6.2 Thermal treatment of Dysprosium-aluminosilicate glasses

The diffraction pattern of the P4–1200°C–50h sample is shown in Fig. 5.32. It consists of reflections of mullite (JCPDS card # 15-776) and two types of Dy-disilicate ($\text{Dy}_2\text{Si}_2\text{O}_7$, Dy_2SiO_5) (JCPDS cards # 28-410, 31-497).

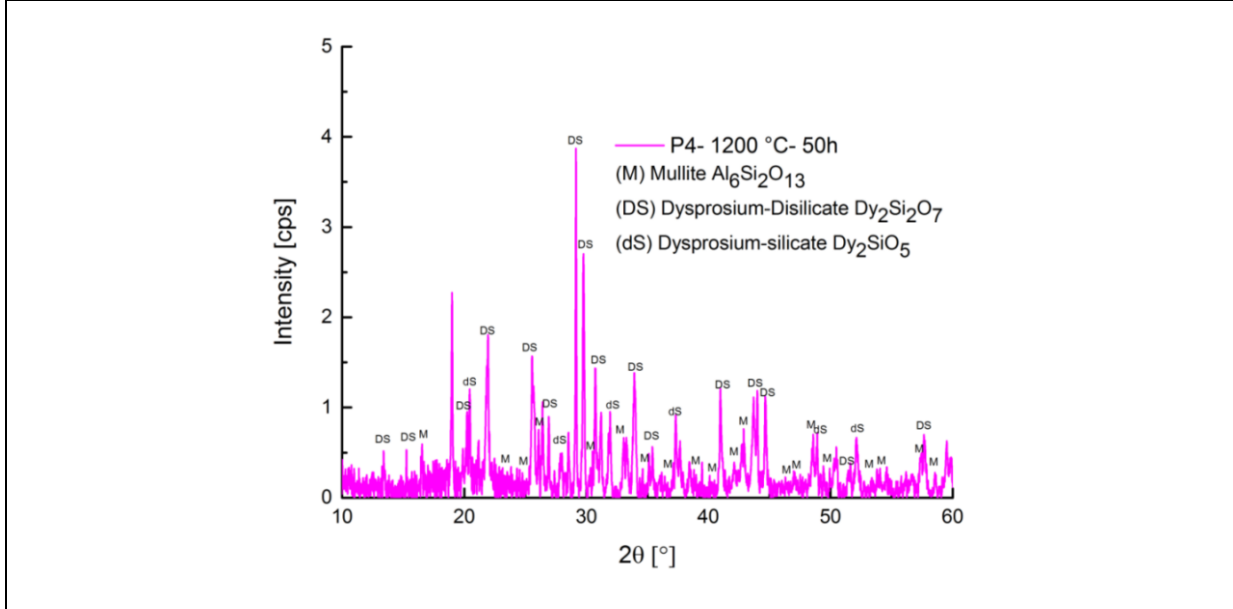


Figure 5.32: XRD analysis of the P4 sample heat-treated at 1200 °C for 50 h.

SEM images of P4–1200°C–50h sample revealed that it contains Dy-disilicate and mullite phases which are embedded in remaining glassy matrix (Fig. 5.33). SEM images of P4–1200°C–50h sample showed feather-type crystal growth of Dy-disilicate crystals, which are interconnected inside each other wings surrounded by mullite crystals.

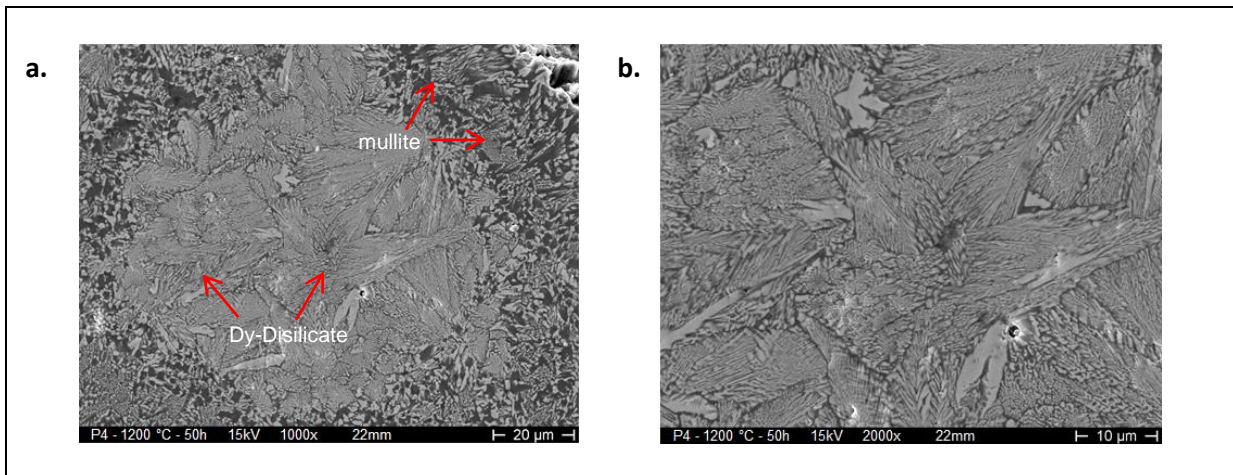


Figure 5.33: SEM images of P4 samples heat-treated at 1200 °C for 50h at mag.; (a) 1000x, (b) 2000x.

5.4.6.3 Raman analysis of the heat-treated samples

Raman spectra of P4–1200°C and P4–1200°C–50h samples are shown in Fig. 5.34. Spectra of both samples were similar (with an exceptional of an extra peak in P4–1200°C–50h at 720 cm⁻¹) with high content of Q³ units due to uniform distribution of the Dy⁺³ ions. The assignment of Raman bands for the P4–1200°C–50h sample is given in Table 5.18.

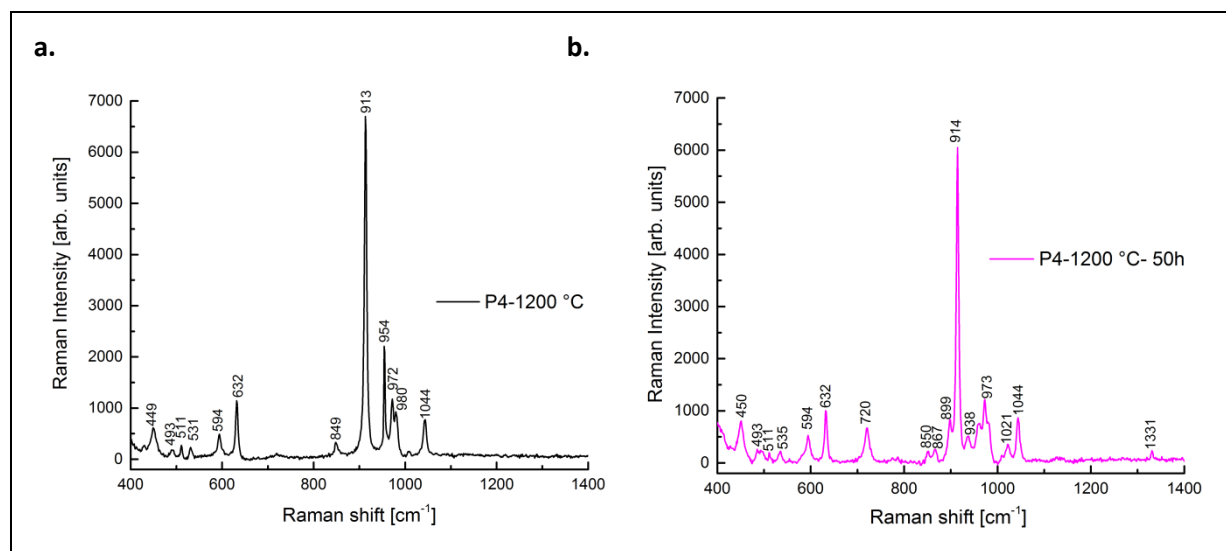


Figure 5.34: Raman spectra of P4 samples annealed at 1200 °C; (a) no holding, (b) 50h holding time.

Table 5.18: Raman bands for P4 sample annealed at 1200 °C for 50h.

Raman band	Assignment of bands
450	Q ⁴
511, 535, 594, 632, 720	Si-O-Si bending
914, 973	Si-O stretching in Q ³
1044	Si-O stretching in Q ²

5.4.6.4 IR analysis of the heat-treated samples

IR spectra of P4–1200°C and P4–1200°C–50h samples are shown in Fig. 5.35. The spectra of both samples were almost similar in shape with exception of a higher peak in P4–1200°C–50h at ~1075 cm⁻¹, which was less pronounced in P4–1200°C. This peak corresponds to Si-O-Si asymmetric stretching. Both samples showed strong symmetric stretching of Si-O-Si. Peak assignment of the IR spectra for P2–1200°C–50h sample is given in Table 5.19.

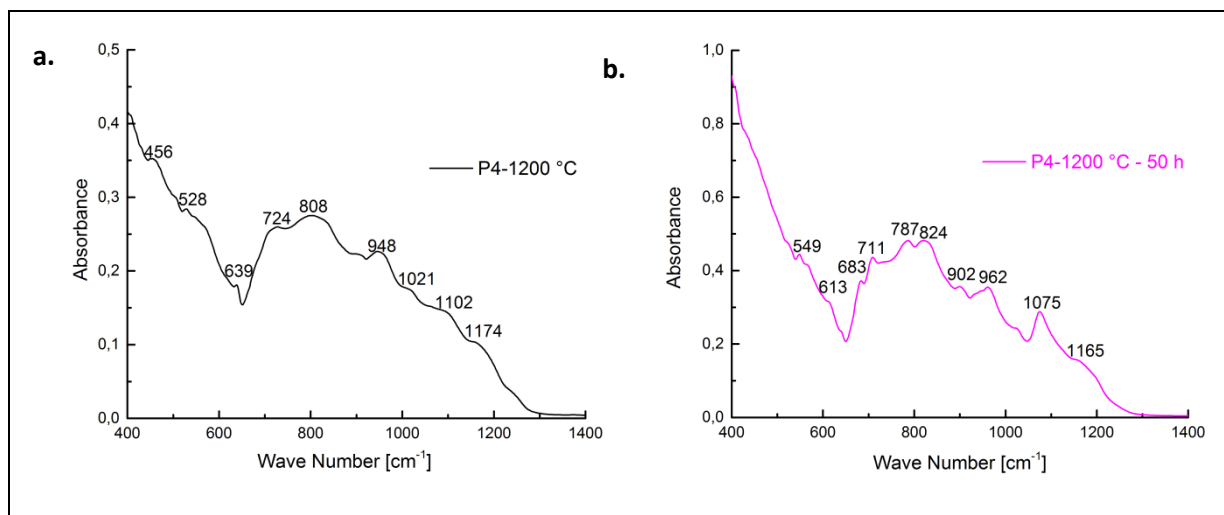


Figure 5.35: IR spectra of P4 samples annealed at 1200 °C; (a) no holding time, (b) 50h holding time.

Table 5.19: Peak assignment for P4 sample annealed at 1200 °C for 50h.

Peak position	Peak assignment
549	(O-Si-O) bending mode
683, 711, 787, 824	(Si-O-Si) symmetric stretching
962, 1075	(Si-O-Si) asymmetric stretching

5.4.7 Crystallization of Neodymium-aluminosilicate glasses

This section contains details of hot-stage XRD of P5 glasses, XRD and SEM analyses of sample heat-treated at 1200 °C for 50h.

5.4.7.1 Hot-stage XRD of Neodymium-aluminosilicate glasses

Hot-stage XRD of the P5 glass powder from 1000–1200 °C is shown in Fig. 5.36. They showed no pronounced crystalline peaks up to 1000 °C. At 1050 °C first peaks of Nd-disilicate were recorded. At around 1100 °C small reflections of mullite (JCPDS card # 15-776) were found along with peaks of Nd-disilicate (JCPDS card # 22-1177). The maximum crystallization took place between 1150–1200 °C. Although no crystallization peak was observed during DTA/DSC analyses of the P5 glass, however crystallization took place when 30 minutes holding time was provided during each scan from 850–1200 °C.

5.4.7.2 Thermal treatment of Neodymium-aluminosilicate glasses

The diffraction pattern of the P5–1200°C is shown in Fig. 5.37 which contains weak and small crystalline reflections which could not be identified and correlated with any XRD data set. SEM analyses of the P5–1200°C sample are given in Fig. 5.38 that show separated clusters of crystals embedded in the glass matrix. It revealed that surface crystallization is more favourable in Nd-containing glasses. This surface crystallization was found more abundant at the edges of the samples as compared to the sample center.

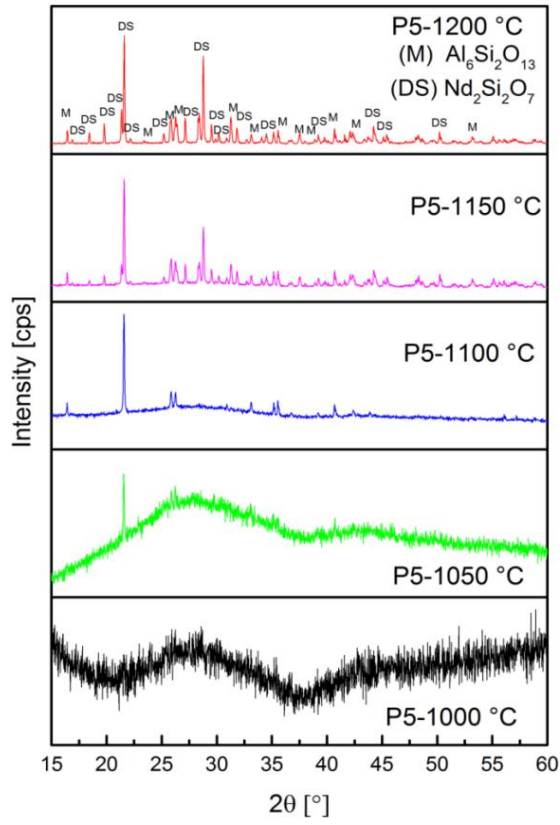


Figure 5.36: In-situ XRD of the P5 glass system.

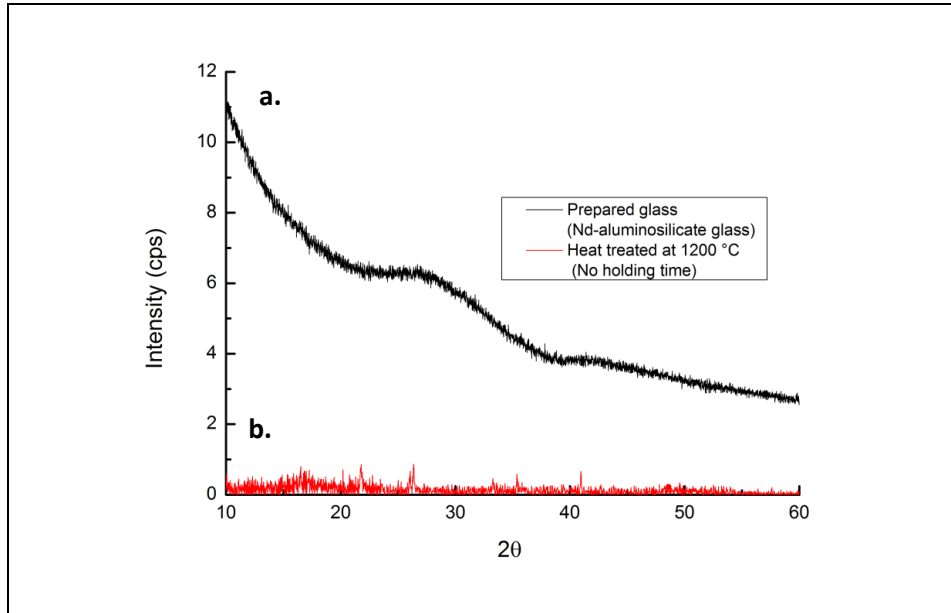


Figure 5.37: XRD analyses of P5 glasses; (a) prepared glass, (b) annealed at 1200 °C no holding time.

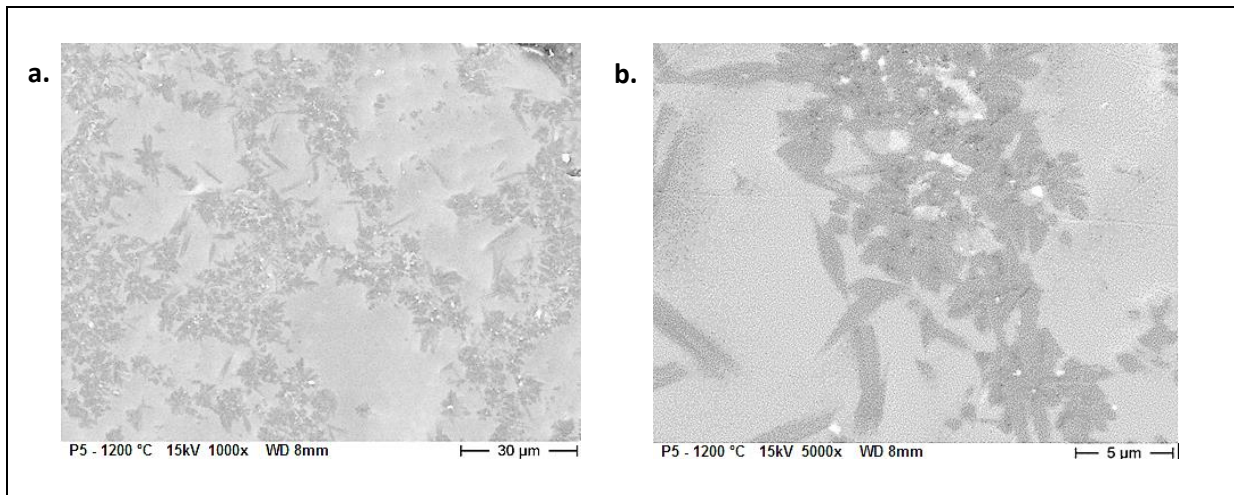


Figure 5.38: SEM images of the P5 sample annealed at 1200 °C with no holding time; (a) at mag. 1000x (b) at mag. 5000x.

The diffraction pattern of the P5–1200°C–50h sample showed reflections of mullite (JCPDS card # 15-776), Nd-disilicate (JCPDS card # 22-1177) and an unknown phase that cannot be correlated with any diffraction data set (Fig. 5.39). SEM analyses of the P5–1200°C–50h sample are shown in Fig. 5.40 that contained embedded Nd-disilicate ($\text{Nd}_2\text{Si}_2\text{O}_7$) crystals with remaining matrix glassy phase. It was found that the specimen edges were extensively crystallised as compared to the centre regions. The crystals were extended from the surface towards the centre of the samples. Moreover, it was noticed that long heat-treatment introduced round pores or holes in the samples. The reason for the existence of these pores could be attributed to the difference in density/molar volume between phases and remaining glassy phase and/or due to the incomplete sintering process of the glass powder.

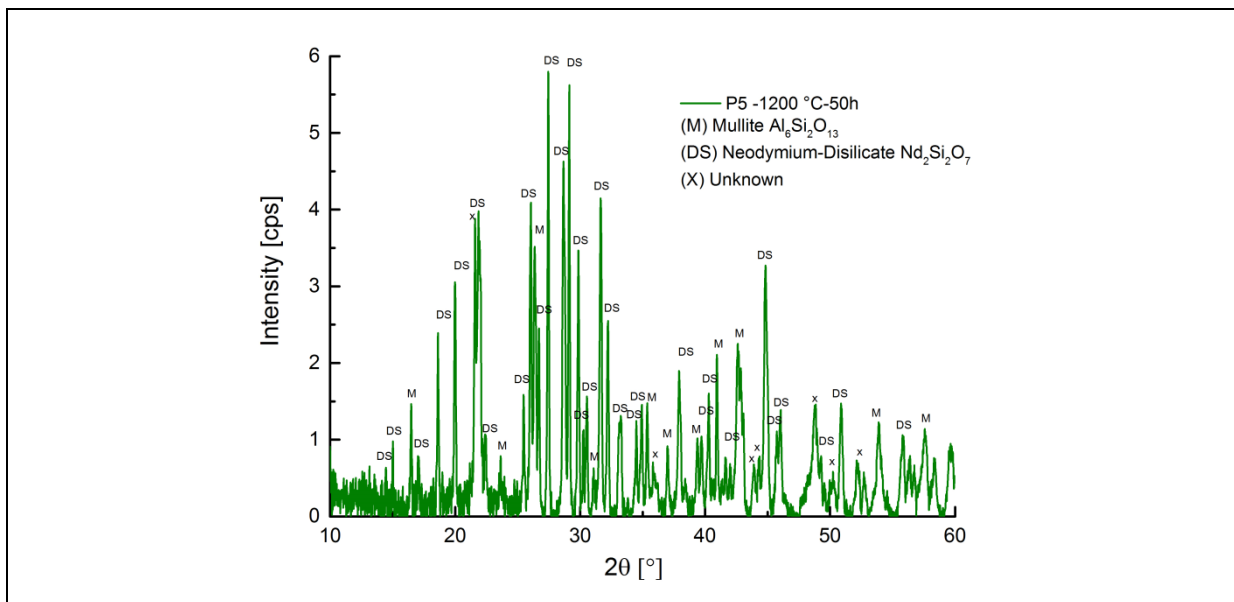


Figure 5.39: XRD analysis of the P5 sample heat-treated at 1200 °C for 50h.

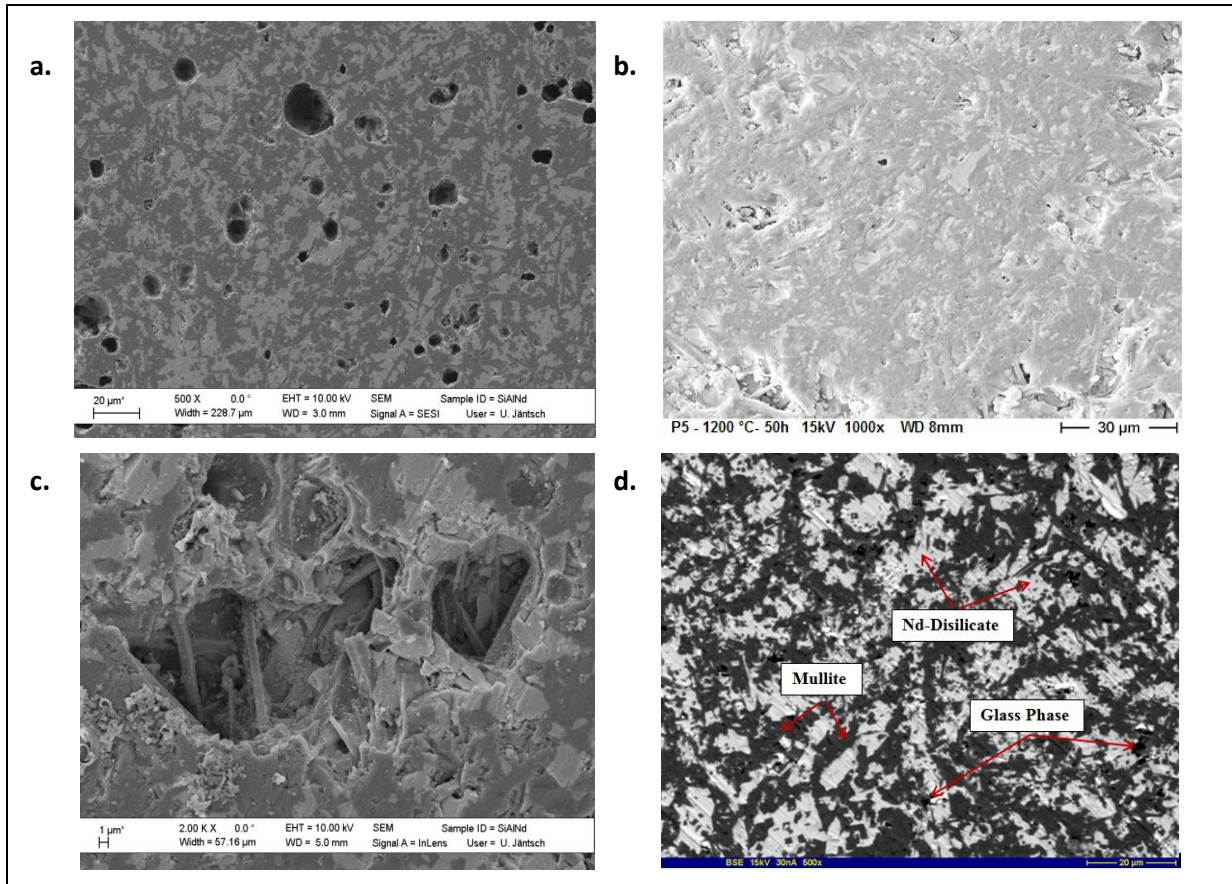


Figure 5.40: Images of P5 sample heat-treated at 1200 °C for 50h; SEM images (a) at mag.500x, (b) at mag. 1000x, (c) at mag. 2000x and (d) BSE at mag. 500x.

5.4.7.3 Raman analysis of the heat-treated samples

Raman spectra of P5–1200°C and P5–1200°C–50h samples are shown in Fig. 5.41. The spectrum of the P5–1200°C sample was found almost similar with the pure P5 glass as shown in Fig. 5.5. It revealed that P5–1200°C sample consists of mostly glassy phase as found during XRD analysis (Fig. 5.38). Raman spectra of P5–1200°C–50h sample revealed high content of Q^3 structural units found at ~ 897 and ~ 933 cm^{-1} , respectively. The assignment of Raman bands for the P5–1200°C–50h sample is given in Table 5.20.

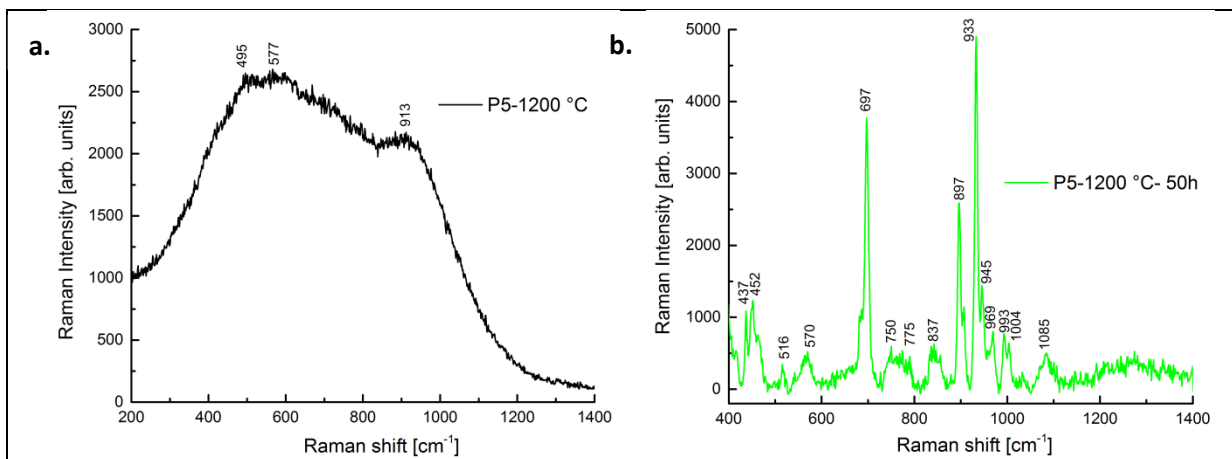


Figure 5.41: Raman spectra of P5 samples aged at 1200 °C; (a) no holding time (b) 50h holding time.

Table 5.20: Raman bands for P5 sample aged at 1200 °C for 50h.

Raman bands	Assignment of bands
437, 452	Q ⁴
516, 570, 687	Si-O-Si bending
897, 933	Q ³
1085	Q ²

5.4.7.4 IR analysis of the heat-treated samples

IR spectra of P5–1200°C and P5–1200°C–50h samples are shown in Fig. 5.42. IR spectra of the P5–1200°C sample showed O-Si-O bending mode at 545 cm⁻¹ and Si-O-Si symmetric stretching at wave number 614, 720 and 857 cm⁻¹, respectively. The spectrum of the P5–1200°C–50h was quite complex. The peak assignment of the P5–1200°C–50h sample is given in Table 5.21. It consists of non-bonding stretching (Si-O-) bending mode (O-Si-O), symmetric stretching (Si-O-Si) and asymmetric stretching (Si-O-Si).

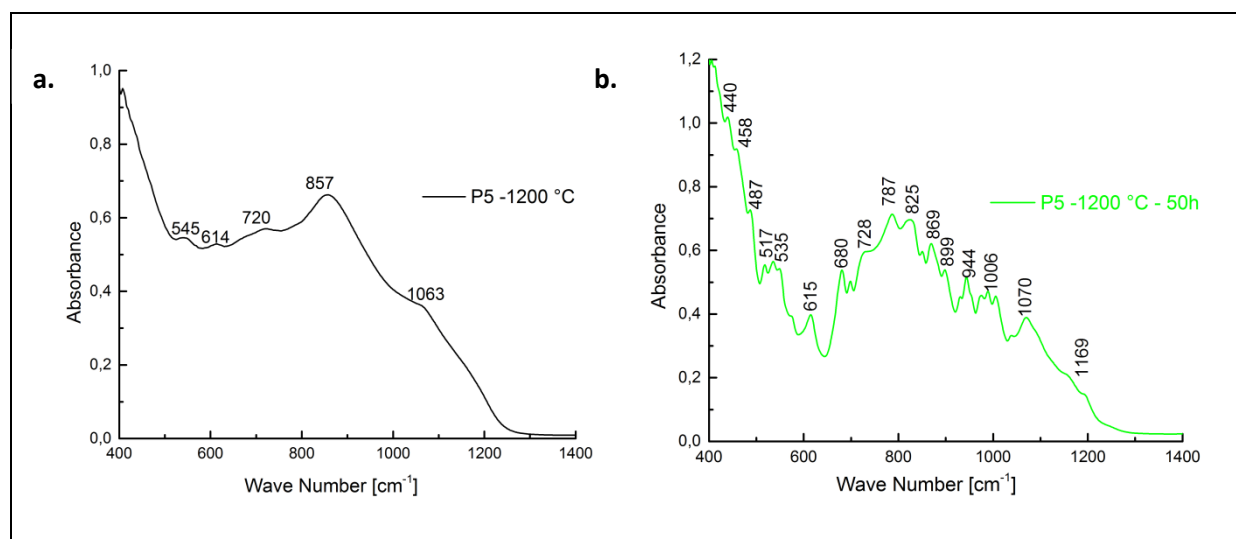


Figure 5.42: IR spectra of P5 samples annealed at 1200 °C; (a) no holding time, (b) 50h holding time.

Table 5.21: Peak assignment for P5 sample annealed at 1200 °C for 50h.

Peak position	Peak assignment
440, 458, 487, 517, 535, 615	(O-Si-O) bending mode
680, 728, 787, 825, 869	(Si-O-Si) symmetric stretching
944	(Si-O-) NB stretching
1070	(Si-O-Si) asymmetric stretching

5.4.8 Crystallization of Scandium-aluminosilicate glasses

This section contains details of hot-stage XRD of P6 glass, XRD and SEM analyses of sample heat-treated at 1200 °C for 50h.

5.4.8.1 Hot-stage XRD of Scandium-aluminosilicate glasses

Figure 5.43 shows hot-stage XRD reflections of the P6 glass from 950–1200 °C. There were no reflections recorded at 900 °C, first reflections of Sc-disilicate (JCPDS card # 20-1037) and mullite (JCPDS card # 15-776) were observed around 1000 °C which were almost 50 °C earlier as compared to other glass systems. The observed peak intensities remain almost similar from 1050–1200 °C. The bulk crystallization process in this glass system was completed at around 1050 °C and did not change up to 1200 °C. The observed crystallization temperature for the P6 in DTA/DSC analyses was around 1075 °C that fits well with hot-stage XRD observations.

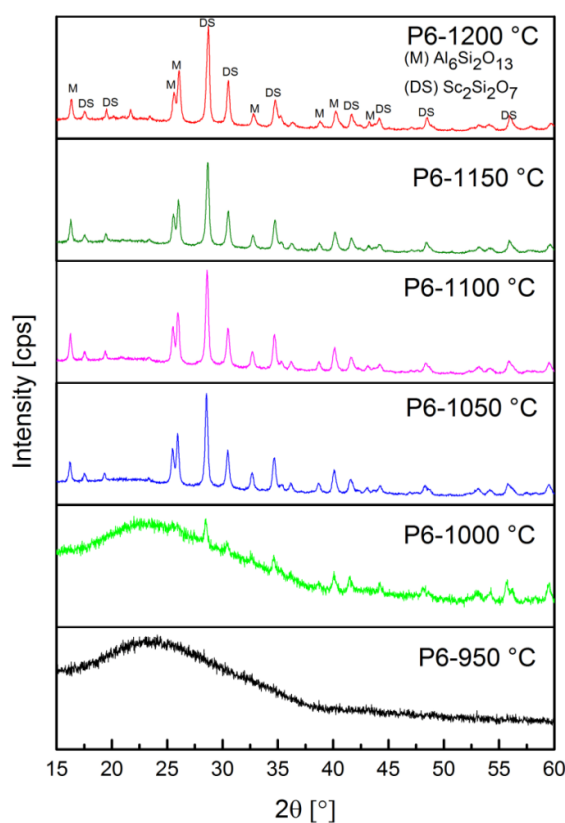


Figure 5.43: In-situ XRD of the P6 glass system.

5.4.8.2 Thermal treatment of Scandium-aluminosilicate glasses

The diffraction pattern of the P5–1200°C–50h sample is shown in Fig. 5.44. The reflections of mullite (JCPDS card # 15-776) and Sc-disilicate (JCPDS card # 20-1037) were found. Figure 5.45 shows SEM images of the P5–1200°C–50h sample that contain Sc-disilicate embedded in the remaining glassy matrix.

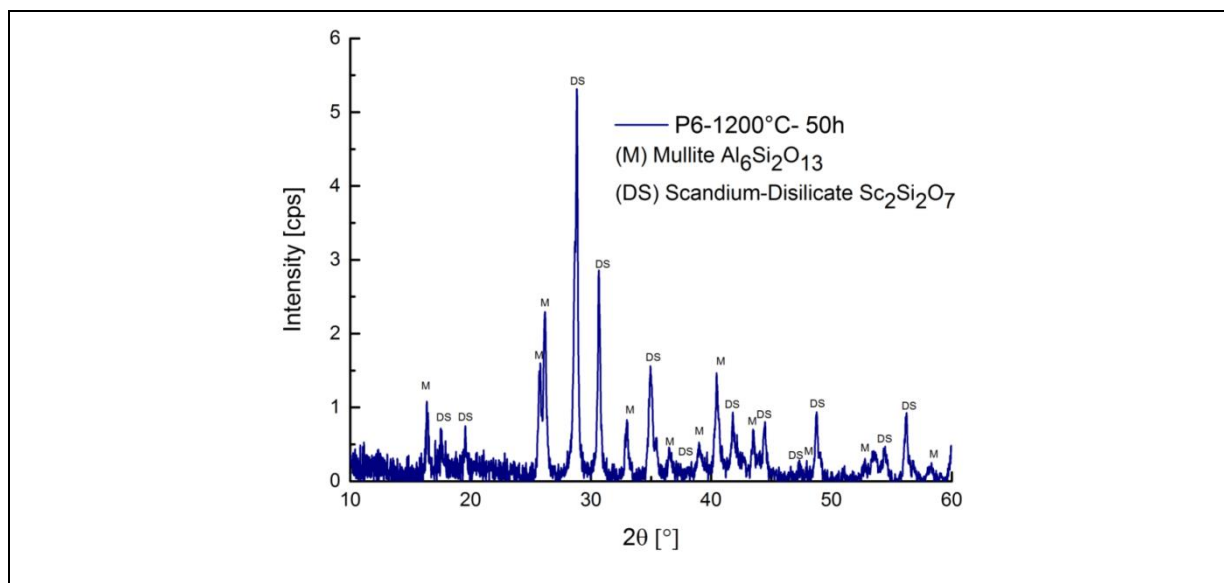


Figure 5.44: XRD analysis of the P6 sample annealed at 1200 °C for 50h.

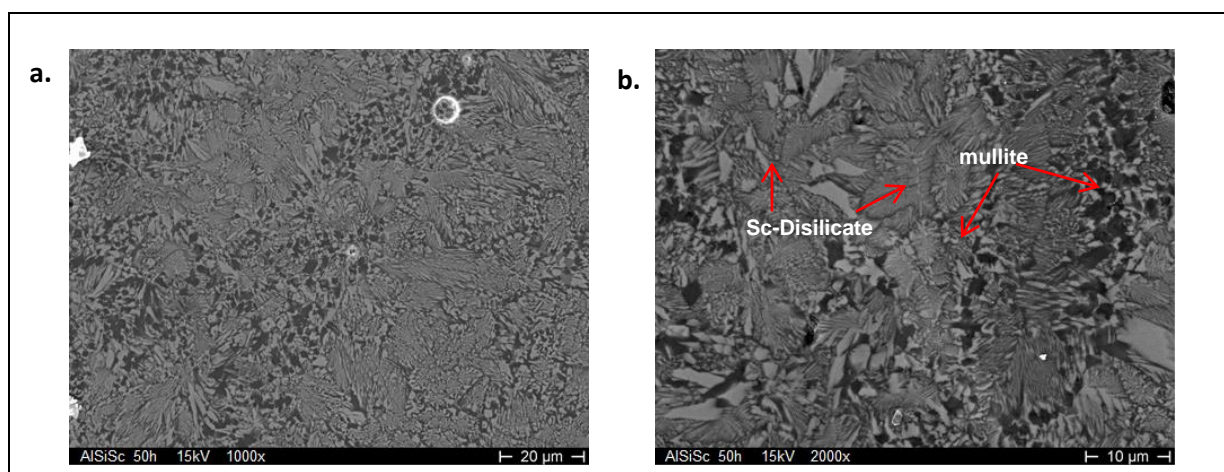


Figure 5.45: SEM images of P6 sample annealed at 1200 °C for 50h; (a) at mag. 1000x, (b) 2000x.

5.4.8.3 Raman analysis of the heat-treated samples

Raman spectra of P6–1200°C and P6–1200°C–50h samples are shown in Fig. 5.46. Spectra of both samples were nearly similar in shape with high content of Q³ units due to the uniform distribution of the Sc⁺³ ions. Assignment of Raman bands for the P6–1200°C–50h sample is given in Table 5.23.

Table 5.22: Raman bands for P6 sample annealed at 1200 °C for 50h.

Raman band	Assignment of bands
437	Q ⁴
510, 639, 668	Si-O-Si bending
829, 932	Q ³
1114	Q ²

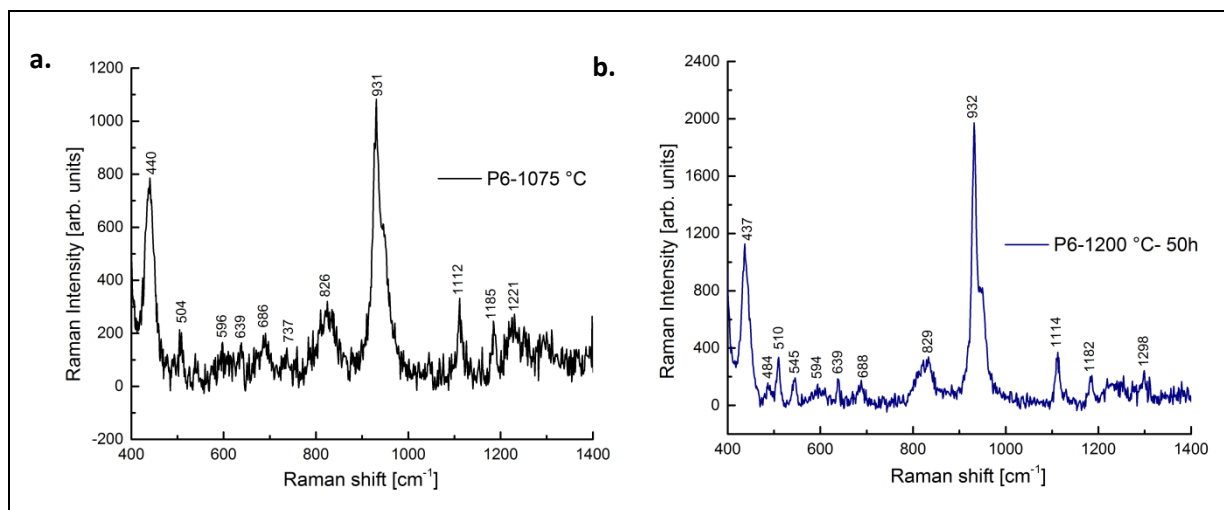


Figure 5.46: Raman spectra of P6 samples aged at 1200 °C; (a) no holding time (b) 50h holding time.

5.4.8.4 IR analysis of the heat-treated samples

IR spectra of P6–1200°C and P6–1200°C–50h samples are shown in Fig. 5.47. Spectra of both samples were almost identical with small variation of wave numbers. Both samples showed strong symmetric stretching of Si-O-Si at wave numbers ~715,791 and 880 cm⁻¹, respectively. Peak assignment of IR spectra for P6–1200°C–50h sample is given in Table 5.23.

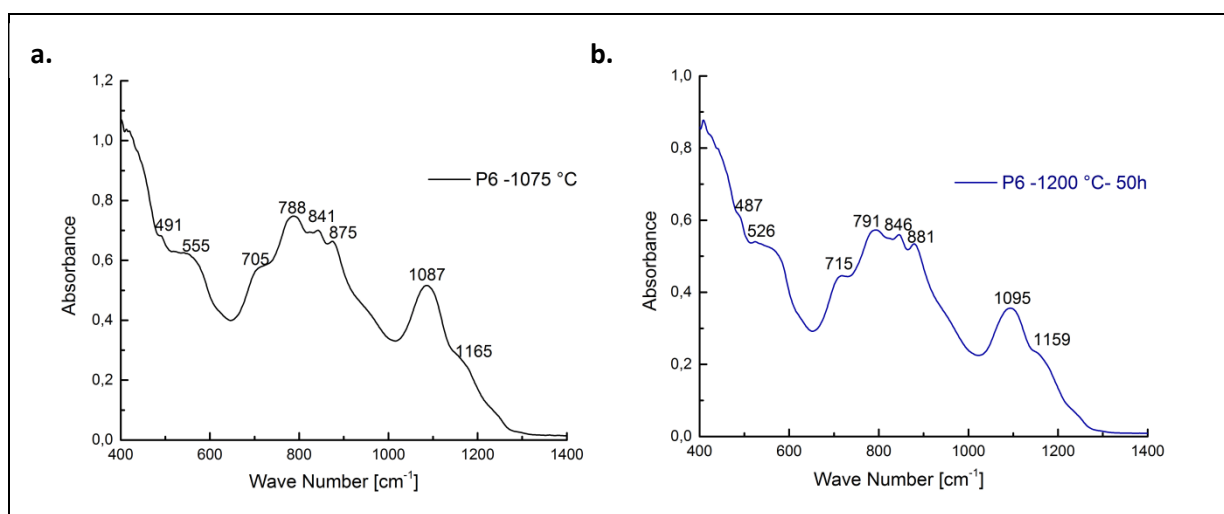


Figure 5.47: IR spectra of P6 samples annealed at 1200 °C; (a) no holding time, (b) 50h holding time.

Table 5.23: Peak assignment for P6 sample annealed at 1200 °C for 50h.

Peak position	Peak assignment
526	(O-Si-O) bending mode
715, 791, 846, 881	(Si-O-Si) symmetric stretching
1095	(Si-O-Si) asymmetric stretching

5.5 Joining of SiC components using rare-earth aluminosilicate glass solders

The prepared glasses were used for joining of SiC components via an optimized laser process at Institute of Power Engineering, Technical University (TU) Dresden. This section contains details of the joining process and the characterization of joints. The joining work was carried out by Dr. Marion Herrmann at TU Dresden. All glasses were melted in joining experiments via laser heating.

5.5.1 Joining of SiC parts via laser process

Slurry was made by mixing the prepared glass powders with ethanol and pasted to the SSiC surfaces to be joined. The quantity of the paste was calculated for a seam thickness of $\sim 20 \mu\text{m}$. The joining process was carried out after the evaporation of ethanol from the deposited paste.

5.5.2 Characteristics of the joining process

The parameters of the joining process are summarized in Table 5.24. The characteristics of the joining process are shown in Fig. 5.48 and their details are presented in section 4.2.19. The joining process was carried out at the maximum laser power P (W) as given in Table 5.24 over a period of 75 seconds (s) for the capsules and 70s for the rods (Fig. 5.49). The laser irradiation was stopped after this with abrupt cut-off of the laser power. The joined samples were cooled to room temperature via free convection and radiation.

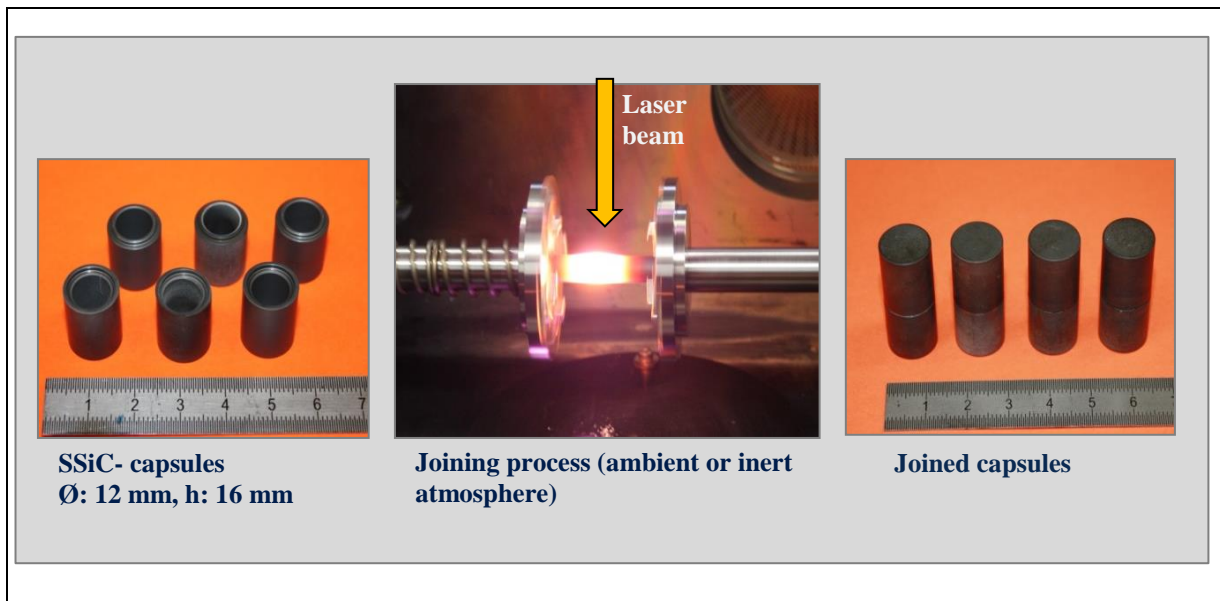


Figure 5.48: Joining of SiC capsules via laser-assisted process.

Table 5.24: Processing parameters for the joining of SiC components.

Solder	T_{melting} (°C)	Atmosphere	Joining of capsules		Joining of rods	
			P (W)	T (°C)	P (W)	T (°C)
P1	1375	ambient	600	1476±19	497	1496±24
P2	1460	Ar: 1 bar	640	1583±25	530	1454±15
P3	1370	ambient	570	1474±16	483	1501±13
P4	1350	ambient	540	1467±28	480	1518±27
P5	1285	ambient	660	1347±7	470	1487±37
P6	>1600	Ar: 1 bar	830	1652±37	585	1592±27

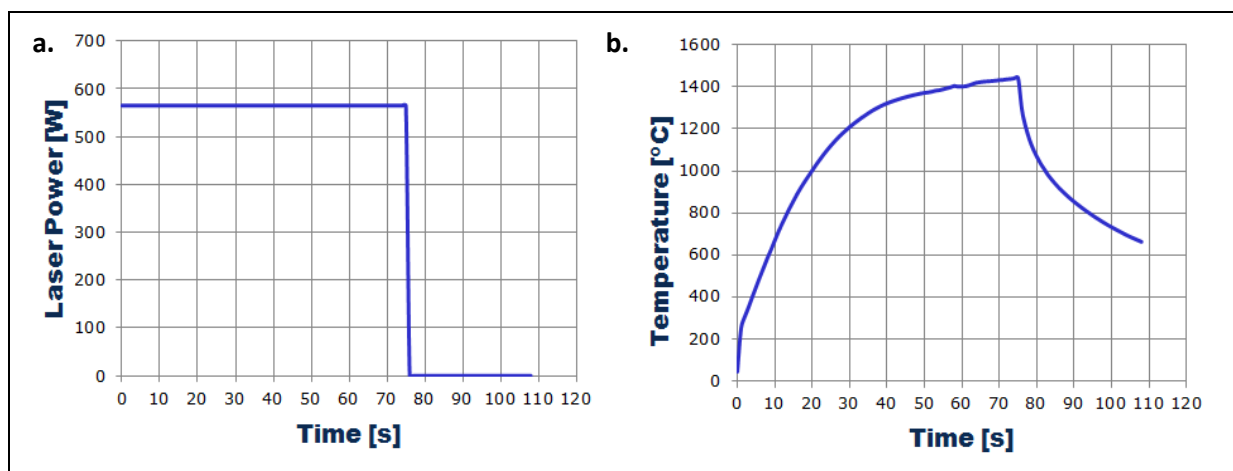


Figure 5.49: Characteristics of the joining process; (a) laser beam for joining of SiC-capsules, (b) surface temperatures on the SiC-capsules.

5.5.3 Characterizations of the joints

For structural analyses of joint seams, one capsule of each solder batch was cut using diamond cutter saw, embedded in epoxy, grinded and polished for the ceramographical examination. The cross-section of the joints made by these glass solders are shown in Fig. 5.50. It showed excellent wetting characteristics of these glasses on SiC surfaces and produced defect-free interfaces between solders and SiC surfaces. Results of electron microprobe analyses for the prepared joints are summarized in Tables 5.25a-b which shows that elemental composition in glassy layers matching closely with initial composition of the prepared glasses determined with XRF and given in Table 5.1.

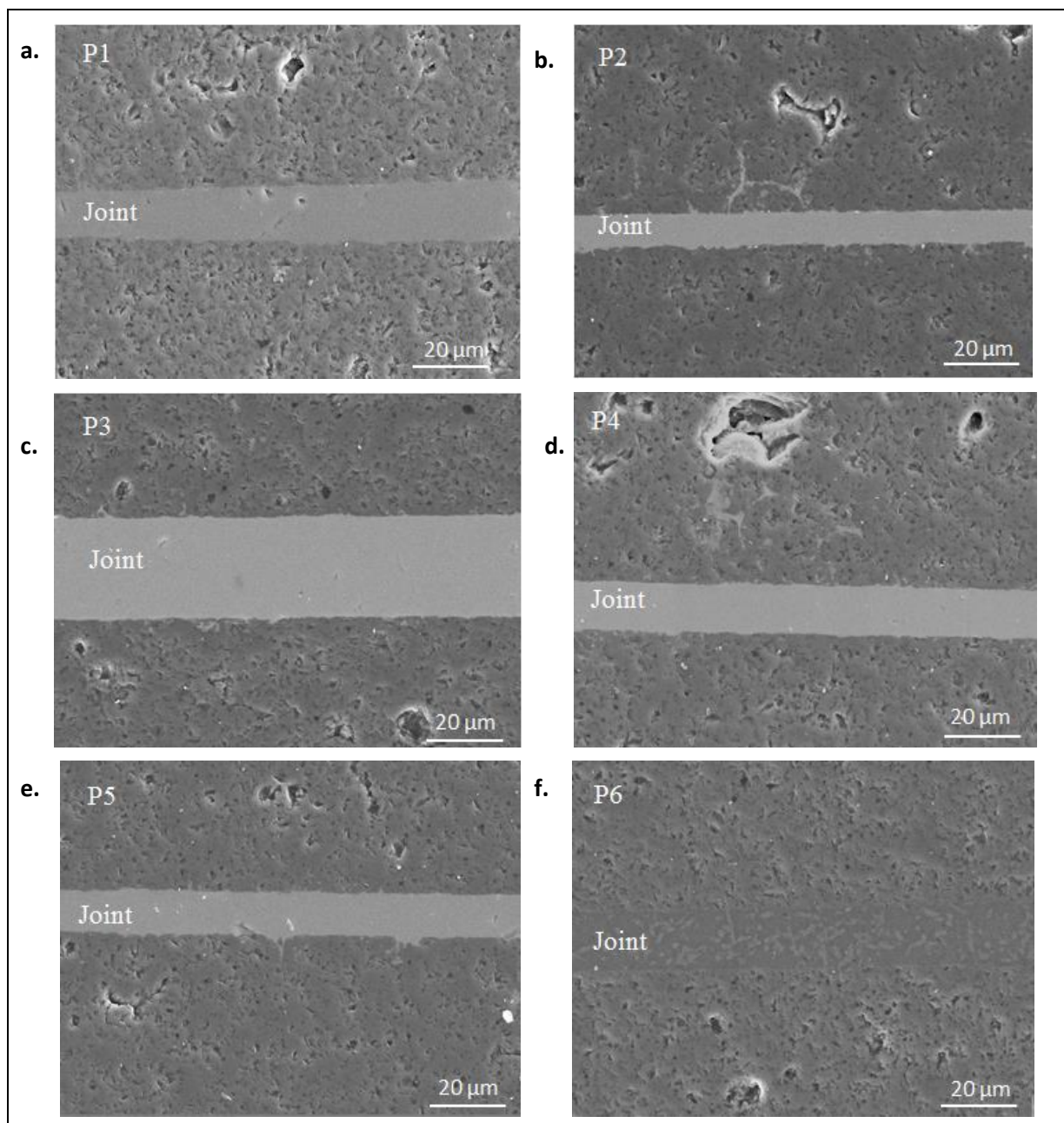


Figure 5.50: Joints made with prepared glass solders; (a) P1, (b) P2, (c) P3, (d) P4, (e) P5, and (f) P6.

Table 5.25 a: Elemental probe analyses of the joint layer (at. %).

Sample	Al	Si	Y	Yb	Ho	Dy	Nd	Sc	O	Sum
P1	13.84	19.71	21.06						43.77	100
P2	11.09	17.24		38.18					31.99	98.5
P3	10.08	16.09			37.07				37.47	100
P4	11.07	17.15				37.47			32.79	98.47
P5	11.42	18.03					35.34		35.66	100.3
P6	16.5	22.18						15.29	44.08	98.04

Table 5.25b: Elemental probe analyses of the joint layer (mass %).

Sample	Al	Si	Y	Yb	Ho	Dy	Nd	Sc	O	Sum
P1	12.22	16.72	5.64						65.19	100
P2	12.66	18.9		6.8					61.6	98.04
P3	10.71	16.42			6.85				66.48	100
P4	12.43	18.5				6.99			62.09	98.90
P5	11.95	18.17					6.9		62.97	100
P6	13.6	17.56						7.57	61.27	99

Mechanical strengths of the joined rods were measured using a 4-point bending strength test with machine type Z010 (Fa. Zwick/Roell). The results of the mechanical testing of the joined samples are given in Table 5.26. The average 4-point bending strength of joints made with glassy solders P1, P3, P4 and P5 was found to be higher than 120 MPa (This work was carried out by Dr. Marion Herrmann at TU Dresden).

Table 5.26: Mechanical properties of joints made with prepared glasses.

Solder composition	Samples joined	Laser power (W)	T _{melting} (°C)	T _{processing} (°C)	Strength (MPa)	Weibull modulus
P1	8	497	1398	1496 ± 24	132 ± 32	5.35
P2	12	530	1460	1454 ± 15	41 ± 12	3.64
P3	9	483	1413	1501 ± 13	136 ± 22	6.60
P4	12	480	1366	1518 ± 27	126 ± 26	7.41
P5	9	470	1299	1478 ± 37	149 ± 22	7.11
P6	11	585	~ 1600	1592 ± 27	75 ± 27	3.07

For leak tests, three joined capsule of each solder composition were used. The tightness of joints was found via measurement of He-leakage-rate. Results of these He-leakage tests are summarized in Table 5.27. The joints with P1 solder resulted in highest tightness; leak rates for all the samples were measured in range of 10^{-10} – 10^{-9} mbar·l·s⁻¹. (This work was carried out at TU Dresden).

Table 5.27: Leak tightness of joints made with different rare-earth aluminosilicate glasses.

Solder composition	Tightness sample 1 (mbar·l·s ⁻¹)	Tightness sample 2 (mbar·l·s ⁻¹)	Tightness sample 3 (mbar·l·s ⁻¹)	Tightness avg. (mbar·l·s ⁻¹)
P1	3.60E-09	1.41E-10	2.54E-10	1.33E-09
P2	9.21E-08	1.77E-09	4.33E-03	5.40E-06
P3	1.58E-07	1.43E-07	1.17E-09	1.01E-07
P4	2.56E-10	3.55E-10	2.65E-09	1.09E-09
P5	1.63E-10	1.66E-08	3.11E-09	6.62E-09
P6	1.76E-06	6.14E-01	5.73E-03	2.07E-01

5.6 Microwave heat-treatment of rare-earth aluminosilicate glasses

Microwave crystallization studies of P1 (AlSiY) and P5 (AlSiNd) glasses were carried out to investigate the effects of microwave heating on their microstructures. These glasses were selected due to their ability to produce tight joints with good mechanical strength. Three powder compacted samples of P1 and P5 glasses were prepared having 8 mm diameter and 5 mm thickness as shown in Fig. 5.51. These compacted glass specimens were annealed at 1200 °C for different times (no holding time, 15 min and 30 min holding time). Microwave crystallization was carried out using frequency of 30 GHz. A compact Gyrotron system having a maximum power of 15 kW was used for generating a frequency of 30 GHz. The compacted glass specimens were kept in a thermal insulation as shown in Fig. 5.51. Thermal insulation was provided to reduce the heat losses and crack formation in the samples during the microwave processing. Temperature control was performed using S-type thermocouple, which had an indirect contact with the glass sample surface.

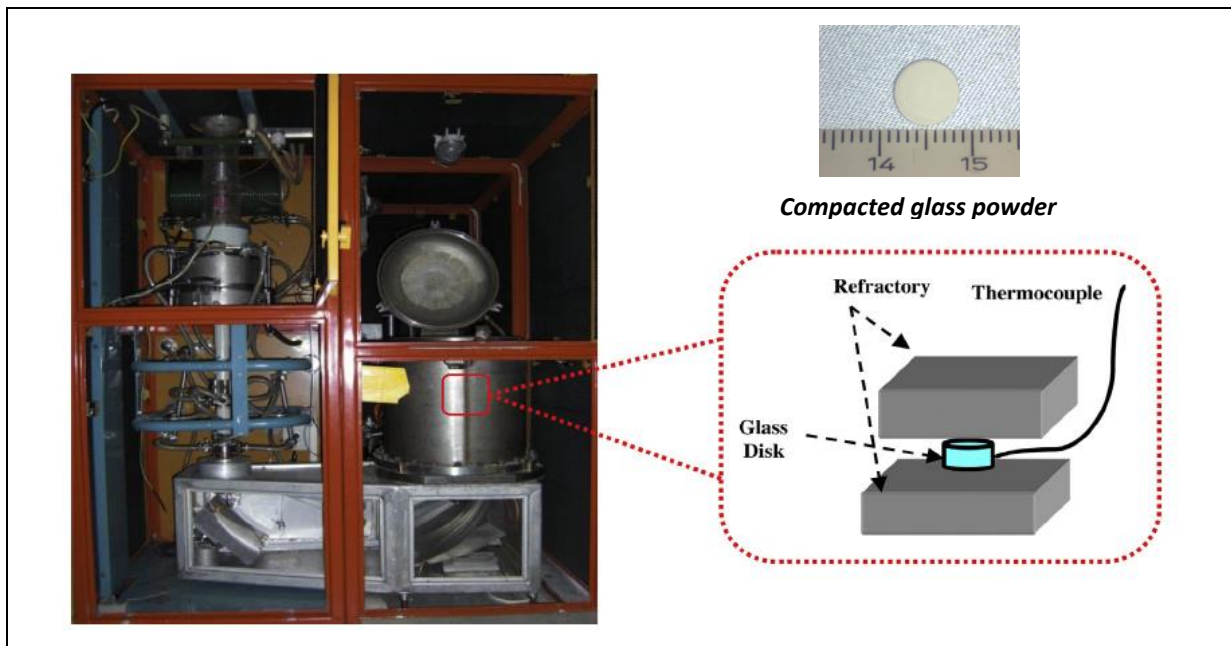


Figure 5.51: GHz Gyrotron system for materials processing setup [72].

5.6.1 Structural analyses of microwave heat-treated samples

Microwave crystallized samples were characterized using XRD, SEM, Raman and IR spectroscopic techniques. For these analyses microwave crystallized samples were prepared following grinding and polishing steps of ceramographical specimen preparation. These microwave heat-treated samples were compared with samples annealed in a conventional furnace (Nabertherm® Germany) with 15 K/min heating rate at 1200 °C for 50h holding time (P1-1200°C-50h, P5-1200°C-50h) .

5.6.1.1 XRD analyses

XRD patterns of P1 and P5 annealed samples using microwave heating source are shown in Fig. 5.52. The main phases identified in P1 samples were mullite (JCPDS card # 15-776) and Y-disilicate (JCPDS card # 22-1103). The intensity of both phases was increased with increasing dwelling time and became constant after 15 minutes holding time. The P1 glass sample heat-treated for 30 min at 1200 °C using microwave processing showed peaks of cristobalite, Y-disilicate and mullite with intensities similar to sample heat-treated for 15 min. This observation suggested that the P1 sample was fully crystallized at 1200 °C within 15 min holding time during microwave processing.

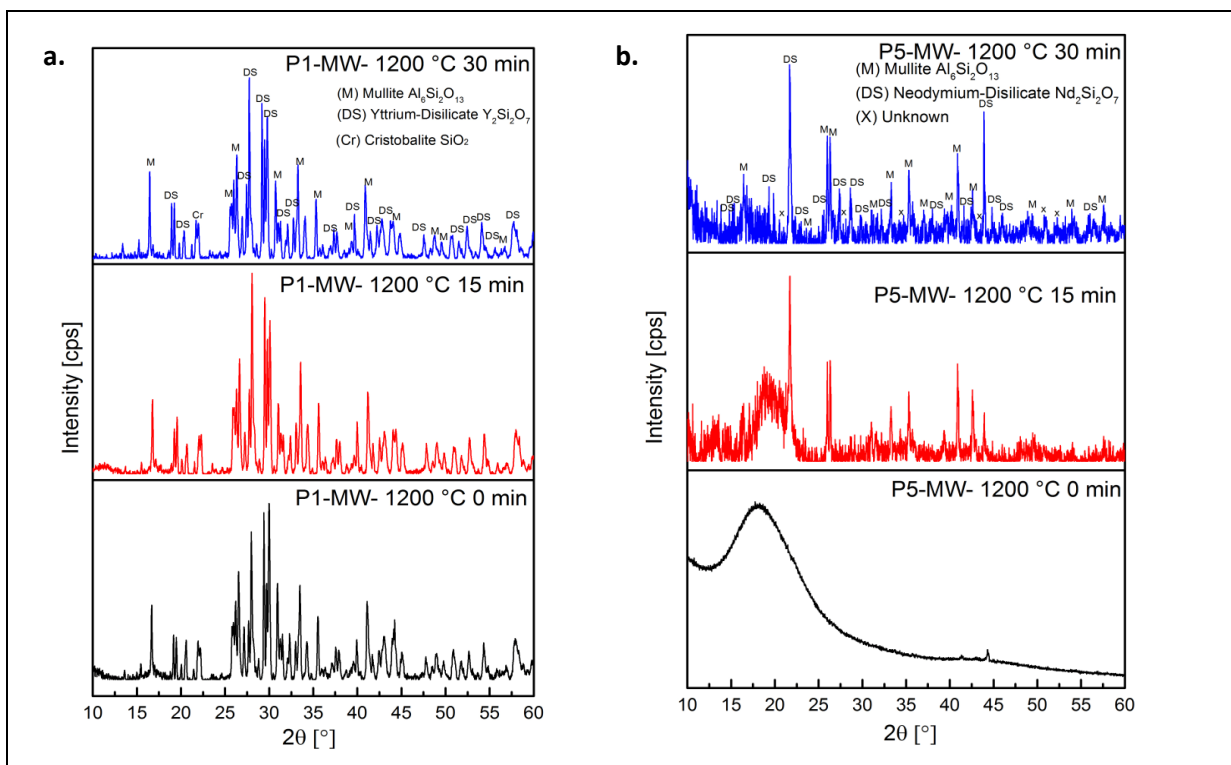


Figure 5.52: XRD of samples annealed at 1200 °C using microwave heating; (a) P1 and (b) P5 glasses.

XRD of P5 samples showed gradual development of mullite (JCPDS card # 15-776), Nd-disilicate (JCPDS card # 22-1177) and an unknown phase with increasing holding time. XRD of the P5 sample heat-treated at 1200 °C with no-holding time showed almost completely amorphous structure (Fig. 5.52b). The sample with 15 min holding time showed typical glassy hub with relatively strong reflections of Nd-disilicate and small reflections of mullite. Diffraction of the P5 sample annealed for 30 min at 1200 °C showed peaks of Nd-disilicate, mullite and unknown phase.

5.6.1.2 SEM analyses

SEM images of P1 samples crystallized using microwave processing are shown in Fig. 5.53. Glass patches were found in the P1 sample heat-treated at 1200 °C with no-holding time. SEM images of the sample heat-treated for 15 min showed completely crystallized behaviour with no evidence of remaining glassy matrix. The images of the sample crystallized for 30 min at 1200 °C showed completely crystallized behaviour, crystals of Y-disilicate and mullite were uniformly distributed.

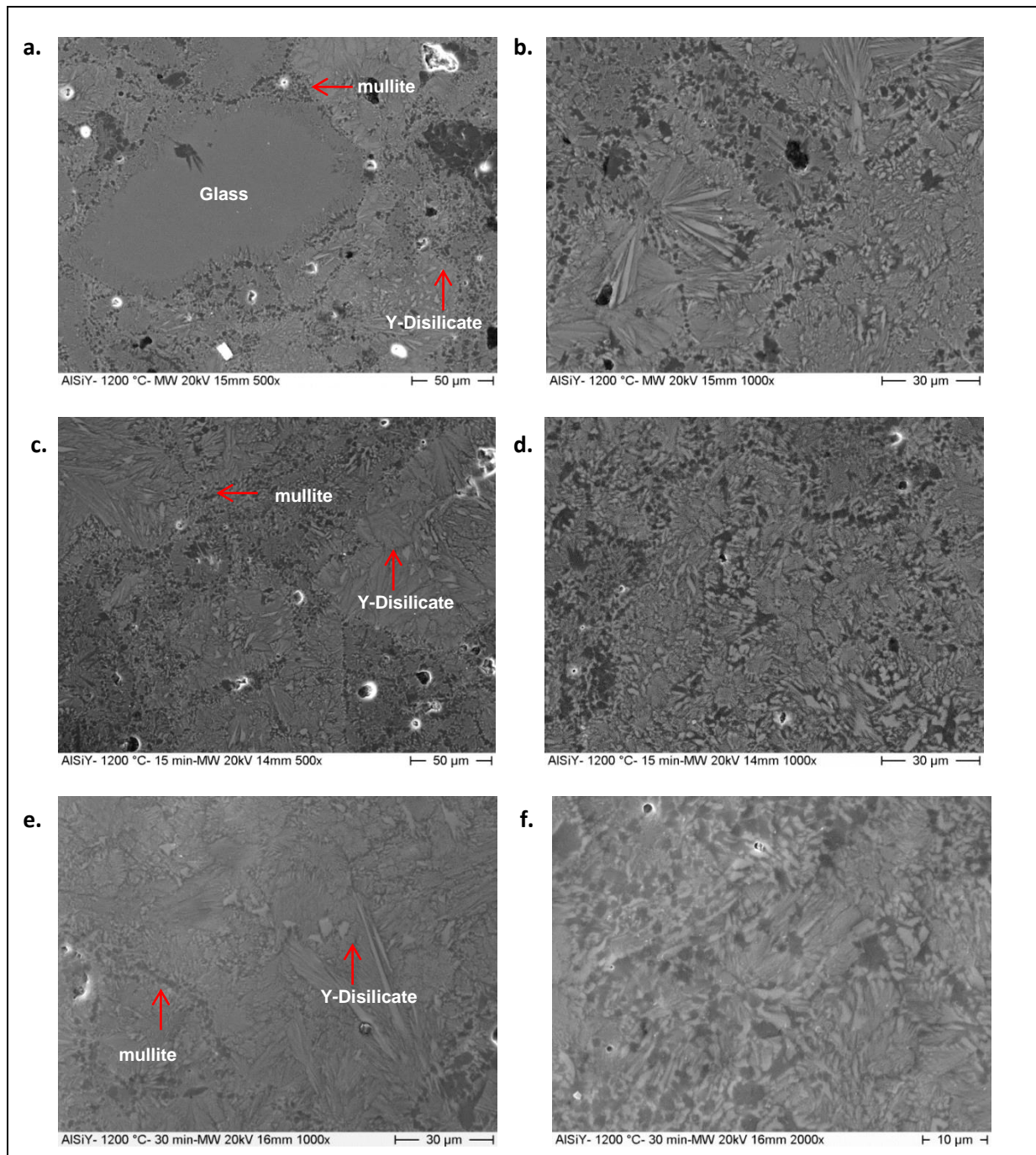


Figure 5.53: SEM images of P1 samples annealed at 1200 °C using microwave heating; (a, b) for no holding time at mag. 500x and 1000x, respectively, (c, d) for 15 min holding at mag. 500x and 1000x, respectively and (e, f) for 30 min holding time at mag. 1000x and 2000x, respectively.

SEM images of microwave-annealed P5 samples are shown in Fig. 5.54. SEM images of the P5 sample heat-treated at 1200 °C with no-holding time shows mostly glassy phase with small crystals of Nd-disilicate. The fractions of these crystals increased in the sample with 15 min holding time and sample was partially/semi crystallized. SEM images of the sample with 30 min holding time showed semi-crystallized sample with relatively larger crystals of Nd-disilicate. This observation revealed that P5 samples need more holding time to be fully crystallized.

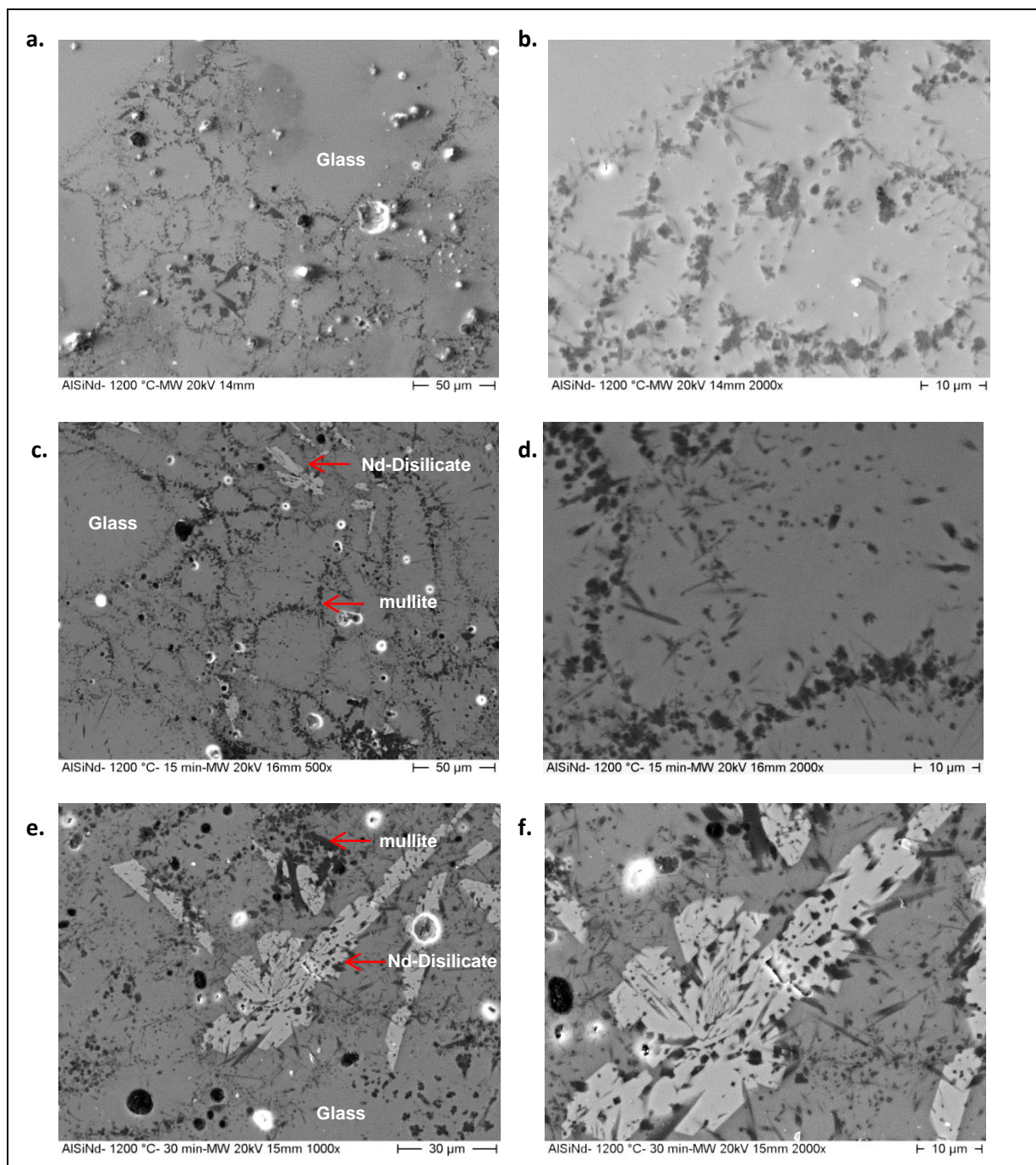


Figure 5.54: SEM images of P5 samples annealed at 1200 °C using microwave heating; (a, b) for no holding time at mag. 500x and 1000x, respectively, (c, d) for 15 min holding at mag. 500x and 1000x, respectively, (e, f) for 30 min holding time at mag. 1000x and 2000x, respectively.

5.6.1.3 Raman analyses

Raman spectra of P1 samples heat-treated at 1200 °C for different periods of time during microwave processing are shown in Fig. 5.55a. Spectra of P1 samples annealed at 1200 °C for 15 min and 30 min were almost identical. The spectrum of the P5 sample annealed at 1200 °C without providing any holding time was similar to the P5 glass as shown in Fig.5.5e. The assignment of Raman bands for P1 and P5 microwave-processed samples is shown in Table 5.28.

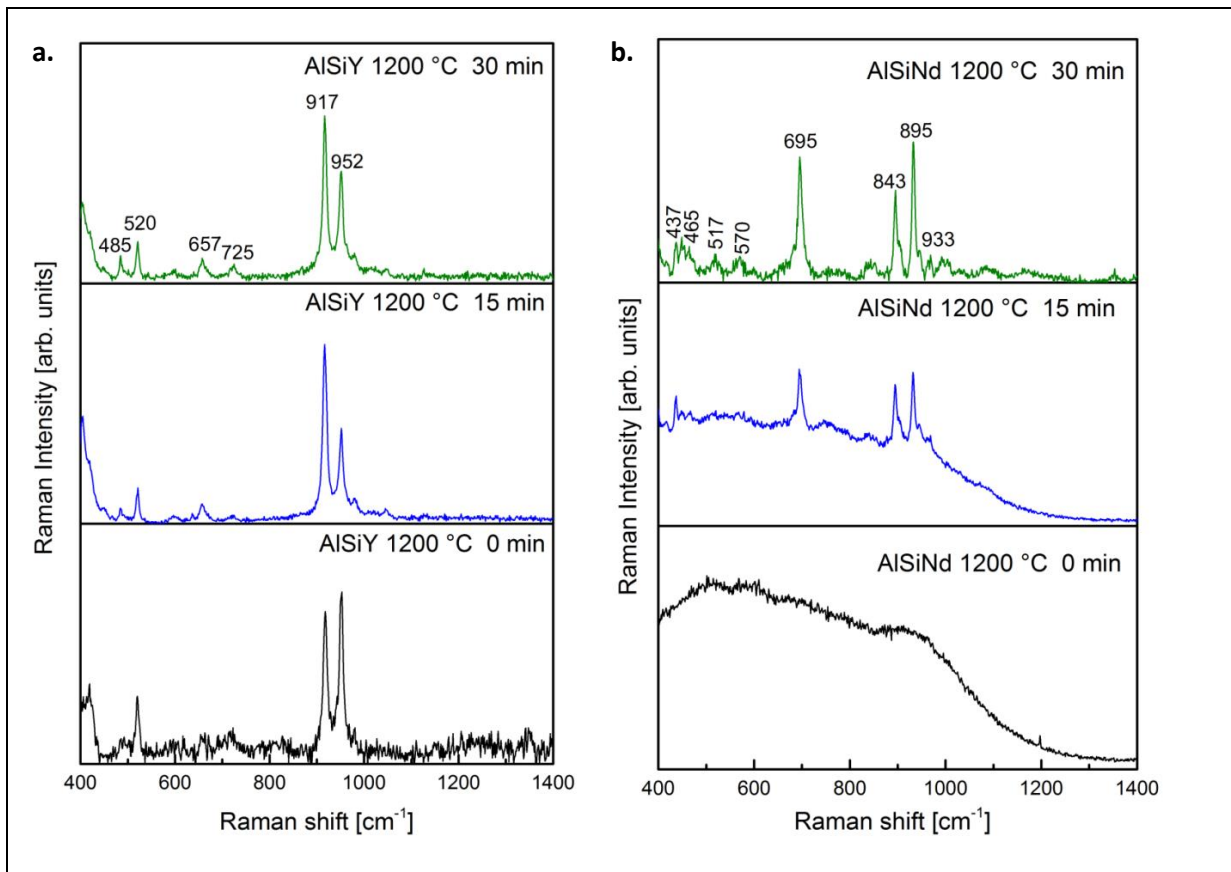


Figure 5.55: Raman spectra of samples annealed at 1200 °C for different holding time using microwave processing; (a) P1 (AlSiY) and (b) P5 (AlSiNd).

Table 5.28: Raman bands for samples heat-treated using microwave processing.

Raman bands of P1 glasses		Raman bands of P5 glasses	
Raman band	Assignment of bands	Raman band	Assignment of bands
485	Q ⁴	437, 465	Q ⁴
520	Si-O-Si bending	517, 570	Si-O-Si bending
657,725	Si-O-Si bending	695	Si-O-Si bending
917	Si-O stretching in Q ³	843	Si-O stretching in Q ³
952	Si-O stretching in Q ³	895,933	Si-O stretching in Q ³

5.6.1.4 IR analyses

IR spectra of P1 samples heat-treated via microwave processing are shown in Fig. 5.56a. It was found that peaks are more pronounced in samples annealed for 30 min at 1200 °C. Spectra showed symmetric stretching of Si-O-Si at wave numbers ~ 715 and ~ 809 cm^{-1} and asymmetric stretching (Si-O-Si) at ~ 1078 cm^{-1} wave number. There was an additional peak observed for the microwave-processed samples at ~ 958 cm^{-1} , which corresponds to (Si-O) NB stretching. IR spectra of P5 samples annealed via microwave processing are shown in Fig. 5.56b. These spectra of P5 samples processed for different periods of time were almost identical. The peak assignment of IR spectra for P1 and P5 glass-ceramic samples processed using microwave is given in Table 5.29.

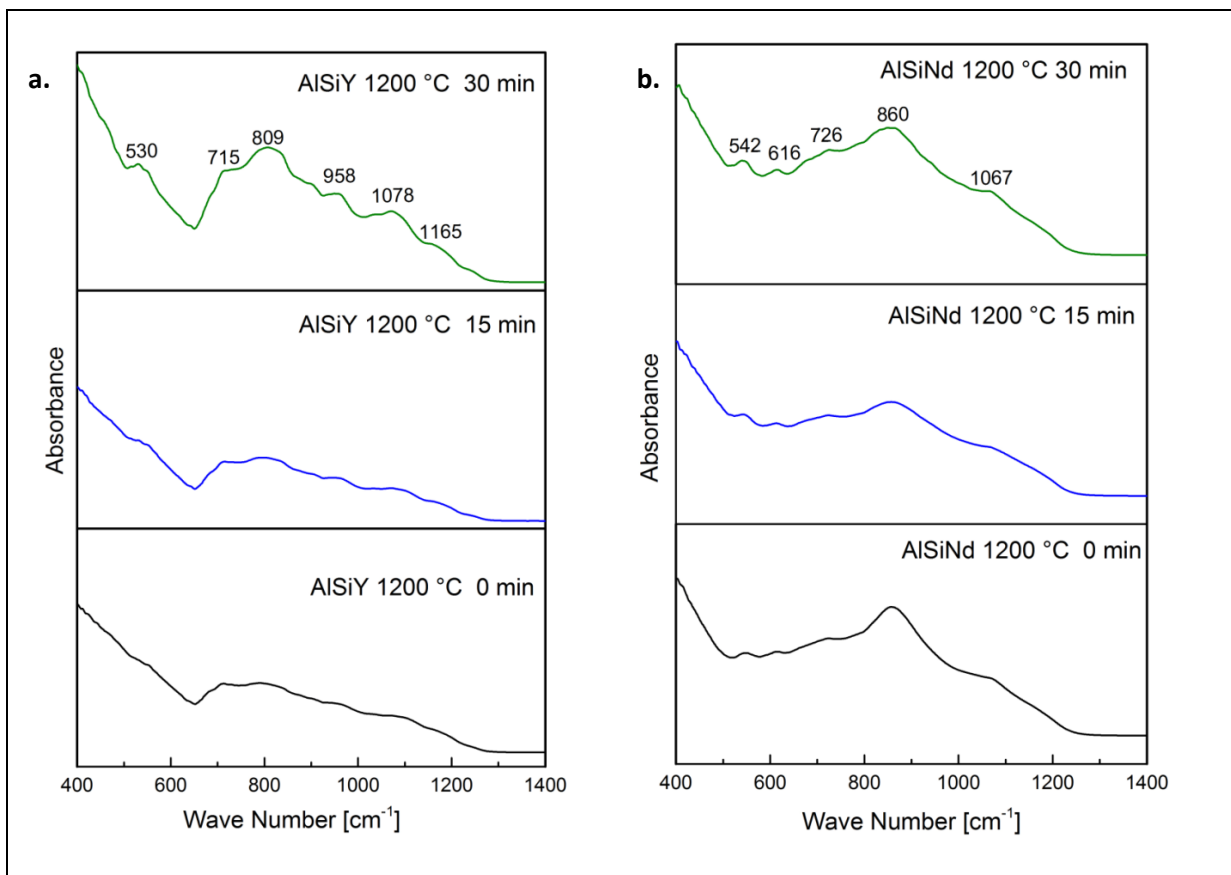


Figure 5.56: IR spectra of samples annealed at 1200 °C for different holding time using microwave heating (a) P1 (AlSiY) and (b) P5 (AlSiNd).

Table 5.29: IR peak assignment for samples heat-treated using microwave processing.

IR peak assignment of P1(AlSiY) glasses		IR peak assignment of P5 (AlSiNd) glasses	
Position	Peak assignment	Position	Peak assignment
530	(O-Si-O) bending mode	542	(O-Si-O) bending mode
715, 809	(Si-O-Si) symmetric stretching	616	(O-Si-O) bending mode
958	(Si-O ⁻) NB stretching	726, 860	(Si-O-Si) symmetric stretching
1078	(Si-O-Si) asymmetric stretching	1067	(Si-O-Si) asymmetric stretching

5.7 Yttria and neodymia aluminosilicate glasses containing nucleating agents

Properties of glasses can be controlled by their chemical compositions, with controlled heat-treatment by getting a required microstructure, and with addition of nucleating agents. Proper amount of nucleating agents affects microstructures and properties significantly. In the present work, the effects of different amounts (4 and 8 mass %, respectively) of TiO₂ and ZrO₂, respectively, on the structures and the properties of P1 and P5 glass systems were explored. These glass systems were chosen due to their ability to produce tight joints with good mechanical strength. This work package contains structural and thermal analyses of these nucleating agents containing rare-earth aluminosilicate glasses.

5.7.1 Structural analyses of glasses containing nucleating agents

Yttria and neodymia aluminosilicate glasses containing nucleating agents (TiO₂ and ZrO₂) were prepared with the procedure as discussed in section 4.1.2. Structural analyses of these glasses were carried out using XRD, Raman and IR spectroscopic techniques.

5.7.1.1 XRD analyses of TiO₂ and ZrO₂ containing prepared glasses

X-ray diffractions of P1 glasses containing 4% TiO₂ (P1-4T), 8% TiO₂ (P1-8T), 4% ZrO₂ (P1-4Z), 8% ZrO₂ (P1-8Z) and P5 glasses containing 4% TiO₂ (P5-4T), 8% TiO₂ (P5-8T), 4% ZrO₂ (P5-4Z), 8% ZrO₂ (P5-8Z) are shown in Fig.5.57, revealing that the prepared glasses have typical amorphous structures.

5.7.1.2 IR analyses of TiO₂ and ZrO₂ containing glasses

IR spectra of nucleating agents (TiO₂, ZrO₂) containing P1 and P5 glass powders were determined from 400 – 1400 cm⁻¹ wave numbers. IR spectra of P1-4T, P1-8T, P1-4Z, and P1-8Z are shown in Fig. 5.58, which contain stretching mode of Si-O bond at around 900 cm⁻¹ wave number. Moreover, asymmetric stretching of Si-O-Si bonds was found at around 1063 cm⁻¹. These spectra match closely with the P1 spectrum shown in Fig. 5.3a.

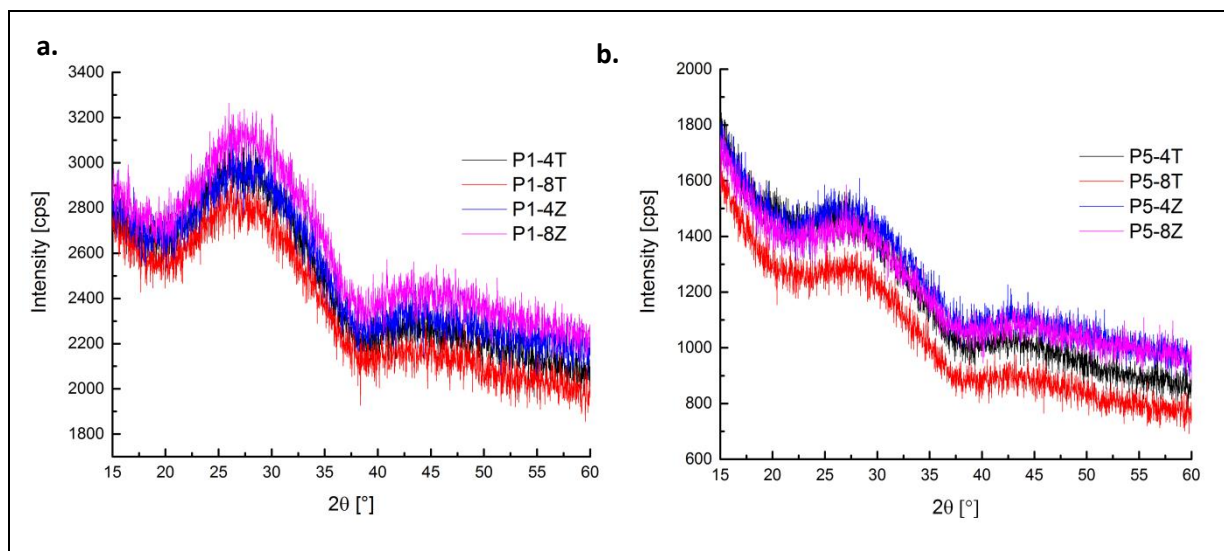


Figure 5.57: XRD analyses of nucleating agents (TiO_2 , ZrO_2) containing glasses; (a) P1 and (b) P5.

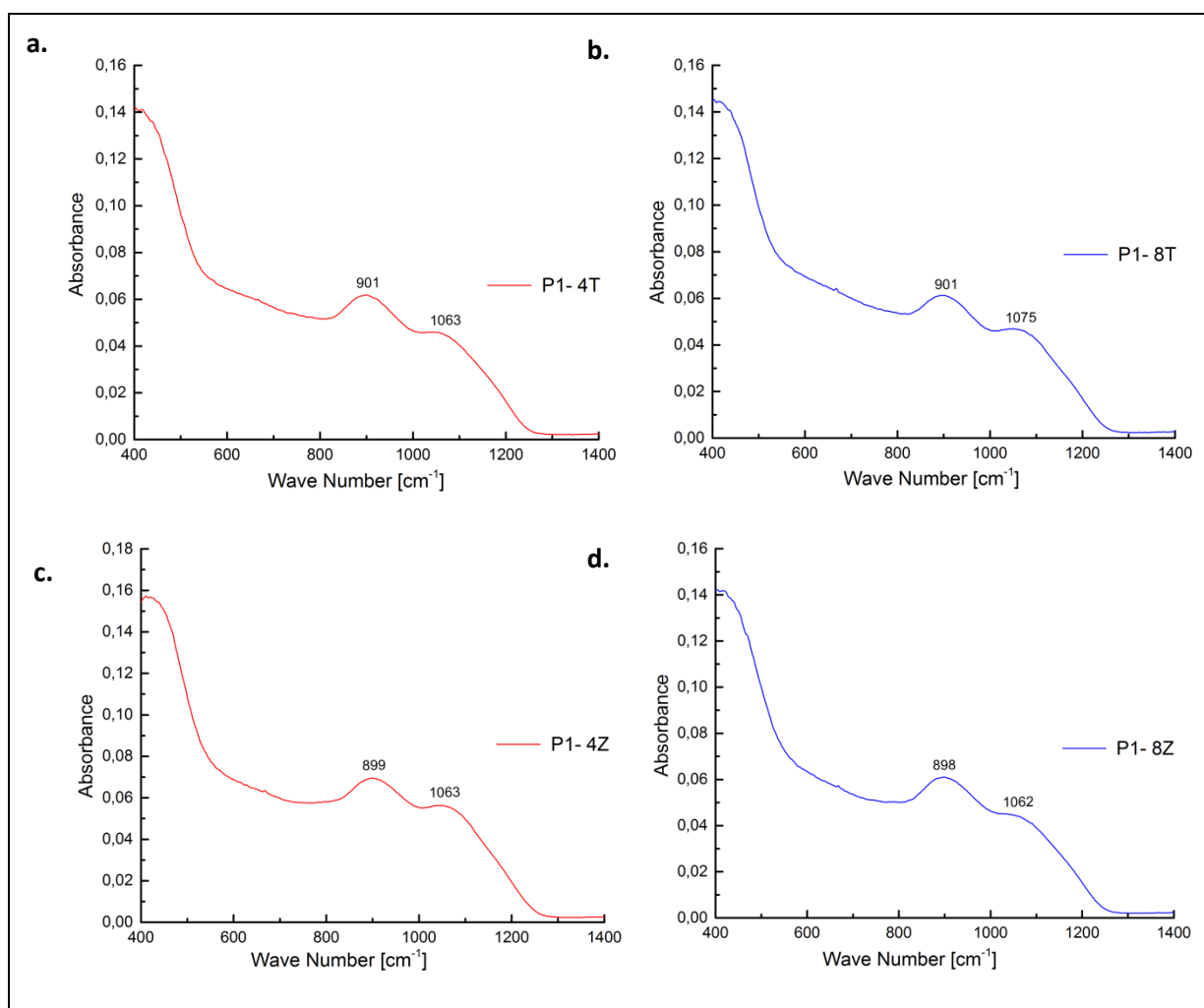


Figure 5.58: IR spectra of TiO_2 and ZrO_2 containing glasses; (a) P1-4T, (b) P1-8T, (c) P1-4Z and (d) P1-8Z.

IR spectra of the P5 glass system containing different nucleating agents are shown in Fig. 5.59. These spectra were identical, with Si-O stretching at around 900 cm^{-1} , and asymmetric stretching

of Si-O-Si bonds was found at around 1065 and 1075 cm^{-1} , respectively. This asymmetric stretching was not so pronounced in the sample P5-8Z. Spectra of these glasses are matching closely with spectrum of the P5 glass as shown in Fig. 5.3e. It shows addition of nucleating agents did not affect stretching modes in yttria and neodymium containing rare-earth aluminosilicate glasses.

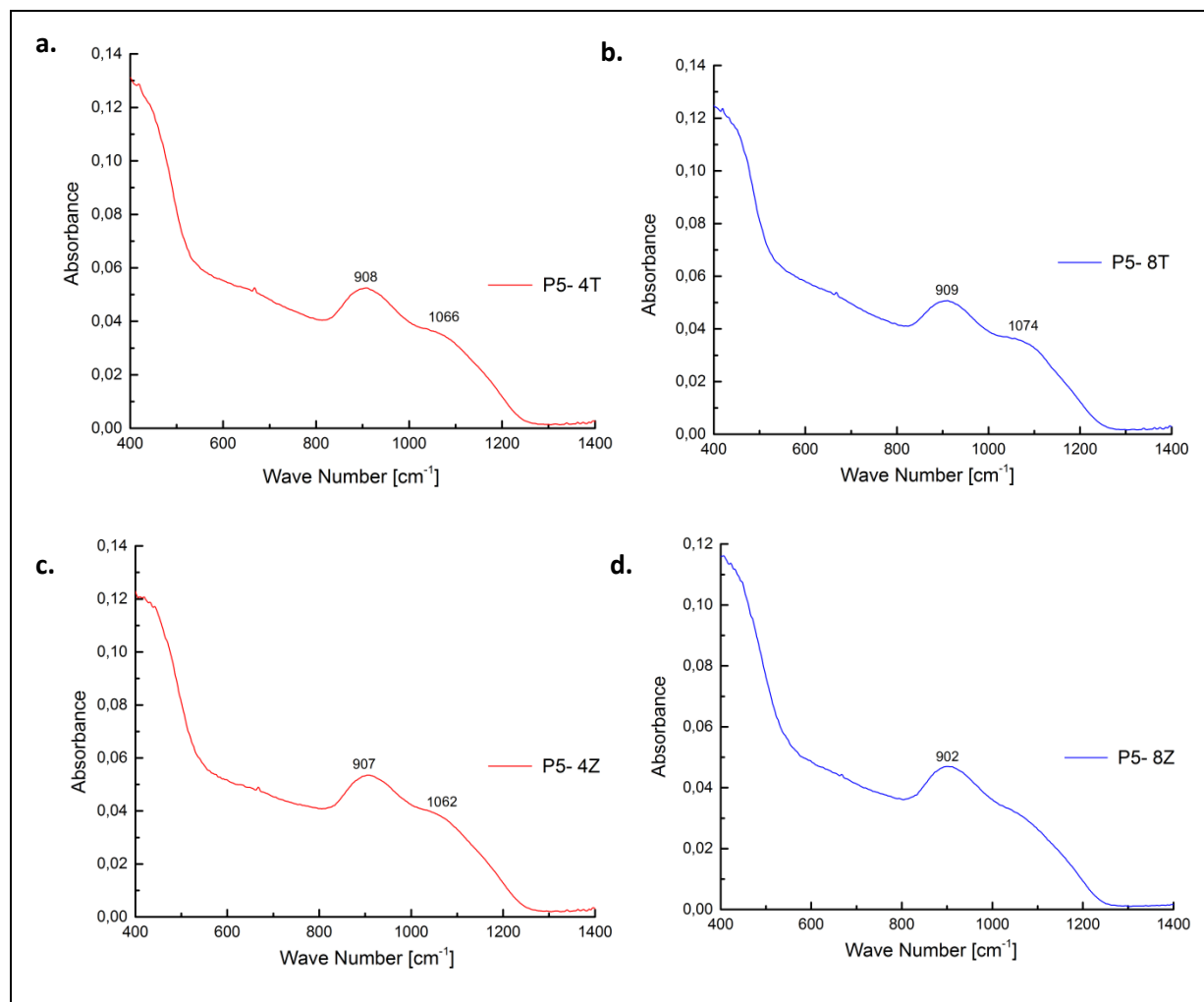


Figure 5.59: IR spectra of TiO_2 and ZrO_2 containing glasses; (a) P5-4T, (b) P5-8T, (c) P5-4Z and (d) P5-8Z.

5.7.1.3 Raman analyses of nucleating agents (TiO_2 , ZrO_2) containing glasses

Raman spectra of nucleating agents containing P1 and P5 glasses were revealed to explore the structural bands in them. Raman spectra of P1 glasses containing different amounts of nucleating agents TiO_2 and ZrO_2 are shown in Fig 5.60. The Raman spectrum of the P1-4T sample contains Q^4 structural units and high content of Si-O-M stretching mode in Q^3 units at around 915 cm^{-1} . The addition of TiO_2 increased the intensity of above bands in the P1-8T sample; and Si-O-M stretching in Q^3 units was found at relatively lower Raman shift. Raman spectra of ZrO_2 containing P1 glasses are shown in Fig. 5.60b. Both spectra are identical in shape and consist of Q^4 structural units, bending mode for Si-O-Si at around 485 cm^{-1} and Si-O-M stretching mode in Q^3 at 995 cm^{-1} .

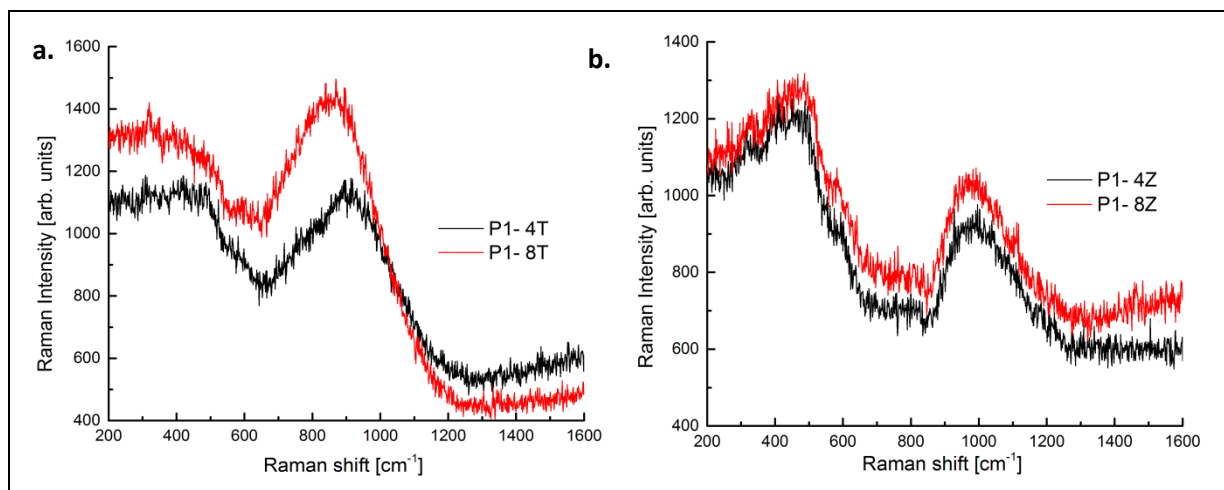


Figure 5.60: Raman spectra of TiO₂ and ZrO₂ containing glasses; (a) P1-4T, P1-8T, and (b) P1-4Z, P1-8Z.

Raman spectra of P5 glasses containing TiO₂ and ZrO₂ nucleating agents are shown in Fig. 5.61. Spectra of these glasses were broader and it was not possible to distinguish between Q⁴ and Q³ structural units. However, one can see differences in Raman peaks for TiO₂ and ZrO₂ containing glasses. Spectra of ZrO₂ containing glasses were identical with the Raman spectrum of the P5 glass system shown in Fig. 5.5e.

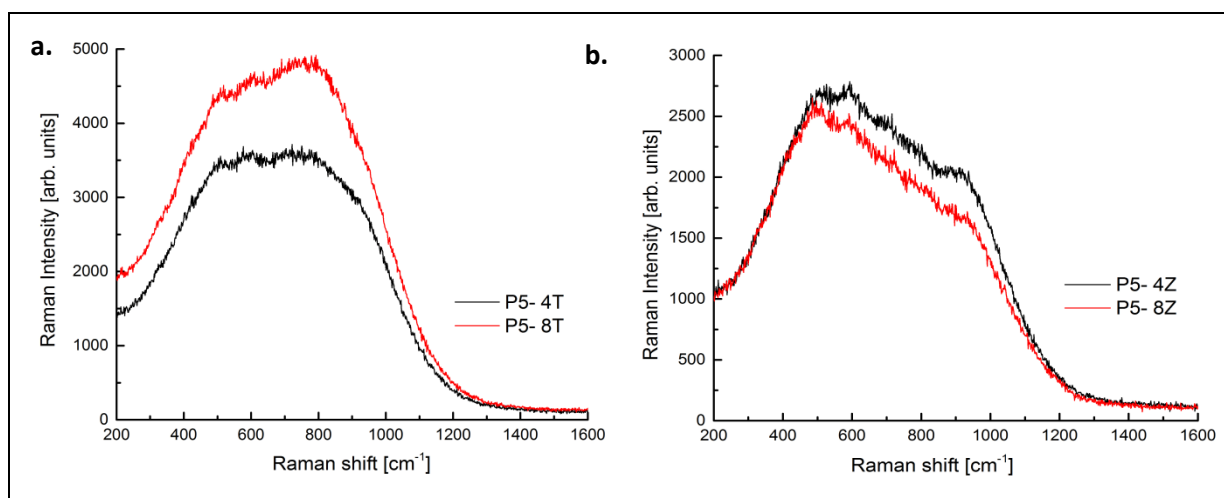


Figure 5.61: Raman spectra of TiO₂ and ZrO₂ containing glasses; (a) P5-4T, P5-8T, and (b) P5-4Z, P5-8Z.

5.7.2 Thermal analyses of glasses containing nucleating agents

Thermal analyses of P1 and P5 glasses containing nucleating agents were conducted to determine the effects of TiO₂ and ZrO₂ additions on their glass transition temperatures (T_g) and crystallization temperatures (T_c). Moreover, specific heats (C_p) and thermal diffusivities (α) of these nucleating agents containing glasses were determined.

5.7.2.1 Thermal analyses of nucleating agents (TiO_2 , ZrO_2) containing Y-aluminosilicate glasses

Transition temperatures of TiO_2 and ZrO_2 containing P1 glasses were determined using DSC with a heating rate of 15 K/min. The results of DSC analyses for these glasses are shown in Fig. 5.62 and summarized in Table 5.30. It was found that the addition of TiO_2 results in significantly decreased glass transition temperatures of P1 glass systems. P1 glasses containing ZrO_2 as nucleating agents (P1-4Z, P1-8Z) showed glass transition temperature at around 916 °C which is similar as found in P1 glass system. Moreover, crystallization temperatures in P1-4Z and P1-8Z glass systems also matched closely with the P1 glass system.

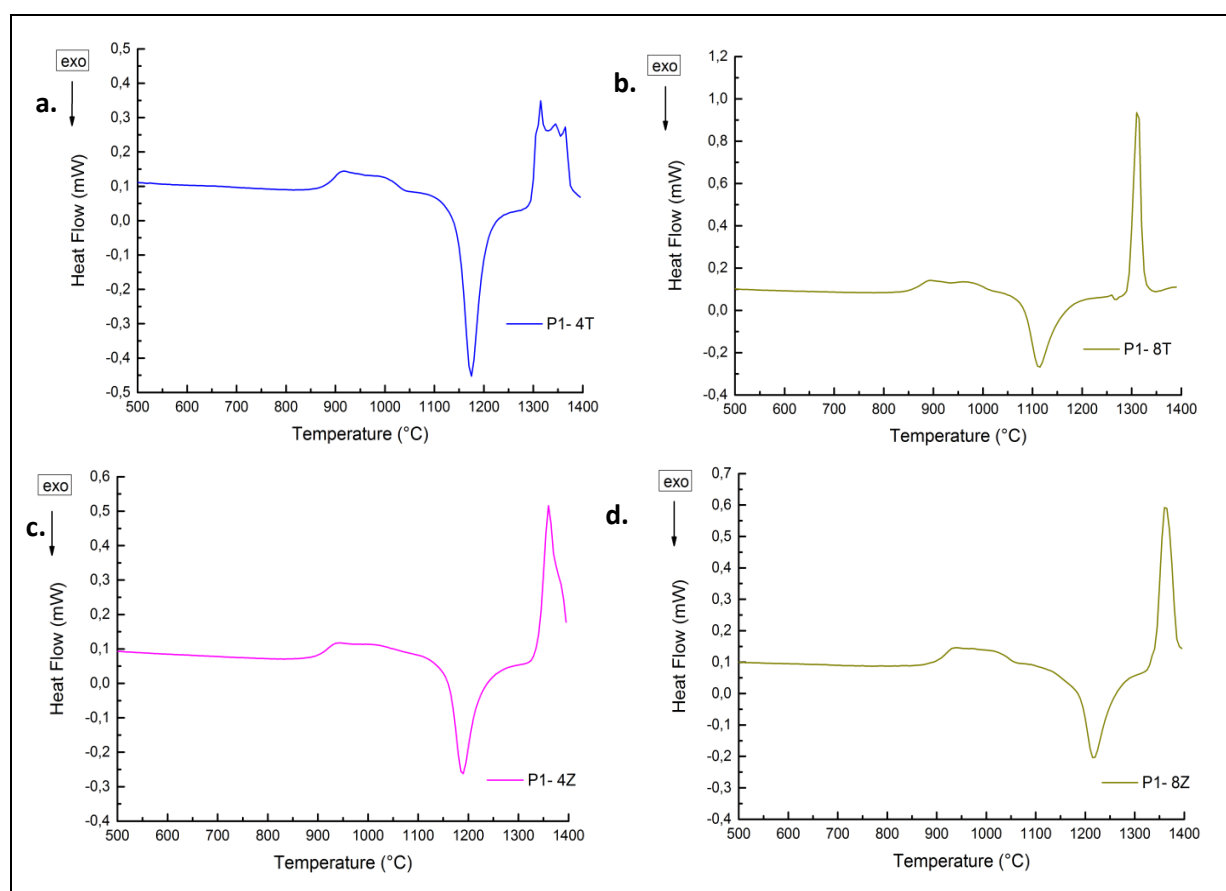


Figure 5.62: DSC analyses of TiO_2 and ZrO_2 containing glasses; (a) P1-4T, (b) P1-8T, (c) P1-4Z, and (d) P1-8Z.

Table 5.30: Transitions temperatures of TiO_2 containing P1 glasses.

Specimen	T _g (°C)	T _c (°C)	T _m (°C)
P1	917	1202	1389
P1- 4T	898	1174	1365
P1- 8T	852	1113	1349
P1- 4Z	916	1188	1385
P1- 8Z	916	1217	1382

5.7.2.2 Specific heats of TiO₂ and ZrO₂ containing Y-aluminosilicate glasses

Specific heat (C_p) values of TiO₂ and ZrO₂ containing P1 glasses were measured up to 800 °C and are summarized in Table 5.31.

Table 5.31: Specific heat capacities of TiO₂ and ZrO₂ containing P1 glasses.

T (°C)	P1 C _p (J/(g·K))	P1-4T C _p (J/(g·K))	P1-8T C _p (J/(g·K))	P1-4Z C _p (J/(g·K))	P1-8Z C _p (J/(g·K))
50	0.644	0.661	0.698	0.586	0.640
100	0.731	0.701	0.758	0.620	0.686
200	0.821	0.793	0.837	0.683	0.784
300	0.874	0.862	0.886	0.711	0.854
400	0.916	0.902	0.919	0.718	0.892
500	0.945	0.930	0.936	0.707	0.912
600	0.964	0.952	0.955	0.696	0.928
700	0.980	0.970	0.969	0.668	0.934
800	1.00	0.984	0.994	0.636	0.938

5.7.2.3 Thermal diffusivity of TiO₂ and ZrO₂ containing glasses

Thermal diffusivities of TiO₂ and ZrO₂ containing P1 glasses were measured up to 700 °C. These measured values are given in Table 5.32.

Table 5.32: Thermal diffusivities of TiO₂ and ZrO₂ containing P1 glasses.

T (°C)	P1 α (mm ² /s)	P1-4T α (mm ² /s)	P1-8T α (mm ² /s)	P1-4Z α (mm ² /s)	P1-8Z α (mm ² /s)
25	0.288	0.270	0.277	0.274	0.265
100	0.256	0.241	0.263	0.241	0.229
200	0.240	0.239	0.242	0.233	0.219
300	0.226	0.213	0.219	0.220	0.230
400	0.210	0.203	0.177	0.194	0.209
500	0.196	0.175	0.246	0.169	0.183
600	0.189	0.205	0.215	0.167	0.193
700	0.181	0.196	0.170	0.137	0.178

5.7.2.4 Thermal analyses of TiO₂ and ZrO₂ containing Nd-aluminosilicate glasses

DSC analyses of TiO₂ and ZrO₂ containing P5 glasses are shown in Fig. 5.63 and summarized in Table 5.33. It was found that additions of TiO₂ decreased glass transition temperatures and resulted in pronounced crystallization peaks. P5 glass samples without nucleating agents (TiO₂, ZrO₂) did not show crystallization peak as mentioned in Fig. 5.8e and Table 5.5. The addition of TiO₂ contents

enhanced surface crystallization. Moreover, addition of TiO_2 affects glass relaxation phenomenon and change glass transition temperature. The effects of ZrO_2 additions on transition temperatures were found less prominent. The addition of ZrO_2 contents enhanced the crystallization process in P5 glasses without changing glass transition temperatures significantly.

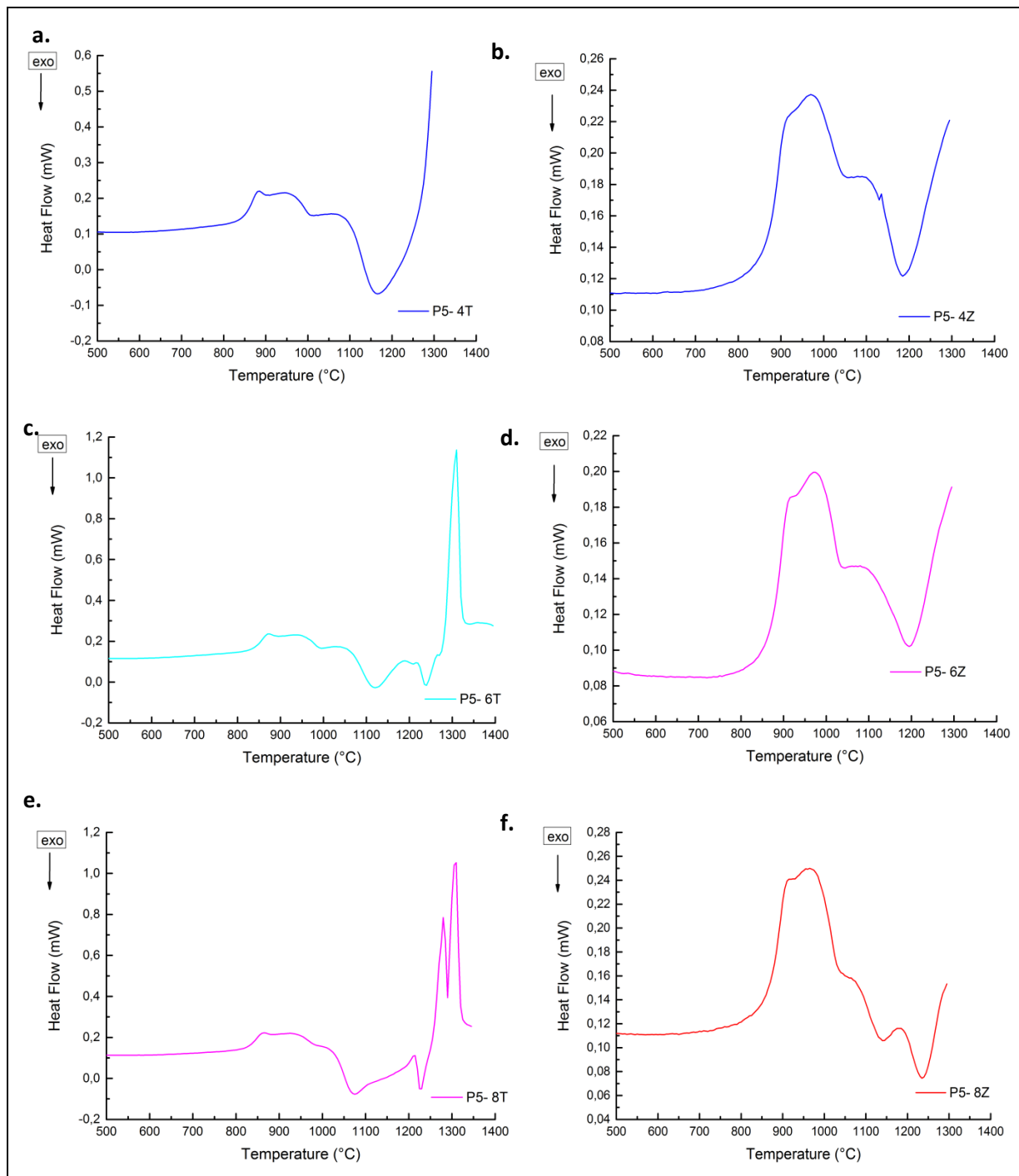


Figure 5.63: DSC analyses of TiO_2 and ZrO_2 containing glasses; (a) P5-4T, (b) P5-4Z, (c) P1-6T, (d) P5-6Z, (e) P5-8T, and (f) P5-8Z.

Table 5.33: DSC analyses for glass transition temperature of TiO₂ and ZrO₂ containing P5 glasses.

Specimen	T _g (°C)	T _{c1} (°C)	T _{c2} (°C)	T _m (°C)	T _m (°C)
P5	887	--	--	--	--
P5- 4T	870	1165	--	--	--
P5- 6T	862	1120	1238	1309	--
P5- 8T	854	1073	1227	1282	1308
P5- 4Z	885	1195	--	--	--
P5- 6Z	885	1210	--	--	--
P5- 8Z	886	1238	--	--	--

5.7.2.5 Specific heats of TiO₂ and ZrO₂ containing Nd-aluminosilicate glasses

Specific heat values of TiO₂ and ZrO₂ containing P5 glasses were measured up to 800 °C and are summarized in Table 5.34. It was found that Cp values of nucleating agents containing P5 glasses were higher as compared to the P5 glass system for the same temperature range.

Table 5.34: Specific heat capacities of TiO₂ and ZrO₂ containing P5 glasses.

T (°C)	P5 Cp (J/(g·K))	P5-4T Cp (J/(g·K))	P5-8T Cp (J/(g·K))	P5-4Z Cp (J/(g·K))	P5-8Z Cp (J/(g·K))
50	0.542	0.668	0.621	0.606	0.611
100	0.554	0.706	0.661	0.650	0.657
200	0.587	0.735	0.714	0.727	0.732
300	0.617	0.775	0.758	0.781	0.785
400	0.628	0.812	0.793	0.812	0.818
500	0.625	0.851	0.826	0.835	0.840
600	0.619	0.875	0.846	0.849	0.859
700	0.603	0.916	0.879	0.852	0.877
800	0.578	0.948	0.916	0.857	0.890

5.7.2.6 Thermal diffusivity of TiO₂ and ZrO₂ containing glasses

Thermal diffusivity of TiO₂ and ZrO₂ containing P5 glasses measured up to 700 °C are summarized in Table 5.35. A decrease in values of thermal diffusivities with increasing temperature was observed for these glass systems.

Table 5.35: Thermal diffusivity of TiO₂ and ZrO₂ containing P5 glasses.

T (°C)	P5 α (mm ² /s)	P5-4T α (mm ² /s)	P5-8T α (mm ² /s)	P5-4Z α (mm ² /s)	P5-8Z α (mm ² /s)
25	0.288	0.248	0.247	0.236	0.238
100	0.256	0.214	0.206	0.206	0.210
200	0.240	0.195	0.192	0.194	0.183
300	0.226	0.203	0.183	0.206	0.200
400	0.210	0.170	0.174	0.169	0.184
500	0.196	0.165	0.164	0.162	0.168
600	0.189	0.144	0.153	0.177	0.161
700	0.181	0.168	0.145	0.156	0.163

5.7.3 Crystallization of nucleating agents containing Yttrium- aluminosilicate glasses

Crystallization studies of TiO₂ and ZrO₂ containing P1 glasses were conducted to evaluate their microstructures. Tablets of P1-4T, P1-8T, P1-4Z and P1-8Z glass powders having 8 mm diameter and 5 mm thickness were prepared using uniaxial pressing with 50 kN force. These compacted glass samples were annealed at a heating rate 15 K/min up to 1200 °C for 50h holding time in closed chamber furnace. Structural analyses of these heat-treated samples were done via XRD, SEM, IR and Raman spectroscopy.

5.7.3.1 *In-situ XRD of nucleating agents (TiO₂, ZrO₂) containing Y- aluminosilicate glasses*

Hot-stage XRD studies of P1 glass powders containing TiO₂ and ZrO₂ (P1-4T, P1-8T, P1-4Z and P1-8Z) were carried out up to 1200 °C to evaluate crystals growth behaviour and phase formation in these glasses. The first scan was recorded at 25 °C, the second at 700 °C, the third at 800 °C, the fourth at 850 °C and holding at each temperature for 30 minutes; then scans were taken after every 50 °C steps up to 1200 °C with 30 minute holding time at each scan. The diffraction patterns recorded for these glass powders at different temperatures are shown in Fig. 5.64.

Hot-stage XRD analyses of P1-4T and P1-8T glasses showed complete amorphous structures up to 900 °C without any reflection peaks. At 1050 °C, first reflections were noticed in P1-4T but their intensities were very weak. The peaks of mullite (JCPDS card # 15-776), cristobalite (JCPDS card # 46-1045), yttrium-titanium oxide (JCPDS card # 39-52) and Y-disilicate (JCPDS card # 22-1103) were prominent at 1050 °C in the P1-8T sample. These phases were observed in the P1-4T sample after 1100 °C, and the intensities of these crystalline phases remained almost the same after 1150 °C. Hence, crystallization process started almost 50 °C earlier in P1-8T as compared to P1-4T sample. The maximum crystallization in these samples took place between 1100–1200 °C. In-situ XRD diffractions of P1-4T and P1-8T at 1200 °C for 30 min holding are shown in Fig. 5.65a, b. One can notice main reflections observed were mullite, yttrium-titanium oxide and Y-disilicate.

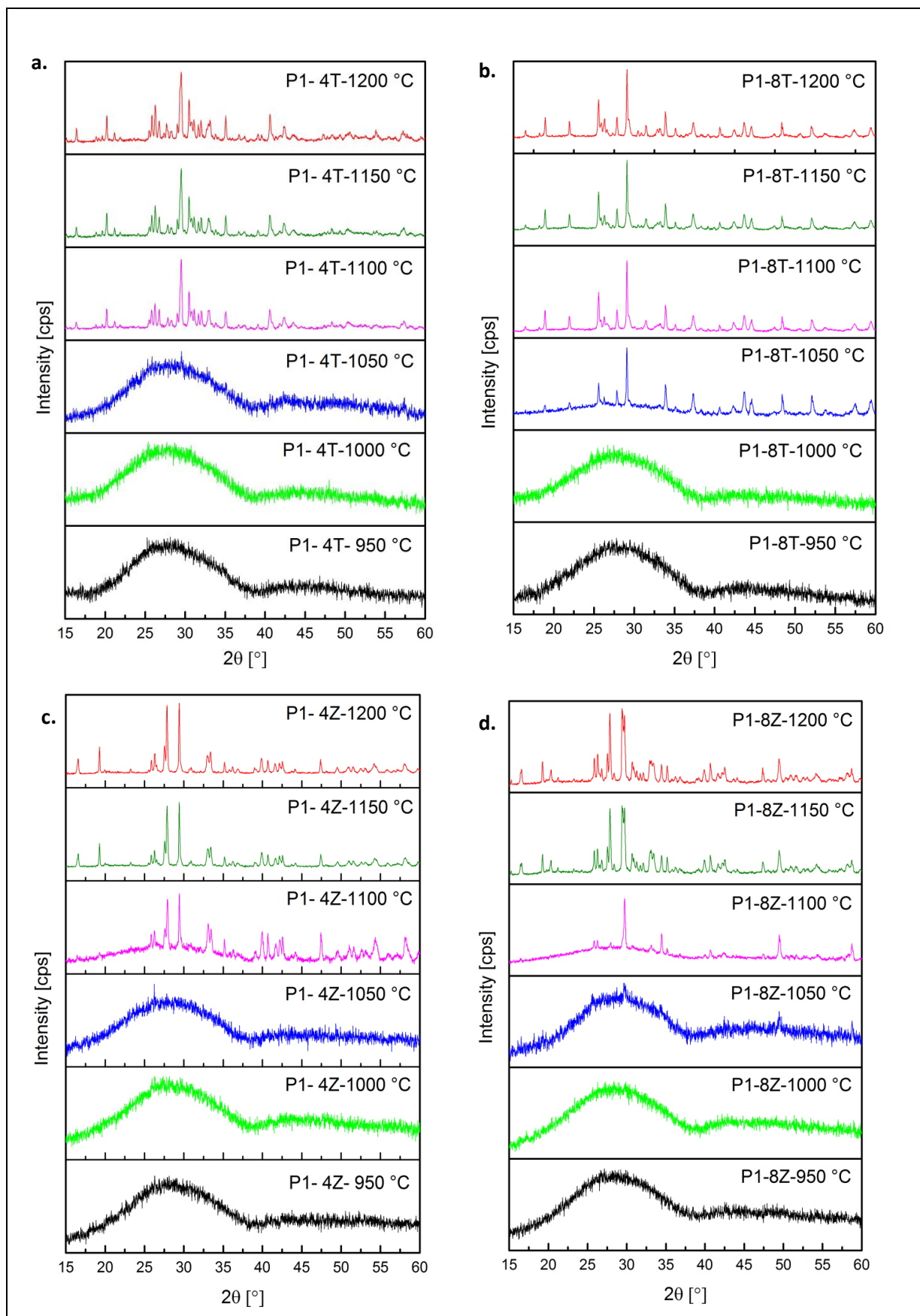


Figure 5.64: In-situ XRD of glasses; (a) P1-4T, (b) P1-8T, (c) P1-4Z, and (d) P1-8Z.

Peaks of mullite (JCPDS card # 15-776), Y-disilicate (JCPDS card # 22-1103) and yttrium-zirconium oxide (JCPDS card # 30-1468) were recorded in P1-4Z and P1-8Z samples at 1100 °C. The intensities of these crystalline phases remained the same after 1150 °C, that showed maximum crystallization in these samples took place between 1150–1200 °C. However, an additional peak of cristobalite (JCPDS card # 46-1045) and higher intensities of yttrium-zirconium oxide were noticed in the P1-8Z sample. These observations showed that yttrium react with ZrO_2 to form yttrium-zirconium oxide. In-situ XRD diffractions of P1-4Z and P1-8Z at 1200 °C for 30 min holding are shown in Fig. 5.65c, d. One can notice main reflections observed were mullite, yttrium-zirconium oxide and Y-disilicate.

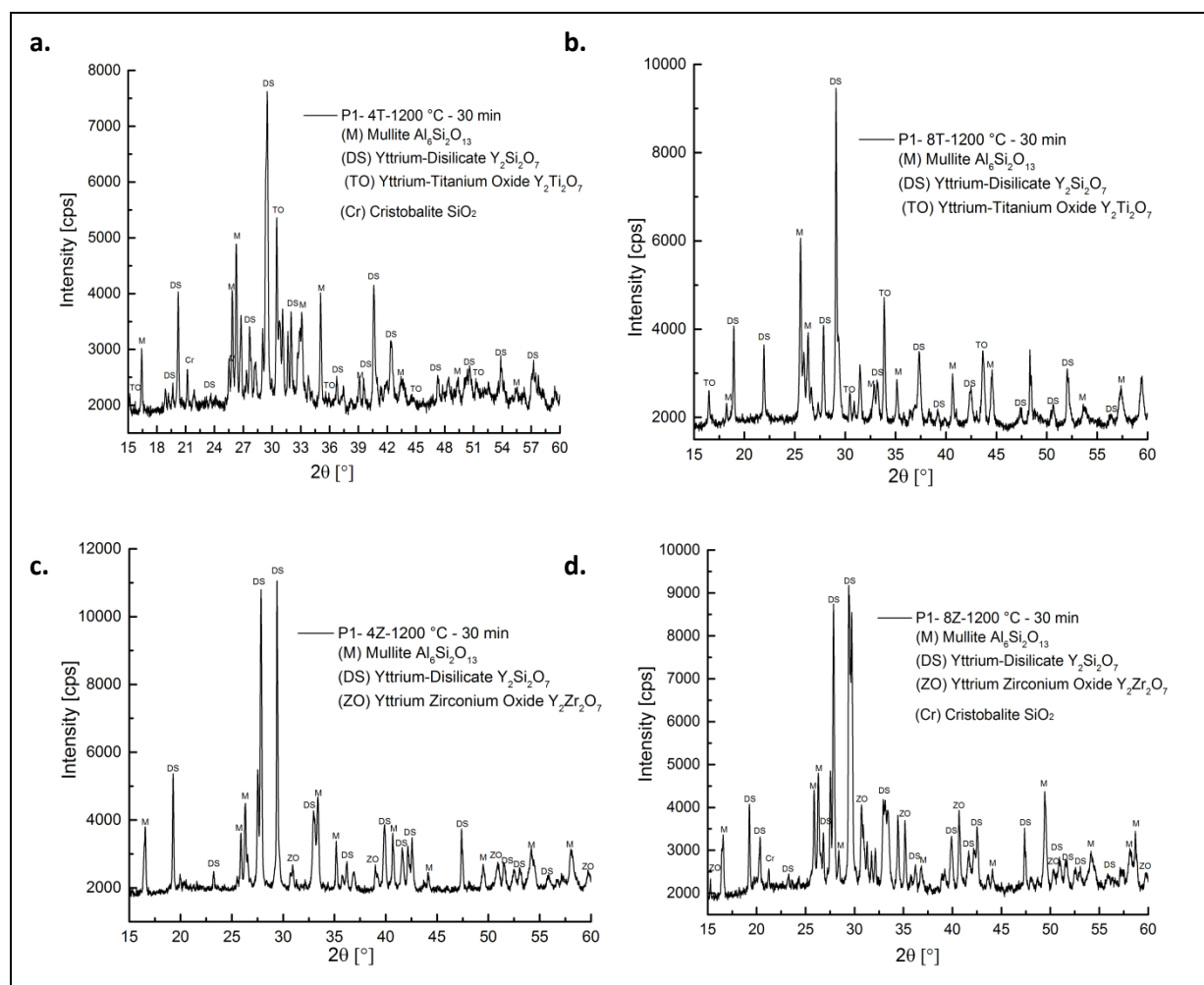


Figure 5.65: In-situ XRD of glasses at 1200 °C for 30 min holding; (a) P1-4T, (b) P1-8T, (c) P1-4Z, and (d) P1-8Z.

5.7.3.2 XRD analyses of TiO_2 and ZrO_2 containing Y- aluminosilicate samples

Compacted powder samples of P1-4T, P1-8T, P1-4Z and P1-8Z glasses were annealed at 1200 °C for 50h holding time in a chamber furnace to reveal possible phases under long heat-treatment conditions. XRD of these samples are shown in Fig. 5.66, P1-4T-1200°C-50h sample shows reflections of mullite (JCPDS card # 15-776), Y-disilicate (JCPDS card # 22-1103) cristobalite (JCPDS card # 46-1045) and yttrium-titanium oxide (JCPDS card # 39-52). The intensities of yttrium-

titanium oxide were more prominent in the P1–8T–1200°C–50h sample as compared to the P1–4T–1200°C–50h. XRD pattern of the P1–4Z–1200°C–50h sample contain reflections of mullite (JCPDS card # 15-776), Y-disilicate (JCPDS card # 22-1103), cristobalite (JCPDS card # 46-1045) and yttrium-zirconium oxide (weak). The intensities of yttrium-zirconium oxide (JCPDS card # 30-1468) were relatively more prominent in the P1–8Z–1200°C–50h sample.

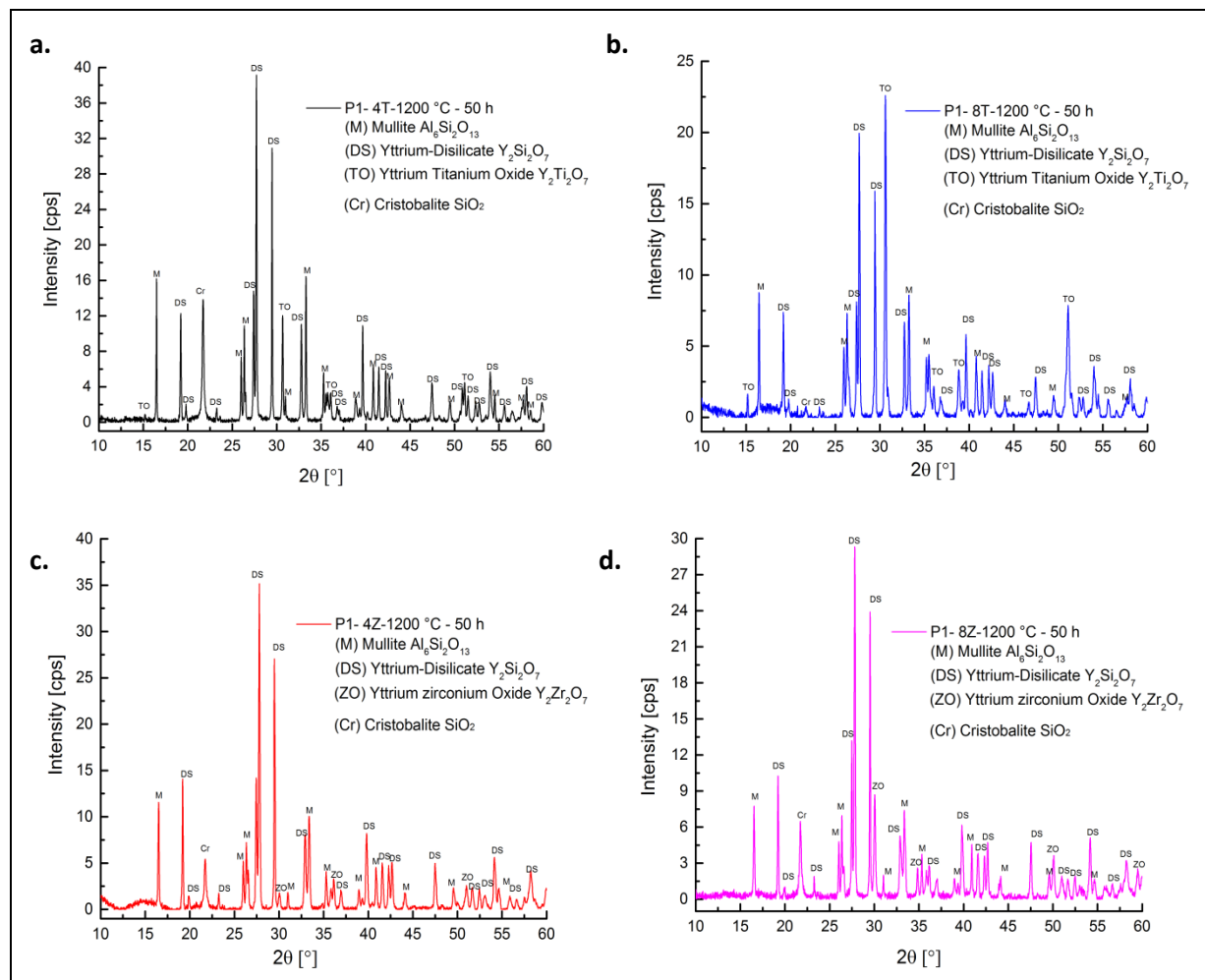


Figure 5.66: XRD of TiO_2 and ZrO_2 containing samples heat-treated at 1200 °C for 50 h; (a) P1–4T, (b) P1–8T, (c) P1–4Z, and (d) P1–8Z.

5.7.3.3 SEM analyses of TiO_2 and ZrO_2 containing Y-aluminosilicate samples

SEM images of P1–4T and P1–8Z glasses annealed at 1200 °C for 50h holding time are given in Fig. 5.67. The P1–4T–1200°C–50h sample contains embedded Y-disilicate crystals in remaining glassy matrix surrounded by mullite crystals at grain boundaries. The feathers like crystals of Y-disilicate were in excess at edges in the P1–8Z–1200°C–50h sample as compared to the centre of the sample. Moreover, bigger islands of zirconium rich phase were found in the P1–8Z–1200°C–50h.

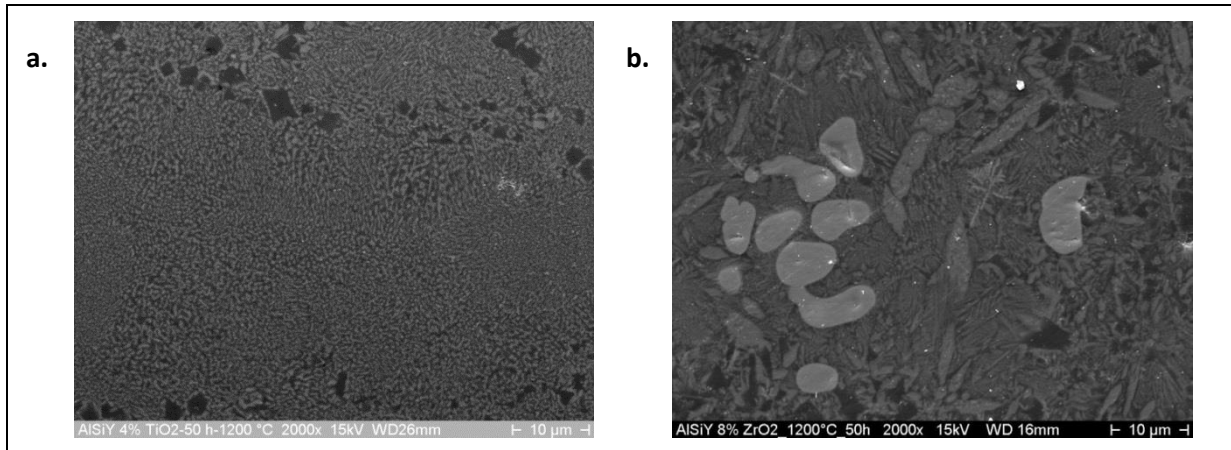


Figure 5.67: SEM at mag. 2000x of samples annealed at 1200 °C for 50 h; (a) P1-4T, (b) P1-8Z.

5.7.3.4 IR analysis of TiO_2 and ZrO_2 containing Y-aluminosilicate samples

IR spectra of P1-4T, P1-8T, P1-4Z and P1-8Z samples heat-treated at 1200 °C for 50h holding time are shown in Fig. 5.68. The stretching modes observed in spectra of P1-4T-1200°C-50h and P1-8T-1200°C-50h samples were at different wave numbers. The spectrum of P1-4T-1200°C-50h sample showed (O-Si-O) bending mode at 547 cm^{-1} , symmetric stretching of Si-O-Si at wave numbers ~742, ~786, ~835 cm^{-1} and strong Si-O-Si asymmetric stretching at ~1070 cm^{-1} , respectively.

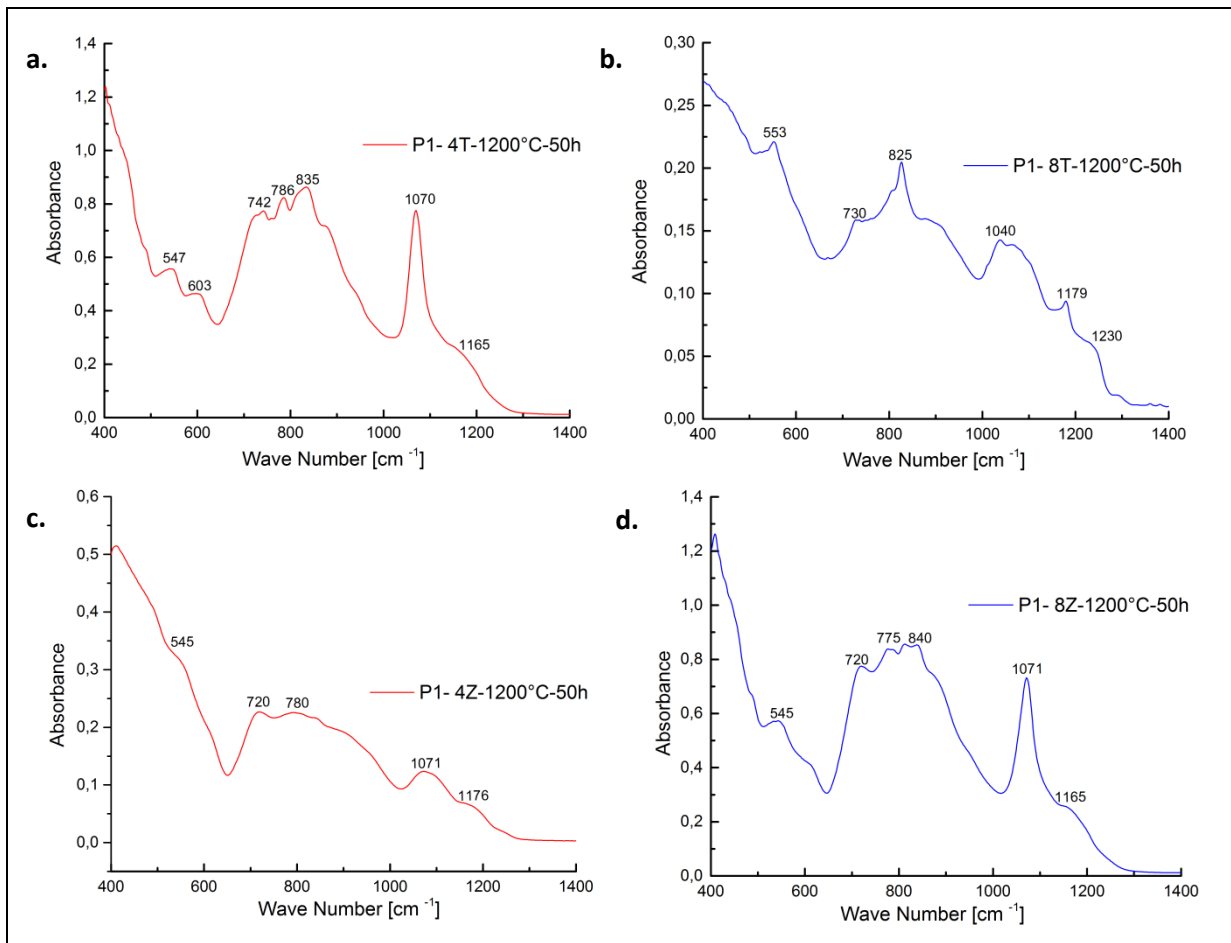


Figure 5.68: IR spectra of samples; (a) P1-4T-1200°C-50h, (b) P1-8T-1200°C-50h, (c) P1-4Z-1200°C-50h, and (d) P1-8Z-1200°C-50h.

The spectrum of P1-8T-1200°C-50h sample contained bending mode ($\sim 553 \text{ cm}^{-1}$), symmetric stretching (825 cm^{-1}) and asymmetric stretching (1040 cm^{-1}) with different wave numbers as compared to P1-4T-1200°C-50h sample. In contrast, IR spectrum of the P1-8Z-1200°C-50h sample was almost identical with the spectrum of P1-1200°C-50h as shown in Fig. 5.19. The spectrum of P1-8Z-1200°C-50h sample consists of a higher peak of Si-O-Si asymmetric stretching at $\sim 1071 \text{ cm}^{-1}$, which was not so pronounced in the P1-4Z-1200°C-50h sample. Moreover, the spectrum of the P1-8Z-1200°C-50h sample consists of bending mode at 545 cm^{-1} and symmetric stretching at $720, 775$ and 840 cm^{-1} respectively.

5.7.3.5 Raman analyses of TiO_2 and ZrO_2 containing Y-aluminosilicate samples

Raman spectra of P1-4T-1200°C-50h, P1-8T-1200°C-50h, P1-4Z-1200°C-50h and P1-8Z-1200°C-50h samples are shown in Fig. 5.69. The P1-4T-1200°C-50h sample showed high structural unit of Q^4 , with relatively strong bending mode of Si-O-Si at around 520 cm^{-1} , Si-O-M stretching modes in Q^3 at 917 and 951 cm^{-1} , respectively.

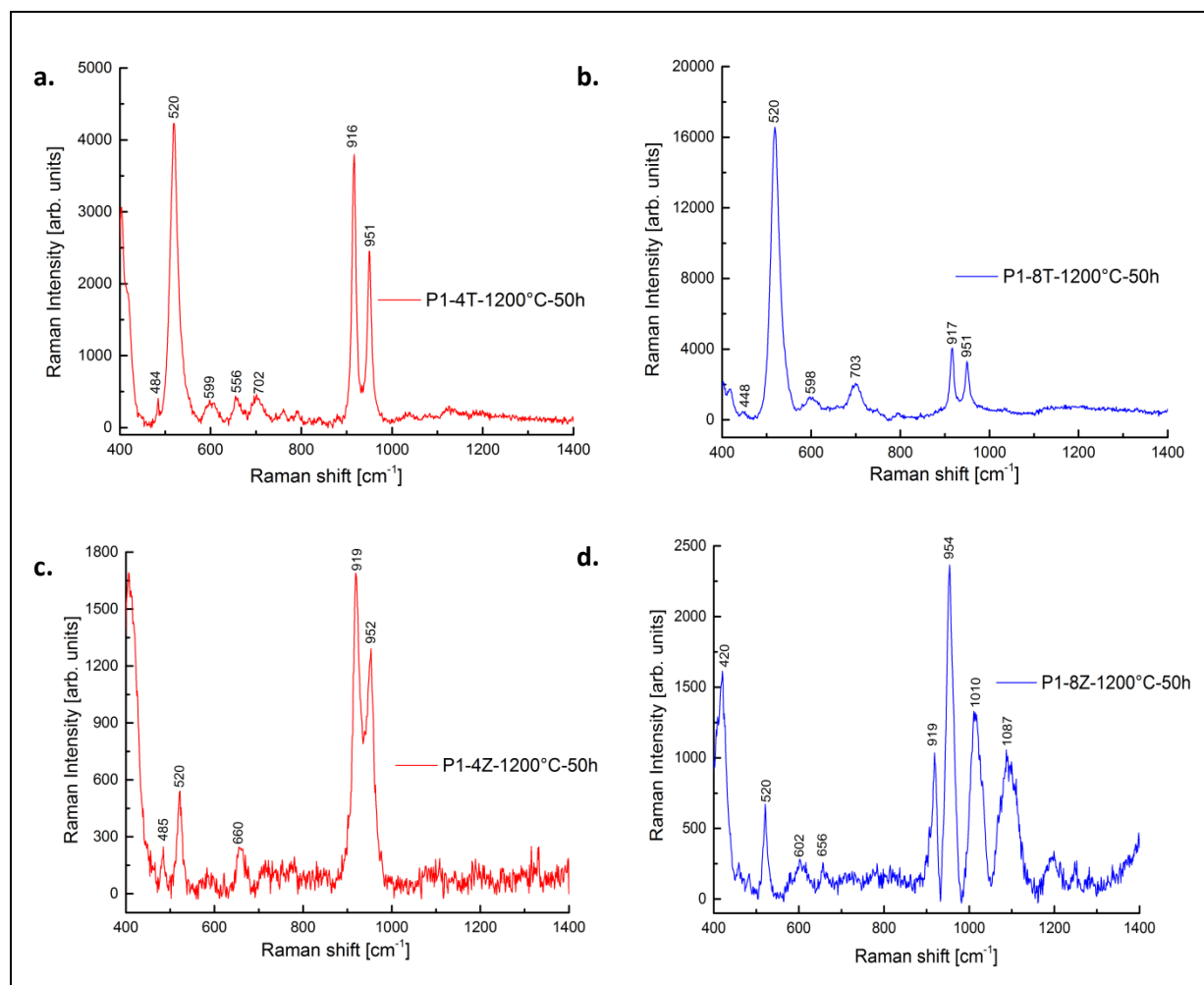


Figure 5.69: Raman spectra of samples; (a) P1-4T-1200°C-50h, (b) P1-8T-1200°C-50h, (c) P1-4Z-1200°C-50h, and (d) P1-8Z-1200°C-50h.

Peak intensities of the Si-O-M stretching mode (Q^3) are higher in the P1-4T-1200°C-50h sample as compared to P1-8T-1200°C-50h. The Raman spectrum of the P1-4Z-1200°C-50h sample consisted of bending mode of Si-O-Si at around 520 cm^{-1} , Si-O-M stretching mode in Q^3 at 919 and 952 cm^{-1} , respectively. The spectrum of P1-8Z-1200°C-50h sample showed bending mode of Si-O-Si at around 520 cm^{-1} , Si-O-M stretching mode in Q^3 at 919, 954 cm^{-1} , and stretching in Q^2 at 1010 and 1087 cm^{-1} , respectively.

5.7.4 Crystallization of nucleating agents containing Neodymium-aluminosilicate glasses

Crystallization studies of P5-4T, P5-8T, P5-4Z and P5-8Z glasses were conducted after annealing with 15 K/min heating rate at 1200 °C for 50h holding time in chamber furnace. Then samples were structurally investigated using XRD, SEM, IR and Raman spectroscopic techniques.

5.7.4.1 *In-situ XRD of nucleating agents (TiO_2 , ZrO_2) containing Nd-aluminosilicate glasses*

Hot-stage XRD of P5-4T, P5-8T, P5-4Z and P5-8Z samples were conducted up to 1200 °C with heating rate of 10 K/min. The same scan scheme as discussed above in section 5.7.3.1 was used for recorded diffraction patterns. The diffraction patterns taken at different temperatures for these glass powders are shown in Fig. 5.70. A complete amorphous structure was recorded for P5-4T glass up to 1000 °C without any reflections. The crystallization process started after 1000 °C and reflections of mullite and unknown phases were found at 1050 °C. The intensities of these crystalline phases remained almost the same after 1100 °C. It suggests that maximum crystallization process in this glass system was completed at around 1100 °C. The crystallization process in the P5-8T glass started at least 50 °C earlier as compared to the P5-4T sample. It showed that increasing amount of TiO_2 reduced the crystallization temperatures in the P5 glass system. This observation fits well with DSC findings as given in Table 5.33. Moreover, diffractions of unknown phases and their intensities recorded in the P5-8T were different as compared to the P5-4T sample. This revealed that additions of titania resulted in the formation of multiple phases in the P5 glass system. In-situ XRD diffractions of P5-4T and P5-8T at 1200 °C for 30 min holding are shown in Fig. 5.71 (a, b), which revealed reflections of mullite and unknown phase (X). This unknown phase cannot be correlated with available diffraction data set.

XRD of P5-4Z and P5-8Z samples showed complete amorphous structures up to 1000 °C without any reflection. Peaks of mullite and unknown phases were recorded for the P5-4Z sample at around 1100 °C and for the P5-8Z sample at around 1050 °C. It was not possible to correlate these unknown reflections with available diffraction data set. It was noticed that addition of zirconia has pronounced effects on crystallization temperatures. Moreover, diffractions of formed phases were different in both ZrO_2 containing phases. Hence, addition of ZrO_2 also resulted in the formation of multiple phases with P5 glasses. Moreover, diffractions of formed phases were different in both ZrO_2 containing phases. In-situ XRD diffractions of P5-4Z and P5-8Z at 1200 °C for 30 min holding are shown in Fig. 5.71 (c, d), which revealed reflections of mullite, Nd-disilicate and unknown phase (X).

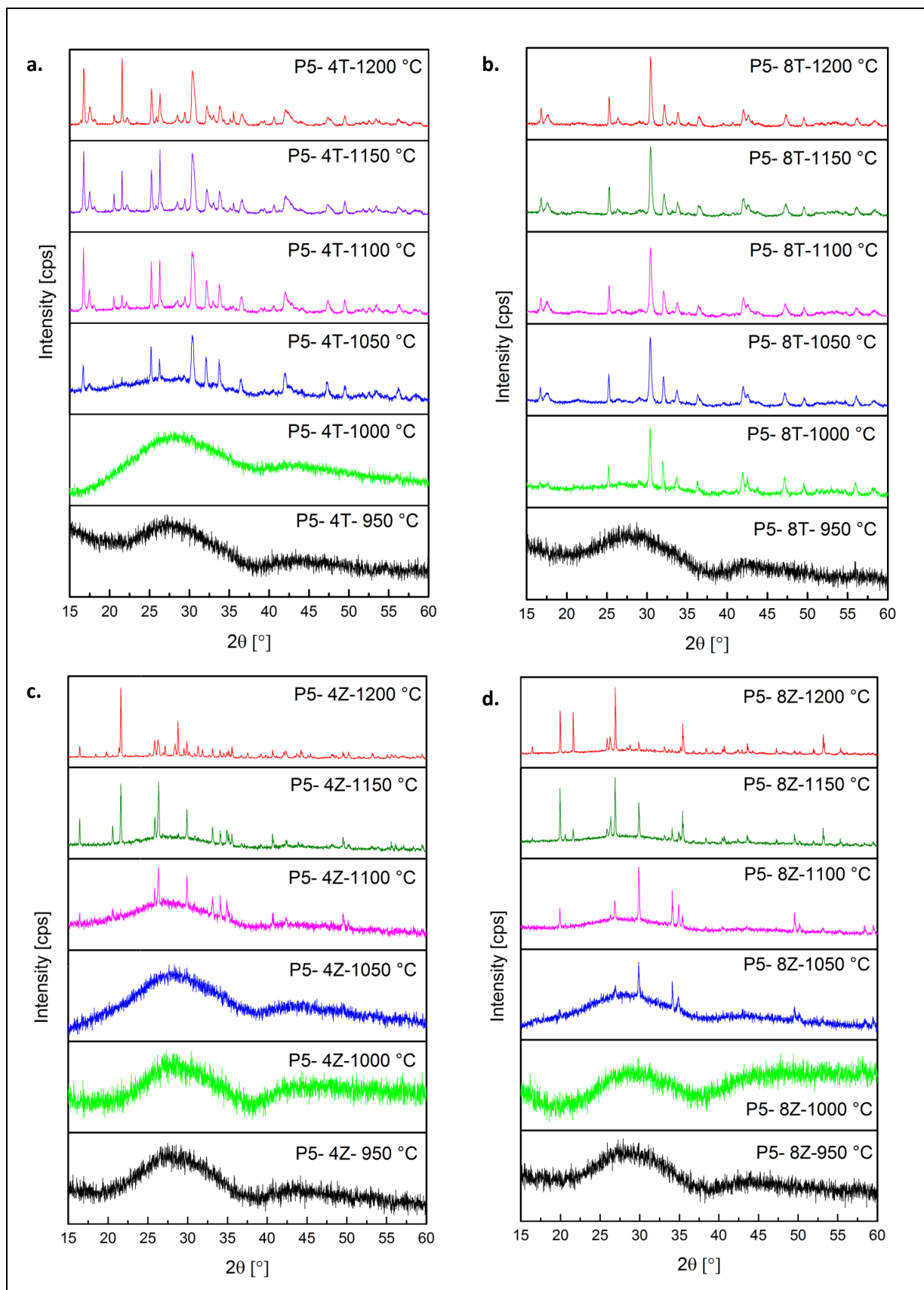


Figure 5.70: In-situ XRD of glasses; (a) P5-4T, (b) P5-8T, (c) P5-4Z, and (d) P5-8Z.

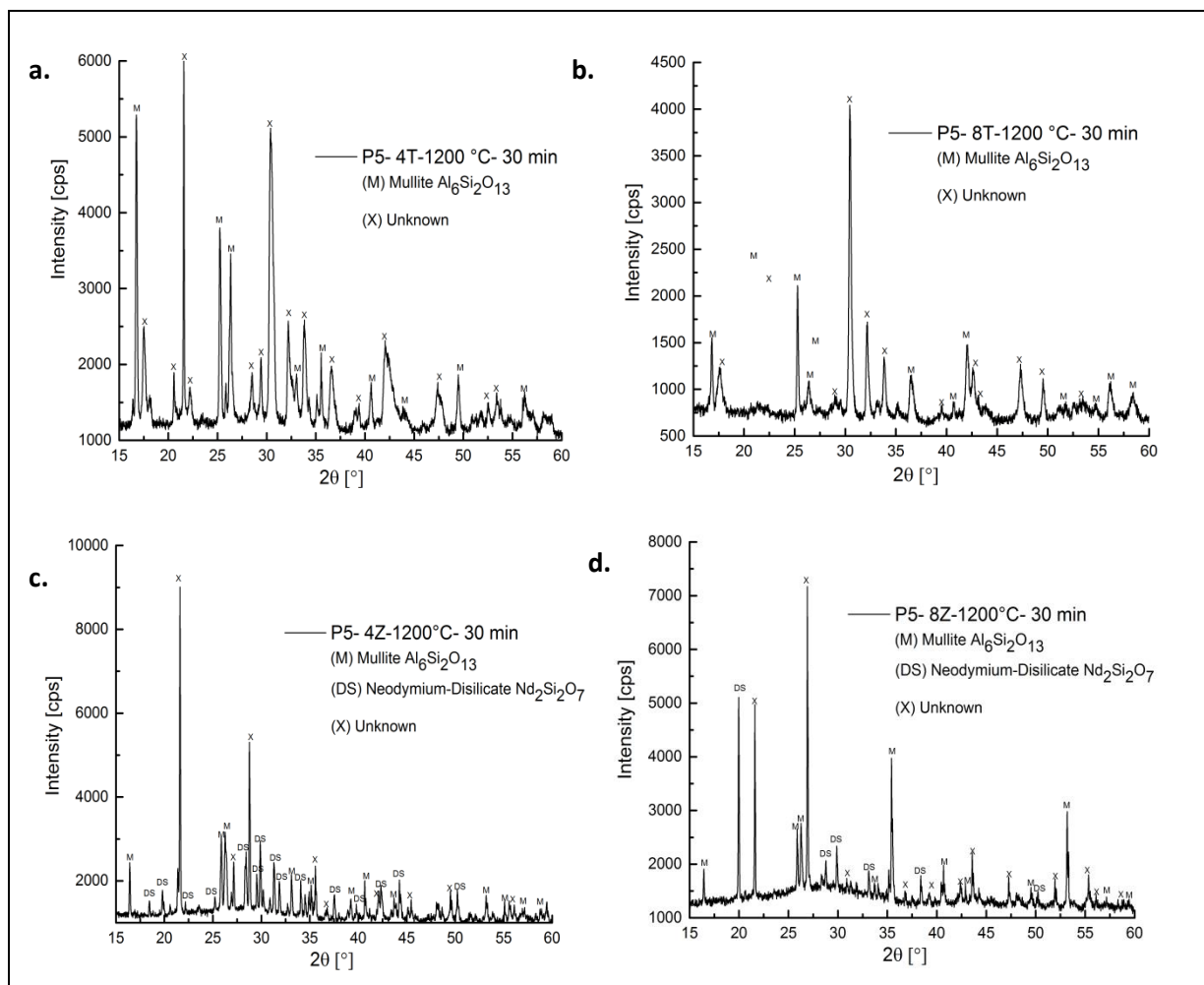


Figure 5.71: In-situ XRD of glasses at 1200 °C for 30 min holding; (a) P5-4T, (b) P5-8T, (c) P5-4Z, and (d) P5-8Z.

5.7.4.2 XRD analyses of TiO_2 and ZrO_2 containing Nd-aluminosilicate samples

XRD patterns of P5-4T-1200°C-50h, P5-8T-1200°C-50h, P5-4Z-1200°C-50h and P5-8Z-1200°C-50h samples are shown in Fig. 5.72. XRD of the P5-4T-1200°C-50h sample contained reflections of mullite (JCPDS card # 15-776) and unknown phases which could not be correlated with available diffraction data sets. X-ray diffractions of the P5-8T-1200°C-50h sample showed reflections of mullite and unknown phases. Here again it was not possible to correlate these unknown phases with known diffraction sets. However, these diffractions were different as compared to peaks found in the P5-4T-1200°C-50h. XRD pattern of the P5-4Z-1200°C-50h sample contained reflections of mullite (JCPDS card # 15-776), Nd-disilicate (JCPDS card # 22-1177) and unknown phases. The intensities of these unknown phases were more prominent in the P5-8Z-1200°C-50h sample.

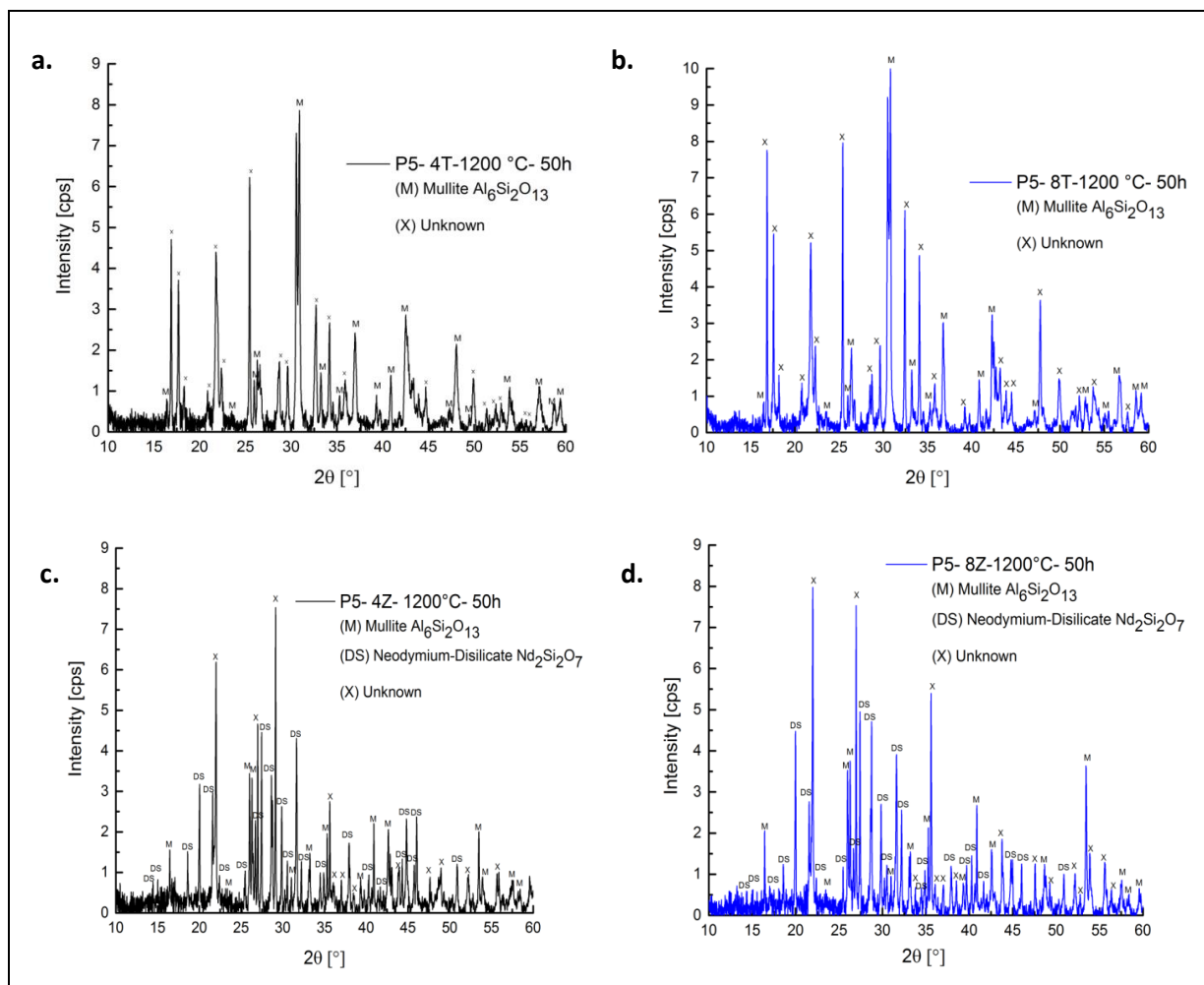


Figure 5.72: XRD of glasses heat-treated at 1200 °C for 50h; (a) P5–4T, (b) P5–8T, (c) P5–4Z, and (d) P5–8Z.

5.7.4.3 SEM analyses of TiO_2 and ZrO_2 containing Nd-aluminosilicate samples

SEM analyses of P5–4T–1200°C–50h, P5–8T–1200°C–50h, P5–4Z–1200°C–50h and P5–8Z–1200°C–50h samples are shown in Fig. 5.73. The SEM image of the P5–4T–1200°C–50h sample showed uniform distribution of titanium-rich-neodymium disilicate crystals in the remaining glassy matrix. The distribution of this titanium-rich phase was found even more homogenous and uniform in the P5–8T–1200°C–50h sample. It was not possible to determine the composition of these titanium-rich crystals due to their small sizes. It was found that edges of P5–4Z–1200°C–50h sample were extensively crystallized as compared to the centre region. The crystals were extended from the surface towards the centre of the samples. However, it was not possible to identify these crystals except mullite. These unknown crystals were rich in ZrO_2 and Nd-disilicate. Moreover, it was noticed that long heat-treatment introduced round pores in these samples.

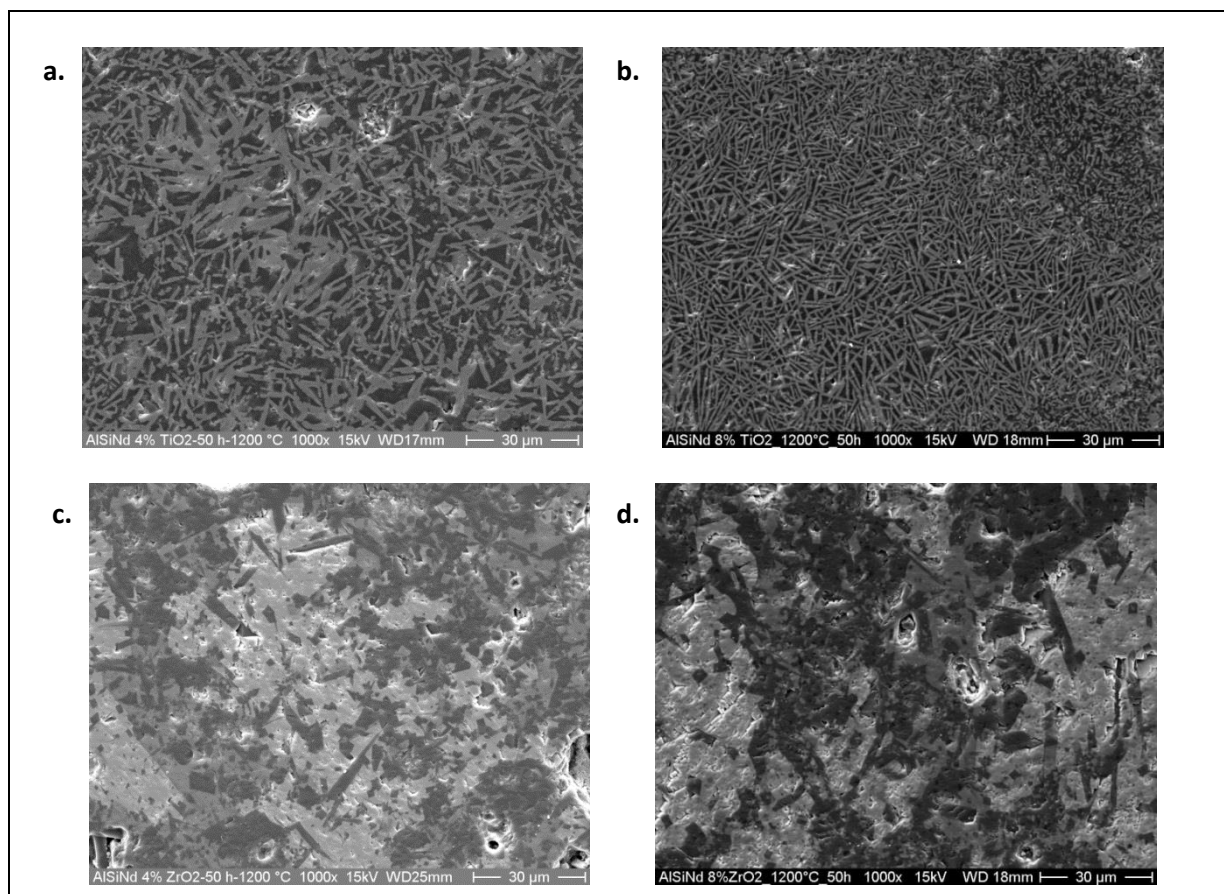


Figure 5.73: SEM images at mag. 1000x of samples annealed at 1200 °C for 50h; (a) P5-4T, (b) P5-8T, (c) P5-4Z, and (d) P5-8Z.

5.7.4.4 IR analysis of TiO_2 and ZrO_2 containing Nd-aluminosilicate samples

IR spectra of P5-4T, P5-8T, P5-4Z and P5-8Z glasses heat-treated at 1200 °C for 50h holding time are shown in Fig. 5.74. The spectrum of P5-4T-1200°C-50h sample showed (O-Si-O) bending mode at 537 cm^{-1} , symmetric stretching of Si-O-Si at wave numbers ~ 687 , ~ 788 , ~ 853 , $\sim 918\text{ cm}^{-1}$ and strong Si-O-Si asymmetric stretching at $\sim 1060\text{ cm}^{-1}$, respectively. The spectrum of P5-8T-1200°C-50h sample was more scattered having peaks and shoulders. It contained bending mode at 562 cm^{-1} , symmetric stretching modes (683 , 739 , 787 , 845 , 910 cm^{-1}), and asymmetric stretching (1049 , 1105 cm^{-1}) with different wave numbers as compared to the P5-4T-1200°C-50h sample.

The IR spectrum of the P5-4Z-1200°C-50h sample was similar to the spectrum of P5-4T-1200°C-50h with bending mode (517 , 536 cm^{-1}), symmetric stretching (615 , 680 , 698 , 787 , 828 , and 869 cm^{-1}), and asymmetric stretching (945 , 998 cm^{-1}). The IR spectrum of P5-8Z-1200°C-50h consists of higher peaks of Si-O-Si symmetric stretching with different shoulders at ~ 785 , ~ 825 , $\sim 867\text{ cm}^{-1}$, respectively and small peaks of asymmetric stretching at 942 , 972 , 1008 and 1038 cm^{-1} respectively, wave numbers.

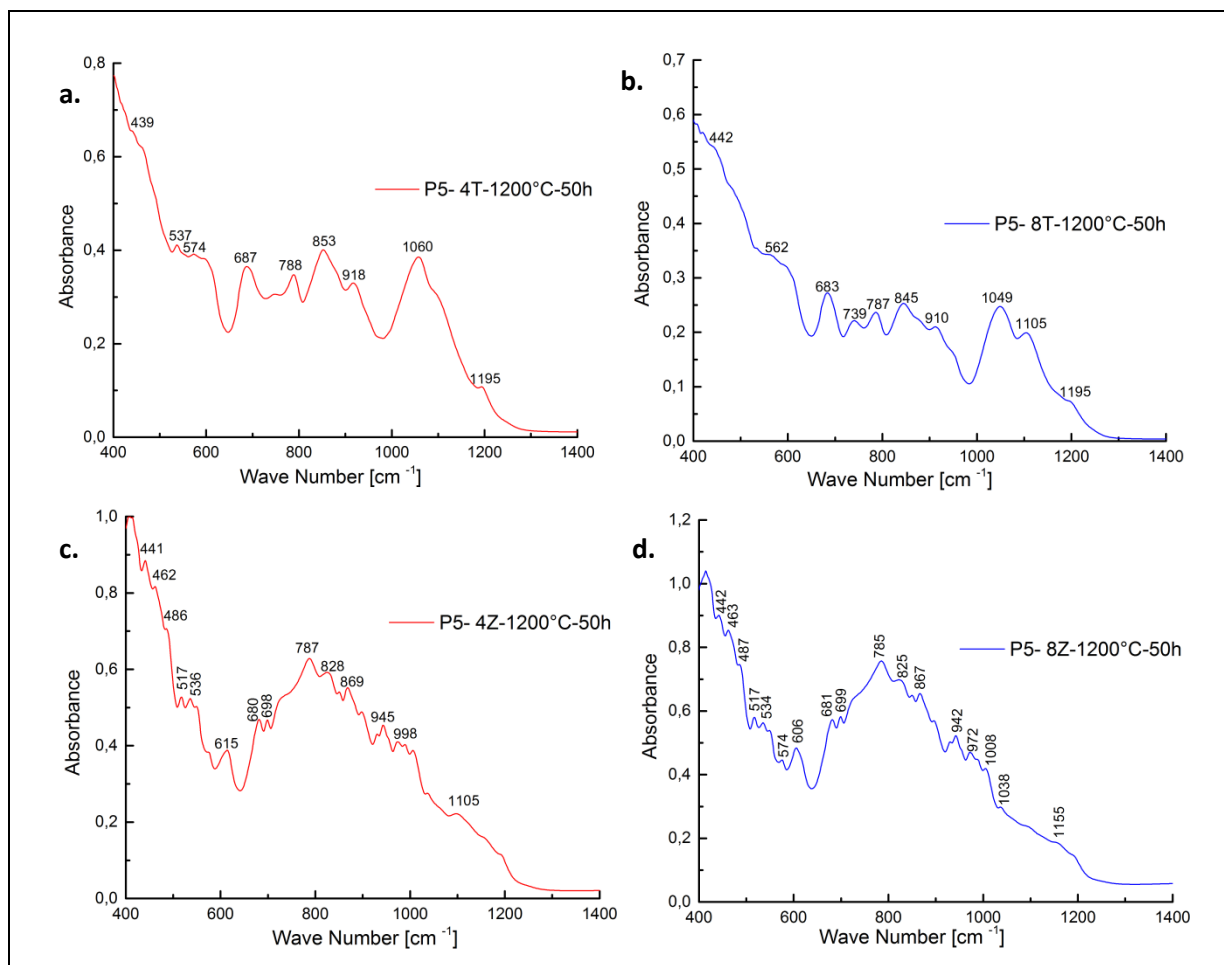


Figure 5.74: IR spectra of P5 glasses heat-treated at 1200 °C for 50h; (a) P5–4T, (b) P5–8T, (c) P5–4Z, and (d) P5–8Z.

5.7.4.5 Raman analyses of TiO_2 and ZrO_2 containing Nd-aluminosilicate samples

Raman spectra of samples P5–4T–1200°C–50h, P5–8T–1200°C–50h, P5–4Z–1200°C–50h and P5–8Z–1200°C–50h, respectively, are shown in Fig. 5.75. The Raman spectrum of P5–4T–1200°C–50h consists of structuring unit of Q^4 with relatively strong bending mode of Si-O-Si at around 479 cm^{-1} , and high Si-O-M stretching mode in Q^3 at 875 and 940 cm^{-1} , respectively. Raman peaks in the P5–8T–1200°C–50h sample were more scattered having intensities of Si-O-M stretching mode (Q^3) at 870 and 932 cm^{-1} , respectively.

Raman spectra of P5–4Z–1200°C–50h and P1–8Z–1200°C–50h samples were almost identical with bending mode of Si-O-Si at around 449 cm^{-1} , Si-O-M stretching in Q^3 at around 934 and 1006 cm^{-1} , respectively. The intensity of Si-O-M stretching in Q^3 at around 934 in the P5–4Z–1200°C–50h was relatively higher as compared to the P1–8Z–1200°C–50h sample.

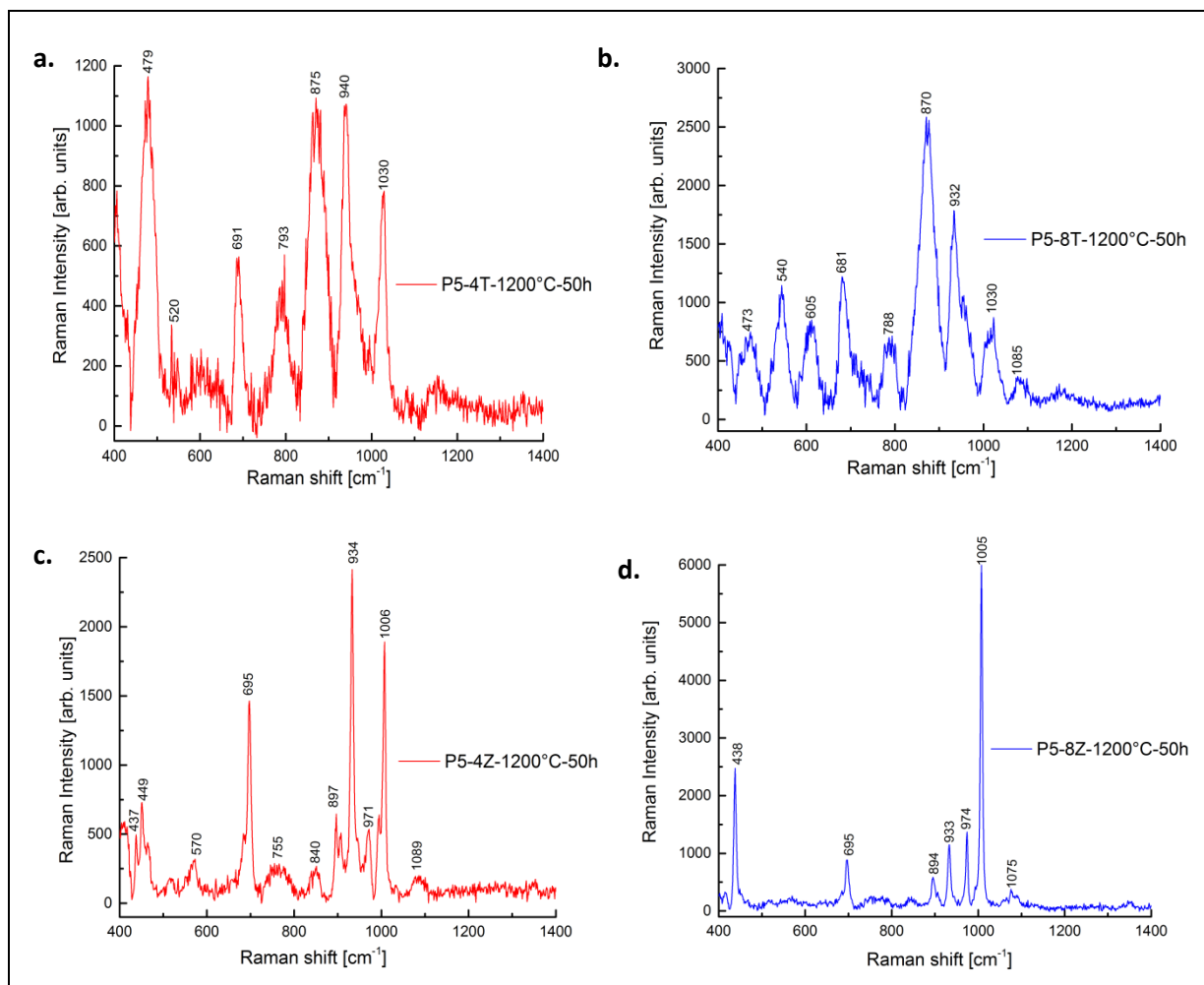


Figure 5.75: Raman spectra of glasses annealed at 1200 °C for 50h; (a) P5-4T, (b) P5-8T, (c) P5-4Z, (d) P5-8Z.

5.8 Nitrogen-containing yttria and neodymia aluminosilicate glasses

Nitrogen-containing yttria and neodymia aluminosilicate glasses (P7, P8, and P9) were prepared with the procedure as discussed in section 4.1.3. Chemical compositions of these nitrogen-containing glasses were found out by using XRF and are presented in Table 5.36. The elemental analyses of these glasses closely match with the initial compositions of the oxides and silicon nitride mixtures as given in Table 4.3.

Table 5.36: XRF analyses of the prepared nitrogen-containing glasses (mass %).

Sample	Y	Nd	Al	Si	O	N
P7	38.2	---	5.83	17.5	31.7	2.30
P8	43.7	---	5.96	15.2	28.4	4.28
P9	---	49.3	4.61	14	26.6	1.99

5.8.1 Structural analyses of nitrogen-containing glasses

This section contains structural analyses of P7, P8, and P9 glasses using XRD, Raman and IR spectroscopic techniques. For XRD and IR analyses, the glasses were fine-grinded using a ball mill. For Raman analyses, bulk samples of the prepared glasses were used.

5.8.1.1 XRD analyses of the prepared nitrogen-containing glasses

X-ray diffractions of P7, P8, and P9 glasses are shown in Fig.5.76, which revealed typical amorphous structures without any pronounced peaks.

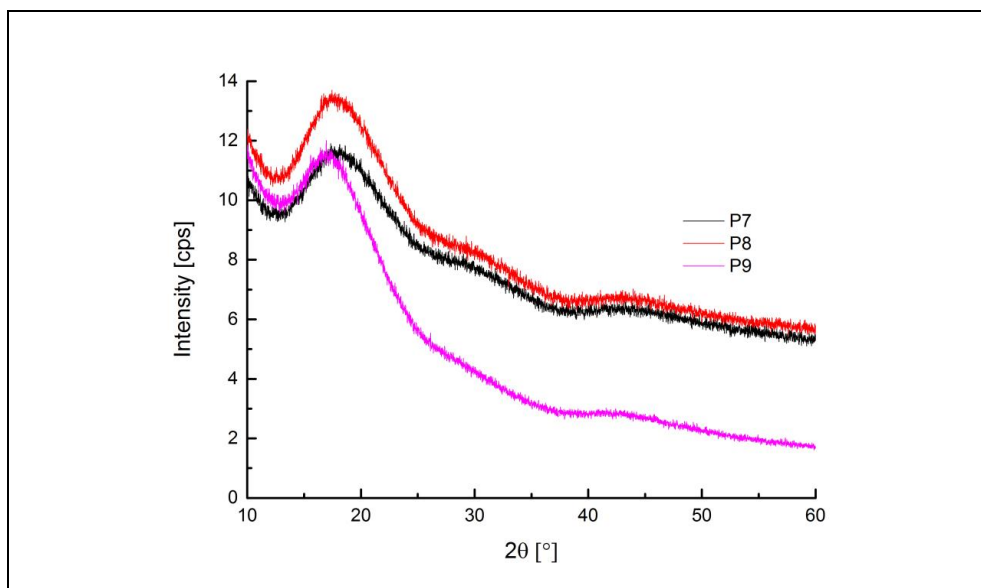


Figure 5.76: XRD analyses of the prepared P7, P8 and P9 glasses.

5.8.1.2 IR analyses of nitrogen-containing rare-earth aluminosilicate glasses

IR spectra of P7, P8 and P9 glass powders were determined in the range 400–1400 cm^{-1} wave numbers. The spectra measured for these glasses are shown in Fig. 5.77. It was found that these glasses heavily consist of stretching mode of Si-O in the range of 860–880 cm^{-1} wave number.

5.8.1.3 Raman analyses of nitrogen-containing rare-earth aluminosilicate glasses

Raman spectra of P7, P8 and P9 glasses were revealed to explore the structural bands in them and are shown in Fig. 5.78. The spectrum of the P7 sample contained Q^4 structure and high content of Si-O-M stretching mode in Q^3 units at around at 958 cm^{-1} . The P8 sample showed higher intensity of bending mode for Si-O-Si at around 520 cm^{-1} as compared to the P7 sample. Raman peak of the P9 sample was relatively broader with bending mode for Si-O-Si (Q^4) at around 520 cm^{-1} and Si-O-M stretching mode in Q^3 units at around at 905 cm^{-1} .

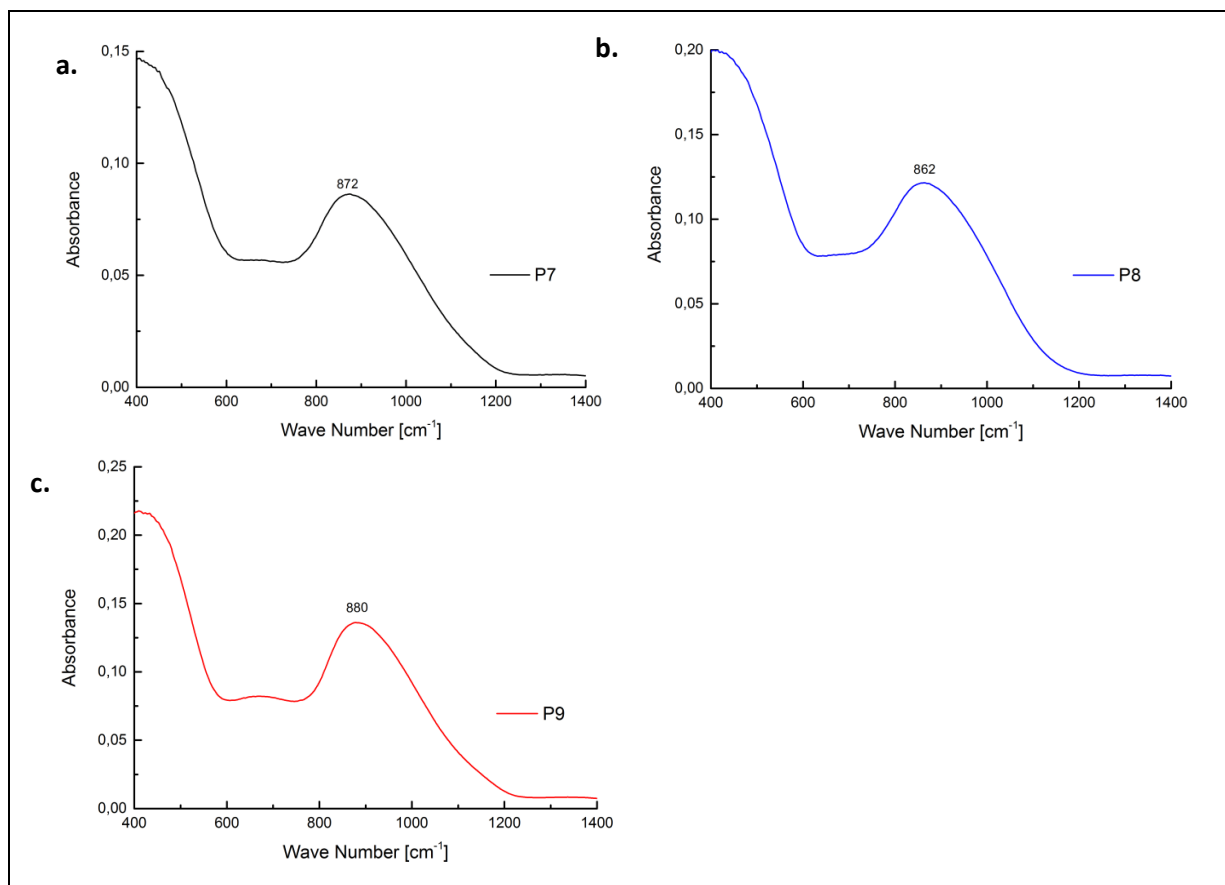


Figure 5.77: IR analyses of glasses; (a) P7, (b) P8, and (c) P9.

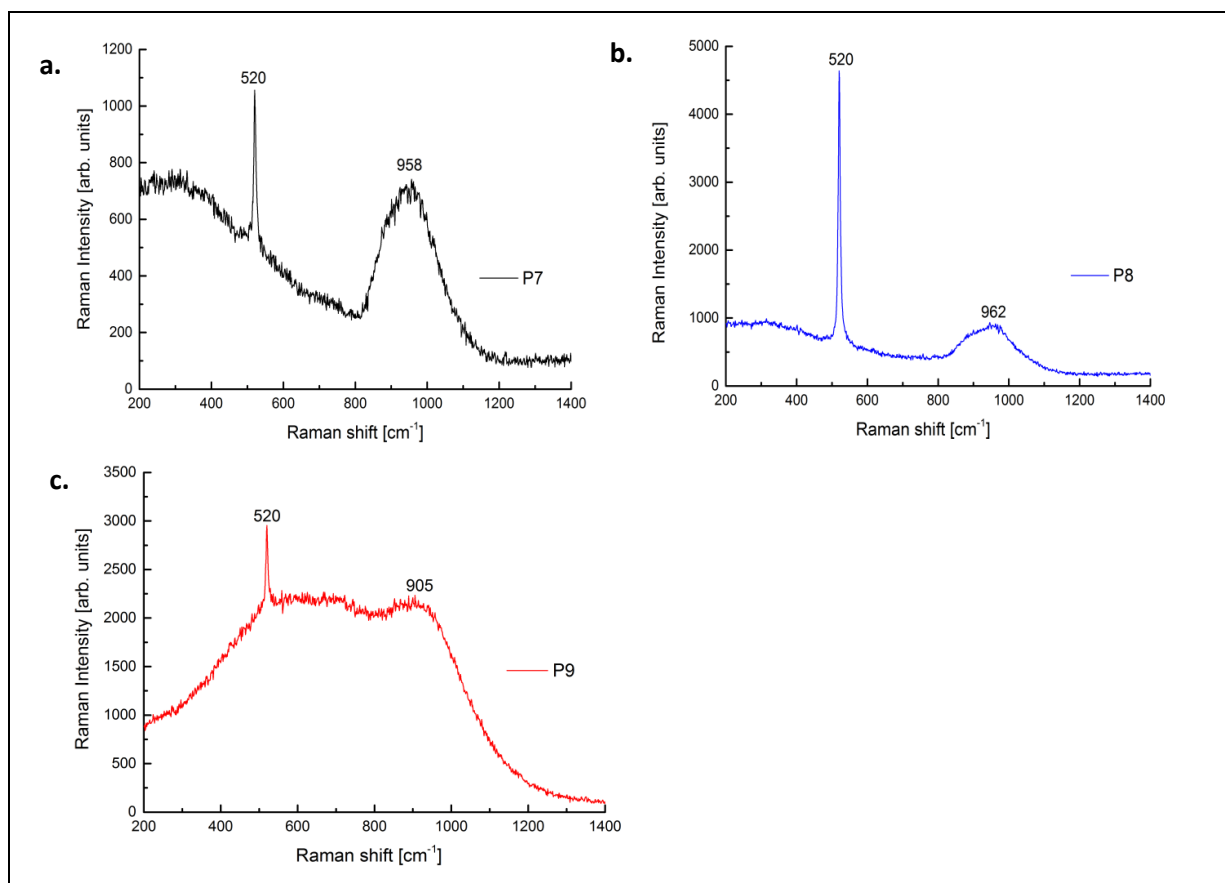


Figure 5.78: Raman spectra of glasses; (a) P7, (b) P8, and (c) P9.

5.8.2 Thermal analyses of nitrogen-containing glasses

Thermal analyses of P7, P8 and P9 glasses conducted to determine the effects of nitrogen addition on glass transition temperatures (T_g), crystallization temperatures (T_c) and specific heats.

5.8.2.1 Differential scanning calorimetry of nitrogen-containing glasses

Glass transition temperatures of P7, P8 and P9 glasses were determined using differential scanning calorimetry with heating rate of 15 K/min under argon. The results of DSC analyses for these glasses are shown in Fig. 5.79 and summarized in Table 5.37.

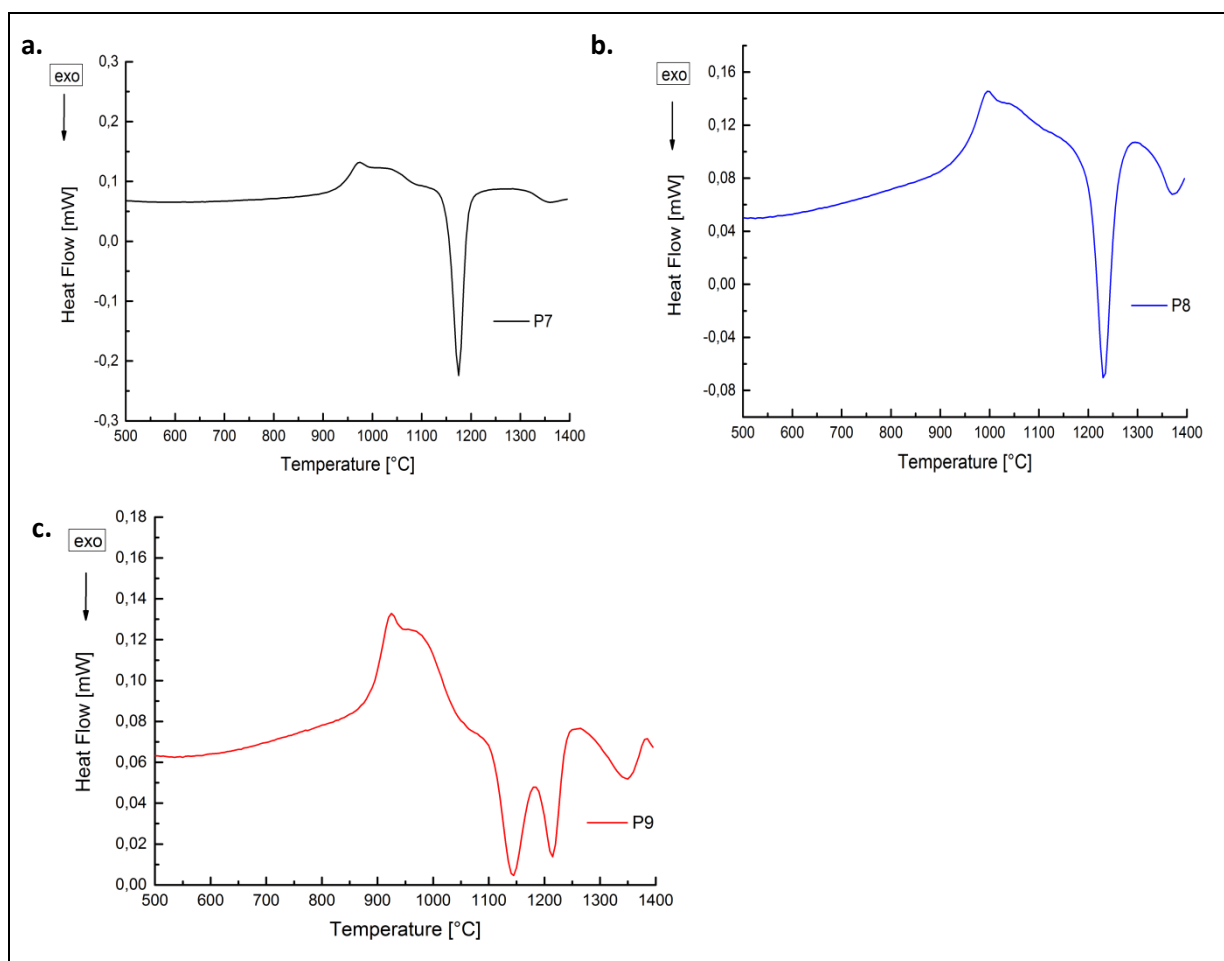


Figure 5.79: DSC analyses of glasses; (a) P7, (b) P8, and (c) P9.

The glass transition temperatures found for these glasses are significantly higher as compared to P1 and P5 glasses. The P7 glass showed T_g at around 956 °C, which is almost 40 °C higher as compared to the P1 glass system. However, T_c of the P7 glass was found at 1175 °C which is comparable to crystallization temperature found in the P1 glass. The P8 glass sample showed even higher T_g at around 976 °C and T_c was at 1231 °C. The glass transition temperature of the P9 glass was found 20 °C higher as compared to the P5 glass system. Moreover, P9 glasses showed two distinct peaks of crystallizations at 1144 °C and 1214 °C, respectively.

Table 5.37: DSC values of P7, P8 and P9 glasses.

Specimen	T_g (°C)	T_c (°C)
P7	957	1175
P8	976	1231
P9	908	1144, 1214

5.8.2.2 Specific heat capacities of nitrogen-containing yttria and neodymia glasses

Specific heat capacities of P7, P8 and P9 glasses were measured up to 800 °C using the 3-step method. Results are summarized in Table 5.38.

Table 5.38: Specific heat capacities values of P7, P8 and P9 glasses.

T (°C)	P7 Cp (J/(g·K))	P8 Cp (J/(g·K))	P9 Cp (J/(g·K))
50	0.591	0.605	0.567
100	0.623	0.643	0.590
200	0.67	0.693	0.618
300	0.726	0.739	0.657
400	0.760	0.773	0.692
500	0.791	0.802	0.725
600	0.814	0.826	0.746
700	0.838	0.854	0.760
800	0.866	0.881	0.786

5.8.3 Crystallization of nitrogen-containing rare-earth aluminosilicate glasses

Crystallization studies of P7, P8 and P9 glasses were conducted to evaluate their microstructures at higher temperatures for longer holding time in different atmospheres. Tablets of glass powders having 8 mm diameter and 5 mm thickness were prepared using uniaxial pressing with 50 kN force. The compacted glass specimens were annealed with 15 K/min up to 1200°C for different holding times under atmospheres of nitrogen, argon, vacuum, air and steam, respectively.

5.8.3.1 In-situ XRD analyses of samples

In-situ XRD analyses of P7 and P9 glasses were performed up to 1200 °C at 10 K/min under argon to evaluate crystals growth behaviour and phase formation in these glasses. The first scan was recorded at 25 °C, the second at 700 °C, the third at 800 °C, the fourth at 850 °C and hold there for 30 minutes; then scans were taken after every 50 °C steps up to 1200 °C with holding time of 30 minutes at each scan. The diffraction patterns recorded for these glass powders at different temperatures are shown in Fig. 5.80 and details are mentioned in discussion sectioned 6.4.

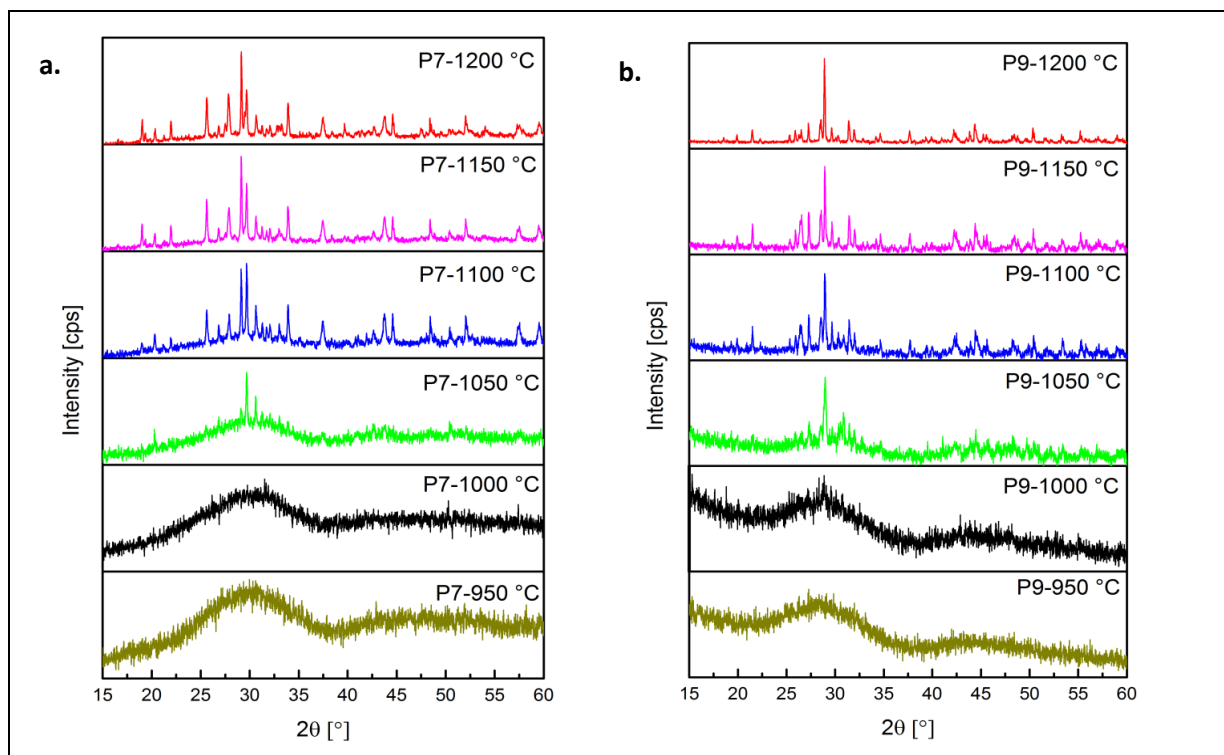


Figure 5.80: Hot-stage XRD analyses of; (a) P7, and (b) P9 glasses.

5.8.1 Thermal treatment of samples under nitrogen

The compacted powder samples of P7, P8 and P9 glasses were annealed at 15 K/min up to 1200 °C in a closed furnace under nitrogen atmosphere (pressure 1 bar, gas flow 20 litre/hour) for 1h and 50h, respectively. These samples were structurally examined with XRD and SEM to evaluate the formed phases. Figure 5.81 shows the samples before and after heat-treatment.

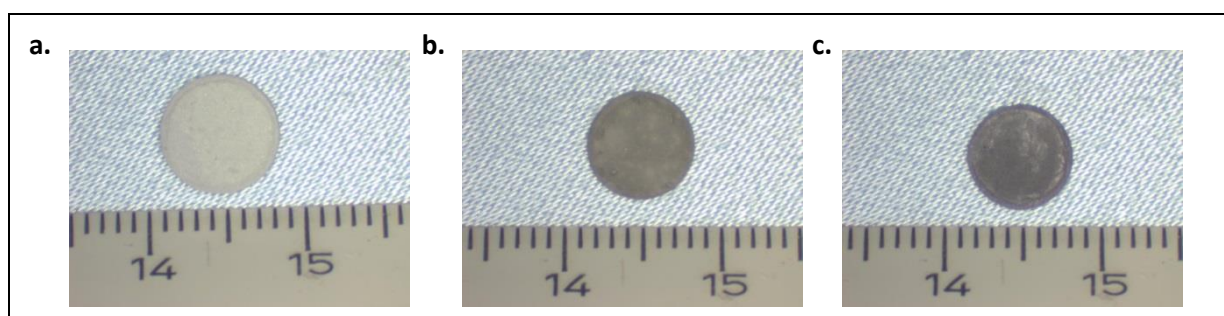


Figure 5.81: Thermal-treatment under nitrogen; (a) sample before heat-treatment, (b, c) P7 and P9 samples after heat-treatment.

The qualitative phase analyses of P7, P8 and P9 samples annealed at 1200 °C for 1h and 50h under nitrogen atmosphere are listed in Table 5.39. The edge regions of the P7 sample annealed at 1200 °C for 1h pointed primarily to different modifications of Y-disilicate (YDS), the sample centre was more prevalent with y-modification of Y-disilicate. The P7 sample annealed at 1200 °C for 50h revealed mullite and y-modification of Y-disilicate. An additional oxynitride phase (D-Phase) was observed in the P8 sample, which was not found in the P7 sample. The P8 sample annealed for 50h resulted in x-ray reflections of Y-disilicate, D-phase and mullite. The P9 sample annealed at 1200 °C

for 1h showed reflections of Nd-disilicate, mullite and an unknown phase which did not match with any known diffraction data set. The P9 sample aged at 1200 °C for 50h contained mainly reflections of Nd-disilicate together with very weak reflections of mullite.

Table 5.39: Qualitative phase analyses of P7, P8 and P9 samples aged in nitrogen atmosphere.

Specimen	Phases
P7-1200°C-1h-nitrogen	Edge: γ -YDS (weak), β -YDS, Υ -YDS, mullite Centre: γ -YDS, mullite
P7-1200°C-50h-nitrogen	γ -YDS, mullite
P8-1200°C-1h-nitrogen	Edge: γ -YDS (weak), Υ -YDS, δ -YDS, D-Phase ($\text{YSi}_2\text{AlO}_4\text{N}_2$) Centre: γ -YDS, Υ -YDS (weak), δ -YDS, D-Phase ($\text{YSi}_2\text{AlO}_4\text{N}_2$)
P8-1200°C-50h-nitrogen	γ -YDS, D-Phase ($\text{YSi}_2\text{AlO}_4\text{N}_2$), mullite
P9-1200°C-1h-nitrogen	Nd-DS, Mullite, unknown reflections
P9-1200°C-50h-nitrogen	Nd-DS, Mullite (very weak)

SEM images of P7, P8 and P9 samples aged at 1200 °C for 50h under nitrogen are shown in Fig. 5.82. P7 and P8 samples showed crystallization with crystals embedded in a matrix having minimum residual glass content. These crystals had grown uniformly in all directions. The P9 sample showed phase separation of Nd-disilicate crystals in residual glass matrix and small crystals of mullite.

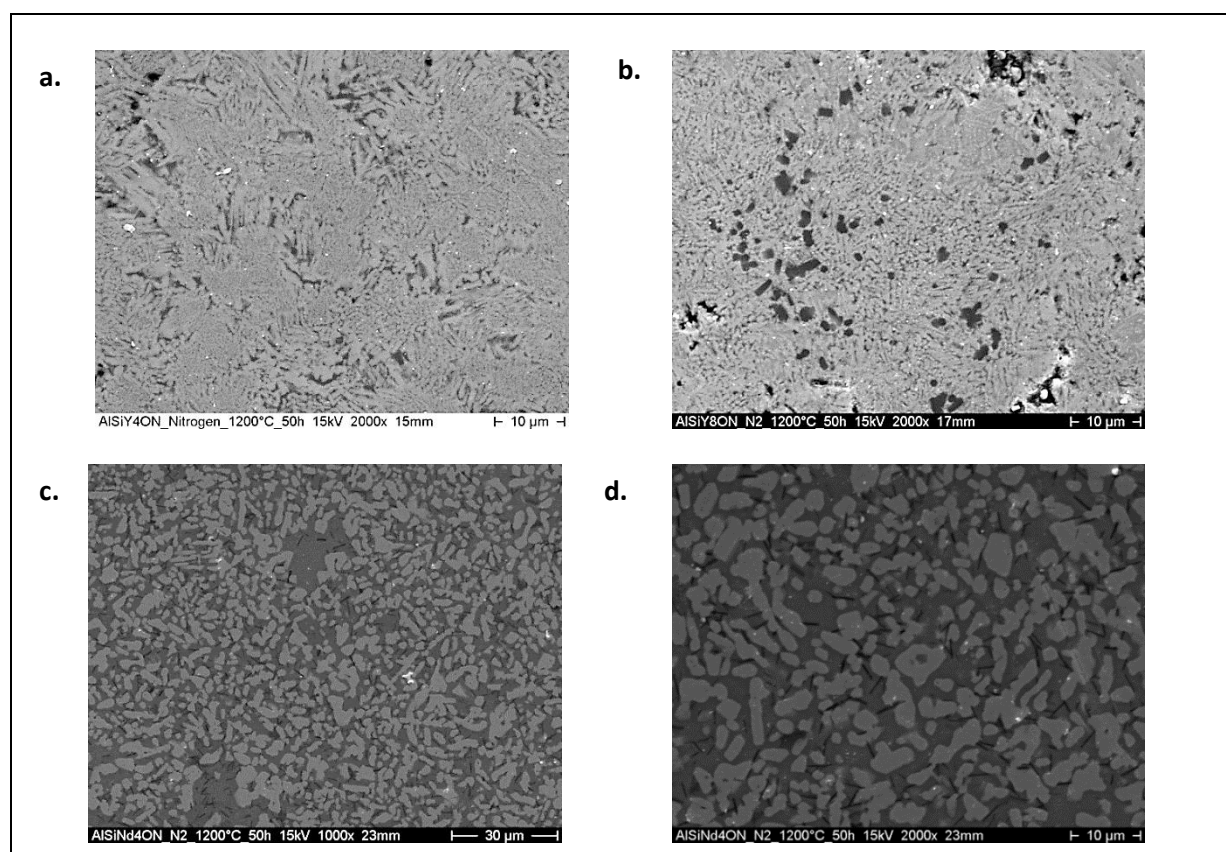


Figure 5.82: SEM images of glasses annealed at 1200 °C for 50h under nitrogen; (a) P7 mag. at 2000x, (b) P8 mag. at 2000x, and (c, d) P9 mag. at 1000x and 2000x, respectively.

5.8.2 Thermal treatment of samples under argon

The compacted powder samples of P7, P8 and P9 glasses were heated up to 1200 °C in a tube furnace under argon atmosphere (pressure 1bar, gas flow 20 litter/hour) for 50h and structurally examined with XRD and SEM to evaluate the formed phases.

XRD analyses of P7, P8 and P9 samples annealed at 1200 °C for 50h are listed in Table 5.40. The main phases observed in the P7 sample were Y-disilicate and mullite. The P8 sample showed reflections of Y-disilicate, D-phase and mullite. The P9 sample contained strong reflections of Nd-disilicate together with weak peaks of mullite.

Table 5.40: Qualitative phase analyses of P7, P8 and P9 samples heat-treated under argon atmosphere.

Specimen	Phases
P7-1200 °C-50h-argon	y-YDS, mullite
P8-1200 °C-50h-argon	y-YDS, D-Phase, mullite
P9-1200 °C-50h-argon	Nd-DS, mullite

SEM images of P7, P8 and P9 samples annealed at 1200 °C in argon for 50h are shown in Fig. 5.83. These images are almost similar as observed in samples heat-treated under nitrogen. P7 and P8 samples showed interconnected crystallization with increased dendrites embedded in the residual glassy matrix. The P9 sample showed Nd-disilicate crystals in the residual glass matrix.

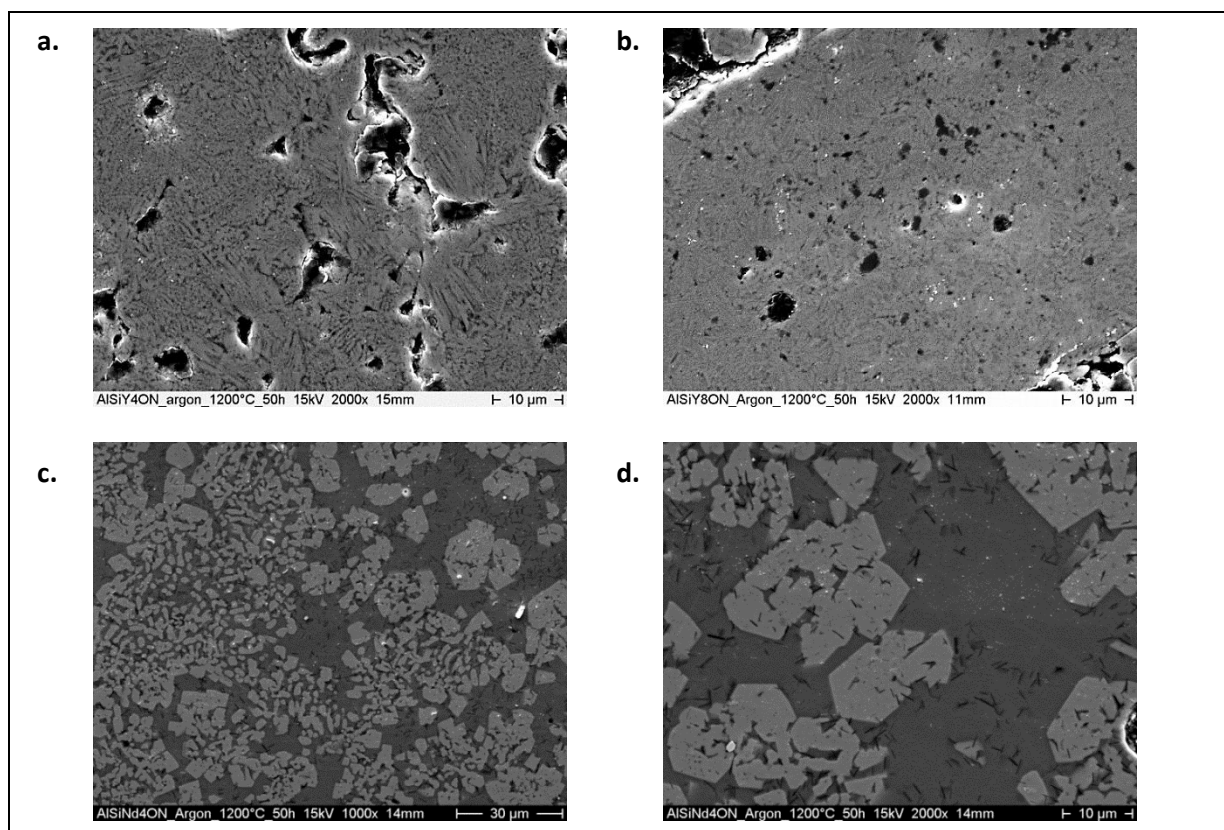


Figure 5.83: SEM images of glasses heat-treated at 1200 °C for 50h under argon; (a) P7 at mag. 2000x, (b) P8 at mag. 2000x, and (c, d) P9 at mag. 1000x and 2000x respectively.

5.8.3 Thermal treatment of samples under vacuum

For crystallization studies of glasses under vacuum, compacted samples of P7, P8 and P9 glasses were annealed at heating rate of 5 K/min up to 1200 °C for 1h and 50h holding time, respectively in a vacuum tube furnace.

The qualitative phase analyses of P7, P8 and P9 samples are listed in Table 5.41. The P7 sample annealed for 1h contained different modifications of Y-disilicate, whereas the sample annealed for 50h showed only γ -modification of Y-disilicate. The D-phase along with different modification of Y-disilicate was found in the P8 sample annealed for 1h, whereas the sample aged for 50h showed reflections of Y-disilicate, D-phase and mullite. XRD analyses of the P9 sample showed reflections of Nd-disilicate, unknown phase and mullite. The reflections of mullite were very weak in the sample aged for 50h as compared to the sample annealed for 1h.

Table 5.41: Qualitative phase analyses of P7, P8 and P9 samples aged under vacuum.

Specimen	Phases
P7-1200 °C-1h-vac	γ -YDS, β -YDS, Υ -YDS, mullite
P7-1200 °C-50h-vac	γ -YDS, mullite
P8-1200 °C-1h-vac	γ -YDS, Υ -YDS, δ -YDS, D-Phase ($YSi_2AlO_4N_2$), mullite
P8-1200 °C-50h-vac	γ -YDS, D-Phase, mullite
P9-1200 °C-1h- vac	Nd-DS, mullite, unknown phase
P9-1200 °C-50h- vac	Nd-DS, mullite

Figure 5.84 shows the microstructure of P7, P8 and P9 specimen annealed in vacuum at 1200 °C for 1h and 50h, respectively. The microstructure of P7 and P8 samples annealed for 1h consisted of Y-disilicate crystals in remaining glassy matrix. Samples aged for 50h showed crystals through cracks in the corner and in the residual glass content. The microstructure of the sample P9 contained crystals of Nd-disilicate in the remaining glassy matrix. The P9 sample aged for 50h showed crystals of neodymium rich disilicate in the remaining glassy matrix and mullite.

5.8.1 Thermal treatment of samples under air

To check oxidation resistance and crystallization behaviour of P7, P8 and P9 glasses in open atmospheric condition, compacted samples were annealed with heating rate of 15 K/min at 1200 °C in a chamber furnace for 1h and 50h, respectively. Figure 5.85 shows that compacted P7 and P8 samples were swelled at least 2 mm in diameter and thickness as compared to the initial samples. The P9 sample shows viscous flow of the glass at 1200 °C, which is around 200 °C less than its flowing temperature.

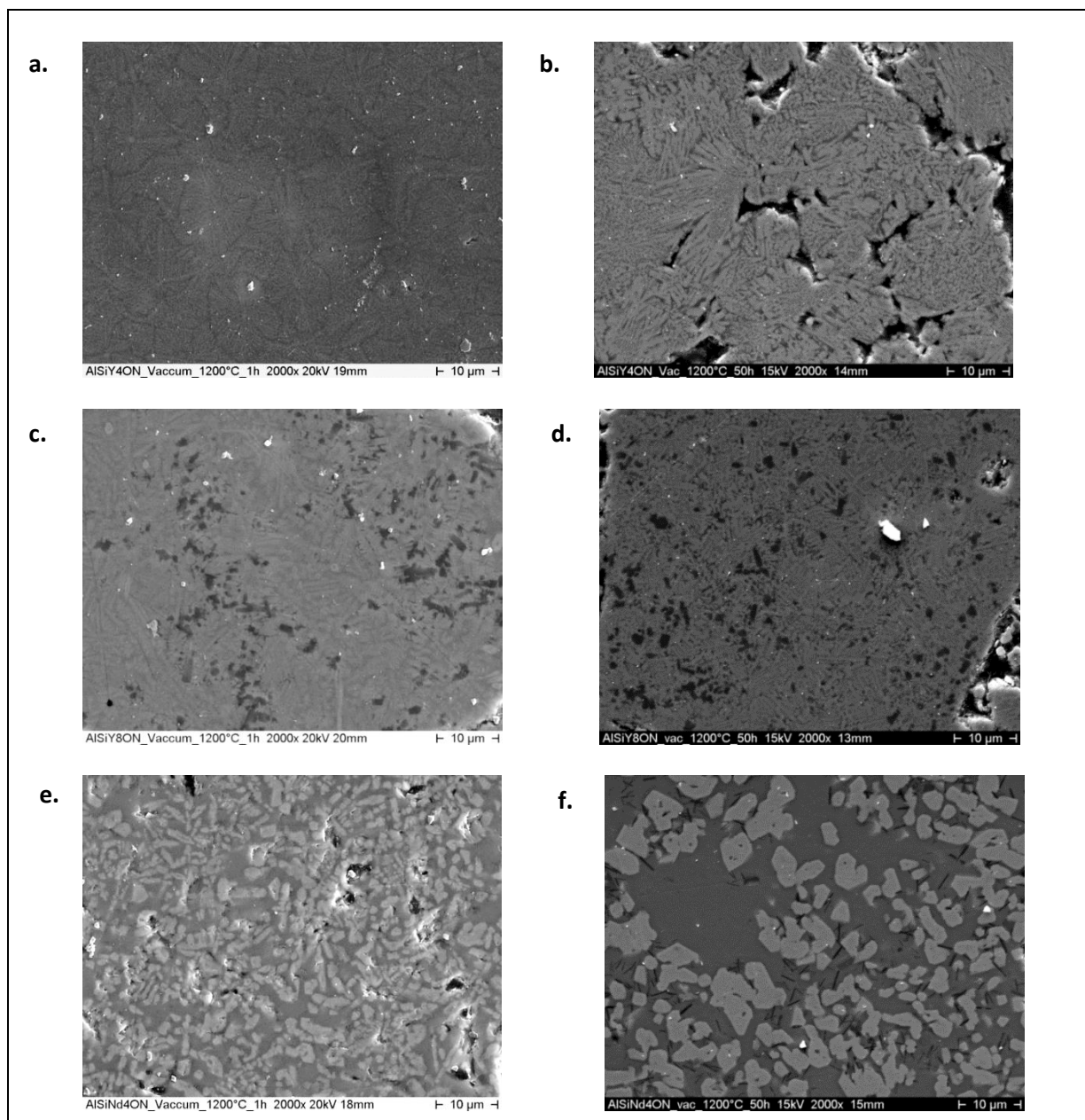


Figure 5.84: SEM images of glasses mag. 2000x annealed at 1200 °C under vacuum for 1 h and 50h; (a, b) P7, (c, d) P8, and (e, f) P9.

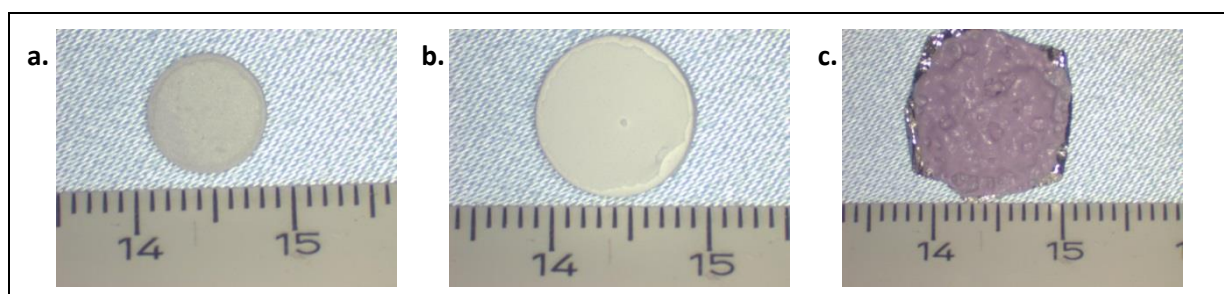


Figure 5.85: Annealing of samples under air; (a) sample before annealing, (b, c) represent P7 and P9 samples after annealing.

XRD analyses of P7 and P8 samples aged for 1h and 50h, respectively, at 1200°C in a chamber furnace showed reflections of Y-disilicate and mullite. The intensities of Y-disilicate phase were almost similar in both aged samples, however the intensity of mullite was weak in samples aged for 50h. Moreover, D-phase was not observed in the P8 sample. It was not possible to obtain diffractions of the P9 sample after annealing in air.

Table 5.42: Qualitative phase analyses of P7 and P8 samples heat-treated in ambient atmosphere.

Specimen	Phases
P7-1200°C-1h-air	YDS, mullite
P7-1200°C-50h-air	YDS, mullite
P8-1200 °C-1h-air	YDS, mullite
P8-1200 °C-50h-air	YDS, mullite

SEM images of P7 and P8 samples heat-treated at 1200 °C for 50h are shown in Fig. 5.86. Both samples showed high volume of interconnected pores. The crystals of Y-disilicate were embedded in a glassy matrix.

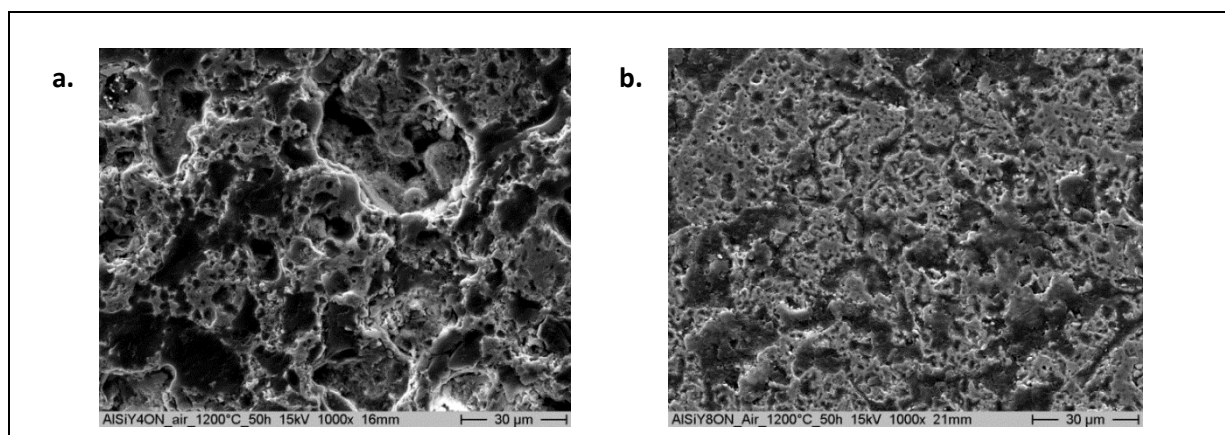


Figure 5.86: SEM images at mag.1000x of glasses heat-treated at 1200°C for 50h in air; (a) P7, (b) P8.

5.9 Joining of SiC with nitrogen-containing yttria and neodymia glasses

Prepared nitrogen-containing glasses were used as solders for joining of SiC components via laser process. The slurries made by mixing P7, P8 and P9 glass powders with ethanol were pasted to SSiC surfaces to be joined. Details of the joining process are summarized in Table 5.43. The joining process was performed under inert atmosphere (nitrogen) to prevent oxidation of the glass solders.

For structural analyses of the joint seams, one capsule of each solder batch was cut, embedded in epoxy, ground and polished for the ceramographical examination. Microprobe analyses for cross-sections of the prepared joints are given in Table 5.44. It was found that the joints contain sufficient amount of nitrogen in the glassy structure interlayer. There were no interface defects between SiC substrate and glassy solders, and a good wetting of glassy solders on SiC surface was determined.

Table 5.43: Parameters of the joining experiments with 3 kW diode-laser (λ : 808 + 940 nm).

Sample shape	Setup	Laser power	Scanning geometry	Scanning velocity	Rotation speed	Processing time
Capsules	rotating samples	680-740 W	circle, 0.1 mm diameter	2.500 mm/s	2 rps	75 s
Rods	fixed samples	500- 530 W	circle, 42.5 mm diameter	2.500 mm/s	---	70 s

Table 5.44: Electron microprobe analysis of joined samples (mass %).

Sample	Y	Nd	Al	Si	O	N	Sum
P7	37.37	---	7.70	18.51	35.25	2.14	100
P8	42.69	---	5.81	17.29	31.75	2.64	100
P9	---	50.28	4.84	15	28.43	1.40	99.94

5.10 Spark plasma sintering joining of SiC components

Spark plasma sintering (SPS) as joining process had shown a number of advantages due to rapid localized heating and short processing time. SiC rods and plates were joined via SPS using P1 glasses as solder material. The details of the joining process and the characterization of the joining layer formed between SiC matrix and glassy solder are presented.

5.10.1 Joining of SiC components using Yttrium-aluminosilicate glass solders

At first, rods of α -SiC (StarCeram H.C. Starck) having length 10 mm and diameter 5 mm were used for SPS joining. Fine grinded powder of the P1 glass was mixed with ethanol to prepare slurry. This slurry was pasted at surfaces of rods to be joined. After evaporation of ethanol, these rods were placed in a cylindrical mould of SPS and heated at a rate of 50 °C/min up to 1500 °C, and minimum pressure of 5 kN. However, rods were scattered into small pieces before joining that show even 5 kN pressure was high enough to scatter rods due to their small surface area.

Then two plates of SiC having length 25 mm, width 25 mm and thickness 4 mm were used for SPS joining. These plates were washed and polished using diamond abrasive paste to remove surface irregularities. The slurry of the P1 glass powder was made by mixing with ethanol and applied on surfaces to be joined as shown in Fig. 5.87. After evaporation of ethanol, both plates were placed exactly on each other and put in a cylindrical mould of the SPS. These plates were joined at 1500 °C with 50 °C/min heating rate and using 5 kN directional pressure. Figure 5.88 shows unfavorable scattered plates in cylindrical mould after applying above mentioned parameters.

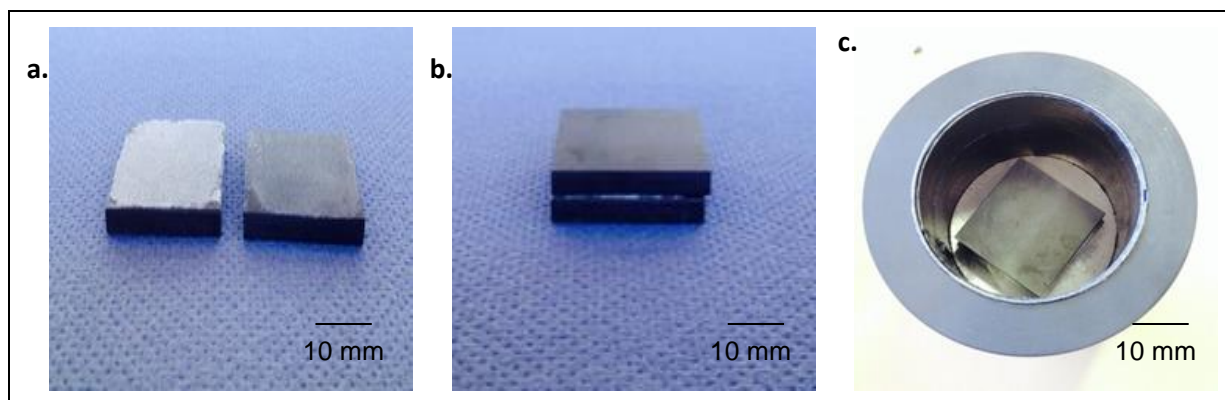


Figure 5.87: Joining of SiC plates using P1 glasses as solder material via SPS; (a) plates with pasted glass slurry (b) couple plates (c) couple plates in cylindrical mould of SPS.

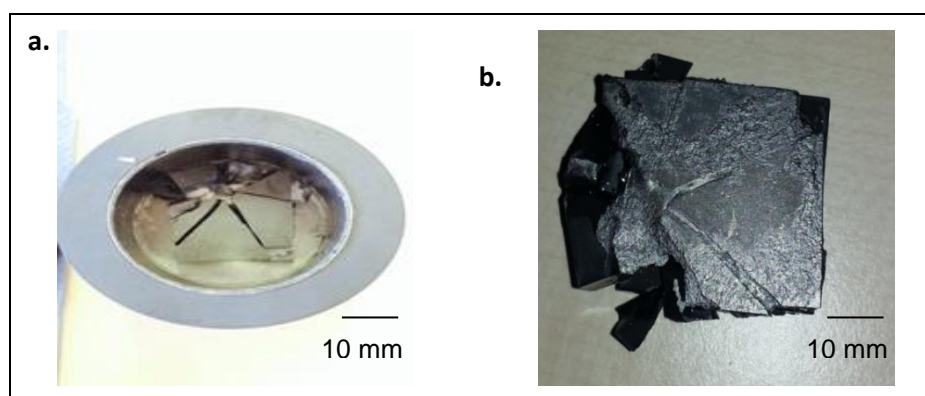


Figure 5.88: SiC plates joining using the SPS process; (a) couple plates in cylindrical mould of SPS (b) scattered plate assembly.

5.10.2 Characterizations of the joined samples

Further efforts were made to join plates using two extra plates of SiC as sacrificial material to reduce effects of pressure on slurry pasted plates. P1 glasses were fine-grinded using a ball mill to get fine glass powder ($< 5 \mu\text{m}$). Slurry prepared by mixing fine-grinded glassy powder and ethanol was applied on polished surfaces of SiC plates. These plates were fixed exactly on each other and kept overnight to evaporate ethanol. One sacrificial plate was placed below the slurry pasted plates (plates to be joined) in a cylindrical mould and the other plate was put above this slurry pasted assembly. The joining process performed with a heating rate of $50 \text{ }^\circ\text{C}/\text{min}$, at $1500 \text{ }^\circ\text{C}$, dwelling time was 5 min and a directional pressure of 5 kN. The application of sacrificial plates worked well for joining SiC plate assembly as shown in Fig. 5.89.

Pasted slurry between SiC plates formed blackish glassy layer between SiC plates. Small slices were cut from this joined plate assembly using saw cutter. These slices were mounted in epoxy and polished using ceramographical specimen preparation steps. Optical analyses of these slices showed a joint layer between plates and glassy solder without any defects. It showed good wetting of glasses with SiC surfaces. However, formed interlayer has thickness of higher than $200 \mu\text{m}$. SEM

images of these slices revealed fine crystals of Y-disilicate and mullite as shown in Fig. 5.90. It revealed that glassy solders were fully crystallized during this SPS joining process.

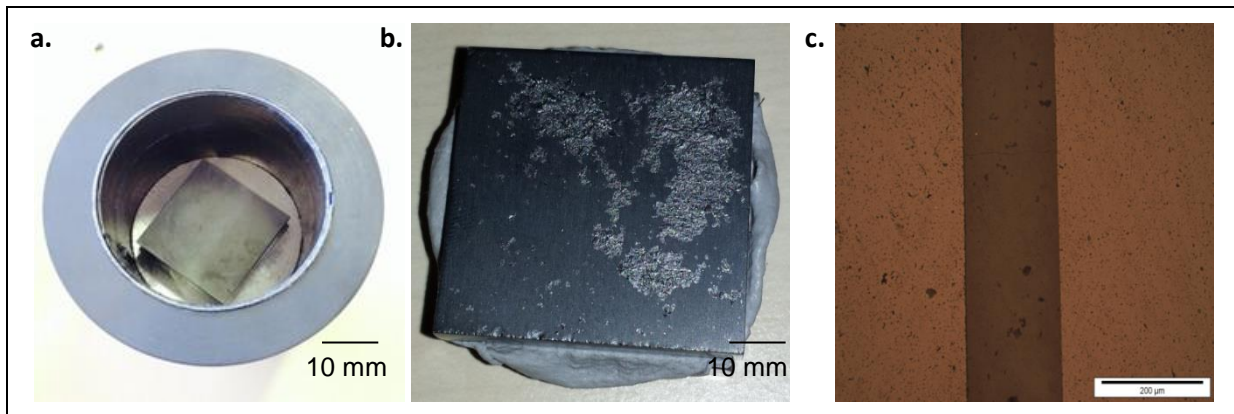


Figure 5.89: SiC plates joined using SPS joining process; (a) couple plates in cylindrical mould of SPS (b) joined plates (c) optical image of joint.

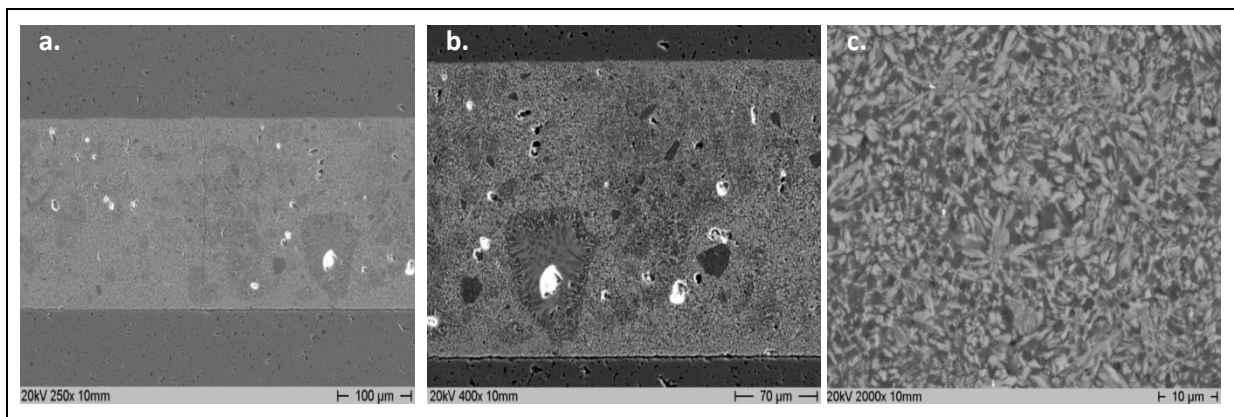


Figure 5.90: SEM images of the joint layer between SiC and glassy solder; (a) at mag.100x, (b) at mag. 200x and (c) at mag. 1000x.

6 Discussion

This chapter contains discussion of results presented in chapter five.

6.1 Rare-earth aluminosilicate glasses

Rare-earth aluminosilicate glasses $\text{RE}_2\text{O}_3\text{-Al}_2\text{O}_3\text{-SiO}_2$ (RE stand for Y, Nd, Yb, Dy, Ho, Sc) were prepared using melt-quench route. The chemical compositions of glasses were found using XRF that revealed they have very similar composition as the oxide mixtures used for preparation of glasses. These glasses were extensively studied by interpretation of literature and own results using qualitative and quantitative tools/techniques. Moreover heat-treatments of glasses were conducted at 1200 °C for different time periods to evaluate crystals formation and phase evaluations.

6.1.1 Structural characterization of rare-earth aluminosilicate glasses

Structural analyses of glasses were conducted using XRD, IR, Raman and solid NMR spectroscopic techniques. XRD analyses of glasses showed typical amorphous structure that makes it impossible to determine absolute structural information from these diffraction patterns. However, XRD revealed they have complete amorphous structures without any pronounced diffraction peaks of crystals. IR analyses of glasses showed symmetrical stretching of Si-O-Si and asymmetric stretching Si-O-M, where M stands for Al^{3+} and/or respective rare-earth ions (Y^{3+} , Yb^{3+} , Ho^{3+} , Dy^{3+} , Nd^{3+} , and Sc^{3+} respectively). Spectra of glasses containing Y^{3+} , Yb^{3+} , Ho^{3+} and Dy^{3+} cations were almost identical with stretching mode of Si-O band at around 893 cm^{-1} , glass containing Nd^{3+} cations showed stretching mode of Si-O band near 902 cm^{-1} and for the glass having Sc^{3+} cations it was found around 885 cm^{-1} wave number. The band at around 890 cm^{-1} is due to Si-O band as mentioned in literature [148]. Moreover, asymmetric stretching of Si-O-Si modes was found for all glasses around 1055 cm^{-1} wave numbers. These findings match with IR spectra for silicate glasses noticed by other authors [148, 153]. IR spectra were noticed slightly affected by the identity of rare-earth ions present in glasses. Raman spectra of glasses showed high amount of Q^4 and Q^3 structural units in them. High amounts of Q^3 structural units revealed uniformly distribution of rare-earth cations in these glasses. The observed structural units were found in line with previously determined Raman spectra for rare-earth silicate glasses with exception of little raman shifts in glasses containing Y^{3+} and Dy^{3+} cations [154].

^{27}Al NMR spectra of rare-earth aluminosilicate glasses provides useful information to know preferential association of rare-earth cations with Al^{+3} , which act as energetic stabilizers and provide local charge environment. ^{27}Al spectra of the glass containing Y^{3+} cations consisted of two peaks with centered at nearly 30 and 50 ppm. Spectra of Yb^{3+} and the Nd^{3+} cations containing glasses showed asymmetric peak shapes, spectra of glass containing Sc^{3+} cations showed peaks at 25, 50 ppm, respectively and an extra shoulder at about 40 ppm. It shows 4-, 5-, and 6-fold-coordinated aluminum (AlO_4^{-5} , AlO_5^{-7} and AlO_6^{-9}) for Sc containing glasses. The spectrum of P1 glass showed generally similarities with spectra reported by Schaller *et al.* [110]. However, differences were reported for 5-

fold and 6-fold-coordinated aluminum intensities could be attributed due to difference amount of Y^{3+} cations in present work and used by them. It was not possible to obtain second-order quadrupolar in the present study due to instrumental availability limits.

6.1.2 Thermal characterization of rare-earth aluminosilicate glasses

DTA and DSC were used to find out glass transition temperatures and crystallization temperatures of glasses. The main objective to use DSC was to countercheck transition temperatures obtained with DTA. Moreover, two heating rates were utilized in DTA (5 K/min) and DSC (15 K/min) experiments to reveal their effects on transition temperatures. The glass transition temperatures determined for rare-earth aluminosilicate glasses (P1-P6) using DTA and DSC were almost identical but crystallization temperature values were different as given in Tables 5.5 and 5.6. This difference in crystallization temperatures can be attributed due to different utilized heating rates. A second crystallization peak was recorded for the P1 glass at around 1345 °C during its DTA experiments. Ludwig [151] also reported in his work second crystallization peak in yttrium aluminosilicate glass at around 1340 °C. An increase in T_g was observed with decreasing ionic radii of rare-earth ion present in them except P6 glass-system. P5 glasses containing Nd^{3+} cations had the lowest glass transition temperature among these glass systems, which can be explained due to their higher ionic radii as compared to other rare-cations used in this work. Moreover, P5 glass did not show any crystallization effects and start to flow after T_g . P2 glasses showed higher glass transition temperature which could be explain on the basis of lower ionic radius of Yb^{3+} and higher cationic field strength (3.982×10^{-10} m) as compared to remaining other rare-earth cations. The values of ionic radii and cationic field strength of rare-cations are presented in Table 2.1. The smaller ionic radii make the structures tighter which results in higher glass transition temperatures for lanthanide series elements. Moreover, rare-earth cations occupied octahedral sites in glass structure and strength of bonds between rare-earth ions and surrounding oxygen have strong effect on glass transition temperature. Glass transition temperature will be higher for stronger rare-earth-oxygen bonds. P6 glasses containing Sc^{3+} cations showed lower glass transition temperature and crystallization temperatures as compared to other glass systems. The reasons for lower transition temperatures in P6 glasses including higher coordination numbers as compared to other rare-earth cations as discussed by Pahari *et al.* [155]. Thermal expansions of glasses are given in Table 5.8 and found comparable with SiC ($4.4 \times 10^{-6} K^{-1}$). Therefore, produced glasses were used as solders for joining SiC components. They reduce residual stresses due to difference of thermal expansion coefficients. Specific heat capacity values of glasses were increasing as a function of temperature from 50-800 °C as expected. This trend was significant in P1 and P6 glasses, moderate in P2, P4 and P5 glasses and relatively weak in the P3 glass. Thermal conductivities were calculated by multiplying their specific heats with thermal diffusivities and densities. The measured thermal conductivity value of the P1 glass at room temperature was found little lower as compared to literature [156]. This difference in values can be due to different composition of yttrium-aluminosilicate glasses used in the present study and available in literature.

6.1.3 Physical properties of rare-earth aluminosilicate glasses

Densities of glasses were found dependent on the atomic mass and radius of the rare-earth ion. P5 glasses containing Nd^{+3} with the highest atomic mass showed the highest density and Sc^{+3} containing P6 glasses have the lowest. This observation was found matching with findings mentioned in literature by Tenable *et al.* and Kohli *et al.* [44, 61]. They also found a linear increase in density of glasses with increasing atomic mass and ionic radii of rare-earth cations.

Hardness values of glasses were found inversely proportional to ionic radii of rare-earth ions. P6 glasses showed the highest value of hardness as it contained Sc^{+3} cations which had lowest ionic radii among all used rare-earth cations in this study. One can notice that lower ionic radii tighter the structure that results in higher hardness. Furthermore, it was found during ^{27}Al NMR of P6 glasses that Sc^{+3} had higher coordination number (AlO_4^{-5} , AlO_5^{-7} and AlO_6^{-9}) as compared to other glasses which results in high hardness of the P6 sample.

Refractive indices values of glasses were found similar with very small variation. There was no linear relationship between refractive indices and ionic radii were found. Although in literature [43, 44] a linear increase in refractive indices with increasing amount of rare-earth cations is mentioned. The reason of this difference could be due to using different instruments/setup for measuring refractive indices. However, effects of ionic radii of different rare-earths on refractive indices are not clear. This work summarized that rare-earth ion type had minor effect on the refractive indices of these glasses.

6.1.4 Crystallization studies of rare-earth-aluminosilicate glasses

Crystallization studies of prepared glasses were carried out to evaluate their crystallization behavior and resulting microstructures under different heat-treatment conditions. It was important because these glasses are considered potential candidate for joining ceramic components. It is possible that during heat-treatment of produced joints, the glassy interlayer converted into different crystalline phases. Firstly, in-situ high temperature XRD of glasses was performed to determine crystal growth behaviour from room temperature up to 1200 °C. It was not possible to go beyond 1200 °C due to instrumental limits. Moreover, maximum crystallization temperatures of prepared glasses are near/below 1200 °C. The diffraction patterns recorded showed complete amorphous structures up to 900 °C and maximum crystallization in P1–P5 glasses took place between 1100–1200 °C and for the P6 glass in the range of 1050–1100 °C. These temperatures matching with crystallization temperatures values found during thermal analysis (DTA/DSC). It was found that glass transition temperatures and crystalline structure morphologies strongly depend on the rare-earth ions present in the glass system.

Glasses were annealed at 1200 °C for 1h holding time and for 50h, respectively in a closed chamber furnace. The main phases observed during long heat-treatment of these glasses were silicates of rare-earth elements and mullite. The feathers like crystals of Y-disilicate surrounded by mullite were in large excess in the sample of P1. To evaluate the secondary crystallization effect observed

during DTA of P1 glass, compacted samples were heat-treated at 1250 °C and 1340 °C for 100h. The quantitative analyses of these heat-treated samples showed reflections of mullite, Y-disilicate and X phase. This X phase has an average composition of Y = 8.42, Si = 16.43, Al = 12.85 and O = 62.28 (at. %). The reflections of this phase were more pronounced in samples aged at 1340 °C for 100h. This observed phase maintains its volume fraction even after an exposure of 100 hours at 1340 °C proposed thermodynamically a stable phase. Although $Y_2O_3-Al_2O_3-SiO_2$ is a relatively well studied system, however this X phase is only explored by Ludwig [151] in his work. A phase with almost identical composition was also mentioned by Lichvar *et al.* [157] in their work but they did not investigate the stability of this phase. Arita *et al.* [47] also mentioned intermediate metastable phases in their work but could not characterize. X-phase was not observed in samples annealed at 1200 °C for different periods of time and only appeared in samples annealed near 1300 °C.

The crystals of Nd-disilicate observed in the P5 samples were embedded in the remaining glassy matrix with small amount of mullite phase (Fig. 5.40). These crystals were extended from the surface towards the centre of the samples which shows that surface crystallization process is favourable for the P5 glass system. Needle-like crystals of Yb-disilicate were distributed through the sample of the P2 and mullite crystals were mainly found at the edges. These phases have been formed very in-homogeneously regarding their shape, the sizes and the orientation. The sizes of formed Yb-disilicate crystals were small as compared to Y-disilicate crystals which could be related to different kinetics of crystal growth. A second reason could be the more uniform distribution of Yb-disilicate nucleates which hinders crystal growth in this glass system. There were relatively large crystals of mullite in P3 samples as compared to other heat-treated samples. Dy-disilicate crystals of feather shape surrounded by mullite were embedded in the remaining glassy matrix of P4 glasses. The morphology of crystals developed during crystallization of the P4 sample was found matching with crystals observed in the P1 sample. SEM images of the P6 sample showed Sc-disilicate and mullite crystals, which were not homogenous regarding their size and ordination.

Raman spectra of annealed samples at 1200 °C for 50h revealed high content of Q^3 structural units due to uniform distribution of RE^{+3} ions and non-bridging oxygen (NBO). Moreover, Q^4 structural units, bending mode for Si-O-Si and stretching mode for Si-O-Si were found in these annealed samples. These bands were observed at different Raman shift for aged samples as compared to rare-earth glasses. IR spectra of these samples showed strong Si-O-Si asymmetric stretching and symmetric stretching of Si-O-Si with slightly different wave numbers.

6.1.5 Laser-joining of SiC components using rare-earth aluminosilicate glasses

Prepared glasses were used as soldering material for joining of SiC components by using laser as heating source. These glasses showed flowing temperatures between 1285 °C for the P5 glass and more than 1600 °C for the P6 glass. Joining of SSiC components by using P1, P3, P4 and P5 glassy solders were carried out under ambient conditions. The maximum processing temperature

recommended for SiC components by supplier (H.C. Starck) was 1600 °C. Although SiC is stable in ambient conditions due to formation of protective SiO₂ surface layer. Different authors [80, 85, 86] have mentioned reaction of SiC with the SiO₂ layer at higher temperature (>1600–1650 °C) as shown below:



The intensity of above mention reaction increases with increasing temperature due to inward diffusion of new oxygen through the SiO₂-layer. It leads to the formation of additional SiO₂ on the SiC surface. These gaseous species can lead to formation of bubbles at the interface. Therefore, SiC components joining with P2 and P6 glassy solders were performed under argon pressure of 1 bar to avoid bubble formations at the interface.

The results of the joining experiments revealed that in-house prepared glassy solders can be used to produce joints of high quality between SiC components. These glassy solders showed good wettability with SiC surfaces and produced tight joints with good mechanical strength (Table 5.26). There were no defects at the interface between SiC substrate and glassy solders. All solders were solidified in the glassy state except P6 glasses which were crystallized into mullite and Sc-disilicate. The highest value of bending strength (195 MPa) was measured for the P5 glass solder. The lowest values of bending strength were found for P2 and P6 solders 63–64 MPa, respectively. Data on the bending strength for joined samples using glass/glass-ceramic solders are relatively seldom, and it is difficult to compare them due to the different test conditions and sample geometries. For instance, Perham *et al.* [158] measured 4-point bending strength for joints between 190 MPa and 250 MPa performed by a cordierite glass-ceramic. They used relatively small test geometry of 3 x 3 x 30 mm and conducted a surface treatment before the mechanical tests. Previous results achieved for the joining of SiC-samples using glass solders by the laser technology were limited by 112 MPa [143] and 120 MPa [159]. Ferraris *et al.* [141] reached 122 MPa for the joining in traditional furnace experiments. All these results were measured on samples joined with Y-aluminosilicate glass solder. The results in the present studies showed the possibility to reach a 4-point bending strength of nearly 150 MPa using Nd-aluminosilicate glass solder. The lower mechanical strength of the joints made with the P2 glass can be explained by low viscosity which can attributed to the reduction of the joining area. The high viscosity of P6 glass melt makes it difficult to fill the joining gaps with a consistently high quality. SiC capsules joined formed with P1–P5 glasses revealed hermetic tightness in the range of 10⁻¹⁰ - 10⁻⁹ mbar·l·s⁻¹. Whereas joints made with the P6 glassy solder showed varied range of leak rates in between 10⁻¹ and 10⁻⁶ mbar·l·s⁻¹. This work showed that prepared rare-earth aluminosilicate glasses have high potential to be used as solder for joining SiC components via optimized laser process.

6.2 Crystallization of glasses using microwave processing

The advantage of microwave processing has been utilized for crystallization studies of P1 and P5 glasses, respectively. These glasses are chosen as they produced tight joints with good mechanical strength as discussed in section 6.1.5. Microwave-annealed samples were structurally investigated using XRD, SEM, IR- and Raman spectroscopic techniques. A comparison of microwave-processed samples was made with samples heat-treated at 1200 °C for 50h under conventional furnace heating.

XRD patterns of P1 samples annealed using microwave heating source contained reflections of mullite, cristobalite and Y-disilicate. The intensities of these phases were increased with increasing dwelling time and became constant after 15 minutes holding time. The P1 sample annealed at 1200 °C for 30 min showed peaks of cristobalite, Y-disilicate and mullite with intensities similar to the sample heat-treated for 15 min. The intensities of these phases were comparable with diffractions obtained from the sample annealed conventionally in a chamber furnace at 1200 °C for 50h. It revealed that P1 samples were fully crystallized during microwave annealing process. SEM images of the P1 sample crystallized using microwave processing with no-holding time showed glass patches. The areas around these patches were crystallized with Y-disilicate crystals surrounded by mullite. Glass patches were not observed in sample annealed for 15 min and was completely crystallized. SEM images of the sample annealed for 30 min showed crystals of Y-disilicate and mullite in completely crystallized behaviour comparable with the images of P1–1200°C–50h sample (Fig. 5.14). IR spectra revealed that bending mode (O-Si-O) and symmetric stretching (Si-O-Si) in the P1 sample annealed at 1200 °C for 30 min using microwave-heating were at slightly different wave numbers as compared to the spectrum of P1-1200°C-50h sample shown in Fig. 5.19. However, wave number of asymmetric stretching (Si-O-Si) was almost same in both samples. Raman spectra of P1 samples annealed at 1200 °C for 15 min and 30 min showed Q^3 structural units at around ~ 917 and ~ 952 cm^{-1} , respectively, which matched with the spectrum of the P1–1200°C–50h sample as shown in Fig. 5.18b. It revealed that microwave-processed samples were fully crystallized in significantly shorter time as compared to conventionally crystallized samples. This enhanced crystallization behaviour of microwave processed samples was reproducible. This observation match with literature [72], where lithium disilicate glasses were crystallized using microwave processing.

XRD of P5 microwave-processed samples showed gradual development of mullite, Nd-disilicate and an unknown phase with increasing holding time. The intensities of mullite in these samples were very weak as compared to furnace annealed sample. XRD of the P5 sample annealed at 1200 °C for no-holding using microwave heating showed amorphous structure, the sample with 15 min holding time showed typical glassy hub with relatively strong reflections of Nd-disilicate and small peaks of mullite. Diffractions of the P5 sample annealed for 30 min at 1200 °C showed peaks of Nd-disilicate, mullite and unknown phase (Fig. 5.52b) which were comparable with reflections recorded for the sample P5–1200°C–50h as shown in Fig. 5.38. SEM images of the P5 sample without

holding time showed mostly glassy phase with small crystals of Nd-disilicate. The fractions of these crystals increased in the sample with 15 min holding time. The sample with 30 min holding time was partially-crystallized with relatively larger crystals of Nd-disilicate. This observation revealed that P5 samples need more holding time for fully crystallization. The Raman spectrum of the P5 sample annealed at 1200 °C without providing any holding time showed spectra similar observed for the P5 glass as shown in Fig.5.5. It showed that major portion of this annealed sample consists of glassy phase as it was also found during XRD and SEM analyses. IR spectra of P5 samples processed using microwave heating for 30min holding were almost identical and comparable with P5–1200°C–50h. An additional peak for (Si-O) non-bonding stretching was observed at 944 cm^{-1} for P5 microwave crystallized sample, which was not found in the P5–1200°C–50h sample. Peak observed for bending mode (O-Si-O) and symmetric stretching (Si-O-Si) in the microwave crystallised samples were at little different wave numbers as compared to the spectrum of P5–1200°C–50h sample. However, wave number of asymmetric stretching (Si-O-Si) was almost identical in both samples. Raman spectra of samples processed using microwave heating for 15 min and 30 min showed similar bands trend as observed in the spectrum of P5–1200°C–50h (Fig. 5.41b). However, there was a slight difference in Raman shift numbers as compared to conventionally crystallized sample.

This worked revealed that microwave heating enhanced kinetic of crystallization in P1 samples while its effects on P5 samples were not so pronounced. Moreover, crystal nucleation and growth mechanism was more homogenous in microwave annealed samples.

6.3 Yttria and Neodymia glasses containing nucleating agents

XRD analyses of Y-aluminosilicate and Nd-aluminosilicate glasses containing TiO_2 and ZrO_2 nucleating agents (P1–4T, P1–8T, P1–4Z, P1–8Z, P5–4T, P5–8T, P5–4Z, and P5–8Z) showed complete amorphous structures without any pronounced crystalline peaks. Spectroscopic studies of glasses P1–4T and P1–8T revealed Q^4 structural units and high content of Si-O-M modes in Q^3 structural units at around 900 cm^{-1} . These spectra did not show bending mode for Si-O-Si (Q^4), which was found in the P1 glass spectrum as shown in Fig. 5.5a. It proposes that addition of TiO_2 has influence on structural units in P1 glasses. Raman spectra of P1–4Z and P1–8Z glasses were found almost similar to the P1 spectrum with small difference in Raman shift. Raman spectra of P5–4T and P5–8T glasses were broader and it was not possible to distinguish between Q^4 and Q^3 structural units. However, one can see differences in Raman peaks for TiO_2 and ZrO_2 containing glasses (P5–4Z and P5–8Z). Spectra of P5–4Z and P5–8Z glasses were identical with the spectrum of the P5 glass system as shown in 5.5e. However, IR spectra of these nucleating agents containing glasses were found closely matching with spectra of P1 and P5 glasses shown in Fig. 5.3a and 5.3e, respectively.

Thermal analyses of P1–4T and P1–8T glasses showed that additions of TiO_2 results in decreased glass transition temperatures. P1–4T glass has T_g at around 898 °C, and T_c at 1175 °C, these

temperatures are almost 20 °C less as compared to the P1 glass system shown in Fig. 5.10 and Table 5.6. One can notice that additions of TiO₂ affects glass relaxation phenomenon and change glass transition temperature. Moreover, addition of TiO₂ contents also strongly enhanced crystallization and decreased crystallization temperature. The glass transition temperature of the P1–8T glass was found around 50 °C lower as compared to the P1 glass system and T_C decreased around 100 °C. P1–4Z and P1–8Z revealed T_g around 916 °C which is almost similar as found in the P1 glass system.

The P5–4T glass showed T_g at around 870 °C which is almost 15 °C lower as compared to the P5 glass shown in Fig. 5.10 and Table 5.6. Moreover, a crystallization peak at 1165 °C was found in the P5–4T glass system. Since P5 glasses did not show crystallization during DSC and DTA, one can observe that addition of TiO₂ enhanced the crystallization process in P5 glasses. DSC of the P5–6T glass sample contained two crystallization peaks, which suggests phase separation or formation of new phase in the P5–6T glass. Furthermore addition of TiO₂ lowered the T_g in P5–8T glasses to 854 °C, which is almost 35 °C less as compared to the P5 glass system. Moreover, it showed two exothermic peaks and two endothermic peaks. It revealed that P5–8T glass had two different types of crystals and concurrent melting of these phases. These results of TiO₂ addition on transition temperatures of P5 glasses were found closely matching with values determined by Kim *et al.* [160]. Moreover, TiO₂ acts as a network modifier in Nd-aluminosilicate glasses as discussed in literature [41, 62, 160]. The effects of ZrO₂ additions on transition temperatures of P5 glass system were found less pronounced. Additions of ZrO₂ enhanced crystallization process in P5 glasses without changing glass transition temperatures significantly. It was found that specific heat values of TiO₂ containing glasses at 50 °C were little higher as compared to the P1 glass system, but at higher temperature these values were almost identical.

X-ray diffraction patterns of P1–4T–1200°C–50h and P1–8T–1200°C–50h samples contained reflections of mullite, Y-disilicate, cristobalite, and yttrium-titanium oxide. Yttrium indicated reaction with TiO₂ to form yttrium-titanium oxide and the amount of this ternary oxide was higher in P1–8T–1200°C–50h sample. SEM images of annealed samples showed embedded Y-disilicate crystals in the remaining glassy matrix surrounded by mullite crystals at grain boundaries. IR spectra of both samples were almost identical with slightly different wave numbers and consisted of bending mode of (O-Si-O), symmetric stretching of Si-O-Si and strong asymmetric stretching Si-O-Si. Raman spectra of these samples revealed high structuring unit of Q⁴ with relatively strong bending mode of Si-O-Si (Q⁴) and Si-O-M stretching mode in Q³. Diffraction patterns of P1–4Z–1200°C–50h and P1–8Z–1200°C–50h samples showed reflections of mullite, Y-disilicate, cristobalite, and yttrium-zirconium oxide. The intensities of yttrium-zirconium oxide were very weak in the P1–4Z–1200°C–50h sample. Feathers like crystals of Y-disilicate were more excessively found at edges as compared to the centre of the samples. Relatively bigger islands of zirconium-rich phase were found in the P1–8Z–1200°C–50h sample. An IR spectrum of this sample revealed higher peaks of Si-O-Si asymmetric stretching, which was not so pronounced in the P1–4Z–1200°C–50h sample. Moreover, bending mode and symmetric

stretching modes were found in them. Raman spectra revealed bending mode of Si-O-Si and Si-O-M stretching mode in these samples. However, the stretching in Q^2 was also found in the P1-8Z-1200°C-50h sample.

X-ray diffractions of P5-4T-1200°C-50h and P5-8T-1200°C-50h samples showed reflections of mullite and unknown phases. These unknown phases were rich in neodymium and titanium but could not correlate with available diffraction data sets. SEM images of the P5-4T-1200°C-50h sample revealed titanium-rich neodymium crystals in the remaining glassy matrix. The distribution of titanium-rich phase was found more uniform and homogenous in P5-8T-1200°C-50h. It was not possible to determine the composition of these titanium-rich crystals due to their small sizes. Kim *et al.* [160] also find needle like titanium-rich neodymium crystals during crystallization of TiO_2 containing Nd-aluminosilicate glasses. Although composition used in literature [160] is slightly different from present study but crystallization effects and formed crystals are very much similar. One can suggest that contents of TiO_2 have strongly affect crystallization of Nd-disilicate glasses. XRD of P5-4Z-1200°C-50h and P5-8T-1200°C-50h samples contained reflections of mullite, Nd-disilicate and unknown phases. The intensities of unknown phases were more prominent in the P1-8Z-1200°C-50h sample. SEM images of both samples were almost similar and consisted crystals of mullite and unknown phase rich in ZrO_2 and Nd-disilicate. Moreover, round pores were observed in these samples. The reason for the existence of these pores could be attributed to different expansion coefficients of developed crystals and the remaining glassy phase. IR spectra of samples were scattering having peaks and shoulders. They revealed bending mode, symmetric stretching of Si-O-Si and strong Si-O-Si asymmetric stretching in them. However, these modes appeared at different wave numbers in both samples. The spectrum of the P5-8Z-1200°C-50h showed higher peaks of Si-O-Si symmetric stretching with different shoulders at ~ 878 , ~ 828 , $\sim 869\text{ cm}^{-1}$ and small peaks of asymmetric stretching. Raman spectra of these samples were contained high structuring unit of Q^4 , with relatively strong bending mode of Si-O-Si and Si-O-M stretching mode in Q^3 at different shift values.

These results showed that additions of nucleating agents (TiO_2 , ZrO_2) significantly affect transition temperatures, crystallization process and structural units in P1 and P5 glasses. The effects of TiO_2 on transition temperatures are more pronounced and interesting.

6.4 Nitrogen-containing yttria and neodymia aluminosilicate glasses

Nitrogen-containing glasses (P7, P8 and P9) were prepared and their structural analyses were conducted to find the effects of nitrogen additions on structures. Chemical compositions of P7, P8 and P9 glasses determined using XRF technique were found closely matching with the initial composition of substances used for the preparation of glasses. XRD analyses revealed that produced glasses are amorphous without any pronounced crystalline peaks. Raman analyses showed high contents of Q^4

structure units and of Si-O-M stretching mode in Q³ units. IR spectra revealed stretching mode of Si-O at around 860 and 880 cm⁻¹, respectively.

It was found that addition of nitrogen increased transition temperatures for P7, P8 and P9 glasses as compared to P1 and P5 glasses. Glass transition temperatures found for P7 and P8 glasses were ~ 40 °C, and ~ 55 °C respectively, higher as compared to the P1 glass system. These determined glass transition temperatures for P7 and P8 glasses were found matching with results of Ludwig [151]. Glass transition temperature of the P9 glass was found 20 °C higher as compared to the P5 glass system (Table 5.5). It was found that the initial nitrogen contents also had a great effect on the crystallization of these glasses and increased their crystallization temperatures. This is due to the incorporation of nitrogen in the glass network that builds 3-fold coordination of bridging ions instead of the 2-fold found in silicate glasses. It makes the network stronger via increasing the viscosity of the glass and decreases the mobility of the network components and consequently the glass transition temperatures shift to higher values [84]. Since the mobility of the different ions play a crucial role in the crystallization of glasses, the crystallization temperatures values also shifted to higher values.

Hot-stage XRD of nitrogen-containing glasses was performed up to 1200 °C. The complete amorphous structures were observed till 950 °C without any reflection peaks. This observation matched with glass transition temperature found for these glasses via DSC. P7 samples crystallized in the temperature range 1050–1100 °C, while the P9 samples in the range 1100–1150 °C. A more accurate description was not possible as the diffraction patterns were taken at intervals of 50 °C. The phase transformation of the primary β-modification into the γ-modification of the crystallized Y-disilicate was observed in P7 sample. The conversion temperature for this transformation was in the temperature range of 1150–1200 °C. This value is consistent with the specified transformation temperature of 1190 ± 50 °C by Felsche [161]. Moreover, reflections of mullite, cristobalite, Y-disilicate and Nd-disilicate were recorded for these glass systems.

A detailed heat-treatment study of P7, P8 and P9 glasses were conducted at temperature of 1200 °C for 1h and for 50h holding time in atmospheres of nitrogen, argon, vacuum, and air respectively. This work was performed to determine the effects of these atmospheres on the crystallization behaviour in glasses and on their oxidation resistance. The structures of studied glasses were found dependent on the atmospheric conditions resulting in different modifications of Y-disilicate. XRD studies of the P7 sample aged at 1200 °C for 1h under nitrogen pointed primarily to different modifications of Y-disilicate. The sample centre was more prevalent with γ-modification of Y-disilicate. An additional oxynitride phase was observed in the P8 sample, which was not found in the P7 sample. This phase was identified as the D-phase having the stoichiometry YSi₂AlO₄N₂ based on the literature [87]. The edge and the centre regions of the P8 sample had different modifications of Y-disilicate with different intensities. In the edge region, the more stable modifications found were γ and δ-modifications, while in the centre was γ-modification. Qualitative phase analyses of the P7

sample annealed at 1200 °C for 50h revealed γ - modification of Y-disilicate and mullite, whereas the P8 sample showed reflections of Y-disilicate, D-phase and mullite. The P9 sample annealed at 1200 °C for 1h showed reflections of Nd-disilicate, mullite and an unknown phase which could not match with any known diffraction data set. Main reflections observed in the P9 sample aged at 1200 °C for 50h were Nd-disilicate together with very weak peaks of mullite. The diffraction patterns of samples aged in nitrogen and argon atmospheres were almost identical.

SEM analyses of aged samples showed that the P7 sample indicates a strong crystallization in the centre as compared to the P8 sample. Moreover, a very small amount of residual glass was found in the centre of the P7 as compared to the P8 sample. It recommends that the crystallization temperature increases with nitrogen content which matches with DSC results. Additionally, it was noted that all samples had crystals of Y-disilicate. The edge region structure suggests a directional crystallization due to heterogeneous nucleation on the surface and the effect of the temperature gradient from the edge toward the centre regions. It caused different modifications of Y-disilicate in the edge and the centre. Phase separation was observed in the edge region in contrast to the centre of the sample. This was most notable in the samples that were treated under vacuum where crystals in the edge region were partially exposed without the surrounding matrix. This can be attributed to a loss of nitrogen in the edge region. The analyses of these individual phases were not possible due to their small size.

Oxynitride glasses are favourable due to their higher glass transition temperatures, good hardness and mechanical properties. However, these glasses contain nitrogen-containing phases makes their oxidation resistance questionable. P7, P8 and P9 glasses heat-treated in chamber furnace under ambient atmospheric conditions revealed their low oxidation resistance. P7 and P8 samples showed swelling after aging in air with porous structures that pointed escaping of nitrogen from glass structures. The P9 glass showed the lowest oxidation resistance and experienced viscous flow at 1200 °C which is almost 200 °C lower temperature as compared to its flowing temperature found during DSC. Moreover, SEM analyses showed highly porous structures for these annealed samples. XRD analyses revealed Y-disilicate and mullite phases in P7 and P8 glasses. There was no D-phase observed in the P8 sample as found in samples heat-treated under nitrogen and argon atmospheres. The experiment in air showed low oxidation resistance of nitrogen-containing glasses. Moreover, oxidation resistance of P9 was even worse as compared to P7 and P8 glasses.

These glasses were used as soldering material for joining SiC components via laser assisted process. These glasses produced glassy interlayer between SiC surfaces. Electron probe analyses of joints revealed sufficient amount of nitrogen in the structure. It showed that nitrogen did not escape during laser joining process. These studies showed that nitrogen-containing glasses can be used as solders for joining of SiC components but joining process should be carried out under inert atmospheres to avoid oxidation of glasses.

6.5 Spark plasma sintering joining of SiC components

The advantages of rapid heating and short processing time of the SPS was utilized for joining SiC components using P1 glass as soldering material. The characterizations of the joining process and joined seams were performed to obtain sound joints between SiC parts.

Firstly, rods of α -SiC were used as matrix for SPS joining, which scattered into small pieces before joining. It shows that even 5 kN pressure was high enough to scatter these rods due to their small surface area. Secondly, plates of SiC were used as matrix and slurry of P1 glass was pasted at the surfaces to be joined. Plates were also scattered during applying directional pressure of 5kN. It was supposed that scattering of plates are either due to coarse glassy powder particles which can act as source of stress concentration or the applied pressure was high enough to break SiC assembly. SPS process was used by Grasso *et al.* [79] for joining of β -SiC by using titanium as soldering material. They found that SPS can be used for joining of SiC components but applied pressure and surface preparation of SiC is very critical steps which must be optimized for sound joint. Rizzo *et al.* [162] utilized SPS process for joining of CVD-SiC coated C/SiC composites. They used different soldering materials for joining that include glasses/glass-ceramics based on calcia, alumina, titanium foils and mixture of SiC powders with 5 wt. % B₄C. They also revealed that SPS can also be used for joining SiC components without applying soldering materials but parameters (pressure, temperature) of joining must be optimized.

By considering above mentioned literature [79, 162], the P1 glass used as solder for joining was grinded to get fine glass powders of less than 5 μm grain sizes so that chances of stress concentration due to coarse grains can be reduced. Two extra plates of SiC were used as sacrificial material to reduced effects of pressure on slurry pasted plates. The application of sacrificial plates worked well for joining SiC plate assembly and produced partially crystalline glassy joints between plates. SEM analyses of the interlayer showed crystals of mullite and Y-disilicate. It revealed that cooling rate was not sufficient to produce glassy interlayer. However, application of P1 glasses provides good wettability with SiC surfaces and continues interfaces without any voids.

This work showed that SPS can be used as joining process for SiC components. However, it is important to optimize parameters of joining in terms of maximum temperature, dwelling time, applied pressure and cooling rate depending upon specimen sizes. Moreover, it will be interesting if joining of SiC components could be conducted with pressureless process, which needs a modification in design of SPS assembly.

7 Conclusion and recommendations

In this study, rare-earth aluminosilicate ($\text{RE}_2\text{O}_3\text{-Al}_2\text{O}_3\text{-SiO}_2$) glasses as solders were used for the joining of SiC components using laser-based process. For this purpose, different $\text{RE}_2\text{O}_3\text{-Al}_2\text{O}_3\text{-SiO}_2$ (RE = Y, Yb, Ho, Dy, Nd and Sc) glasses having composition 12.18% $\text{RE}_2\text{O}_3\text{-22% Al}_2\text{O}_3\text{-65.82% SiO}_2$ (mole %) were prepared using the melt-quench route. The chemical compositions of AlSiY (P1), AlSiYb (P2), AlSiHo (P3), AlSiDy (P4), AlSiNd (P5) and AlSiSc (P6) glasses were determined with XRF and found closely matching with the initial compositions of the oxide mixtures. Structural analyses of glasses revealed typical amorphous structures. They contained symmetric and asymmetric stretching of Si-O-Si bonds, and high contents of Q^3 and Q^4 structural units. The high contents of Q^3 structural units showed uniform distribution of the rare-earth ions and the non-bridging oxygen (NBO). ^{27}Al spectra of P1, P2, and P5 glasses showed higher fractions of AlO_5 and AlO_6 groups. ^{27}Al spectra of P6 glasses revealed 4-, 5-, and 6-fold-coordinated aluminum in this glass system.

Physical properties of glasses were determined to establish a structure-property relationship. It was found that the densities were depending on the atomic mass and on the radii of the rare-earth ions. P5 glasses containing Nd-cations showed the highest density while P6 glasses with Sc-cations have the lowest. The measured hardness values of these glasses have increased with decreasing radii of the rare-earth cations. The refractive indices of glasses were found in the range of 1.68–1.74.

Thermal analyses of prepared rare-earth aluminosilicate glasses showed high glass transition temperatures ($\sim 884\text{--}918\text{ }^\circ\text{C}$) and revealed that smaller cationic radii resulted in higher glass transition temperatures. P2 glasses containing Yb-cations showed the highest value of glass transition temperature which could be attributed to the smaller ionic radius of Yb^{+3} , which tighten structures. Hot-stage XRD of glass powders was performed up to $1200\text{ }^\circ\text{C}$ to evaluate crystals growth behaviour and phase formation. The diffraction patterns recorded showed complete amorphous structures up to $900\text{ }^\circ\text{C}$, and maximum crystallization in P1, P2, P3, P4, and P5 glasses took place between $1100\text{--}1200\text{ }^\circ\text{C}$ and for P6 glasses in the range of $1050\text{--}1100\text{ }^\circ\text{C}$.

Glasses were annealed at $1200\text{ }^\circ\text{C}$ for 1h and 50h holding time, to characterize the formed crystalline structures. The main phases observed were silicates of rare-earth elements and mullite. The feathers like crystals of Y-disilicate surrounded by mullite were in large excess in the P1 sample. The crystals of Yb-disilicate were distributed through the P2 sample and mullite crystals were mainly found at their edges. The crystals of Ho-silicate and mullite were found in the P3 samples. The crystals of Dy-disilicate having feather shapes and surrounded by mullite were found in the P4 sample. The needles like crystals of Nd-disilicate were observed in the P5 sample, which were embedded in the remaining glassy matrix with small amount of mullite phase. The crystals of Sc-disilicate and mullite were observed in the P6 sample, which were not homogenous regarding their size and orientation. Raman spectra of these heat-treated samples revealed high contents of Q^3 structural units due to

uniform distribution of RE^{+3} ions and NBO. IR spectra of these heat-treated samples showed strong asymmetric and symmetric stretching of Si-O-Si with slightly different wave numbers. It was found that crystalline structure morphologies strongly depend on the rare-earth ions present in the glass system.

The prepared glasses were used as solders for joining SiC (SSiC) components with a laser-based process. Glasses showed good wettability with SiC surfaces and produced glassy interlayers except P6 glasses which were crystallized. The joints produced with P1, P3, P4 and P5 glasses showed hermetic tightness in the range of 10^{-10} - 10^{-9} mbar \cdot l \cdot s $^{-1}$ and bending strength to be higher than 120 MPa. The joints made with P5 glasses showed the highest bending strength of 149 ± 22 MPa, whereas joints made with P2 and P6 glasses had the lowest bending strength of 63 and 64 MPa, respectively.

The advantages of microwave heating have been utilized for the crystallization of RE_2O_3 - Al_2O_3 - SiO_2 (RE stands for Nd, Y) glasses. They were heat-treated at 1200 °C for different period of times (no-holding time, 15 min and 30 min) using frequency of 30 GHz. A comparison was made of these microwave-processed samples with samples heat-treated at 1200 °C for 50h in a conventional furnace. It was noticed that crystal nucleation and growth mechanisms were more homogenous in microwave annealed samples. Moreover, it was found that microwave heating enhanced kinetics of crystallization in Y_2O_3 - Al_2O_3 - SiO_2 glass samples. However, its effects on Nd_2O_3 - Al_2O_3 - SiO_2 samples were not so pronounced.

The effects of different nucleating agents (TiO_2 , ZrO_2) and their amounts (4–8 mass %) on the properties and the structures of RE_2O_3 - Al_2O_3 - SiO_2 (RE stands for Nd, Y) glasses were explored. The structural investigations of these nucleating agents containing glasses revealed that additions of TiO_2 contents have significance influence on the structural units in RE_2O_3 - Al_2O_3 - SiO_2 glasses as compared to ZrO_2 . The addition of TiO_2 contents resulted in decreased glass transition and crystallization temperatures in these glasses. A decrease of around 50 °C in glass transition temperature and nearly 100 °C in crystallization temperature were noticed for P1 glasses containing 8% TiO_2 . However, the effects of ZrO_2 addition on transition temperatures were minor as compared to TiO_2 . The heat-treatment of glasses was carried out at 1200 °C for 50h and showed reflections of mullite, Y-disilicate, cristobalite, yttrium-titanium oxide and yttrium-zirconium oxide for P1 glasses. The amount of ternary oxides increased with increasing TiO_2 and ZrO_2 contents in the samples. It was found that addition of nucleating agents strongly enhanced crystallization process in these glasses.

Glasses (RE_2O_3 - Al_2O_3 - SiO_2 - Si_3N_4 , RE stands for Nd, Y) containing different amount of nitrogen contents (4–8.33 mole %) were prepared to find out the effects of changing anions on the structures and the properties of glasses. Thermal analyses of glasses showed that additions of nitrogen have significantly increased glass transition temperatures. Glasses were annealed for different periods of time at 1200 °C under atmospheres of nitrogen, argon, vacuum and air, respectively. The formed crystalline phases were dependent on the composition of the parent glass and annealing conditions. It

was found that addition of nitrogen contents has strong impact on the crystallization and formed crystals. Oxynitride phase (D-phase) was only observed in $Y_2O_3-Al_2O_3-SiO_2-Si_3N_4$ glasses containing 8.33 mole % nitrogen contents. $RE_2O_3-Al_2O_3-SiO_2-Si_3N_4$ glasses showed low oxidation resistance, and have porous structures. $Nd_2O_3-Al_2O_3-SiO_2-Si_3N_4$ glass showed the lowest oxidation resistance and experienced viscous flow at 1200 °C which is almost 200°C lower temperature as compared to its flowing temperature. SiC structural components were joined by using these glasses as solders via laser-assisted method. The joining process was performed under nitrogen atmosphere to avoid oxidation of nitrogen-containing glasses. The qualitative and quantities phase analyses of the prepared joints showed a sound joint between SiC surfaces and glassy interlayer. It was found that nitrogen-containing glasses can be used as soldering material for joining of SiC components. However, it is important that joining process should be performed under inert atmospheres (argon, nitrogen) to avoid the oxidation of these glasses.

Lastly, efforts were made to join SiC (SSiC) components via SPS by using yttrium aluminosilicate glasses as solders. The process parameters for SPS joining were optimized to obtain a sound joint between SiC parts. The characterization of the interface layer between SiC matrix and glassy solder showed crystals of Y-disilicate and mullite.

This work showed that prepared rare-earth aluminosilicate glasses have great potential to be used as solders for joining SiC components. SiC is an important structural ceramic material that finds application different fields of science and technology such as in automotive industry, aerospace industry, heat-exchangers etc. Moreover, SiC is a potential cladding material for nuclear industry. Therefore, it will be interesting to determine stability of these joint components under nuclear atmospheres. It will increase applications of SiC components joined with rare-earth aluminosilicate glasses in nuclear industry. Moreover, these glasses have shown high crystallization and melting temperatures, which shows potential of these glasses as coating materials for high temperature applications. These glasses have potential to be used as vessels to store nuclear waste for longer period of time due to their radiation and oxidation resistance properties. It will be interesting if further experiments scheduled to join SiC components using pressureless SPS process. It will help to establish a comparison between properties of joints made with SPS process and laser-based process.

Acknowledgements

I would like to thank my Professor Hans Juergen Seifert for providing me an opportunity to work at Institute for Applied Materials and Applied Materials Physics (IAM-AWP). I will thanks for his guidance, help and acknowledgement throughout my work. It was great honor for me to work with his team and got professional guidance. I am thankful for his suggestions to make thesis valuable to read.

I would thank Dr. Martin Steinbrueck for his guidance and support. I also paid my deepest gratitude to others members of my group, especially Ulrike Stegmaier and Petra Severloh for their help in purchasing chemicals.

I appreciated all the people at IAM-AWP department. I am particularly indebted to my colleagues who supported me throughout my work. I am thankful for Dr. Harald Leiste for helping in getting X-ray diffractions of samples. I will acknowledge Dr. Thomas Bergfeldt for the chemical analyses of glasses. I am grateful to Dr. Monika Rinke for helping me to get Raman spectra of samples. I will also like to thank Dr. Magnus Rohde for allowing to use differential scanning calorimetry, dilatometers and furnaces. I am obliged for Dr. Morsi Mahmoud for his suggestions and guidance for conducting experiments. I am also grateful to Prof. Michael Hoffmann for allowing working at IAM-KWT. I like to thanks Rainer Muller and Dr. Günter Schell for helping in the preparation of nitrogen-containing glasses and joining of SiC components using sparking plasma sintering equipment at IAM-KWT. I would also thankfulness to Dr. Holger Geßwein for helping in hot-stage XRD experiments at IAM-WPT. I would like to appreciate Stefan Heissler from Institute of Functional Interfaces (IFG) for helping in getting IR spectra and Dr. Stephan Grage from Chair of Biochemistry (IOC) and Department of Molecular Biophysics (IBG-2) for solid state NMR spectra of glasses. I acknowledge Ms. Cathrin Schuler and Ms. Jutta Howell for their help during these years.

The scope of this work could not be completed without the help of Dr. Marion Herrmann and Dr. Wolfgang Lippmann from Technical University of Dresden. The joining experiments of SiC components using laser were conducted by Dr. Marion Herrmann. I am thankful for Dr. Marion Herrmann and Dr. Wolfgang Lipmann for their collaboration throughout in these years.

I am grateful for my parents and family members for their love and support throughout my life. It was great fun to come Karlsruhe and met many new peoples.

Lastly, I am thankful for German research foundation (DFG) for financial support (SE 647/17/1-2) of this work.

8 References

1. Arun K. V., Kathleen A. R., Marlene Wightman, L. David Pye, *Processing, properties, and applications of glass and optical materials*. Vol. 231. 2012.
2. Mauro, J.C. and Zanotto, E.D., *Two centuries of glass research: historical trends, current status, and grand challenges for the future*. Int. J. Appl. Glass Sci. 2014. **5**(3): p. 313-327.
3. Zakery, A. and Elliott, S.R., *Optical properties and applications of chalcogenide glasses: a review*. J. Non-Cryst. Solids, 2003. **330**(1-3): p. 1-12.
4. Lemerrier, H., Rouxel, T., Fargeot, D., Besson, J.L., and Piriou, B., *Yttrium SiAlON glasses: structure and mechanical properties—elasticity and viscosity*. J. Non-Cryst. Solids, 1996. **201**(1): p. 128-145.
5. Menke, Y., Peltier-Baron, V., and Hampshire, S., *Effect of rare-earth cations on properties of sialon glasses*. J. Non-Cryst. Solids, 2000. **276**(1-3): p. 145-150.
6. Can, A., Herrmann, M., McLachlan, D.S., Sigalas, I., and Adler, J., *Densification of liquid phase sintered silicon carbide*. J. Eur. Ceram. Soc., 2006. **26**(9): p. 1707-1713.
7. Hampshire, S. and Pomeroy, M.J., *Oxynitride Glasses*. Int. J. Appl. Ceram. Tech., 2008. **5**(2): p. 155-163.
8. White J. E, Day D.E., *Rare-earth aluminosilicate glasses for in vivo radiation delivery*. Key Eng. Mater., 1994. **94-95**: p. 181-208.
9. Caurant, D., Majerus, O., Loiseau, P., Bardez, I., Baffier, N., and Dussossoy, J.L., *Crystallization of neodymium-rich phases in silicate glasses developed for nuclear waste immobilization*. J. Nucl. Mater., 2006. **354**(1-3): p. 143-162.
10. Baesso, M., Bento, A., Miranda, L., De Souza, D., Sampaio, J., and Nunes, L., *Rare-earth doped low silica calcium aluminosilicate glasses for near and mid infrared applications*. J. Non-Cryst. Solids, 2000. **276**(1): p. 8-18.
11. Herrmann, M., Lippmann, W., and Hurtado, A., *Y_2O_3 - Al_2O_3 - SiO_2 -based glass-ceramic fillers for the laser-supported joining of SiC*. J. Eur. Ceram. Soc., 2014. **34**(8): p. 1935-1948.
12. Ahmad, S., Herrmann, M., Mahmoud, M.M., Lippmann, W., Hurtado, A., and Seifert, H.J., *Application of Nd_2O_3 - Al_2O_3 - SiO_2 glass solder for joining of silicon carbide components*. J. Eur. Ceram. Soc., 2016. **36**(7): p. 1559-1569.
13. Hyatt, M.J. and Day, D.E., *Glass properties in the yttria-alumina-silica system*. J. Am. Ceram. Soc., 1987. **70**(10): p. C-283-C-287.
14. Johnson, J., Weber, R., and Grimsditch, M., *Thermal and mechanical properties of rare-earth aluminate and low-silica aluminosilicate optical glasses*. J. Non-Cryst. Solids, 2005. **351**(8-9): p. 650-655.
15. Marchi, J., Morais, D., Schneider, J., Bressiani, J., and Bressiani, A., *Characterization of rare earth aluminosilicate glasses*. J. Non-Cryst. Solids, 2005. **351**(10): p. 863-868.
16. Sadiki, N., Coutures, J.P., Fillet, C., and Dussossoy, J.L., *Crystallization of lanthanum and yttrium aluminosilicate glasses*. J. Nucl. Mater., 2006. **348**(1): p. 70-78.
17. Snead, L.L., Nozawa, T., Katoh, Y., Byun, T.-S., Kondo, S., and Petti, D.A., *Handbook of SiC properties for fuel performance modeling*. J. Nucl. Mater., 2007. **371**(1-3): p. 329-377.
18. Nozawa, T., Hinoki, T., Hasegawa, A., Kohyama, A., Katoh, Y., Snead, L.L., Henager, C.H., and Hegeman, J., *Recent advances and issues in development of silicon carbide composites for fusion applications*. J. Nucl. Mater., 2009. **386**: p. 622-627.
19. Halbig, M.C., Singh, M., Shpargel, T., and Kiser, J.D., *Diffusion bonding of silicon carbide for MEMS-LDI applications, in mechanical properties and performance of engineering ceramics and composites III*. 2009, John Wiley & Sons, Inc. p. 491-501.
20. Nascimento, R.M.d., Martinelli, A.E., and Buschinelli, A.J.A., *Review Article: recent advances in metal-ceramic brazing*. Cerâmica, 2003. **49**: p. 178-198.
21. Vogel, W., *Glass Chemistry*. Vol. 2. 1994: Springer Berlin Heidelberg.
22. Shelby, J.E., *Introduction to glass science and technology*. Vol. 2. 2005: Royal society of chemistry, Cambridge.
23. Zachariasen, W.H., *The atomic arrangement in glass*. J. Am. Chem. Soc., 1932. **54**(10): p. 3841-3851.

24. Warren, B.E., Krutter, H., and Morningstar, O., *Fourier analysis of X-ray patterns of vitreous SiO₂ and B₂O₂*. J. Am. Ceram. Soc., 1936. **19**(1-12): p. 202-206.
25. Warren, B.E., *Summary of work on atomic arrangement in glass*. J. Am. Ceram. Soc., 1941. **24**(8): p. 256-261.
26. Dietzel, A., *Die Kationenfeldstärken und ihre Beziehungen zu Entglasungsvorgängen, zur Verbindungsbildung und zu den Schmelzpunkten von Silicaten*. Zeitschrift für Elektrochemie und angewandte physikalische Chemie, 1942. **48**(1): p. 9-23.
27. Smekal, G., *On the structure of glass*. J. Soc. Glass Tech., 1951. **35**: p. 392-394.
28. Stanworth, J.E., *Physical properties of glass*. 1950: Clarendon Press.
29. Sun, K.-H., *Fundamental condition of glass formation*. J. Am. Ceram. Soc., 1947. **30**(9): p. 277-281.
30. Rawson, H., *Inorganic glass-forming systems* 1967: Academic Press.
31. Schmelzer, J.W.P., *Crystal nucleation and growth in glass-forming melts: Experiment and theory*. J. Non-Cryst. Solids, 2008. **354**(2-9): p. 269-278.
32. Kalikmanov, V.I., *Classical nucleation theory* 2013, Springer Netherlands: Dordrecht. p. 17-41.
33. Rawlings, J.B., Miller, S.M., and Witkowski, W.R., *Model identification and control of solution crystallization processes: a review*. Ind. Eng. Chem. Res., 1993. **32**(7): p. 1275-1296.
34. Fokin, V.M., Zanutto, E.D., Yuritsyn, N.S., and Schmelzer, J.W.P., *Homogeneous crystal nucleation in silicate glasses: A 40 years perspective*. J. Non-Cryst. Solids, 2006. **352**(26-27): p. 2681-2714.
35. Zanutto, E.D., *Glass crystallization research—A 36-Year retrospective. Part I, fundamental studies*. Int. J. Appl. Glass Sci., 2013. **4**(2): p. 105-116.
36. Zanutto, E.D., *Glass crystallization research—A 36-Year retrospective. Part II, methods of study and glass-ceramics*. Int. J. Appl. Glass Sci., 2013. **4**(2): p. 117-124.
37. Condrate Sr, R., *Infrared and raman spectra of glasses containing rare earth ions*. in *Key Eng. Mater.* 1994. Trans Tech Publ.
38. McMillan, P., *Structural studies of silicate glasses and melts—applications and limitations of Raman spectroscopy*. J. Am. Mineral, 1984. **69**(7-8): p. 622-644.
39. Shannon, R., *Revised effective ionic radii and systematic studies of interatomic distances in halides and chalcogenides*. Acta Crystallographica Section A: Crystal Physics, Diffraction, Theoretical and General Crystallography, 1976. **32**(5): p. 751-767.
40. Shelby, J.E., *Rare elements in glasses*. Vol. 94-95. 1994: Trans tech publications.
41. Makehima, A., Tamura, Y., and Sakaino, T., *Elastic moduli and refractive indices of aluminosilicate glasses containing Y₂O₃, La₂O₃ and TiO₂*. J. Am. Ceram. Soc., 1978. **61**(5-6): p. 247-249.
42. Makishima, A., Kobayashi, M., Shimohira, T., and Nagata, T., *Formation of aluminosilicate glasses containing rare-earth oxides*. J. Am. Ceram. Soc., 1982. **65**(12): p. C-210-C-211.
43. Shelby, J.E. and Kohli, J.T., *Rare-earth aluminosilicate glasses*. J. Am. Ceram. Soc., 1990. **73**(1): p. 39-42.
44. Kohli, J. and Shelby, J., *Formation and properties of rare-earth aluminosilicate glasses*. Phys. Chem. Glasses, 1991. **32**(2): p. 67-71.
45. Kohli, J.T. and Shelby, J.E., *Rare-earth aluminogermanate glasses*. J. Am. Ceram. Soc, 1991. **74**(5): p. 1031-1035.
46. J. E. White, D.E.D., *Rare-earth aluminosilicate glasses for in vivo radiation delivery*. Key Eng. Mater., 1994. **94-95**: p. 181-208.
47. Arita, I.H., Wilkinson, D.S., and Purdy, G.R., *Crystallization of yttria–alumina–silica glasses*. J. Am. Ceram. Soc., 1992. **75**(12): p. 3315-3320.
48. Bondar, I.A. and Galakhov, F.Y., *Phase equilibria in the system Y₂O₃-Al₂O₃-SiO₂*. Bulletin of the Academy of Sciences of the USSR, Division of chemical science, 1964. **13**(7): p. 1231-1232.
49. Shelby, J.E. *Scandium, yttrium and indium in oxide glasses*. in *Key Eng. Mater.*, 1994. Trans Tech Publ.
50. Kolitsch, U., Seifert, H., Ludwig, T., and Aldinger, F., *Phase equilibria and crystal chemistry in the Y₂O₃–Al₂O₃–SiO₂ system*. J. Mater. Res., 1999. **14**(02): p. 447-455.

51. Kamitsos, E.I., *Infrared spectroscopy of glasses*, in *modern glass characterization*. 2015, John Wiley & Sons, Inc. p. 1-42.
52. Wang, J., Brocklesby, W.S., Lincoln, J.R., Townsend, J.E., and Payne, D.N., *Local structures of rare-earth ions in glasses: the 'crystal-chemistry' approach*. *J. Non-Cryst. Solids*, 1993. **163**(3): p. 261-267.
53. Stevansson, B. and Edén, M., *Structural rationalization of the microhardness trends of rare-earth aluminosilicate glasses: Interplay between the RE³⁺ field-strength and the aluminum coordinations*. *J. Non-Cryst. Solids*, 2013. **378**: p. 163-167.
54. Rawson, H., *Properties and applications of glass*. 1980: Elsevier Scientific Pub. Co.
55. Kohli, J., Condrate, R., and Shelby, J., *Raman and infrared spectra of rare-earth aluminosilicate glasses*. *Phys. Chem. Glasses*, 1993. **34**(3): p. 81-87.
56. Todea, M., Frentiu, B., Turcu, R.F.V., and Simon, S., *Structural properties of yttrium aluminosilicates microspheres*. *J. Phys. Chem. Solids*, 2011. **72**(3): p. 164-168.
57. Du, J., *Molecular dynamics simulations of the structure and properties of low silica yttrium aluminosilicate glasses*. *J. Am. Ceram. Soc.*, 2009. **92**(1): p. 87-95.
58. Murakami, Y. and Yamamoto, H., *Phase equilibria and properties of glasses in the Al₂O₃-Yb₂O₃-SiO₂ system*. *J. Ceram. Soc. Jpn.*, 1993. **101**(1178): p. 1101-1106.
59. Li, L., Tang, Z., Sun, W., and Wang, P., *Calculation of phase diagrams of Al₂O₃-SiO₂-R₂O₃ systems*. *Phys. Chem. Glasses*, 1997. **38**(6): p. 323-326.
60. Ball, R.K., Lewis, M.H., Szweda, A., and Butler, E., *Ceramics and glasses in the Sc-Si-Al-O-N system*. *Mat. Sci. and Eng.*, 1985. **71**(Supplement C): p. 137-145.
61. Tanabe, S., Hirao, K., and Soga, N., *Elastic properties and molar volume of rare-earth aluminosilicate glasses*. *J. Am. Ceram. Soc.*, 1992. **75**(3): p. 503-506.
62. Makishima, A., Kubo, H., Kotani, K., Tsutsumi, M., and Asami, M., *Formation and crystallization in the yttrium aluminosilicate glasses containing zinc oxide*. *J. Am. Ceram. Soc.*, 1986. **69**(12): p. 294-296.
63. Erbe, E.M. and Day, D.E., *Properties of Sm₂O₃-Al₂O₃-SiO₂ glasses for in vivo applications*. *J. Am. Ceram. Soc.*, 1990. **73**(9): p. 2708-2713.
64. Pèlegri, E., Calas, G., Ildefonse, P., Jollivet, P., and Galois, L., *Structural evolution of glass surface during alteration: Application to nuclear waste glasses*. *J. Non-Cryst. Solids*, 2010. **356**(44-49): p. 2497-2508.
65. Kohli, J.T. and Shelby, J.E., *Magneto-optical properties of rare-earth aluminosilicate glasses*. *Phys. Chem. Glasses*, 1991. **32**(3): p. 109-114.
66. Clark, D.E. and Sutton, W.H., *Microwave processing of materials*. *Annu. Rev. Mater. Sci.*, 1996. **26**(1): p. 299-331.
67. Singh, S., Gupta, D., Jain, V., and Sharma, A.K., *Microwave processing of materials and applications in manufacturing industries: a review*. *Mater. Manuf. Processes*, 2015. **30**(1): p. 1-29.
68. Sutton, W.H., *Microwave processing of ceramics - An overview*. *MRS Proceedings*, 1992. **269**.
69. Freeman, S., Booske, J., and Cooper, R., *Novel method for measuring intense microwave radiation effects on ionic transport in ceramic materials*. *Rev. Sci. Instrum.*, 1995. **66**(6): p. 3606-3609.
70. Thostenson, E.T. and Chou, T.W., *Microwave processing: fundamentals and applications*. *composites Part A: Appl. Sci. and Manu.*, 1999. **30**(9): p. 1055-1071.
71. Clark, D.E., Folz, D.C., and West, J.K., *Processing materials with microwave energy*. *Mater. Sci. and Eng.: A*, 2000. **287**(2): p. 153-158.
72. Mahmoud, M.M. and Thumm, M., *Crystallization of lithium disilicate glass using high frequency microwave processing*. *J. Eur. Ceram. Soc.*, 2015. **35**(10): p. 2915-2922.
73. Sun, J., Wang, W., and Yue, Q., *Review on microwave-matter interaction fundamentals and efficient microwave-associated heating strategies*. *Materials*, 2016. **9**(4): p. 231.
74. David E. Clark, Stephen J. Oda, Richard S., *Microwaves: theory and application in materials processing III (Ceramic Transactions)* 1995.
75. Clark, D.E., *Microwave processing: present status and future promise*, in *proceedings of the 17th annual conference on composites and advanced ceramic materials: Ceramic Engineering and Science Proceedings*. 2008, John Wiley & Sons, Inc. p. 3-21.

76. Janney, M.A. and Kimrey, H.D. *Diffusion-controlled processes in microwave-fired oxide ceramics*. in *MRS Proceedings*. 1990. Cambridge Univ Press.
77. Pert, E., Carmel, Y., Birnboim, A., Olorunyolemi, T., Gershon, D., Calame, J., Lloyd, I.K., and Wilson, O.C., *Temperature measurements during microwave processing: the significance of thermocouple effects*. *J. Am. Ceram. Soc.*, 2001. **84**(9): p. 1981-1986.
78. Sakamoto, A. and Yamamoto, S., *Glass–Ceramics: engineering principles and applications*. *Int. J. Appl. Glass Sci.*, 2010. **1**(3): p. 237-247.
79. Grasso, S., Tatarko, P., Rizzo, S., Porwal, H., Hu, C., Katoh, Y., Salvo, M., Reece, M.J., and Ferraris, M., *Joining of β -SiC by spark plasma sintering*. *J. Eur. Ceram. Soc.*, 2014. **34**(7): p. 1681-1686.
80. Jacobson, N.S., *Corrosion of silicon-based ceramics in combustion environments*. *J. Am. Ceram. Soc.*, 1993. **76**(1): p. 3-28.
81. Fernie, J.A., Lewis, M.H., and Leng-Ward, G., *Crystallisation of Nd–Si–Al–O–N glasses*. *Mater. Lett.*, 1989. **9**(1): p. 29-32.
82. Murakami, Y. and Yamamoto, H., *Properties of oxynitride glasses in the Ln–Si–Al–O–N systems (Ln=Rare–earth)*. *J. Ceram. Soc. Jpn.*, 1994. **102**(1183): p. 231-236.
83. Ohashi, M., Nakamura, K., Hirao, K., Kanzaki, S., and Hampshire, S., *Formation and properties of Ln–Si–O–N glasses (Ln = Lanthanides or Y)*. *J. Am. Ceram. Soc.*, 1995. **78**(1): p. 71-76.
84. Hampshire, S., *Oxynitride glasses, their properties and crystallisation – a review*. *J. Non-Cryst. Solids*, 2003. **316**(1): p. 64-73.
85. Mailliar, O., Hodaj, F., Chaumat, V., and Eustathopoulos, N., *Influence of oxygen partial pressure on the wetting of SiC by a Co–Si alloy*. *Mater. Sci. Eng.: A*, 2008. **495**(1): p. 174-180.
86. Guinel, M.J.F. and Norton, M.G., *Blowing of silica microforms on silicon carbide*. *J. Non-Cryst. Solids*, 2005. **351**(3): p. 251-257.
87. Liddell, K., Mandal, H., and Thompson, D.P., *X-ray data for new Y–Si–Al–O–N glass ceramics*. *J. Eur. Ceram. Soc.*, 1997. **17**(6): p. 781-787.
88. Liddell, K. and Thompson, D.P., *Heat treatment of wollastonite-type Y–Si–Al–O–N glasses*. *J. Mater. Sci.*, 1997. **32**(4): p. 887-892.
89. Sakka, S., *Structure, properties and application of oxynitride glasses*. *J. Non-Cryst. Solids*, 1995. **181**(3): p. 215-224.
90. Chen, J., Wei, P., and Huang, Y., *Formation and properties of La–Y–Si–O–N oxynitride glasses*. *J. Mater. Sci. Lett.*, 1997. **16**(18): p. 1486-1488.
91. Graaf, D., *Chemistry, structure and properties of rare-earth containing Si–Al–O–N glasses*. 2004: Technische Universiteit Eindhoven.
92. Hampshire, S. and Pomeroy, M.J., *Silicon nitride—grain boundary oxynitride glass interfaces: deductions from glass bulk properties*. *Int. J. Appl. Ceram. Tech.*, 2013. **10**(5): p. 747-755.
93. Becher, P.F., Hampshire, S., Pomeroy, M.J., Hoffmann, M.J., Lance, M.J., and Satet, R.L., *An overview of the structure and properties of silicon-based oxynitride glasses*. *Int. J. Appl. Glass Sci.*, 2011. **2**(1): p. 63-83.
94. Sebai, M., Sjöberg, J., Goursat, P., Nestor, E., Flynn, R., Ramesh, R., and Hampshire, S., *Oxidation behaviour of yttrium and neodymium oxynitride glasses*. *J. Eur. Ceram. Soc.*, 1995. **15**(10): p. 1015-1024.
95. Ramesh, R., Nestor, E., Pomeroy, M.J., Hampshire, S., Liddell, K., and Thompson, D.P., *Potential of Nd–Si–Al–O–N glasses for crystallisation to glass-ceramics*. *J. Non-Cryst. Solids*, 1996. **196**: p. 320-325.
96. Lofaj, F., Dériano, S., LeFloch, M., Rouxel, T., and Hoffmann, M.J., *Structure and rheological properties of the RE–Si–Mg–O–N (RE = Sc, Y, La, Nd, Sm, Gd, Yb and Lu) glasses*. *J. Non-Cryst. Solids*, 2004. **344**(1–2): p. 8-16.
97. Pomeroy, M.J., Nestor, E., Ramesh, R., and Hampshire, S., *Properties and crystallization of rare–earth Si–Al–O–N glasses containing mixed trivalent modifiers*. *J. Am. Ceram. Soc.*, 2005. **88**(4): p. 875-881.
98. Hampshire, S. and Pomeroy, M.J., *Properties of rare-earth oxynitride glasses and the implications for high temperature behaviour of silicon nitride ceramics*, in *28th international*

- conference on advanced ceramics and composites B: Ceram. Eng. Sci. Proceedings. 2008, John Wiley & Sons, Inc. p. 2-8.
99. Kamitsos, E.I., Yiannopoulos, Y.D., Varsamis, C.P., and Jain, H., *Structure-property correlation in glasses by infrared reflectance spectroscopy*. J. Non-Cryst. Solids, 1997. **222**: p. 59-68.
 100. Schrader, B., *Infrared and Raman spectroscopy: methods and applications*. 2007.
 101. Gunzler, H.U., *IR Spectroscopy: An introduction*, 2002: Wiley-Vch Verlag GmbH.
 102. Nakamoto, K., *Infrared and Raman spectra of inorganic and coordination compounds: Part A: Theory and Applications in Inorganic Chemistry*. 6th ed. 2008.
 103. Müller, U., *M. Diem: Introduction to modern vibrational spectroscopy*, J. Wiley, New York, Chichester, 1994. **98**(10): p. 1347-1348.
 104. Maehara, T., Yano, T., Shibata, S., and Yamane, M., *Structure and phase transformation of alkali silicate melts analysed by Raman spectroscopy*. Philosophical Magazine, 2004. **84**(29): p. 3085-3099.
 105. McMillan, P. and Piriou, B., *Raman spectroscopic studies of silicate and related glass structure—a review*. Bull. Mineral, 1983. **106**(5): p. 7-75.
 106. McMillan, P., *Structural studies of silicate glasses and melts—applications and limitations of Raman spectroscopy*. Am. Mineral, 1984. **69**(7-8): p. 622-644.
 107. Mahmoud, M.M., *Crystallization of lithium disilicate glass using variable frequency microwave processing*. 2007.
 108. Stebbins, J.F., *NMR studies of oxide glass structure, in solid-state NMR spectroscopy principles and applications*. 2007, Blackwell Science Ltd. p. 391-436.
 109. Duer, M.J., *The basics of solid-state NMR, in solid-state NMR spectroscopy principles and applications*. 2007, Blackwell Science Ltd. p. 1-72.
 110. Schaller, T. and Stebbins, J.F., *The structural role of lanthanum and yttrium in aluminosilicate glasses: A ²⁷Al and ¹⁷O MAS NMR study*. J. Phys. Chem. B, 1998. **102**(52): p. 10690-10697.
 111. Gabbott, P., *Principles and applications of thermal analysis*. 2008: John Wiley & Sons.
 112. Günther Höhne, W.H., H.-J. Flammersheim, *Differential scanning calorimetry: An introduction for practitioners*. 2nd ed. 2003: Springer-Verlag.
 113. Goela, J., Burns, L., and Taylor, R., *Transparent chemical vapor deposited β -SiC*. Appl. Phys. Lett., 1994. **64**(2): p. 131-133.
 114. Xu, S.J., Zhou, J.G., Yang, B., and Zhang, B.Z., *Effect of deposition temperature on the properties of pyrolytic SiC*. J. Nucl. Mater., 1995. **224**(1): p. 12-16.
 115. Yajima, S., Hayashi, J., Omori, M., and Okamura, K., *Development of a silicon carbide fibre with high tensile strength*. Nature, 1976. **261**(5562): p. 683-685.
 116. Ishikawa, T., Kohtoku, Y., Kumagawa, K., Yamamura, T., and Nagasawa, T., *High strength alkali-resistant sintered SiC fibre stable to 2200 °C*. Nature, 1998. **391**(6669): p. 773-775.
 117. Jepps, N.W. and Page, T.F., *Polytypic transformations in silicon carbide*. Progress in crystal growth and characterization, 1983. **7**(1): p. 259-307.
 118. Pirouz, P. and Yang, J.W., *Polytypic transformations in SiC: the role of TEM*. Ultramicroscopy, 1993. **51**(1): p. 189-214.
 119. Fisher, G. and Barnes, P., *Towards a unified view of polytypism in silicon carbide*. Philos. Mag. B, 1990. **61**(2): p. 217-236.
 120. Dhanaraj, G., Raghothamachar, B., and Dudley, M., *Growth and characterization of silicon carbide crystals*. 2010, Springer Berlin Heidelberg: p. 797-820.
 121. Singhal, S.C., *Thermodynamic analysis of the high-temperature stability of silicon nitride and silicon carbide*. Ceram. Int., 1976. **2**(3): p. 123-130.
 122. Collins, A.K., Pickering, M.A., and Taylor, R.L., *Grain size dependence of the thermal conductivity of polycrystalline chemical vapor deposited β -SiC at low temperatures*. J. Appl. Phys., 1990. **68**(12): p. 6510-6512.
 123. Sigl, L.S., *Thermal conductivity of liquid phase sintered silicon carbide*. J. Eur. Ceram. Soc., 2003. **23**(7): p. 1115-1122.
 124. Katoh, Y., Snead, L.L., Cheng, T., Shih, C., Lewis, W.D., Koyanagi, T., Hinoki, T., Henager Jr, C.H., and Ferraris, M., *Radiation-tolerant joining technologies for silicon carbide ceramics and composites*. J. Nucl. Mater., 2014. **448**(1-3): p. 497-511.

125. Halbig, M.C., Singh, M., Shpargel, T., and Kiser, J.D. *Diffusion bonding of silicon carbide for MEMS-LDI applications*. *Ceram. Eng. and Sci. Proc.* 2008.
126. Cockeram, B.V., *Flexural strength and shear strength of silicon carbide to silicon carbide joints fabricated by a molybdenum diffusion bonding technique*. *J. Am. Ceram. Soc.*, 2005. **88**(7): p. 1892-1899.
127. Gottselig, B., Gyarmati, E., Naoumidis, A., and Nickel, H., *Joining of ceramics demonstrated by the example of SiC/Ti*. *J. Eur. Ceram. Soc.*, 1990. **6**(3): p. 153-160.
128. Suyama, S., Itoh, Y., Kohyama, A., and Katoh, Y., *Development of high strength reaction-sintered silicon carbide*. *J. Ceram. Soc. Jap.*, 2001. **109**(1268): p. 315-321.
129. Katoh, Y., Snead, L.L., Cheng, T., Shih, C., Lewis, W.D., Koyanagi, T., Hinoki, T., Henager, C.H., and Ferraris, M., *Radiation-tolerant joining technologies for silicon carbide ceramics and composites*. *J. Nucl. Mater.*, 2014. **448**(1): p. 497-511.
130. Sherwood, W.J., Whitmarsh, C.K., Jacobs, J.M., and Interrante, L.V., *Joining ceramic composites using active metal/HPCS preceramic polymer slurries*. *Ceram. Eng. and Sci. Proc.*, 1997. **18**(3 A): p. 177-184.
131. Lewinsohn, C.A., Colombo, P., Reimanis, I., and Ünal, Ö., *Stresses occurring during joining of ceramics using preceramic polymers*. *J. Am. Ceram. Soc.*, 2001. **84**(10): p. 2240-2244.
132. Interrante, L.V., Whitmarsh, C.W., Sherwood, W., Wu, H.J., Lewis, R., and Maciel, G. *High yield polycarbosilane precursors to stoichiometric SiC. Synthesis, pyrolysis and application*. *Mater. Res. Soc. Symp. - Proc.* 1994.
133. Kotani, M., Inoue, T., Kohyama, A., Katoh, Y., and Okamura, K., *Effect of SiC particle dispersion on microstructure and mechanical properties of polymer-derived SiC/SiC composite*. *Mater. Sci. Eng.: A*, 2003. **357**(1-2): p. 376-385.
134. A. Gasse, F.S.A., G. Coing Boyat, *Specific nonreactive basic alloys for SiC-SiC joining*, . Commissariat à l'énergie atomique et aux énergies alternatives, Grenoble, France, 1997.
135. Chaumat, G., Drevet, B., and Vernier, L., *Reactive brazing study of a silicon nitride to metal joining*. *J. Eur. Ceram. Soc.*, 1997. **17**(15-16): p. 1925-1927.
136. Katoh, Y., Dong, S.M., and Kohyama, A., *Thermo-mechanical properties and microstructure of silicon carbide composites fabricated by nano-infiltrated transient eutectoid process*. *Fusion Eng. Des.*, 2002. **61-62**: p. 723-731.
137. Koyanagi, T., Ozawa, K., Hinoki, T., Shimoda, K., and Katoh, Y., *Effects of neutron irradiation on mechanical properties of silicon carbide composites fabricated by nano-infiltration and transient eutectic-phase process*. *J. Nucl. Mater.*, 2014. **448**(1-3): p. 478-486.
138. Barsoum, M.W., and Tamer El-Raghy, *The MAX phases: unique new carbide and nitride materials ternary ceramics turn out to be surprisingly soft and machinable, yet also heat-tolerant, strong and lightweight*. *Am. Sci.*, 2001. **89**: p. 334-343.
139. Dong, H., Man, W., and Li, S., *Joining of SiC ceramic with ternary carbide Ti_3SiC_2* , in *Mater. Sci. Forum.* 2005. p. 1255-1258.
140. Ferraris, M., Salvo, M., Casalegno, V., Ciampichetti, A., Smeacetto, F., and Zucchetti, M., *Joining of machined SiC/SiC composites for thermonuclear fusion reactors*. *J. Nucl. Mater.*, 2008. **375**(3): p. 410-415.
141. Ferraris, M., Salvo, M., Casalegno, V., Han, S., Katoh, Y., Jung, H.C., Hinoki, T., and Kohyama, A., *Joining of SiC-based materials for nuclear energy applications*. *J. Nucl. Mater.*, 2011. **417**(1-3): p. 379-382.
142. Lippmann, W., Knorr, J., Wolf, R., Rasper, R., Exner, H., Reinecke, A.-M., Nieher, M., and Schreiber, R., *Laser joining of silicon carbide—a new technology for ultra-high temperature resistant joints*. *Nucl. Eng. Des.*, 2004. **231**(2): p. 151-161.
143. Herrmann, M., Lippmann, W., and Hurtado, A., *High-temperature stability of laser-joined silicon carbide components*. *J. Nucl. Mater.*, 2013. **443**(1-3): p. 458-466.
144. Pinc, W.R., Di Prima, M., Walker, L.S., Wing, Z.N., and Corral, E.L., *Spark plasma joining of ZrB_2 -SiC composites using zirconium-boron reactive filler layers*. *J. Am. Ceram. Soc.*, 2011. **94**(11): p. 3825-3832.
145. Brown, M.S. and Arnold, C.B., *Fundamentals of laser-material interaction and application to multiscale surface modification*, in *laser precision microfabrication*. 2010, Springer Berlin Heidelberg: p. 91-120.

146. Majumdar, J.D. and Manna, I., *Introduction to laser assisted fabrication of materials*, in *laser-assisted fabrication of materials*. 2013, Springer Berlin Heidelberg: p.1-67.
147. Drew, R.A.L., Hampshire, S., and Jack, K.H., *Preparation and properties of oxynitride glasses*, in *Progress in Nitrogen Ceramics*, Riley, F.L., Editor. 1983, Springer Netherlands: p. 323-330.
148. Efimov, A.M., *Vibrational spectra, related properties, and structure of inorganic glasses*. J. Non-Cryst. Solids, 1999. **253**(1-3): p. 95-118.
149. Labet, V. and Colomban, P., *Vibrational properties of silicates*. J. Non-Cryst. Solids, 2013. **370**: p. 10-17.
150. Iftekhar, S., Grins, J., Gunawidjaja, P.N., and Edén, M., *Glass Formation and Structure-Property-Composition Relations of the RE₂O₃-Al₂O₃-SiO₂ (RE=La, Y, Lu, Sc) Systems*. J. Am. Ceram. Soc., 2011. **94**(8): p. 2429-2435.
151. Ludwig, T., *Thermoanalytische und konstitutionelle Charakterisierung des Systems Si₃N₄-Y₂O₃-Al₂O₃-SiO₂*. 2008.
152. Baghshahi, S., Brungs, M.P., Sorrell, C.C., and Kim, H.S., *Surface crystallization of rare-earth aluminosilicate glasses*. J. Non-Cryst. Solids, 2001. **290**(2-3): p. 208-215.
153. Fuxi, G., *Optical and spectroscopic properties of glass*. 1992: Springer Berlin.
154. Yadav, A.K. and Singh, P., *A review of the structures of oxide glasses by Raman spectroscopy*. RSC Advances, 2015. **5**(83): p. 67583-67609.
155. Pahari, B., Iftekhar, S., Jaworski, A., Jansson, K., Grins, J. Edén, M., *Composition-property-structure correlations of scandium aluminosilicate glasses revealed by multinuclear ⁴⁵Sc, ²⁷Al, and ²⁹Si Solid-State NMR*. J. Am. Ceram. Soc., 2012. **95**(8): p. 2545-2553.
156. Samal, S., Lee, J., Jeong, D.-Y., and Kim, H., *Characterization of thermal conductivity of SiO₂-Al₂O₃-Y₂O₃ glasses*. Thermochim Acta, 2015. **604**: p. 1-6.
157. Lichvár, P., Šajgalík, P., Liška, M., and Galusek, D., *CaO-SiO₂-Al₂O₃-Y₂O₃ glasses as model grain boundary phases for Si₃N₄ ceramics*. J. Eur. Ceram. Soc., 2007. **27**(1): p. 429-436.
158. Perham, T.J., de Jonghe, L.C., and MoberlyChan, W.J., *Joining of silicon carbide with a cordierite glass-ceramic*. J. Am. Ceram. Soc., 1999. **82**(2): p. 297-305.
159. Hille, C., Lippmann, W., and Hurtado, A., *Electrically conductive ceramics and new joining technology for applications in HTR engineering*. Nucl. Eng. Des., 2012. **251**: p. 222-229.
160. Kim, H. and Choi, W., *Surface and bulk crystallization in Nd₂O₃-Al₂O₃-SiO₂-TiO₂ glasses*. J. Eur. Ceram. Soc., 2004. **24**(7): p. 2103-2111.
161. Felsche, J., *Crystal data on the polymorphic disilicate Y₂Si₂O₇*. Naturwissenschaften, 1970. **57**(3): p. 127-128.
162. Rizzo, S., Grasso, S., Salvo, M., Casalegno, V., Reece, M.J., and Ferraris, M., *Joining of C/SiC composites by spark plasma sintering technique*. J. Eur. Ceram. Soc., 2014. **34**(4): p. 903-913.